

Wing Mounted Ice Penetrating Radar Array for a Medium Altitude Long Endurance Remote Aircraft

by

Dustin James Grorud

B.S., University of Kansas, Lawrence, Kansas 2009

Submitted to the graduate degree program in Aerospace Engineering and the Graduate Faculty
of the University of Kansas in partial fulfillment of the requirements for the degree of Master of
Science

Chairperson Dr. Richard Hale

Dr. Mark Ewing

Dr. Shahriar Keshmiri

Date Defended: August 27th, 2012

The Thesis Committee for Dustin James Grorud

Certifies that this is the approved version of the following thesis

**Wing Mounted Ice Penetrating Radar Array for a Medium Altitude
Long Endurance Remote Aircraft**

Chairperson Dr. Richard Hale

Date Approved: August 27th, 2012

Abstract

A wing mounted ice penetrating radar array for remote sensing is presented. The structure is designed to carry radar antennas on a representative unmanned aircraft to enable airborne sounding and imaging of ice sheets in cryospheric climates. Current unmanned aircraft are presented and representative aircraft characteristics are selected based on currently fielded aircraft. A brief structural analysis of the possible platforms is presented to assess the relative wing flexibility of such platforms, and thus to establish the interface boundary displacement and rotation conditions associated with a wing curvature that the wing mounted array must withstand during flight. The aircraft characteristics and wing curvature are used to develop a sizing condition for the wing mounted array. The sized array is presented component by component with geometry and stress information. A modal analysis is also presented to ensure that the structure is safe from possible sources of vibration. The aircraft performance impacts are then explored to verify the feasibility of the platform. A three antenna array pylon mounted array near each wing root is shown to be feasible in preliminary design, though service issues associated with icing, vortex shedding and downstream performance effects on the pusher-propeller configuration must be examined in greater detail.

Table of Contents

	Page #
List of Figures.....	v
List of Tables	xi
List of Symbols.....	xiii
1 Introduction.....	1
2 Related Work	4
2.1 Remote Sensing	4
2.2 Unmanned Aerial Vehicles (UAVs)	5
2.3 Summary.....	8
3 Sizing of Array	9
3.1 Description of the Problem.....	9
3.2 Curvature Model and Loads Development.....	13
3.3 Geometry	64
3.4 FEM Model.....	72
3.5 Sizing	81
3.6 Fastener Sizing.....	156
3.7 Modal Analysis	166
4 Performance Comparison	169
5 Conclusions and Recommendations	177
5.1 Conclusions.....	177
5.2 Recommendations.....	178
6 References.....	180
Appendix A: Aerodynamic Regions.....	A-1
Appendix B: AAA Model Information.....	A-10

List of Figures

Figure 1: Sea level Effects [8]	2
Figure 2: MQ-1B MALE UAV [18].....	6
Figure 3: MQ-9A MALE UAV [18]	7
Figure 4: Eitan [21].....	8
Figure 5: Representative Wing Planform	10
Figure 6: Representative UAV	11
Figure 7: Original P-3 Array.....	12
Figure 8: Pressure Distribution for Similar Array in Prior Aerodynamic Study [22]	13
Figure 9: Wing Mounted Array	14
Figure 10: Loading Regions	15
Figure 11: 3 Spar Structure.....	16
Figure 12: 5 Spar Structure.....	17
Figure 13: 7 Spar Structure.....	18
Figure 14: Three Spar Wing Displacement	20
Figure 15: Three Spar Hardpoint Displacements	21
Figure 16: Five Spar Wing Displacement	21
Figure 17: Five Spar Hardpoint Displacements.....	22
Figure 18: Seven Spar Wing Displacement.....	22
Figure 19: Seven Spar Hardpoint Displacements.....	23
Figure 20: Curvature Model Reaction Load.....	24
Figure 21: Boundary Conditions	25
Figure 22: Model Epsilon Value.....	25
Figure 23: X Unit Displacement Check.....	26
Figure 24: Y Unit Displacement Check.....	26
Figure 25: Z Unit Displacement Check	26
Figure 26: Wing Element Coordinate System	27
Figure 27: Upper Skin ϵ_1 Component Compressive Strains.....	29
Figure 28: Lower Skin ϵ_1 Component Compressive Strain Distribution	30
Figure 29: Upper Skin ϵ_1 Component Compressive Critical Region 1	30
Figure 30: Upper Skin ϵ_1 Component Compressive Critical Region 2	31
Figure 31: Upper Skin ϵ_1 Component Compressive Critical Region 3	31
Figure 32: Upper Skin ϵ_1 Component Compressive Critical Strains Region 1	31
Figure 33: Upper Skin ϵ_1 Component Compressive Critical Strains Region 2	32
Figure 34: Upper Skin ϵ_1 Component Compressive Critical Strains Region 3	32
Figure 35: Upper Skin ϵ_1 Component Tensile Strain	33
Figure 36: Lower Skin ϵ_1 Component Tensile Strain.....	33
Figure 37: Lower Skin ϵ_1 Component Tensile Strain Critical Region 1	34
Figure 38: Lower Skin ϵ_1 Component Tensile Strain Critical Region 2	34
Figure 39: Lower Skin ϵ_1 Component Tensile Strain Critical Region 3	35
Figure 40: Lower Skin ϵ_1 Component Tensile Critical Strain Region 1	35
Figure 41: Lower Skin ϵ_1 Component Tensile Critical Strain Region 2	35
Figure 42: Lower Skin ϵ_1 Component Tensile Critical Strain Region 3	35
Figure 43: Upper Skin ϵ_2 Component Tensile Strain	36

Figure 44: Lower Skin ε_2 Component Tensile Strain	37
Figure 45: Lower Skin ε_2 Component Tensile Strain Region 1	37
Figure 46: Lower Skin ε_2 Component Tensile Strain Region 2	37
Figure 47: Lower Skin ε_2 Component Tensile Strain Region 3	38
Figure 48: Lower Skin ε_2 Component Tensile Strain Critical Stress Region 1	38
Figure 49: Lower Skin ε_2 Component Tensile Strain Critical Stress Region 2	38
Figure 50: Lower Skin ε_2 Component Tensile Strain Critical Stress Region 3	38
Figure 51: Upper Skin ε_2 Component Compressive Critical Strain	39
Figure 52: Lower Skin ε_2 Component Compressive Strain Distribution	40
Figure 53: Upper Skin ε_2 Component Compressive Critical Region 1	40
Figure 54: Upper Skin ε_2 Component Compressive Critical Region 2	41
Figure 55: Upper Skin ε_2 Component Compressive Critical Region 3	41
Figure 56: Upper Skin ε_2 Component Compressive Critical Strain Region 1	41
Figure 57: Upper Skin ε_2 Component Compressive Critical Strain Region 2	42
Figure 58: Upper Skin ε_2 Component Compressive Critical Strain Region 3	42
Figure 59: Upper Skin γ_{12} Component Shear Strain Distribution	43
Figure 60: Lower Skin γ_{12} Component Shear Strain Distribution	43
Figure 61: Lower Skin γ_{12} Component Shear Strain Distribution Region 1	44
Figure 62: Lower Skin γ_{12} Component Shear Strain Distribution Region 2	44
Figure 63: Lower Skin γ_{12} Component Shear Strain Distribution Region 3	45
Figure 64: Lower Skin γ_{12} Component Critical Shear Strain Region 1	45
Figure 65: Lower Skin γ_{12} Component Critical Shear Strain Region 2	45
Figure 66: Lower Skin γ_{12} Component Critical Shear Strain Region 3	45
Figure 67: Spars ε_1 Component Tensile Strain Distribution	47
Figure 68: Spars ε_1 Component Tensile Strain Critical Region 1	48
Figure 69: Spars ε_1 Component Tensile Strain Critical Region 2	48
Figure 70: Spars ε_1 Component Tensile Strain Critical Region 3	49
Figure 71: Spars ε_1 Component Tensile Critical Strain Region 1	49
Figure 72: Spars ε_1 Component Tensile Critical Strain Region 2	49
Figure 73: Spars ε_1 Component Tensile Critical Strain Region 3	50
Figure 74: Spars ε_2 Component Tensile Strain Distribution	51
Figure 75: Spars ε_2 Component Tensile Strain Critical Region 1	51
Figure 76: Spars ε_2 Component Tensile Strain Critical Region 2	52
Figure 77: Spars ε_2 Component Tensile Strain Critical Region 3	52
Figure 78: Spars ε_2 Component Tensile Critical Strain Region 1	53
Figure 79: Spars ε_2 Component Tensile Critical Strain Region 2	53
Figure 80: Spars ε_2 Component Tensile Critical Strain Region 3	53
Figure 81: Spars ε_2 Component Compressive Strain Distribution	54
Figure 82: Spars ε_2 Component Compressive Strain Critical Region 1	54
Figure 83: Spars ε_2 Component Compressive Strain Critical Region 2	55
Figure 84: Spars ε_2 Component Compressive Strain Critical Region 3	55
Figure 85: Spars ε_2 Component Compressive Critical Strain Region 1	56
Figure 86: Spars ε_2 Component Compressive Critical Strain Region 2	56
Figure 87: Spars ε_2 Component Compressive Critical Strain Region 3	56
Figure 88: Spars ε_1 Component Compressive Strain Distribution	57
Figure 89: Spars ε_1 Component Compressive Strain Critical Region 1	57

Figure 90: Spars ε_1 Component Compressive Strain Critical Region 2	58
Figure 91: Spars ε_1 Component Compressive Strain Critical Region 3	58
Figure 92: Spars ε_1 Component Compressive Critical Strain Region 1	58
Figure 93: Spars ε_1 Component Compressive Critical Strain Region 2	59
Figure 94: Spars ε_1 Component Compressive Critical Strain Region 3	59
Figure 95: Spars γ_{12} Component Shear Strain Distribution	60
Figure 96: Spars γ_{12} Component Shear Strain Critical Region 1	60
Figure 97: Spars γ_{12} Component Shear Strain Critical Region 2	61
Figure 98: Spars γ_{12} Component Shear Strain Critical Region 3	61
Figure 99: Spars γ_{12} Component Shear Critical Strain Region 1	61
Figure 100: Spars γ_{12} Component Shear Critical Strain Region 2	62
Figure 101: Spars γ_{12} Component Shear Critical Strain Region 3	62
Figure 102: Array on Representative UAV	64
Figure 103: Transparent Upper Skin Reveals Internal Antenna Elements and Ribs	64
Figure 104: Fairing Skins	65
Figure 105: Fairing Skin Sections	65
Figure 106: Fairing Structure	67
Figure 107: Attachment Plates	68
Figure 108: Pylon Substructure	68
Figure 109: Fairing Ribs	69
Figure 110: Fairing Rib Inserts	69
Figure 111: Rib Insert, Spar, and Rib Interaction	70
Figure 112: Fairing Spars	70
Figure 113: Trailing Edge Ribs	71
Figure 114: Fairing Boundary Conditions	77
Figure 115: Applied Loads	78
Figure 116: Displacement of the Fairing and Pylons	78
Figure 117: Fairing X Unit Displacement Check	79
Figure 118: Fairing Y Unit Displacement Check	79
Figure 119: Fairing Z Unit Displacement Check	80
Figure 120: Epsilon Verification	80
Figure 121: First Mode Buckling at Buckling Factor of 2.72	82
Figure 122: Second Mode Buckling at Load Factor of 3.002	82
Figure 123: Third Mode Buckling at Load Factor of 3.2571	83
Figure 124: Fourth Mode Buckling at Load Factor of 3.387	83
Figure 125: Fifth Mode Buckling at Load Factor of 3.389	84
Figure 126: Sixth Mode Buckling at Load Factor of 3.8324	84
Figure 127: Lower Skins σ_1 Component Tensile Stress	86
Figure 128: Lower Skins σ_1 Component Tensile Critical Region	86
Figure 129: Lower Skins σ_1 Component Tensile Critical Stress	87
Figure 130: Lower Skins σ_2 Component Tensile Stress	87
Figure 131: Lower Skins σ_2 Component Tensile Critical Region	88
Figure 132: Lower Skins σ_2 Component Tensile Critical Stress	88
Figure 133: Lower Skins σ_1 Component Compressive Stress	89
Figure 134: Lower Skins σ_1 Component Compressive Critical Region	90
Figure 135: Lower Skins σ_1 Component Compressive Critical Stress	90

Figure 136: Lower Skins σ_2 Component Compressive Stress	91
Figure 137: Lower Skins σ_2 Component Compressive Critical Region	91
Figure 138: Lower Skins σ_2 Component Compressive Critical Stress	91
Figure 139: Lower Skins τ_{12} Component Shear Stress	92
Figure 140: Lower Skins τ_{12} Component Shear Stress Critical Region	93
Figure 141: Lower Skins τ_{12} Component Shear Critical Stress	93
Figure 142: Upper Skins σ_1 Component Tensile Stress Distribution	95
Figure 143: Upper Skins σ_1 Component Tensile Stress Critical Region	95
Figure 144: Upper Skins σ_1 Component Tensile Critical Stress	95
Figure 145: Upper Skins σ_2 Component Tensile Stress Distribution	96
Figure 146: Upper Skins σ_2 Component Tensile Stress Critical Region	97
Figure 147: Upper Skins σ_2 Component Tensile Critical Stress	97
Figure 148: Upper Skins σ_1 Component Compressive Stress Distribution	98
Figure 149: Upper Skins σ_1 Component Compressive Stress Critical Region	98
Figure 150: Upper Skins σ_1 Component Compressive Critical Stress	98
Figure 151: Upper Skins σ_2 Component Compressive Stress Distribution	100
Figure 152: Upper Skins σ_2 Component Compressive Stress Critical Region	100
Figure 153: Upper Skins σ_2 Component Compressive Critical Stress	101
Figure 154: Upper Skins τ_{12} Component Shear Stress Distribution	101
Figure 155: Upper Skins τ_{12} Component Shear Critical Region	102
Figure 156: Upper Skins τ_{12} Component Shear Critical Stress	102
Figure 157: Trailing Edge σ_1 Component Tensile Stress Distribution	104
Figure 158: Trailing Edge σ_1 Component Tensile Stress Critical Region	104
Figure 159: Trailing Edge σ_1 Component Tensile Critical Stress	104
Figure 160: Trailing Edge σ_2 Component Tensile Stress Distribution	105
Figure 161: Trailing Edge σ_2 Component Tensile Stress Critical Region	106
Figure 162: Trailing Edge σ_2 Component Tensile Critical Stress	106
Figure 163: Trailing Edge σ_2 Component Compressive Stress Distribution	107
Figure 164: Trailing Edge σ_2 Component Compressive Stress Critical Region	107
Figure 165: Trailing Edge σ_2 Component Compressive Critical Stress	108
Figure 166: Trailing Edge σ_1 Component Compressive Stress Distribution	108
Figure 167: Trailing Edge σ_1 Component Compressive Stress Critical Region	109
Figure 168: Trailing Edge σ_1 Component Compressive Critical Stress	109
Figure 169: Trailing Edge τ_{12} Shear Stress Distribution	110
Figure 170: Trailing Edge τ_{12} Shear Stress Critical Region	110
Figure 171: Trailing Edge τ_{12} Shear Critical Stress	111
Figure 172: Spars σ_1 Component Compressive Stress Distribution	113
Figure 173: Spars σ_1 Component Compressive Stress Distribution	113
Figure 174: Spars σ_1 Component Compressive Critical Stress	113
Figure 175: Spars σ_2 Component Compressive Stress Distribution	114
Figure 176: Spars σ_2 Component Compressive Stress Critical Region	115
Figure 177: Spars σ_2 Component Compressive Critical Stress	115
Figure 178: Spars σ_1 Component Tensile Stress Distribution	117
Figure 179: Spars σ_1 Component Tensile Stress Critical Region	117
Figure 180: Spars σ_1 Component Tensile Critical Stress	117
Figure 181: Spars σ_2 Component Tensile Stress Distribution	118

Figure 182: Spars σ_2 Component Tensile Critical Stress	119
Figure 183: Spars σ_2 Component Tensile Critical Stress	119
Figure 184: Spars τ_{12} Shear Stress Distribution.....	120
Figure 185: Spars τ_{12} Shear Stress Distribution.....	120
Figure 186: Spars τ_{12} Shear Critical Stress	120
Figure 187: Ribs σ_1 Component Compressive Stress Distribution.....	123
Figure 188: Ribs σ_1 Component Compressive Stress Critical Region	123
Figure 189: Ribs σ_1 Component Compressive Critical Stress	123
Figure 190: Ribs σ_2 Component Compressive Stress Distribution.....	124
Figure 191: Ribs σ_2 Component Compressive Stress Critical Region	125
Figure 192: Ribs σ_2 Component Compressive Critical Stress	125
Figure 193: Ribs σ_1 Component Tensile Stress Distribution.....	126
Figure 194: Ribs σ_1 Component Tensile Stress Critical Region	126
Figure 195: Ribs σ_1 Component Tensile Critical Stress	126
Figure 196: Ribs σ_2 Component Tensile Stress Distribution.....	127
Figure 197: Ribs σ_2 Component Tensile Stress Critical Region	128
Figure 198: Ribs σ_2 Component Tensile Critical Stress	128
Figure 199: Ribs τ_{12} Shear Stress Distribution	129
Figure 200: Ribs τ_{12} Shear Stress Critical Region	130
Figure 201: Ribs τ_{12} Shear Critical Stress	130
Figure 202: Ribs Inserts Tensile Stress Distribution	131
Figure 203: Ribs Inserts Tensile Stress Critical Region.....	132
Figure 204: Ribs Inserts Tensile Critical Stress	132
Figure 205: Ribs Inserts Compressive Stress Distribution	133
Figure 206: Ribs Inserts Compressive Stress Critical Region.....	133
Figure 207: Ribs Inserts Compressive Critical Stress	134
Figure 208: Ribs Inserts Shear Stress Distribution.....	134
Figure 209: Ribs Inserts Shear Stress Critical Region.....	135
Figure 210: Ribs Inserts Shear Critical Stress	135
Figure 211: Pylon Substructure Shear Stress Distribution	136
Figure 212: Pylon Substructure Shear Stress Critical Region	137
Figure 213: Pylon Substructure Shear Critical Stress.....	137
Figure 214: Pylon Substructure Tensile Stress Distribution.....	138
Figure 215: Pylon Substructure Tensile Stress Critical Region	138
Figure 216: Pylon Substructure Tensile Critical Stress	139
Figure 217: Pylon Substructure Compressive Stress Distribution	139
Figure 218: Pylon Substructure Compressive Stress Critical Region	140
Figure 219: Pylon Substructure Compressive Critical Stress.....	140
Figure 220: Attachment Plates Compressive Stress Distribution.....	141
Figure 221: Attachment Plates Compressive Stress Critical Region.....	142
Figure 222: Attachment Plates Compressive Critical Stress	142
Figure 223: Attachment Plates Tensile Stress Distribution.....	143
Figure 224: Attachment Plates Tensile Stress Critical Region.....	143
Figure 225: Attachment Plates Tensile Critical Stress	143
Figure 226: Attachment Plates Shear Stress Distribution.....	144
Figure 227: Attachment Plates Shear Stress Critical Region	144

Figure 228: Attachment Plates Shear Critical Stress	145
Figure 229: Pylon Skins Shear Stress Distribution.....	146
Figure 230: Pylon Skins Shear Stress Critical Region	146
Figure 231: Pylon Skins Shear Critical Stress	146
Figure 232: Pylon Skins Tensile Stress Distribution.....	147
Figure 233: Pylon Skins Tensile Stress Critical Region.....	148
Figure 234: Pylon Skins Tensile Critical Stress	148
Figure 235: Pylon Skins Compressive Stress Distribution.....	149
Figure 236: Pylon Skins Compressive Stress Distribution.....	149
Figure 237: Pylon Skins Compressive Critical Stress	150
Figure 238: Trailing Edge Ribs Compressive Stress Distribution.....	151
Figure 239: Trailing Edge Ribs Compressive Stress Critical Region	152
Figure 240: Trailing Edge Ribs Compressive Critical Stress	152
Figure 241: Trailing Edge Ribs Tensile Stress Distribution.....	153
Figure 242: Trailing Edge Ribs Tensile Stress Critical Region	153
Figure 243: Trailing Edge Ribs Tensile Critical Stress	153
Figure 244: Trailing Edge Ribs Shear Stress Distribution	154
Figure 245: Trailing Edge Ribs Shear Stress Critical Region	155
Figure 246: Trailing Edge Ribs Shear Critical Stress.....	155
Figure 247: Upper Skin Nodal Forces	156
Figure 248: Spar to Trailing Edge Fastener Critical Region	157
Figure 249: Spar to Upper Skin Critical Region	158
Figure 250: Ribs to Upper Skin Critical Region	159
Figure 251: Lower Skin Nodal Forces.....	160
Figure 252: Spar to Leading Edge Critical Region	160
Figure 253: Lower Skin to Spar Critical Region	161
Figure 254: Lower Skin to Ribs Fasteners	162
Figure 255: Rib Nodal Stress Distribution	163
Figure 256: Rib to Pylon Fasteners	163
Figure 257:Pylon Skin Nodal Forces.....	164
Figure 258: Pylon Fasteners Critical Region.....	165
Figure 259: First Fairing Mode (76.29 Hz)	166
Figure 260: Second Fairing Mode (79.556 Hz).....	167
Figure 261: Third Fairing Mode (79.944 Hz).....	167
Figure 262: Fourth Fairing Mode (111.24 Hz).....	168
Figure 263: Aircraft Range (Out and back)	172
Figure 264: Center Fairing Region (-0.63817 lb/in ²)	A-1
Figure 265: Inboard Fairing Region (-1.36335 lb/in ²).....	A-1
Figure 266: Outboard Inboard Fairing Region (-1.2473246 lb/in ²)	A-2
Figure 267: Outboard Outboard Fairing Region (-0.89923 lb/in ²).....	A-2
Figure 268: Inboard Lower Triangle Fairing Region (-1.59542 lb/in ²).....	A-3
Figure 269: Lower Trapezoid Fairing Region (-2.0885434 lb/in ²)	A-3
Figure 270: Outboard Lower Triangle Fairing Region (-1.3053401 lb/in ²).....	A-4
Figure 271: Leading Edge Fairing Region (1.914498 lb/in ²).....	A-4
Figure 272: Trailing Edge Fairing Region (-0.69618112 lb/in ²).....	A-5
Figure 273: Forward Inboard Pylon Region (-0.43511 lb/in ²)	A-5

Figure 274: Forward Outboard Pylon Region (-1.45038 lb/in^2).....	A-6
Figure 275: Aft Inboard Pylon Region (-1.01526 lb/in^2)	A-6
Figure 276: Aft Outboard Pylon Region (-2.03053 lb/in^2).....	A-7
Figure 277: Leading Edge Pylon Region ($0.69618112 \text{ lb/in}^2$)	A-7
Figure 278: Aft Middle Pylon Region (-1.01526 lb/in^2)	A-8
Figure 279: Forward Middle Pylon Region (-0.43511 lb/in^2)	A-8
Figure 280: Trailing Edge Pylon Region ($-1.1666255 \text{ lb/in}^2$)	A-9
Figure 281: AAA Wing Geometry	A-10
Figure 282: AAA Tail Geometry.....	A-10
Figure 283: AAA Clean Aircraft Range Calculation	A-11
Figure 284: AAA Sharp Trailing Edges Ranges Calculation.....	A-11
Figure 285: AAA Sharp Fairing, Circular Pylons Trailing Edges Range Calculation.....	A-12
Figure 286: AAA Sharp Pylons, Circular Fairing Trailing Edges Range Calculation.....	A-12
Figure 287: AAA Circular Trailing Edges Range Calculation.....	A-13
Figure 288: Clean Takeoff Distance.....	A-13
Figure 289: Sharp Trailing Edges Takeoff Distance	A-14
Figure 290: Sharp Fairing Circular Pylon Trailing Edges Takeoff Distance	A-14
Figure 291: Circular Fairing Sharp Pylon Trailing Edges Takeoff Distance	A-15
Figure 292: Circular Trailing Edges Takeoff Distance	A-15

List of Tables

Table 1: MQ-1B Characteristics [18], [19].....	6
Table 2: MQ-9A Characteristics [18], [20]	7
Table 3: Heron TP Characteristics [21]	8
Table 4: Aircraft Specifications.....	9
Table 5: Array Aerodynamic Conditions	12
Table 6: Curvature Model Material	14
Table 7: Curvature Model Core.....	15
Table 8: Curvature Model Loading	16
Table 9: Forward 3 Spar Layups	17
Table 10: Aft 3 Spar Layups.....	17
Table 11: Forward 5 Spar Layups	18
Table 12: Aft 5 Spar Layups.....	18
Table 13: Forward 7 Spar Layups	19
Table 14: Aft 7 Spar Layups.....	19
Table 15: Deflection Results	20
Table 16: Tip Deflection.....	20
Table 17: Hardpoint Deflection	20
Table 18: Curvature Skin Strains.....	28
Table 19: Curvature Skin Margins	28
Table 20: Curvature Spar Critical Strains.....	46
Table 21: Curvature Spar Critical Margins	46
Table 22: Lower Skin Ply Drops from Pad Up.....	66
Table 23: Aerodynamic Loads for Each Array.....	72

Table 24: 2024-T351 Aluminum Extrusion [22]	74
Table 25: 2024-T3 Aluminum Sheet, RT, QQ-A-250/4 [22]	74
Table 26: 6061-T6 Aluminum Extrusion, RT, QQ-A-200/3 [22]	75
Table 27: ACG S-2 Glass 6781/MTM45-1 [22]	75
Table 28: Rohacell 71 IG Properties [22]	76
Table 29: 7075-T651 Aluminum Plate [22]	76
Table 30: AN Bolt Allowables [22]	76
Table 31: Critical Margins by Component	81
Table 32: Lower Skin Failure Methods	85
Table 33: Upper Skin Failure Methods	94
Table 34: Trailing Edge Skin Failure Methods	103
Table 35: Spar Failure Methods	112
Table 36: Spar Crippling Terms	116
Table 37: Rib Failure Methods	122
Table 38: Rib Insert Failure Methods	131
Table 39: Pylon Substructure Failure Methods	136
Table 40: Pylon Plate Failure Modes	141
Table 41: Pylon Substructure Failure Methods	145
Table 42: Trailing Edge Ribs Failure Modes	151
Table 43: Aircraft Clean Drag	169
Table 44: Drag Coefficients of Fairing Components	170
Table 45: Drag Coefficient by Configuration	171
Table 46: Range Comparison	171
Table 47: Takeoff Distance Variables	173
Table 48: Takeoff Distance Results	174
Table 49: Climb Performance Comparison	175

List of Symbols

<u>Symbol</u>	<u>Description</u>	<u>Units</u>
α_1	Coefficient of Thermal Expansion on Primary Material Axis	in/in/°F
α_2	Coefficient of Thermal Expansion on Secondary Material Axis	in/in/°F
ϵ_1^C	Compressive Strain Allowable on Primary Material Axis	in/in
ϵ_1^T	Tensile Strain Allowable on Primary Material Axis	in/in
ϵ_2^C	Compressive Strain Allowable on Secondary Material Axis	in/in
ϵ_2^T	Tensile Strain Allowable on Secondary Material Axis	in/in
$\epsilon_{allowable}$	Strain Allowable	in/in
ϵ_{actual}	Actual Strain	in/in
η_p	Propeller Efficiency	(~)
$\tau_{shear\ actual}$	Actual Shear Stress	psi
$\tau_{shear\ allowable}$	Allowable Shear Stress	psi
σ_{BRU}	Fastener Ultimate Bearing Stress	psi
ρ	density	lb/in ²
γ_{12}	Shear Strain between Primary and Secondary Material Axis	(~)
ν	Poisson's ratio	(~)
ν_{12}	Poisson's ratio between Primary and Secondary Material Axis	(~)
A	Reference Area	ft ²
$A_{Aircraft}$	Aircraft Reference Area	ft ²
A_{Pylon}	Pylon Reference Area	ft ²
AR	Aspect Ratio	(~)
$B_{DP_{Clean}}$	Drag Calculation Factor	(~)
C_D	Drag Coefficient	(~)
$C_{D_{0\ Clean}}$	Parasitic Drag Coefficient	(~)
$C_{D_{Pylon}}$	Pylon Drag Coefficient	(~)

<u>Symbol</u>	<u>Description</u>	<u>Units</u>
$C_{D_{fairing}}$	Fairing Drag Coefficient	(~)
C_L	Lift Coefficient	(~)
c_p	Specific Fuel Consumption	lbs/hp-hr
D	Diameter	in.
E	Modulus of Elasticity	psi
E^C	Compressive Modulus of Elasticity	psi
E_1	Modulus of Elasticity on Primary Material Axis	psi
E_1^C	Compressive Modulus of Elasticity on Primary Material Axis	psi
E_1^T	Tensile Modulus of Elasticity on Primary Material Axis	psi
E_2	Modulus of Elasticity on Secondary Material Axis	psi
E_2^C	Compressive Modulus of Elasticity on Secondary Material Axis	psi
E_2^T	Tensile Modulus of Elasticity on Secondary Material Axis	psi
F_{12}	Shear Stress Allowable	psi
F_1^C	Compressive Stress Allowable on Primary Material Axis	psi
F_1^T	Tensile Stress Allowable on Primary Material Axis	psi
F_2^C	Compressive Stress Allowable on Secondary Material Axis	psi
F_2^T	Tensile Stress Allowable on Secondary Material Axis	psi
F_{cy}	Compressive Yield Stress Allowable	psi
F_D	Drag Force	lbs
F_{su}	Shear Ultimate Stress Allowable	psi
F_{tu}	Tensile Ultimate Stress Allowable	psi
F_{ty}	Tensile Yield Stress Allowable	psi
FS	Factor of Safety	(~)
G	Shear Modulus	psi
G_{12}	Shear Modulus between Primary and Secondary Material Axis	psi

<u>Symbol</u>	<u>Description</u>	<u>Units</u>
G_{23}	Shear Modulus between Secondary and Tertiary Material Axis	psi
G_{13}	Shear Modulus between Primary and Tertiary Material Axis	psi
MS	Margin of Safety	(~)
mgc	Mean Geometric Chord	feet
P_{actual}	Bolt Load	lbs
$R_{C_{V=const}}$	Cruise Range at Constant Velocity	nm
s.f.c	Specific Fuel Consumption	lbs/hp-hr
t	thickness	inches
V	Velocity	fps
W_{Cr}	Cruise Weight	lbs
$W_{F_{Cr}}$	Fuel Cruise Weight	lbs
W_{Empty}	Aircraft Empty Weight	lbs
W_{Fuel}	Fuel Weight	lbs
$W_{Payload}$	Aircraft Payload Weight	lbs
W_{TO}	Aircraft Takeoff Weight	lbs

Abbreviations

AAA	Advanced Aircraft Analysis Software
CFD	Computational Fluid Dynamics
CRISIS	The Center for Remote Sensing of Ice Sheets
IAI	Israel Aerospace Industries
MALE	Medium Altitude Long Endurance
MCoRDS	Multichannel Coherent Radar Depth Sounder
NASA	National Aeronautics and Space Administration
OIB	Operation Ice Bridge
SAR	Synthetic Aperture Radar
SLR	Sea Level Rise
UAV	Unmanned Aerial Vehicle

1 Introduction

Oceans cover approximately 71.1% of the Earth's surface [1] but that number has not always been the same and will probably change in the future. One of the largest mysteries is how changes in the global climate will affect the rise and fall of the ocean. Historical trends give us accurate predictions of how global populations will grow and people will migrate. We also have detailed topological geography of the world so we know how rises and falls in sea level will change the face of the planet. But, what we currently do not have high confidence in is how fast the ice on the surface of the planet is changing and how those changes are affecting sea level rise (SLR). To put it very simply we know how large the bathroom tub is and we know what will happen if it overfills but we are not entirely sure how fast water is flowing into the tub of the world oceans.

To address this issue, NASA has designed a research campaign called Operation Ice Bridge (OIB) which is the largest airborne research campaign ever flown in the polar regions. The goal of this mission is to monitor the effects of climate change on ice sheets in Greenland and Antarctica. The changes in these sheets will affect global sea levels. What makes this research critical now is the dramatic trend of changing SLR rates. Since 1990, the SLR rates have doubled in comparison to the last 50 years [2], [3]. During this time the polar ice sheets have been steadily shrinking, but recent data points to that changing. Instead of a steady retreat, new data [4], [5] shows a possible exponential loss in the last decade. Studies also indicate that when the sheets thaw the melt water penetrates beneath the ice sheet and accelerates the melting process [6],[7] as well as the flow rate.

If sea levels continue to rise then there will be global economic impacts. As water levels rise areas which used to be populated will be underwater. This effect is more prominent in less

developed countries across the world where significant population centers are located in river deltas and other low lying areas which will first experience flooding. According to the Intergovernmental Panel on Climate Change more than one million people will be directly affected by flooding in each of the Ganges, Mekong and Nile river deltas [8]. The rising water will flood ecosystems, displace millions of people, and necessitate billions of dollars of spending to protect land from the rising water. A plot of this data is shown in Figure 1.

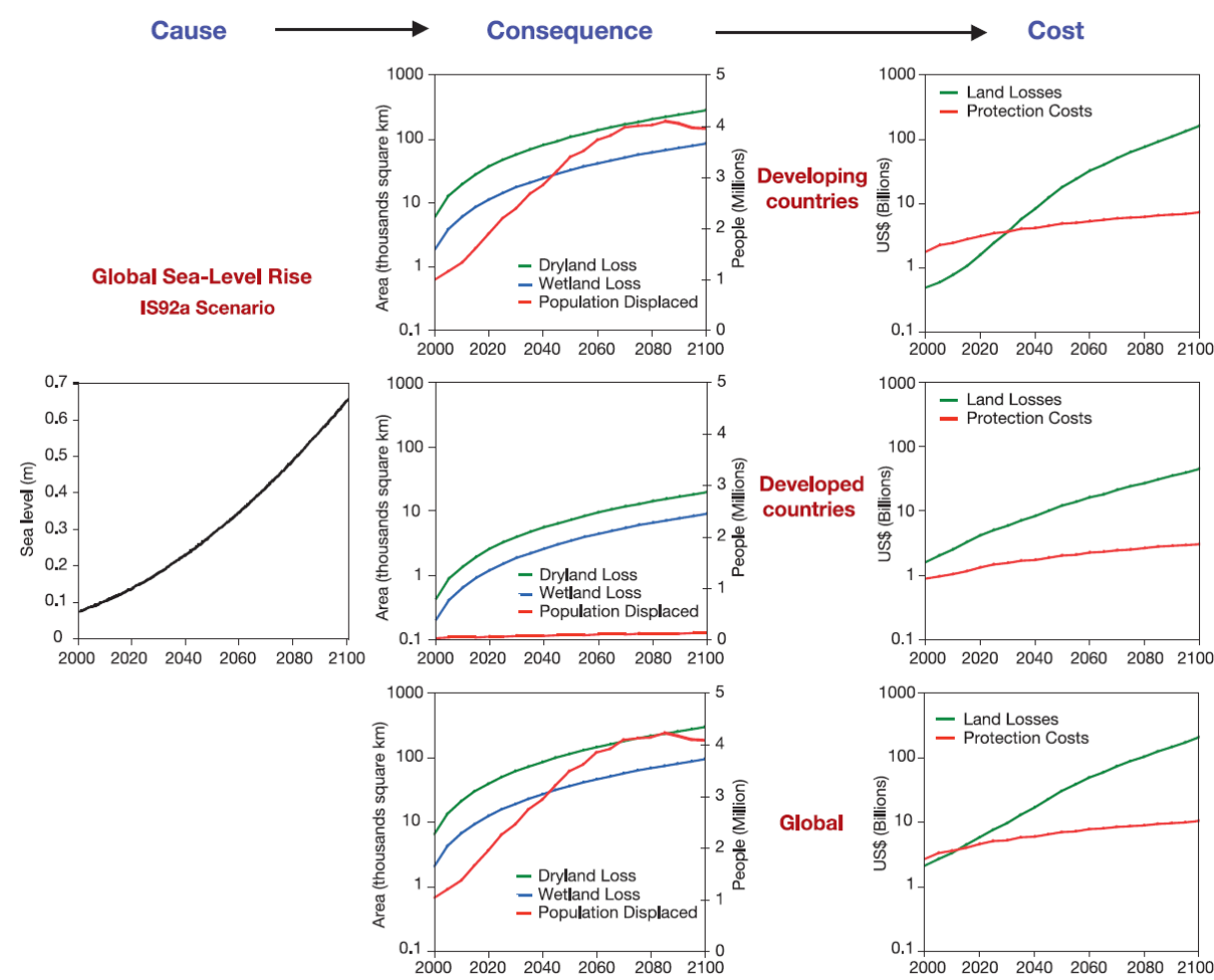


Figure 1: Sea level Effects [8]

To fully understand the sea level rise scenarios we need to better understand the conditions of the ice sheets, especially at the ice/bed or ocean/bed interface, but the current methods of

predicting ice sheet behavior contain significant gaps and uncertainties [9]. To fill these gaps and uncertainties with data would require a sustained airborne remote sensing campaign of the primary glaciers of Greenland and Antarctica, and in particular the faster-moving outlet glaciers. Due to the large geographic extent of these glaciers, the remote and unpopulated characteristics of the regions, the sparse ground and basing infrastructure, range limitations of available manned platforms, the cost of fuel and other logistics, and the repetitive nature of the mission, operation from an unmanned platform has merit. This why the research platform in this paper has been presented, as a feasibility study for a potential future mission.

What is presented is an array of ice penetrating radar antennas mounted below the wing of an unmanned remote sensing aircraft which can collect imaging information of the ice sheets simply by flying over them. The aircraft selected for this mission is based on currently available unmanned aerial vehicles (UAVs). Unmanned aerial vehicles can collect this data without having to place pilots in dull mission scenarios in these remote regions and operate at reduced fuel consumption to typical manned aircraft. . The on-board autopilot and avionics in a UAV do not need rest, and ground crews may be more readily swapped, so mission endurance times can be in excess of 24 hours. This paper explores whether it is structurally feasible to integrate a wing-mounted array into the current generation of unmanned aircraft and if it can do so without significantly reducing the performance of the aircraft.

2 Related Work

There are several UAV platforms that are currently being fielded by the international military complex and there is also current work being done for remote sensing of ice sheets. As of now these two fields have not been brought together in the class of UAV that is explored herein. The current work that is related is presented below.

2.1 Remote Sensing

The first thing that will be explored is what is currently being done to gather scientific data for the ice sheets in Greenland and Antarctica. The critical data is at the interface between the ice sheet and the bed and the simplest way used to collect that data is to dig boreholes down to the base of the ice sheet and install sensors there. Many of these boreholes have been drilled [10] but to use this method to track entire ice sheets is impractical. The next step in sensing was to develop a radar system which could be run over the ice surface to collect the information. The radar can be calibrated by borehole information and then enable much larger ice sheets to be monitored. These radar systems were first mounted to sleds behind tracked vehicles and driven over the ice sheets to gather data [11]. The next step to gather larger amounts of data was to move the radar from a tracked vehicle and onto an aircraft. UAV's have started to fill this role in similar missions. Low-altitude long-endurance (LALE) UAV's have been equipped with LIDAR instrumentation to retrieve surface topography in a cyrosphere environment [12]. The NSF Center for Remote Sensing of Ice Sheets (CReSIS) has developed a variety of ice penetrating radar systems to collect ice depth and layering information. A radar altimeter that operates in the 13 to 17 GHz range has been used to take precision surface measurements of the ice sheets [13]. The Multichannel Coherent Radar Depth Sounder (MCoRDS) system has been

adapted for a variety of NASA aircraft including the P-3 and DC-8 [14] [15] [16]. The Synthetic Aperture Radar (SAR) was developed as an eight-channel wideband radar that does bed imaging and sounding to 1 meter depth resolution. The radar operates in the 120 to 230 MHz spectrum. To analyze the upper layer of the ice sheet an Accumulation Radar was developed [17]. This radar operates in the 600-900 MHz spectrum and gives 28 cm resolution. This accuracy allows the radar to differentiate the variation in the annual accumulation layers on the ice sheet. A Snow Radar was developed over the 2 to 8 GHz spectrum which maps the near surface internal layers in the sheet [17]. This radar has also been adapted to measure snow on top of sea ice [13].

2.2 Unmanned Aerial Vehicles (UAVs)

The primary customers in the UAV market are militaries across the globe. The United States military alone has purchased a large variety of aircraft varying in weight from less than one pound to over 40,000 pounds and varying in cost from a few thousand dollars to tens of millions of dollars. [18]. Many of these UAVs are for surveillance missions that require high endurance and/or high range, and missions are typically at high altitude. The qualities which make for an effective surveillance platform match fairly well with the requirements for a scientific platform. One of the classes of UAVs which match well with the mission requirements of a cryospheric research platform is the MALE (Medium Altitude Long Endurance) class of unmanned aircraft. There are several aircraft in this class that are deployed worldwide. Three of them are presented here.

The first UAV shown is the MQ-1 Predator. This vehicle designed by General Atomics is one of the first widely adopted MALE UAVs and remains in service today. It was originally constructed as a reconnaissance platform but was later modified and fitted with hard points and munitions. It was the first UAV to be weaponized [19]. A three view of the aircraft is shown in Figure 2.

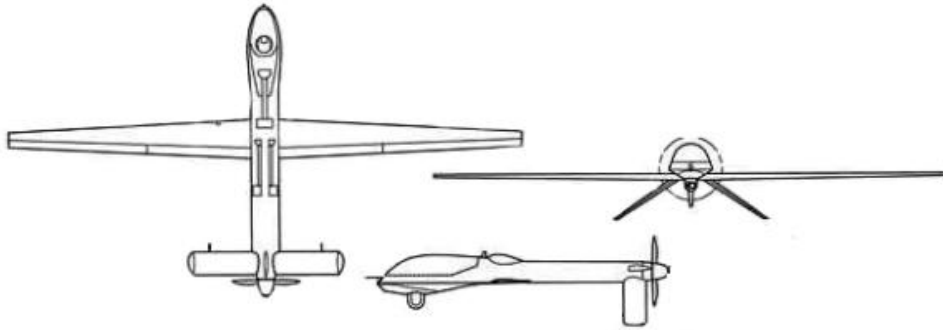


Figure 2: MQ-1B MALE UAV [18]

While this aircraft is considered to fall into the MALE class of UAVs it is on the bottom end of the class in terms of payload, service ceiling, and speed. Its endurance capability falls in line with the other aircraft and is included since it pioneered the field and still serves as a capable platform. MQ-1B vehicle characteristics are presented in Table 1.

Table 1: MQ-1B Characteristics [18], [19]

MQ-1B			
Length	26.7 ft	Payload	450 lbs
Gross Weight	2,250 lbs	Power	115 hp
Fuel Capacity	665 lbs	Endurance	24+ hrs
Engine	Rotax 914F	Ceiling	25,000 ft
Wing Span	48.7 ft	Max/Loiter Speed	118/70 kts
Aircraft Cost	\$2.7 M		

The next UAV included is the evolution of the MQ-1B presented above. The MQ-9A Reaper is the big brother that has evolved from the MQ-1B. The aircraft is significantly larger in both length and wingspan. The propulsion system was changed from a conventional Avgas fueled

reciprocating engine to the Honeywell TPE-331 heavy-fueled turbine engine powering the pusher turbo-prop. General Atomics changed the empennage design, but otherwise the MQ-9A is very similar to the MQ-1B. The design planned for munitions from the beginning so there is significantly more payload capacity in this aircraft. A three view of the aircraft is shown in Figure 3.



Figure 3: MQ-9A MALE UAV [18]

The characteristics of the MQ-9A Reaper are presented below in Table 2

Table 2: MQ-9A Characteristics [18], [20]

MQ-9A Reaper (Predator B)			
Length	36 ft	Payload	3850 lbs
Gross Weight	10,500 lbs	Power	940 hp
Fuel Capacity	4,000 lbs	Endurance	32 hrs
Engine	TPE-331-10	Ceiling	50,000 ft
Wing Span	66 ft	Max/Loiter Speed	225/160 kts
Aircraft Cost	\$5.2 M		

Several countries outside the United States have companies developing and operating excellent UAV platforms also. The one presented for comparison below is the Heron TP Eitan. This MALE UAV was developed in Israel by Israel Aerospace Industries (IAI). The design features a pusher prop similar to the other designs but the empennage is significantly different from the American designs. A view of the Eitan taxiing is shown in Figure 4.



Figure 4: Eitan [21]

The maximum takeoff weight of the Eitan and the Reaper are almost identical but the Israeli aircraft has significantly more power and is a longer aircraft from nose to tail.

Table 3: Heron TP Characteristics [21]

Heron TP Eitan			
Length	46 ft	Payload	2204 lbs
Gross Weight	10,251 lbs	Power	1200 hp
Engine	PT6A-67	Endurance	36 hrs
Wing Span	85 ft	Ceiling	45,000 ft

2.3 Summary

The current environment is ripe for unmanned aircraft and remote sensing technologies to be combined into a package for scientific research. Efforts to combine these two have already begun on a smaller scale. The Meridian UAV is an unmanned aircraft designed to carry its own eight channel radar to provide sounding information as well as SAR imaging of the ice-bed boundary. The Meridian has a payload 50 lbs and a range of around 900 nm [see Ref in note] and has flown domestically as well as in Greenland and Antarctica. The payload and range capabilities of the MALE class of UAVs could supplement the other scientific aircraft already in operation and greatly expand the available ground track survey lines.

3 Sizing of Array

3.1 Description of the Problem

One of the challenges involved with the current generation of MALE UAVs is their close integration with the military, and the potential limitations on their use as imposed by International Traffic in Arms (ITAR) regulations. This severely restricts the information publically available on the platforms since many of them are currently involved in military conflicts across to the globe. In addition, if specific information on the structural arrangement of the platforms is acquired any work based on that information will likely fall under the same publication restrictions. With that in mind, instead of designing an array for one specific aircraft a representative array has been designed for the spectrum of MALE aircraft. Aircraft information is required to develop the loads which size the array so a representative design was chosen. The aircraft specifications for the representative UAV are shown in Table 4.

Table 4: Aircraft Specifications

Parameter	Value	Units
Weights		
Max W_{TO}	10,500	lbs
W_{Empty}	4,400	lbs
W_{Fuel}	4,000	lbs
Max $W_{Payload}$	4,000	lbs
Cruise Speed	160	kts
Wing Geometry		
Area	271.6	ft ²
Span	66	ft
Aspect Ratio	16.04	~
Taper Ratio	0.52	~
mgc	4.25	ft
Engine Data		
Propeller Efficiency	0.8	~
s.f.c	0.53	lbs/hp-hr
Engine	TPE-331	~

The engine selected was a TPE-331 turbo-prop engine. This engine was chosen because of its use in the field and also because of the availability of engine performance data. The heavy-fuel is known to be compatible with the mission and available in the field, and the combustion ignition cycle is known to be compatible with the electromagnetic and radio frequency interference requirements of the ice penetrating radars. The wing geometry includes a high aspect ratio due to the low drag requirements of a high endurance aircraft. The representative wing layout is shown in Figure 5.

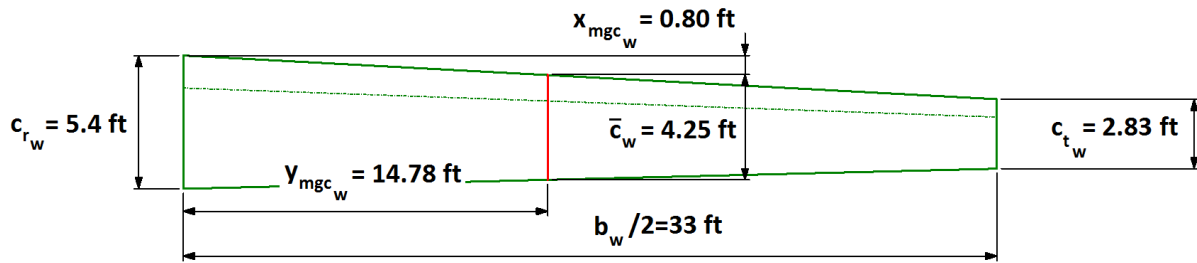


Figure 5: Representative Wing Planform

All of the MALE designs presented included a pusher prop so that configuration was also selected for the representative UAV. A computer-aided design (CAD) image of the representative UAV is shown in Figure 6. This model was developed in NX version 6 and was based upon three view drawings, pictures, and images largely from the UAV roadmap and Jane's aircraft of the MQ-9 Reaper [18, 20]. The critical information for the model like wing span and aircraft length listed in these sources. Things such as the chord length and thickness of the wing could be determined in comparison to given lengths. When a geometric detail could not be determined from those methods then a standard value for similar configurations was chosen. Since exact technical data of the aircraft was not used it is likely that there are several

slight differences with the real aircraft and the representative model but for the comparisons that are being investigated in this paper the model should be sufficient.

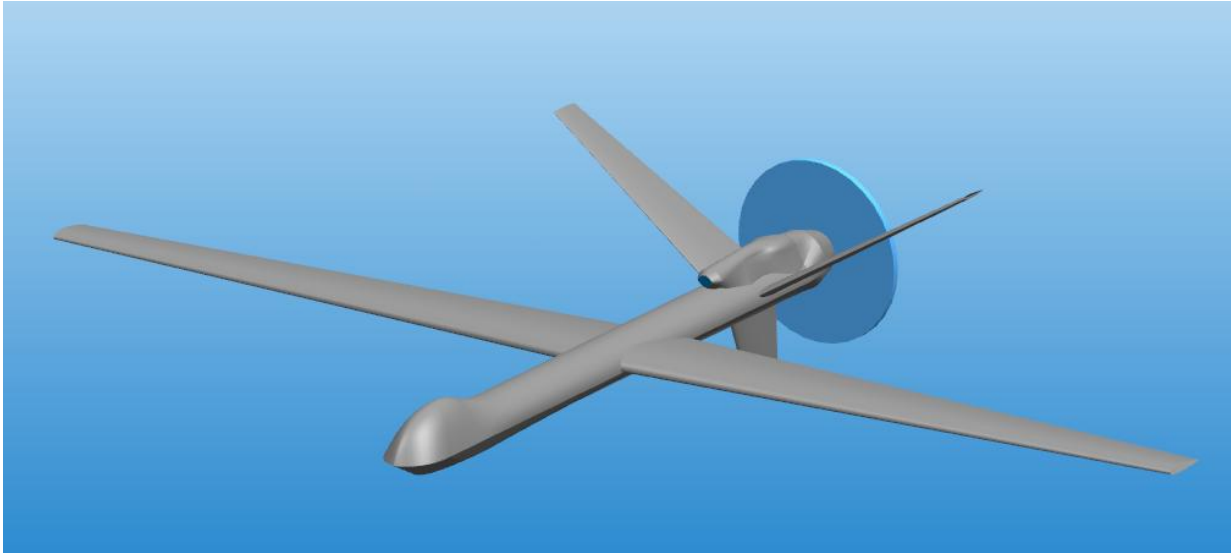


Figure 6: Representative UAV

With the platform selected the next step is to select a radar system. A 15 element MCoRDS array has been flown on NASA's P-3 research aircraft [22]. This design utilizes the hardpoints which were originally designed for munitions, allowing this platform to carry research instruments without significant work needing to be done to modify the aircraft wing. This method holds potential since many MALE UAVs also have wing mounted hard points for munitions. This paper will focus on the integrations of a wing-mounted MCoRDS system, but the high payload capacity of the MALE UAVs means that it is also possible for other radar systems such as a snow or accumulation radar to be included in the fuselage of the aircraft. An integration like this would need specific information on the fuselage layout and payload bays and thus while it is not explored further in this paper it is worth noting that the MALE UAV platform has potential beyond an MCoRDS array.

Since the mission of the array is very similar, the geometry of the fairing for the array is also very similar to the outboard fairing design for the P-3 array presented in Reference 22. A CAD image of the previous array is shown in Figure 7

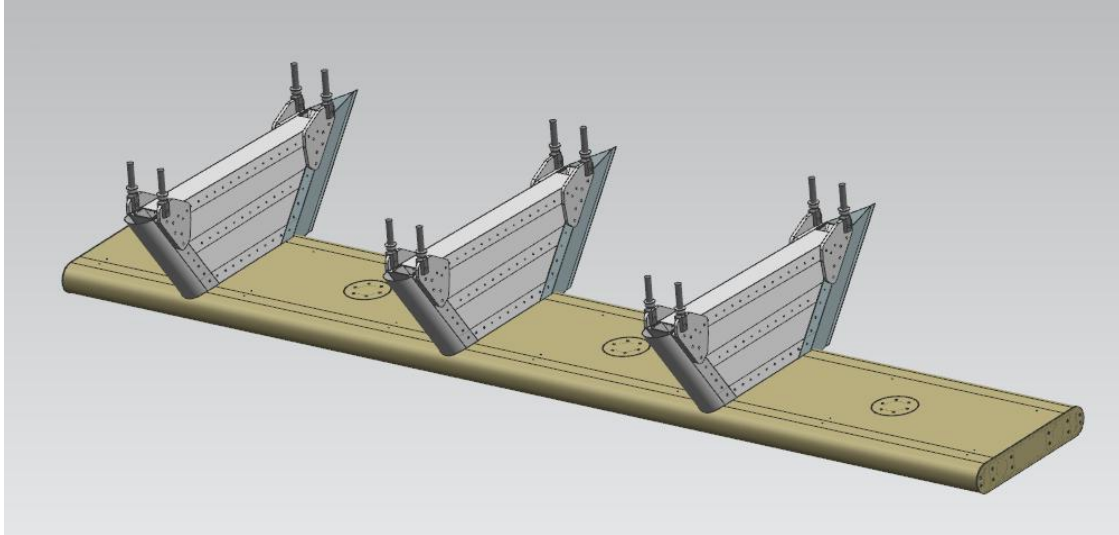


Figure 7: Original P-3 Array

For that fairing a computational fluid dynamics (CFD) aerodynamic study was conducted to develop loads and determine the impact of the structure on the aircraft performance. Since the P-3 flies significantly faster than our representative UAV the aerodynamic loads cannot be used directly, however these results can be used to establish pressure regions and anticipate the local variations in the loading of the structure. The flight conditions of the P-3 aerodynamic study and the representative aircraft are known and are shown in Table 5. This information was used to estimate a pressure loading profile for the representative unmanned aircraft, using the detailed CFD results available for the similar P-3 array, and scaling the total pressures by the ratio of the dynamic pressures.

Table 5: Array Aerodynamic Conditions

	Altitude	Speed	Dynamic Pressure	Temperature Offset
P-3	8,000 ft	420 kts	550 psf	-75 Fahrenheit
Representative UAV	2,000 ft	240 kts	220 psf	-75 Fahrenheit

$$\Delta pressure = \frac{new \bar{q}}{old \bar{q}} = \frac{220 psf}{550 psf} = .4$$

As shown above the change in altitude and airspeed results in a drop to 40% of the original aerodynamic loads when compared to the P-3 fairing. An image from the original aerodynamic study is shown in Figure 8. This method was used to develop the aerodynamic loads for the fairing for the radar array. The other predominate form of load which derives from vehicle flexibility is described in the next section.

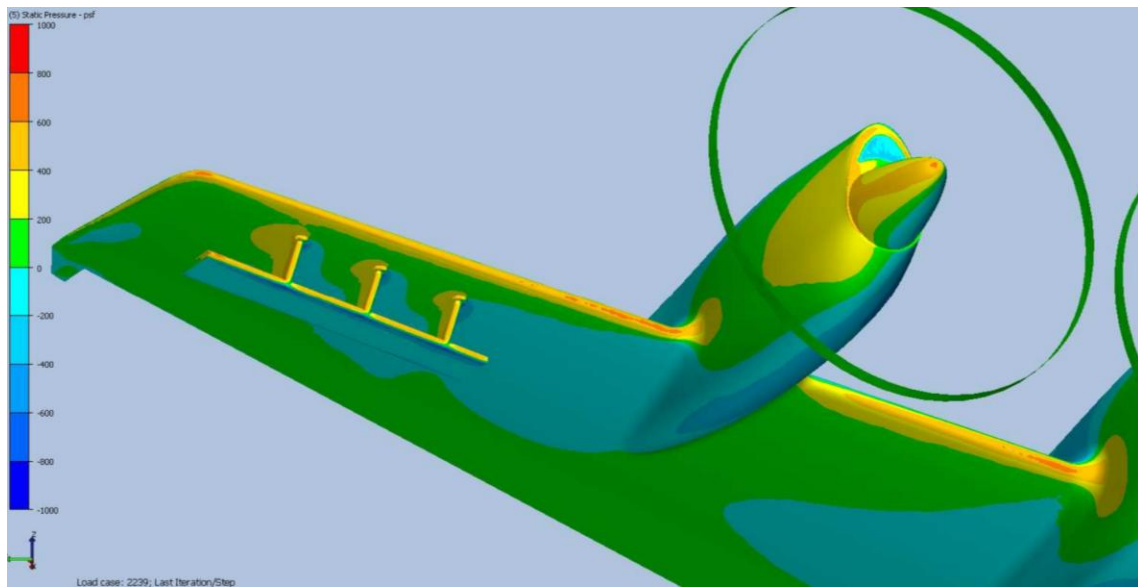


Figure 8: Pressure Distribution for Similar Array in Prior Aerodynamic Study [22]

3.2 Curvature Model and Loads Development

3.2.1 Curvature Model Description and Material Properties

The other major source of loads for the fairing is that induced from the platform itself. When aerodynamic loads are applied to the UAV the wing deflects and curves which increases the distance between the hardpoints. Since the fairing connects these hardpoints at a significant distance below the wing, as shown in Figure 9, the fairing then experiences an extensional load

as the wing flexes. As such, any preliminary sizing of the array structure will require a representative model of the expected wing curvature for this class of aircraft.



Figure 9: Wing Mounted Array

Background information [20] indicated that the example UAVs used advanced composites in their construction, so carbon composites were chosen for the representative UAV. Table 6 shows the material properties assumed for the uniaxial composite chosen for the wing structure. In addition to uniaxial composites a core material was used to stiffen parts of the structure. The material properties of the core are shown in Table 7

Table 6: Curvature Model Material

Intermediate Modulus Carbon-Epoxy		
E_1	22,800,000	psi
E_2	1,290,000	psi
ν_{12}	0.3	(~)
G_{12}	790,000	psi
ϵ_1^T	0.0128	(~)
ϵ_1^C	0.0111	(~)
ϵ_2^T	0.00702	(~)
ϵ_2^C	0.0132	(~)
γ_{12}	0.0292	(~)
t	.005	in
ρ	0.059	lb/in ³

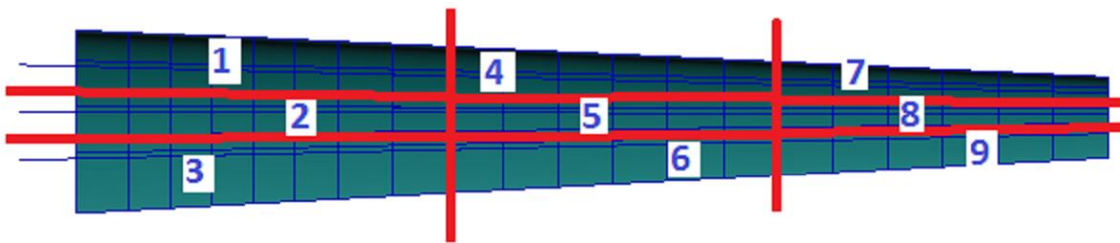
Table 7: Curvature Model Core

Honeycomb Core		
E_1	91	psi
E_2	45.5	psi
ν_{12}	0.3	(~)
G_{23}	3100	psi
G_{13}	5700	psi
ρ	0.007	lb/in ³

Since the exact curvature of the wing was not known structural designs were investigated to develop a possible range of curvatures. These designs are not fully mature designs, but instead are only first cut models designed to provide a good estimate of the wing curvature expected across a range of substructure configurations. Any subsequent details design would require knowledge of the wing details for the selected platform, and ideally flight test data confirming actual wing curvature.

3.2.2 Curvature Model Loading

The loading scenario chosen for the wing models was a 3.95G dive condition at the maximum aircraft weight of 10,500 lbs. A safety factor of 1.5 was applied to this loading condition, resulting in a total ultimate lift of $1.5 \times 2.95 \times 10,500 = 62,200$ lbs. This load was distributed over the wing to try to imitate the pressure distribution of the wing. This wing was divided into nine pressure regions and their boundaries can be seen in Figure 10.

**Figure 10: Loading Regions**

The actual loadings for these regions are shown in Table 8. These loads were applied across the upper and lower skins in these regions. These same loads were applied to all of the different structural designs investigated.

Table 8: Curvature Model Loading

Region	Load (lbs)	Region	Load (lbs)	Region	Load (lbs)
1	12471	4	8813	7	5515
2	1467	5	1037	8	607
3	734	6	518	9	303

3.2.3 Curvature Model Geometry

Three designs were chosen, representing a three spar, five spar, and seven spar structure. All of the wings were split into three different regions along the half-span since the total load decreases traveling outboard. The wing design includes three hardpoints in region 1 spaced 30" apart. This requirement decreases the rib spacing to 15". In the other bays the ribs are spaced 20" apart. This rib pattern is repeated in all three designs. These regions are shown in Figure 11 on the three spar design.

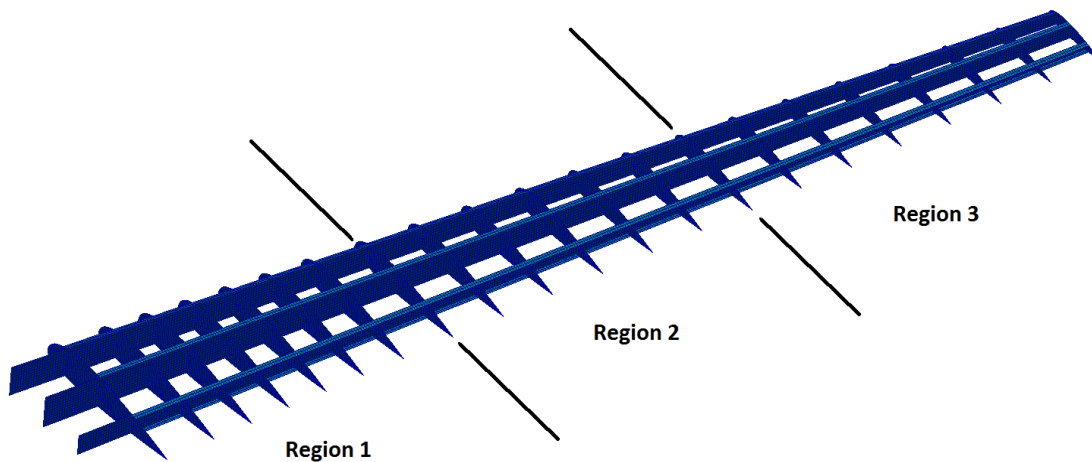


Figure 11: 3 Spar Structure

The skin and spars were also analyzed and sized into forward and aft layups since the loading of the wing is higher toward the forward part of the wing, with a maximum near the quarter-

chord. The layups for the forward two spars and the skin forward of the middle spar is shown in Table 9. The aft spar and aft skins are shown in Table 10. Core is utilized in regions 1 and 2 where it is necessary.

Table 9: Forward 3 Spar Layups

	Skin	Spar
Region 1	54/41/4 - 48 Layers 1/4" Core in Bays	55/35/11 - 150 Layers
Region 2	40/40/20 - 10 Layers 1/4" Core in Bays	53/39/8 - 72 Layers
Region 3	40/40/20 - 10 Layers	40/40/20 - 10 Layers

Table 10: Aft 3 Spar Layups

	Skin	Spar
Region 1	53/42/5 - 38 Layers 1/4" Core in Bays	29/57/14 - 14 Layers
Region 2	25/50/25 - 8 Layers	25/50/25 - 8 Layers
Region 3	25/50/25 - 8 Layers	25/50/25 - 8 Layers

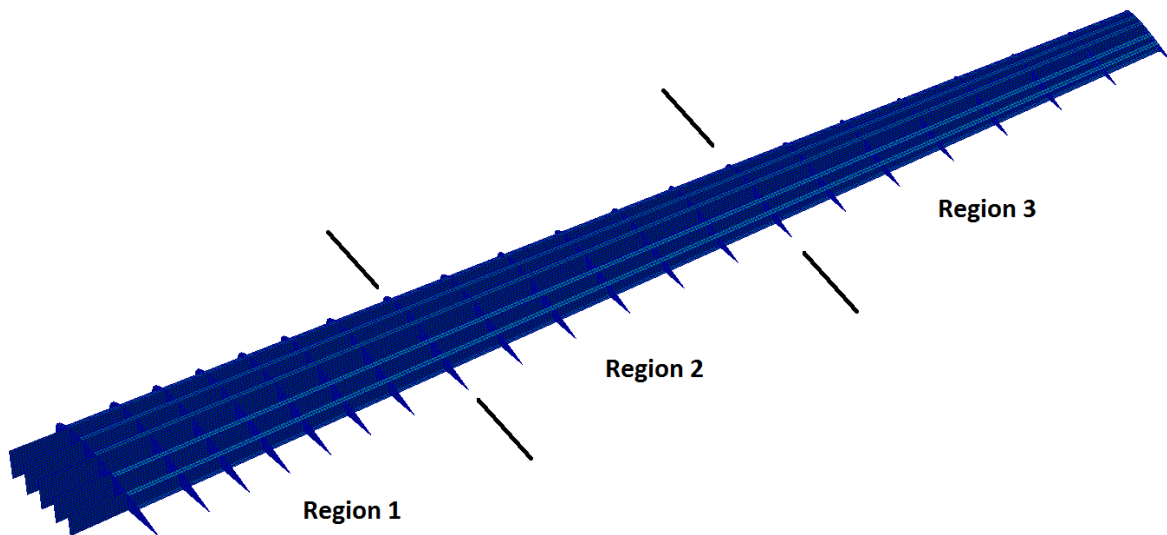


Figure 12: 5 Spar Structure

The five spar design uses similar regions to the three spar design. The substructure and regions can be seen in Figure 12. Core is utilized in regions 1 and 2 where it is needed. The forward

three spars and the forward skin layups are shown in Table 11 and the aft two spars and aft skin are shown in Table 12.

Table 11: Forward 5 Spar Layups

	Skin	Spar
Region 1	42/50/8 - 24 Layers 1/4" Core in Bays	58/35/8 - 80 Layers
Region 2	29/57/14 - 14 Layers 1/4" Core in Bays	50/43/8 - 28 Layers
Region 3	25/50/25 - 8 Layers	25/50/25 - 8 Layers

Table 12: Aft 5 Spar Layups

	Skin	Spar
Region 1	29/57/14 - 14 Layers 1/4" Core in Bays	50/43/7 - 28 Layers
Region 2	25/50/25 - 8 Layers	38/50/13 - 16 Layers
Region 3	25/50/25 - 8 Layers	25/50/25 - 8 Layers

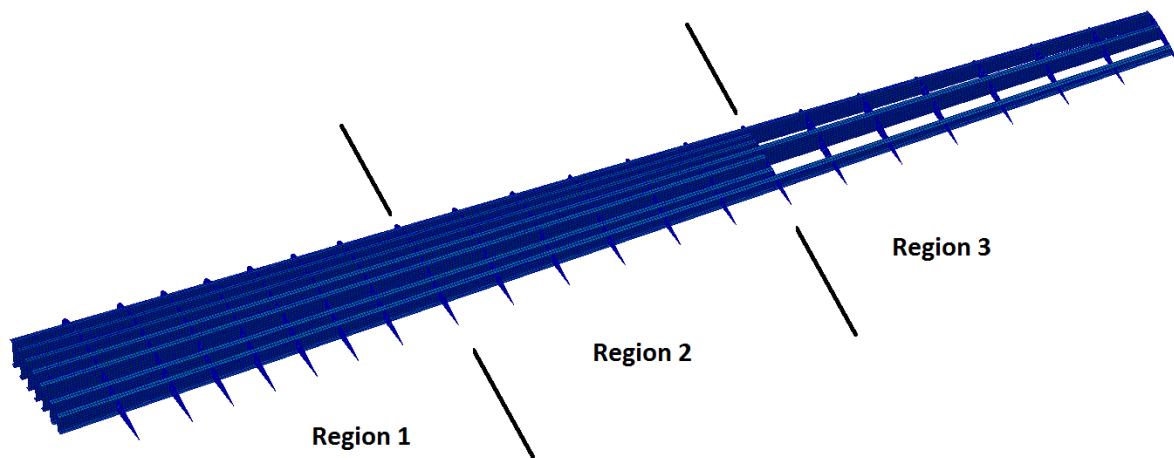


Figure 13: 7 Spar Structure

The seven spar design uses the regions shown in Figure 13. One difference is that since the spars are so close together it does not use core in any of the bays. The composite families are

shown in Table 13 for the forward four spars and skins and the families for the aft three spars and skin are shown in Table 14.

Table 13: Forward 7 Spar Layups

	Skin	Spar
Region 1	38/50/13 - 16 Layers	56/35/9 - 68 Layers
Region 2	29/57/14 -14 Layers	53/40/7 - 30 Layers
Region 3	25/50/25 - 8 Layers	50/33/17 - 12 Layers

Table 14: Aft 7 Spar Layups

	Skin	Spar
Region 1	29/57/14 -14 Layers	50/43/7 - 28 Layers
Region 2	25/50/25 - 8 Layers	38/50/13 - 16 Layers
Region 3	40/40/20 - 10 Layers	25/50/25 - 8 Layers

3.2.4 Curvature Model Deflections

The displacement results from the three different designs are shown in Figure 14, Figure 16, and Figure 18. While all three designs resulted in different curvatures they all were fairly similar, and especially so in the five and seven spar designs. Table 15 shows the maximum tip deflection and the amount of deflection across the hardpoint locations. Table 16 and Table 17 show the deflection results in comparison to one another. Despite different structural arrangements the curvature varied less than around 15% in tip deflection and less than 20% in the deflections across the hardpoints. The five spar and seven spar designs differed by less than 2% across the hardpoints. Figure 14 through Figure 19 show the displacements graphically across the wing and across the hardpoint locations from a top view.

Table 15: Deflection Results

	Tip Deflection (in.)	Hardpoint Deflection (in.)
Three Spar	37.1	2.24
Five Spar	46.7	2.72
Seven Spar	43.7	2.76

Table 16: Tip Deflection

	Tip Deflection in % of Half Span	% Change from Seven Spar
Three Spar	9.4%	-15.1%
Five Spar	11.8%	6.9%
Seven Spar	11.0%	-

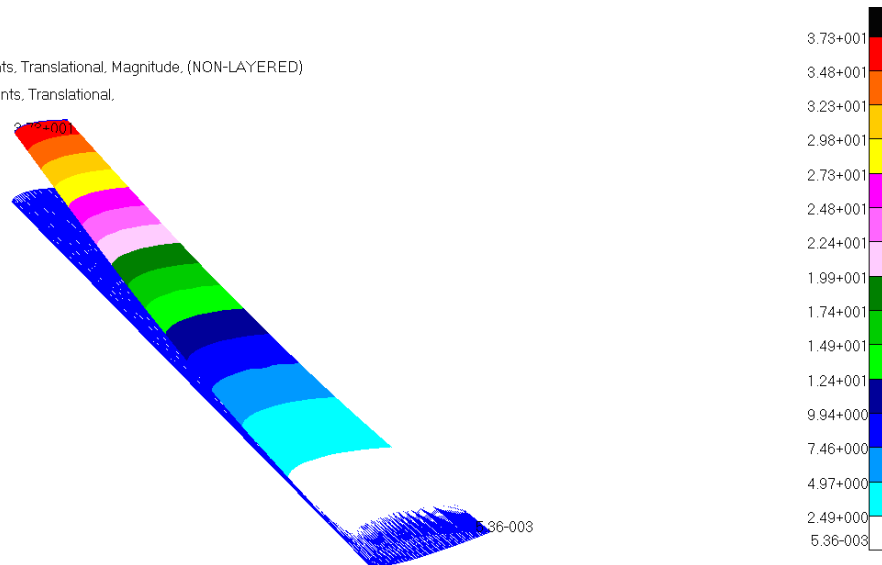
Table 17: Hardpoint Deflection

	Tip Deflection in % of Hardpoint Locations	% Change from Seven Spar
Three Spar	3.7%	-18.8%
Five Spar	4.5%	-1.4%
Seven Spar	4.6%	-

Patran 2008r1 22-Aug-11 12:54:54

Fringe: Default, A1:Static Subcase, Displacements, Translational, Magnitude, (NON-LAYERED)

Deform: Default, A1:Static Subcase, Displacements, Translational,

**Figure 14: Three Spar Wing Displacement**

Patran 2008r1 22-Aug-11 12:13:49

Fringe: Default, A1:Static Subcase, Displacements, Translational, Magnitude, (NON-LAYERED)

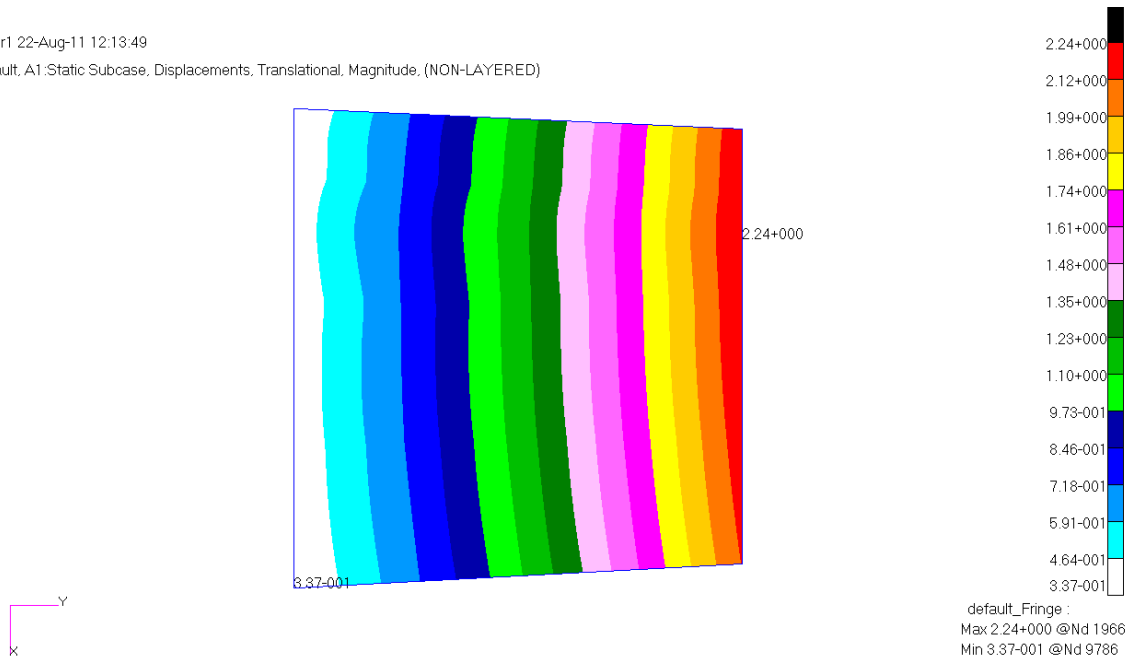


Figure 15: Three Spar Hardpoint Displacements

Patran 2008r1 22-Aug-11 12:31:42

Fringe: Default, A1:Static Subcase, Displacements, Translational, Magnitude, (NON-LAYERED)

Deform: Default, A1:Static Subcase, Displacements, Translational,

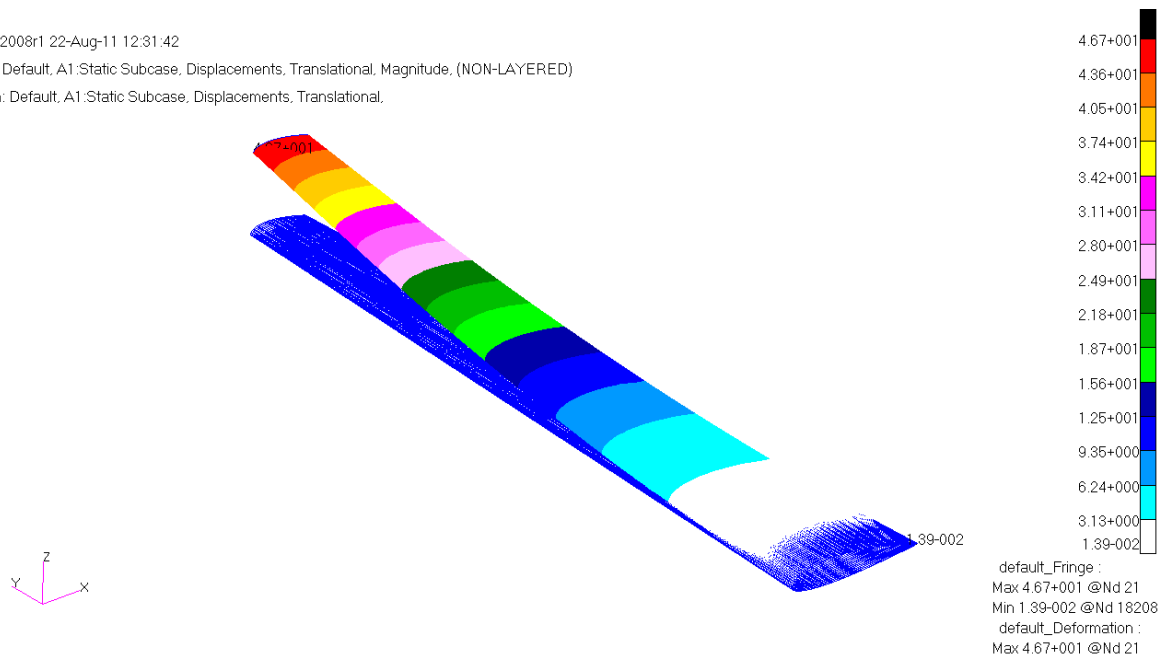


Figure 16: Five Spar Wing Displacement

Patran 2008r1 22-Aug-11 12:08:52

Fringe: Default, A1:Static Subcase, Displacements, Translational, Magnitude, (NON-LAYERED)

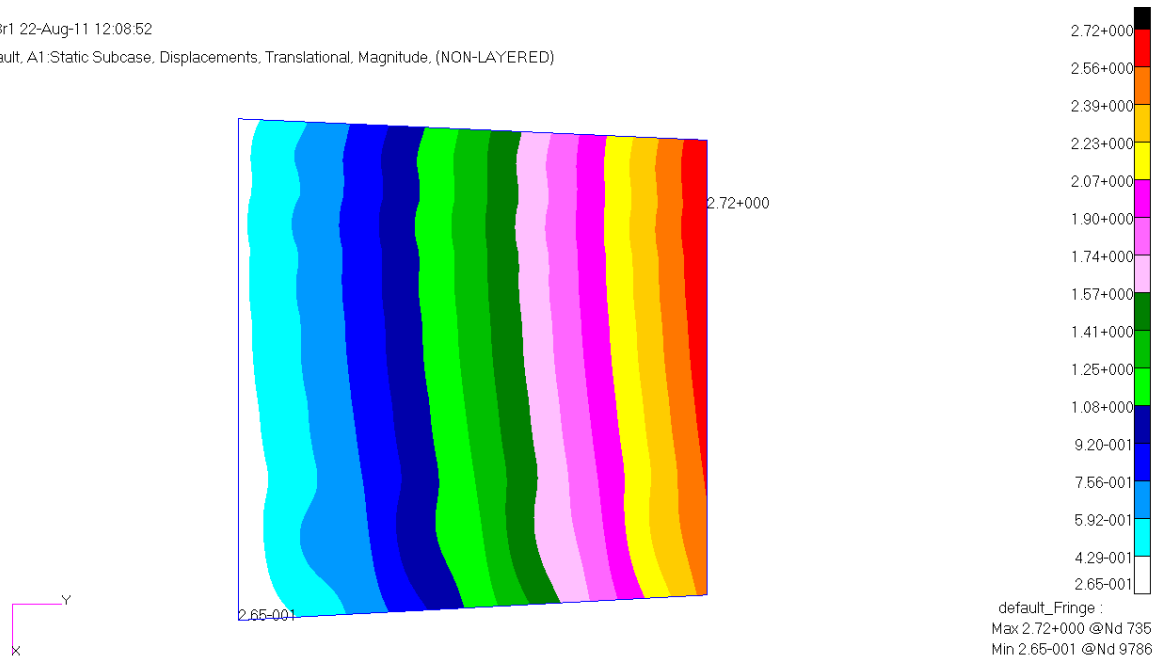


Figure 17: Five Spar Hardpoint Displacements

Patran 2008r1 22-Aug-11 12:27:52

Fringe: Default, A1:Static Subcase, Displacements, Translational, Magnitude, (NON-LAYERED)

Deform: Default, A1:Static Subcase, Displacements, Translational,

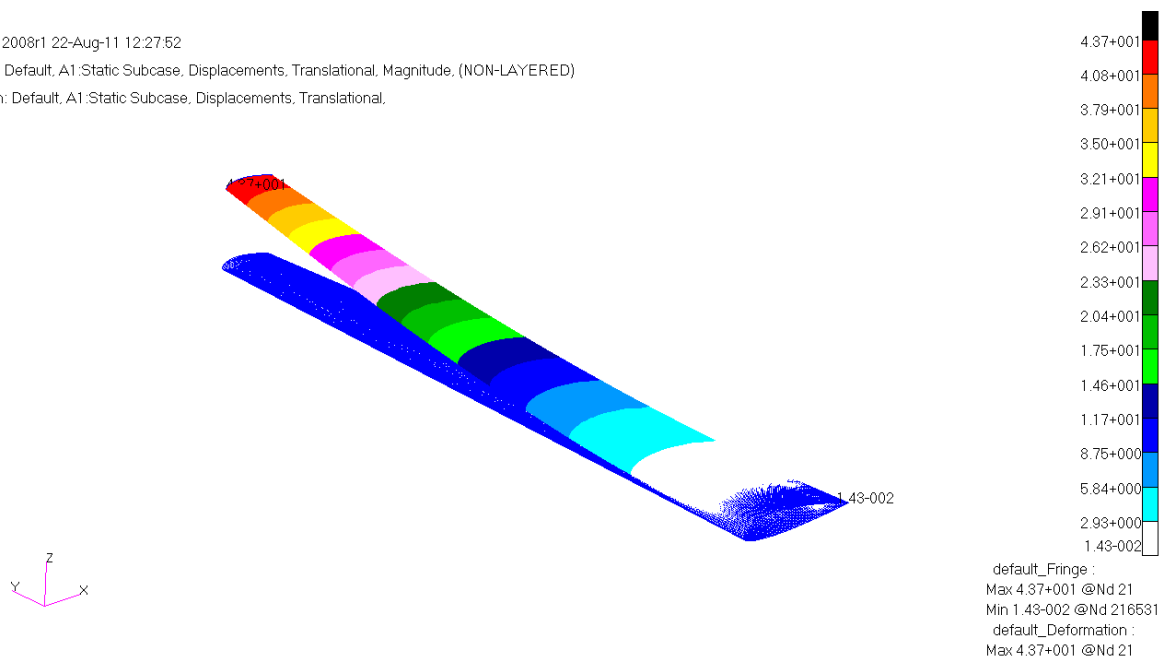


Figure 18: Seven Spar Wing Displacement

Patran 2008r1 22-Aug-11 12:21:40

Fringe: Default, A1:Static Subcase, Displacements, Translational, Magnitude, (NON-LAYERED)

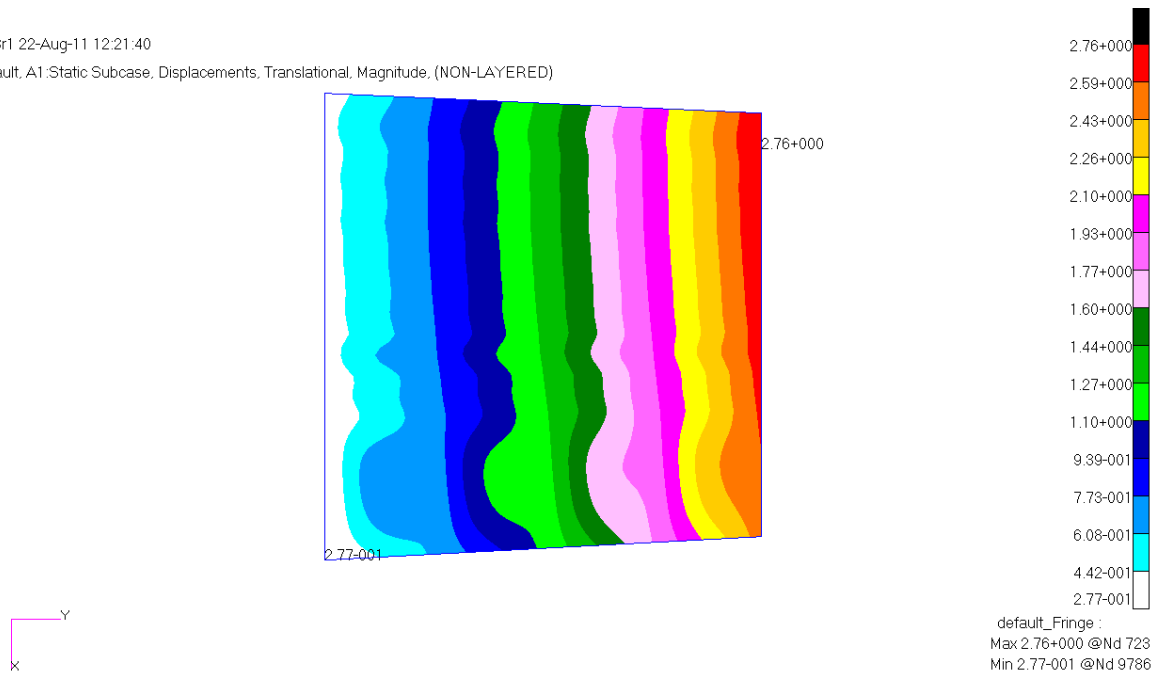


Figure 19: Seven Spar Hardpoint Displacements

The results showed the seven spar design had the largest deflection across the aircraft hardpoint locations. This curvature was used to size the fairing for the representative UAV, since the larger curvature induces a conservatively higher load on the wing-mounted fairing and pylons. It is important to note that these are clearly representative curvatures, since a preliminary sizing of three different skin and substructure arrangements resulted in displacements and curvatures within ~20% of one another. Since only the seven spar model was used and the methodology for sizing the other models was the same only the seven spar design sizing will be presented.

3.2.5 Curvature Model Verification

As stated above the total aerodynamic loads applied to the aircraft should be just over sixty-two thousand pounds of lift. Since only one of the wings of the aircraft is modeled half of that weight should be applied to the wing. The verified reaction load from the model is shown

in Figure 20. For this analysis drag is ignored. This is done since the exact drag isn't known and since the desired result is wing curvature. With reasonable torsional rigidity the drag component of the load is unnecessary. A representative rib spacing was chosen and conventional design was chosen to ensure that the torsional strength is sufficient.

```

*** USER INFORMATION MESSAGE 7310 (VECPRN)
ORIGIN OF SUPERELEMENT BASIC COORDINATE SYSTEM WILL BE USED AS REFERENCE LOCATION.
RESULTANTS ABOUT ORIGIN OF SUPERELEMENT BASIC COORDINATE SYSTEM IN SUPERELEMENT BASIC SYSTEM COORDINATES.
0
SUBCASE/   LOAD
DAREA ID  TYPE      T1      T2      T3      R1      R2      R3
0          1  FX      0.000000E+00  -----  -----  -----  0.000000E+00  0.000000E+00
  FV      -----  0.000000E+00  -----  -----  0.000000E+00  -----  0.000000E+00
  FZ      -----  -----  3.146498E+04  5.196844E+06  -8.425675E+06  -----
  MX      -----  -----  -----  0.000000E+00  -----  -----
  MY      -----  -----  -----  0.000000E+00  -----  -----
  MZ      -----  -----  -----  0.000000E+00  -----  0.000000E+00
TOTALS    0.000000E+00  0.000000E+00  3.146498E+04  5.196844E+06  -8.425675E+06  0.000000E+00
1 MSC.NASTRAN JOB CREATED ON 10-AUG-11 AT 15:13:19 MARCH 29, 2012 MD NASTRAN 5/ 9/08 PAGE 11

```

Figure 20: Curvature Model Reaction Load

The spars, skins and ribs were all modeled as 2D shell elements since all are expected to undergo axial, shear, and bending loads. To improve accuracy quad elements were used throughout the model unless element angles or aspect ratios necessitated triangular elements but these were used sparingly and never in critical regions. The model contains 75,886 elements of which only 242 are triangular elements. This results in an estimated 307,620 degrees of freedom in the model

3.2.6 Curvature Model Boundary Conditions

The boundary conditions for the model are shown in Figure 21. To simulate the fuselage wing interaction a plate was added around the wing at the fuselage location. The edges of this plate and the root section of the spars were fixed to provide the boundary conditions for the curvature model.

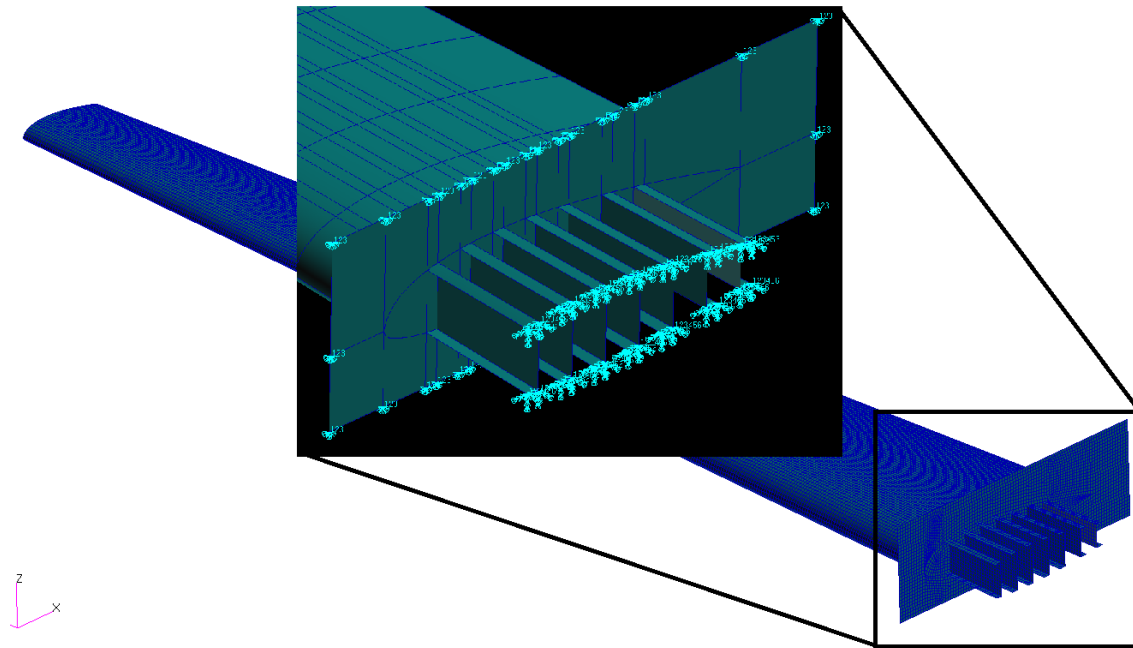


Figure 21: Boundary Conditions

To verify the accuracy of the model several things were checked. First, as shown above, the total loads were checked against expected values. Secondly a unit displacement check was done. The results are shown in Figure 23 through Figure 25. Next the displacements of the model were plotted. These displacements were compared with images of the MQ-1B in flight. The tip rotation angle and total tip displacement of real life vehicle in flight appeared to agree with the stiffness of the curvature model generated here. Since these values seem reasonable the epsilon value of the model was verified. Since the epsilon value shown in Figure 22 is low it suggests the model is acceptable.

LOAD SEQ. NO.	1	EPSILON	EXTERNAL WORK	EPSILONS LARGER THAN 0.001 ARE FLAGGED WITH ASTERISKS
		-4.5341484E-11	1.6339733E+05	
1	MSC.NASTRAN JOB CREATED ON 10-AUG-11 AT 15:13:19			APRIL 9, 2012 MD NASTRAN 5/ 9/08 PAGE 1173

Figure 22: Model Epsilon Value

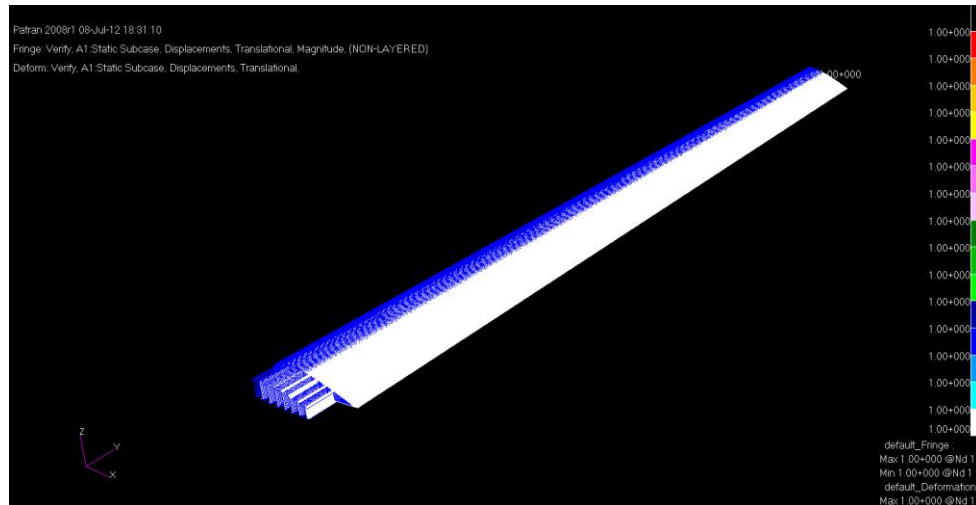


Figure 23: X Unit Displacement Check

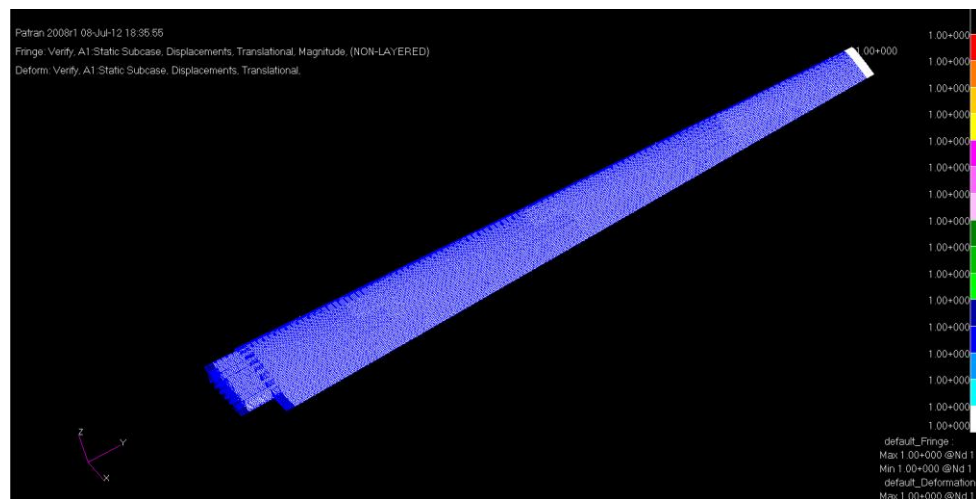


Figure 24: Y Unit Displacement Check

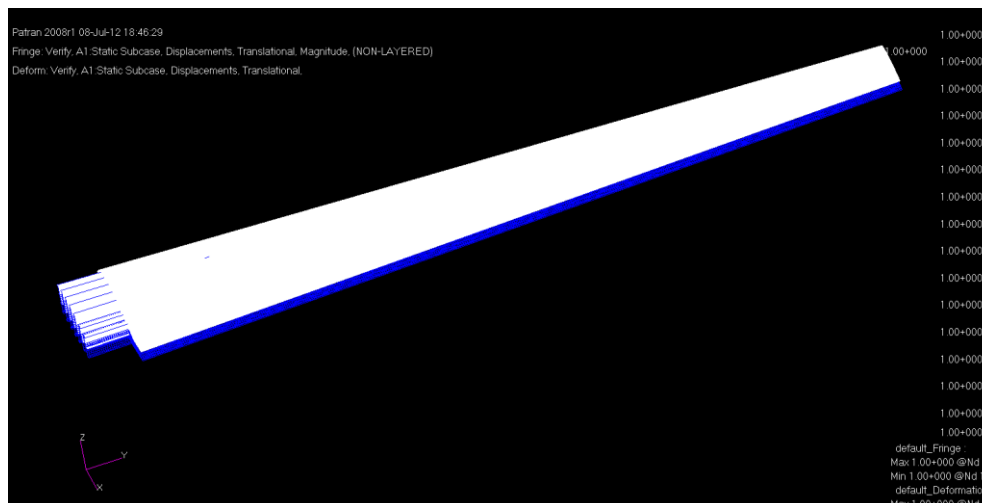


Figure 25: Z Unit Displacement Check

3.2.7 Curvature Model Sizing

The sizing for the representative UAV is presented below component by component. The material properties and margins described above were used along with a first ply failure method. The only other additional requirement placed on the design was to limit the compressive on-axis strain to .005 in/in. This was done to preserve the reparability of the structure, by designing to a strain limit tolerant of local impact damage, or holes associated with drilled repair.

3.2.7.1 Skins

The sizing for skin section is presented below. The plots are presented in element coordinate systems unless otherwise indicated. The coordinates for the elements are shown in Figure 26. Composite materials were aligned with the global Y axis in the model.

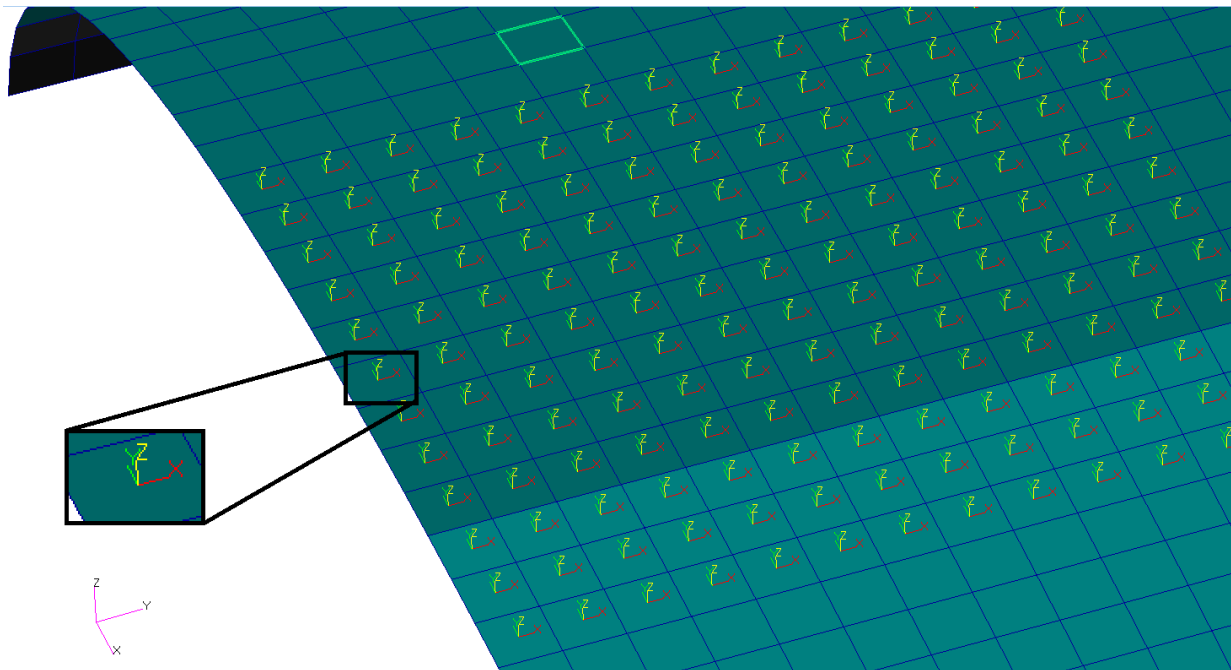


Figure 26: Wing Element Coordinate System

The margins of safety for the failure methods examined for the upper skin are presented in Table 19. The critical margin of safety for each region has been highlighted in yellow and the wings critical margin is highlighted in orange.

Table 18: Curvature Skin Strains

M.S	Region 1	Region 2	Region 3
ε_1^C	-0.00470	-0.00446	-0.00408
ε_1^T	0.00463	0.00455	0.00498
γ_{12}	0.00569	0.00569	0.00484
ε_2^C	-0.00452	-0.00452	-0.00478
ε_2^T	0.00445	0.00434	0.00430

Table 19: Curvature Skin Margins

M.S	Region 1	Region 2	Region 3
ε_1^C	0.065	0.122	0.226
ε_1^T	1.766	1.814	1.571
γ_{12}	4.132	4.133	5.033
ε_2^C	0.105	0.106	0.050
ε_2^T	0.579	0.618	0.632

Each of these failure methods will be examined and the strains for each failure method will be presented next.

3.2.7.1.1 Primary Material Axis Compressive Strain

The on axis compressive strain for the upper skin is presented in Figure 27 and the lower skin is shown in Figure 28. The upper skin is expected to see the most compression but the lower skin is also verified. The boundary regions between the three regions are clearly visible. The bending load down the wing drops fairly linearly but the stiffness of the structure drops at the region boundaries and then remains constant until the next region boundary is reached. As

previously mentioned this is the failure method where strain was limited to allow the structure to be repairable. As expected the upper skin plies experience more compressive load so the critical region is found in the upper skin in region 3 and shown in Figure 29. The highest loaded areas in the other regions are presented below. Local boundary effects are seen near the root of the wing. Some of these boundary effects should be expected since the wing fuselage interaction will cause the load in these regions to rise. A fair amount of the stress concentration is real and to be expected but some of it is artificial. Since the model is sized to withstand this concentration this increases the stiffness of the wing and decreases the curvature in this section of the curvature model.

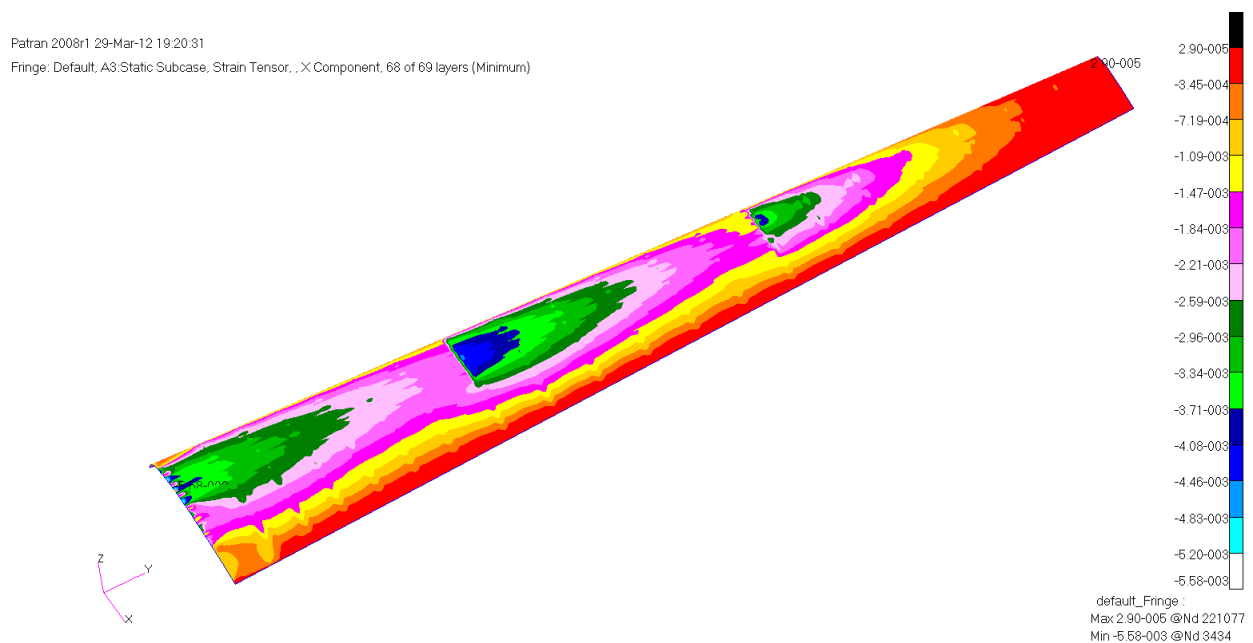


Figure 27: Upper Skin ϵ_1 Component Compressive Strains

Patran 2008r1 29-Mar-12 20:21:26
 Fringe: Default, A3:Static Subcase, Strain Tensor, X Component, 68 of 69 layers (Minimum)

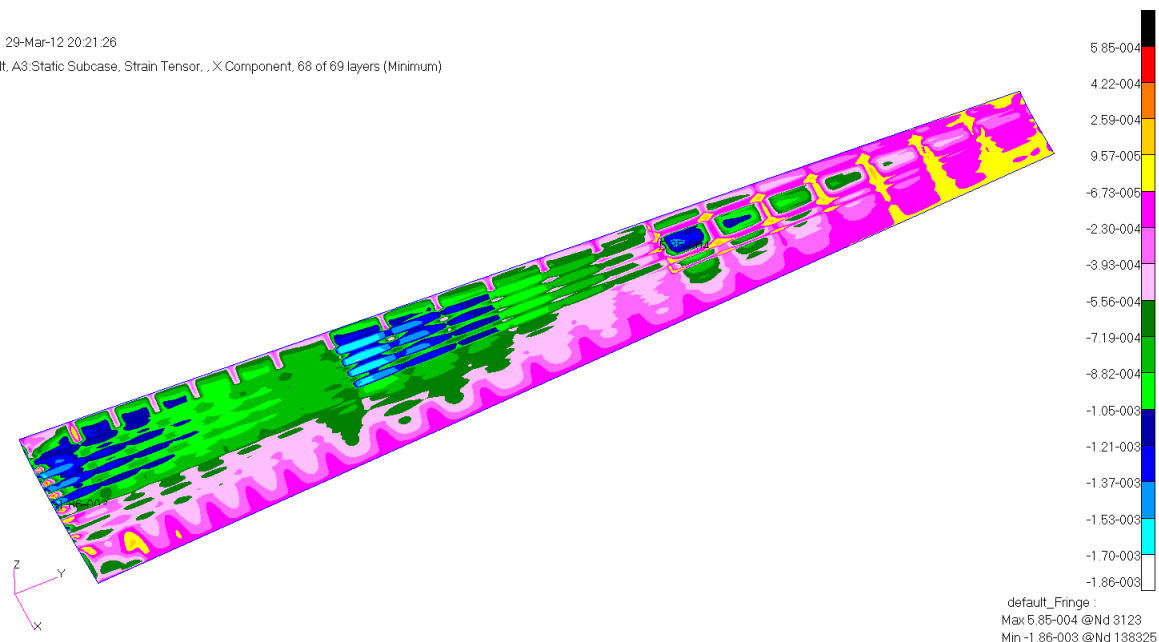


Figure 28: Lower Skin ϵ_1 Component Compressive Strain Distribution

Patran 2008r1 29-Mar-12 19:20:31
 Fringe: Default, A3:Static Subcase, Strain Tensor, X Component, 68 of 69 layers (Minimum)

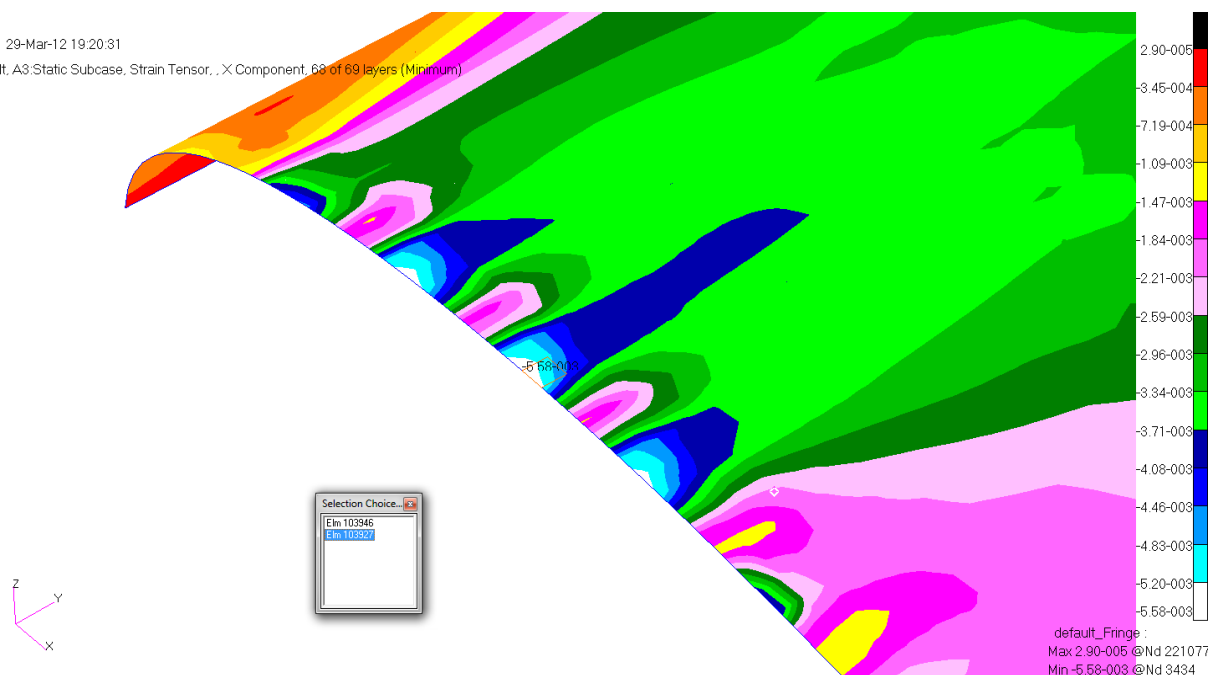


Figure 29: Upper Skin ϵ_1 Component Compressive Critical Region 1

Patran 2008r1 05-Jul-12 21:08:19
 Fringe: Default, A1: Static Subcase, Strain Tensor, .X Component, Minimum:68 of 69 layers

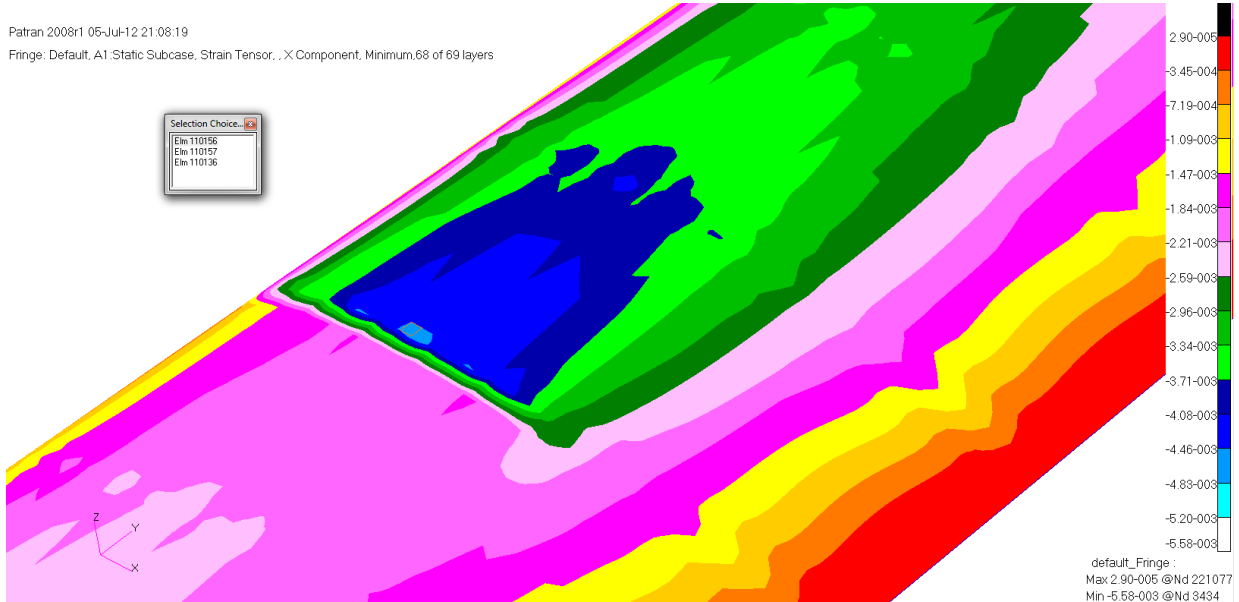


Figure 30: Upper Skin ε_1 Component Compressive Critical Region 2

Patran 2008r1 05-Jul-12 21:08:19
 Fringe: Default, A1: Static Subcase, Strain Tensor, .X Component, Minimum:68 of 69 layers

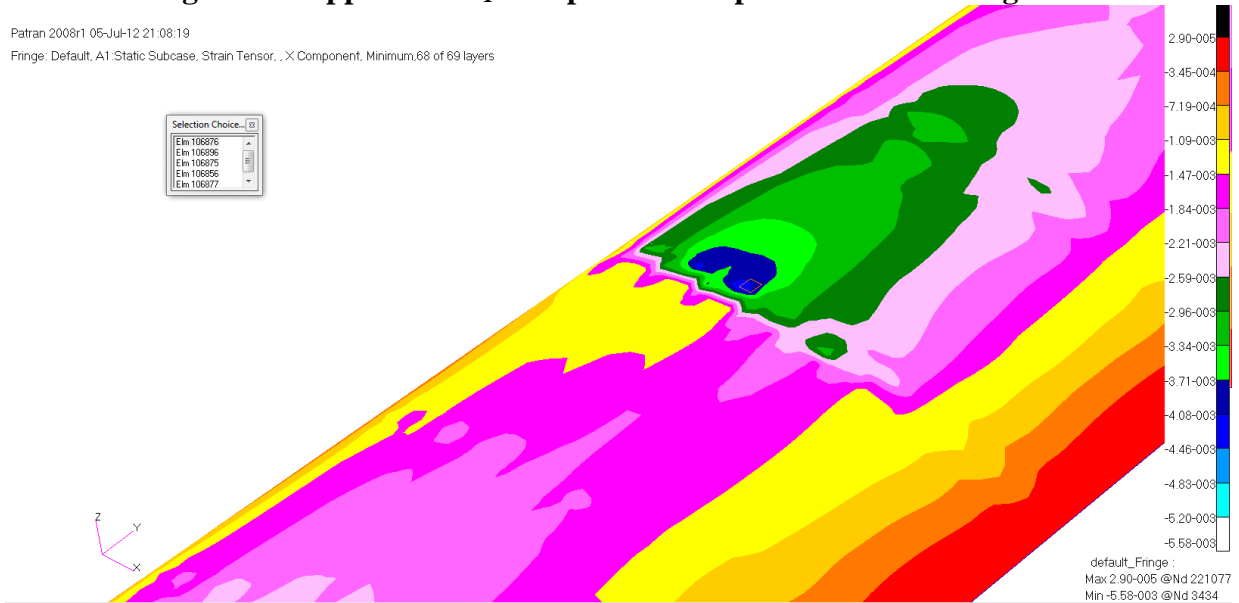


Figure 31: Upper Skin ε_1 Component Compressive Critical Region 3

STRAINS IN LAYERED						COMPOSITE ELEMENTS (QUAD4)					
ELEMENT ID	PLY ID	STRAINS IN FIBER AND MATRIX DIRECTIONS			INTER-LAMINAR STRAINS		PRINCIPAL STRAINS (ZERO SHEAR)		MAX SHEAR		
		NORMAL-1	NORMAL-2	SHEAR-12	SHEAR XZ-MAT	SHEAR YZ-MAT	ANGLE	MAJOR		MINOR	
0	103927	1	-1.31639E-03	-1.67025E-03	-4.92441E-03	0.0	0.0	-42.94	9.75235E-04	-3.96187E-03	4.93711E-03
0	103927	2	-1.67650E-03	-1.35724E-03	4.99111E-03	0.0	0.0	46.83	9.83785E-04	-4.01752E-03	5.00131E-03
0	103927	3	-4.06933E-03	9.88482E-04	-2.84674E-04	0.0	0.0	-88.39	9.92485E-04	-4.07333E-03	5.06581E-03
0	103927	4	-4.12623E-03	9.98280E-04	-2.50082E-04	0.0	0.0	-88.60	1.00133E-03	-4.12928E-03	5.13061E-03
0	103927	5	-1.47978E-03	-1.69527E-03	-5.19121E-03	0.0	0.0	-43.81	1.01031E-03	-4.18536E-03	5.19568E-03
0	103927	6	1.01788E-03	-4.24003E-03	1.80897E-04	0.0	0.0	0.99	1.01943E-03	-4.24159E-03	5.26102E-03
0	103927	7	-1.70778E-03	-1.56148E-03	5.32461E-03	0.0	0.0	45.79	1.02868E-03	-4.29794E-03	5.32662E-03
0	103927	8	-4.35383E-03	1.03747E-03	-1.11712E-04	0.0	0.0	-89.41	1.03805E-03	-4.35441E-03	5.39246E-03
0	103927	9	-4.41074E-03	1.04727E-03	-7.71190E-05	0.0	0.0	-89.60	1.04754E-03	-4.41101E-03	5.45855E-03
0	103927	10	-1.72655E-03	-1.68402E-03	5.52471E-03	0.0	0.0	45.22	1.05715E-03	-4.46772E-03	5.52487E-03
0	103927	11	1.06687E-03	-4.52454E-03	7.93388E-06	0.0	0.0	0.04	1.06687E-03	-4.52454E-03	5.59141E-03
0	103927	12	-1.76572E-03	-1.73906E-03	-5.65810E-03	0.0	0.0	-45.13	1.07669E-03	-4.58147E-03	5.65817E-03
0	103927	13	-4.63834E-03	1.08646E-03	6.12512E-05	0.0	0.0	89.69	1.08663E-03	-4.63851E-03	5.72513E-03
0	103927	14	-4.65524E-03	1.09626E-03	9.58438E-05	0.0	0.0	89.53	1.09666E-03	-4.69564E-03	5.79230E-03
0	103927	15	-1.75783E-03	-1.88826E-03	5.85820E-03	0.0	0.0	44.36	1.10678E-03	-4.75287E-03	5.85966E-03
0	103927	16	-1.92911E-03	-1.76408E-03	-5.92490E-03	0.0	0.0	-45.80	1.11700E-03	-4.81020E-03	5.92720E-03

Figure 32: Upper Skin ε_1 Component Compressive Critical Strains Region 1

ELEMENT ID	PLY ID	STRAINS IN LAYERED STRAINS IN FIBER AND MATRIX DIRECTIONS			COMPOSITE ELEMENTS (QUAD4)							MAX SHEAR
		NORMAL-1	NORMAL-2	SHEAR-12	INTER-LAMINAR SHEAR XZ-MAT	STRAINS SHEAR YZ-MAT	PRINCIPAL ANGLE	STRAINS (ZERO SHEAR)		MAJOR	MINOR	
0	110157	1	-4.45552E-03	1.07612E-03	-3.54502E-04	0.0	0.0	-88.17	1.08180E-03	-4.46119E-03	5.54299E-03	
0	110157	2	-1.52224E-03	-1.88542E-03	-5.45082E-03	0.0	0.0	-43.09	1.02762E-03	-4.43528E-03	5.46291E-03	
0	110157	3	9.67039E-04	-4.40296E-03	3.71874E-04	0.0	0.0	1.98	9.73470E-04	-4.40939E-03	5.38286E-03	
0	110157	4	-1.92237E-03	-1.54181E-03	5.28918E-03	0.0	0.0	47.06	9.19335E-04	-4.38352E-03	5.30285E-03	
0	110157	5	-1.94085E-03	-1.55160E-03	5.20836E-03	0.0	0.0	47.14	8.65219E-04	-4.35767E-03	5.22289E-03	
0	110157	6	8.03415E-04	-4.32413E-03	3.97933E-04	0.0	0.0	2.22	8.11124E-04	-4.33184E-03	5.14296E-03	
0	110157	7	-1.57118E-03	-1.97780E-03	-5.04672E-03	0.0	0.0	-42.70	7.57051E-04	-4.30603E-03	5.06308E-03	
0	110157	8	-4.27157E-03	6.94333E-04	-4.15306E-04	0.0	0.0	-87.61	7.03001E-04	-4.28024E-03	4.98324E-03	

Figure 33: Upper Skin ϵ_1 Component Compressive Critical Strains Region 2

ELEMENT ID	PLY ID	STRAINS IN LAYERED STRAINS IN FIBER AND MATRIX DIRECTIONS				COMPOSITE ELEMENTS (QUAD4)							MAX SHEAR
		NORMAL-1		NORMAL-2		SHEAR-12		INTER-LAMINAR STRAINS		PRINCIPAL STRAINS (ZERO SHEAR)			
		NORMAL-1	NORMAL-2	SHEAR-12	SHEAR XZ-MAT	SHEAR YZ-MAT	ANGLE	MAJOR	MINOR				
0	106876	1	-4.07781E-03	1.02736E-03	1.35313E-03	0.0	0.0	82.58	1.11550E-03	-4.16595E-03	5.28145E-03		
0	106876	2	-4.07534E-03	1.00832E-03	1.28506E-03	0.0	0.0	82.91	1.08828E-03	-4.15530E-03	5.24357E-03		
0	106876	3	-2.15030E-03	-9.33294E-04	-5.06216E-03	0.0	0.0	-51.76	1.06140E-03	-4.14500E-03	5.20640E-03		
0	106876	4	9.70246E-04	-4.07041E-03	-1.14894E-03	0.0	0.0	-6.42	1.03489E-03	-4.13505E-03	5.16994E-03		
0	106876	5	-1.01793E-03	-2.09881E-03	5.01915E-03	0.0	0.0	38.92	1.00874E-03	-4.12548E-03	5.13422E-03		
0	106876	6	-1.06024E-03	-2.07307E-03	4.99765E-03	0.0	0.0	39.27	9.82967E-04	-4.11628E-03	5.09924E-03		
0	106876	7	9.13130E-04	-4.06301E-03	-9.44764E-04	0.0	0.0	-5.38	9.57575E-04	-4.10746E-03	5.06503E-03		
0	106876	8	-2.02158E-03	-1.14488E-03	-4.95464E-03	0.0	0.0	-50.02	9.32574E-04	-4.09903E-03	5.03160E-03		
0	106876	9	-4.05808E-03	8.75052E-04	8.08643E-04	0.0	0.0	85.35	9.07971E-04	-4.09100E-03	4.99897E-03		
0	106876	10	-4.05561E-03	8.56013E-04	7.40583E-04	0.0	0.0	85.71	8.83773E-04	-4.08337E-03	4.96715E-03		

Figure 34: Upper Skin ϵ_1 Component Compressive Critical Strains Region 3

Figure 32 shows the maximum ϵ_1 component strain of .0047 in the upper skin captured from the results file at region 1. Since the material is aligned with the Y axis and the fringe plot is aligned with the element X axis there is some disparity between the plot and the .f06 result. The taper in the wing causes these vectors not to match. As previously mentioned the loading for the curvature model has the factor of safety applied to the load. This simplifies the calculation for the margin of safety shown below.

$$MS = \frac{\epsilon_{allowable}}{\epsilon_{actual}} - 1 = \frac{.005 (in / in)}{.00407781 (in / in)} - 1 = .050$$

3.2.7.1.2 Primary Material Axis Tensile Strain

The on axis tensile strain for the upper skin is presented in Figure 35 and the lower skin is shown in Figure 36. Overall the lower skin plies experience more tensile load thus the critical region is found in the lower skin at the at region 3. This is shown in Figure 39 and the highest loaded areas in the other regions are presented below.

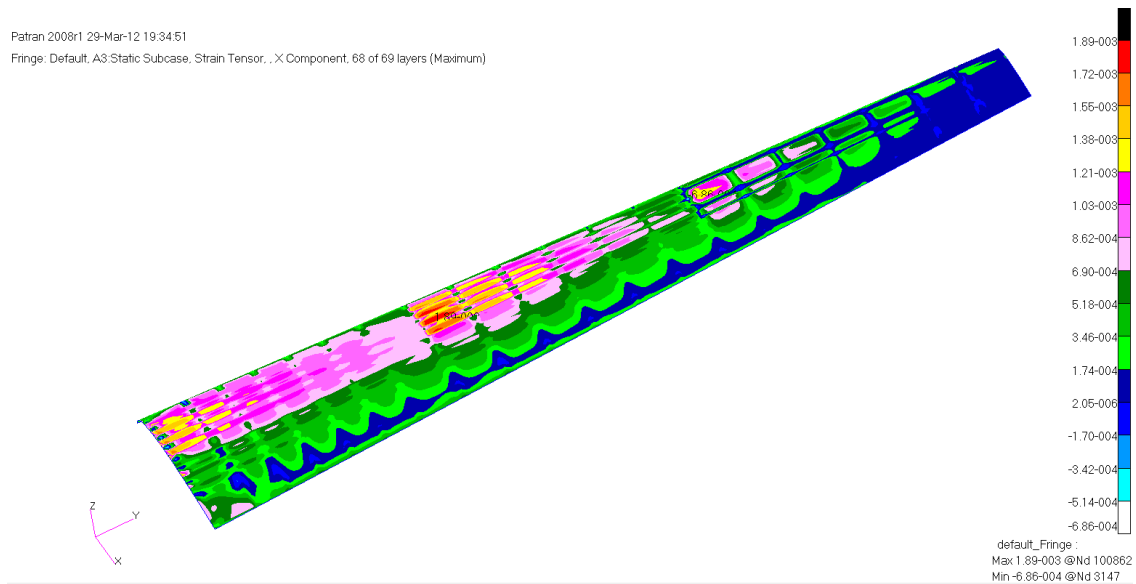


Figure 35: Upper Skin ϵ_1 Component Tensile Strain

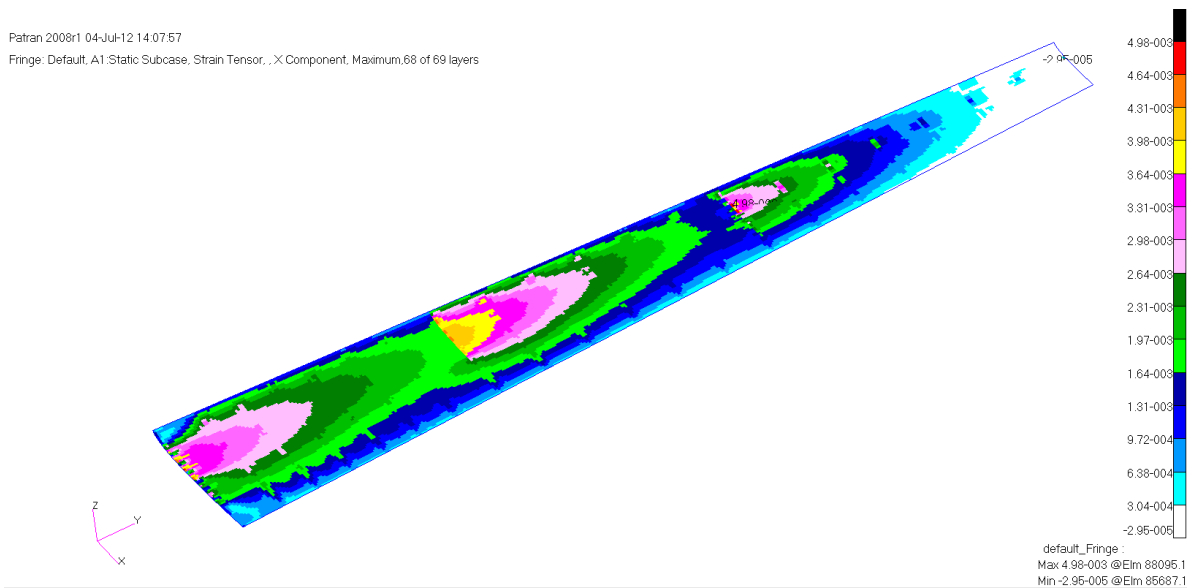


Figure 36: Lower Skin ϵ_1 Component Tensile Strain

Patran 2008r1 04-Jul-12 14:45:43

Fringe: Default, A1 Static Subcase, Strain Tensor, X Component, Maximum:68 of 69 layers

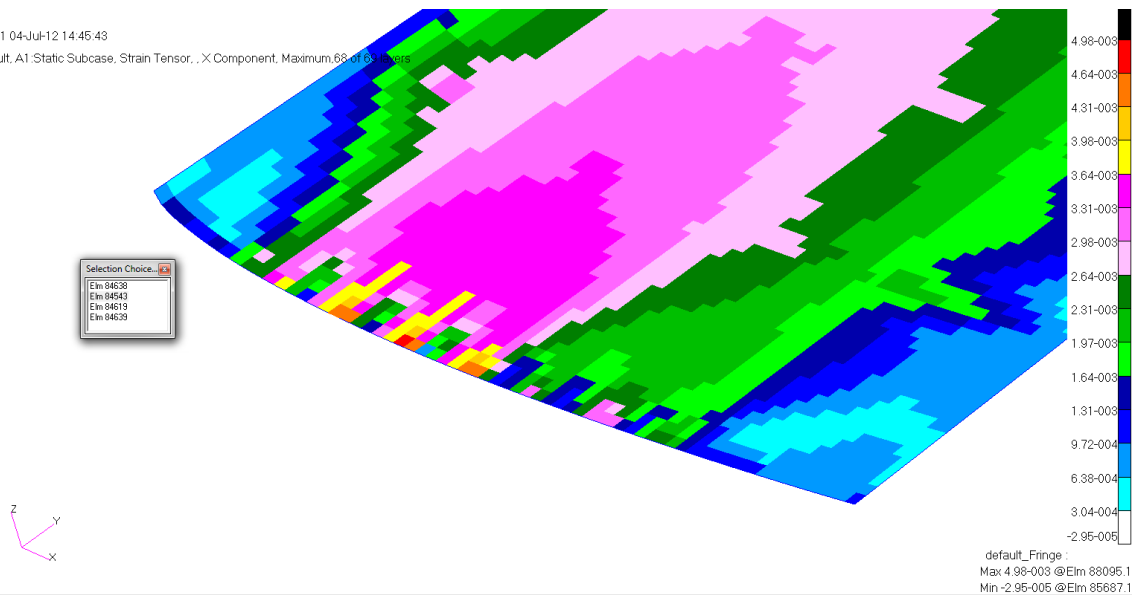


Figure 37: Lower Skin ε_1 Component Tensile Strain Critical Region 1

Patran 2008r1 04-Jul-12 14:07:57

Fringe: Default, A1 Static Subcase, Strain Tensor, X Component, Maximum:68 of 69 layers

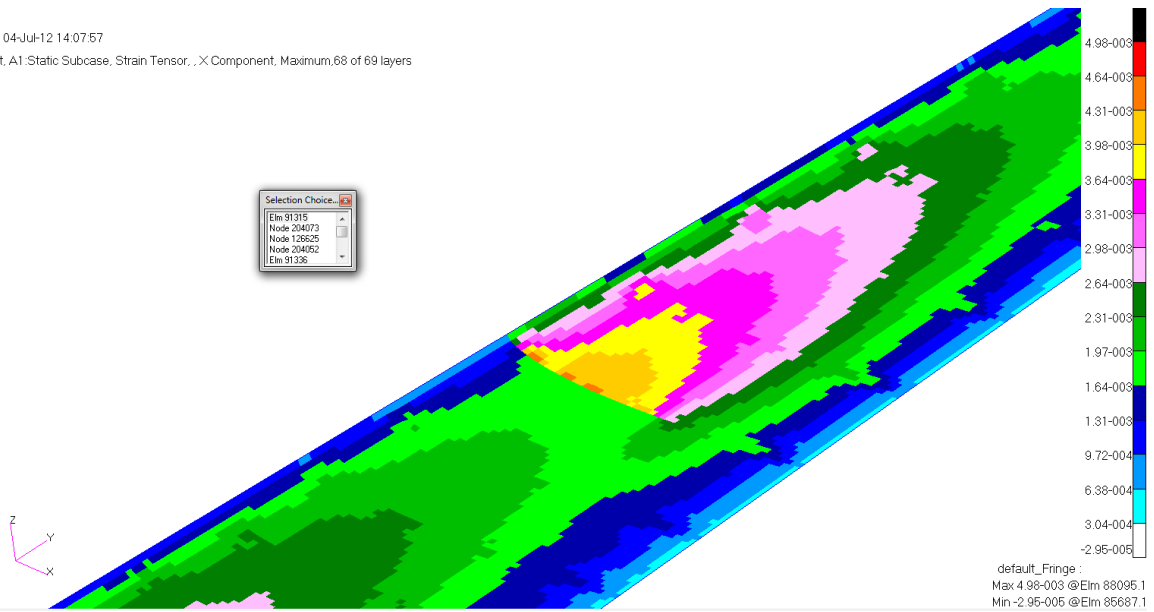


Figure 38: Lower Skin ε_1 Component Tensile Strain Critical Region 2

Patran 2008r1 04-Jul-12 14:07:57

Fringe: Default, A1:Static Subcase, Strain Tensor, X Component, Maximum,68 of 69 layers

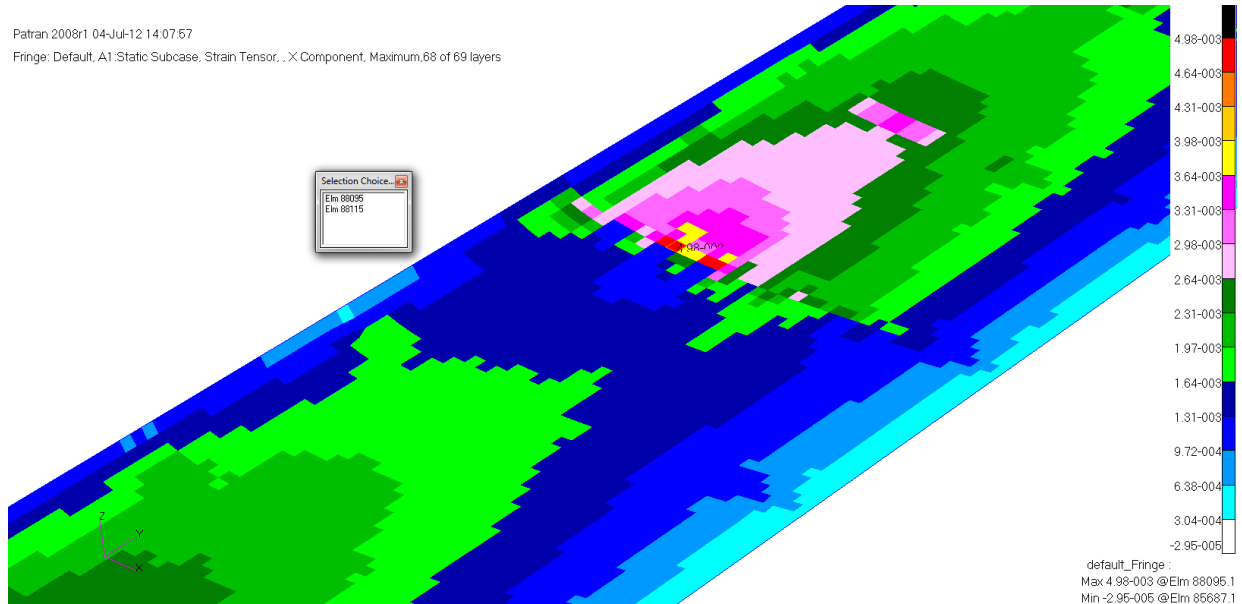


Figure 39: Lower Skin ϵ_1 Component Tensile Strain Critical Region 3

ELEMENT ID	PLY ID	STRAINS IN LAYERED STRAINS IN FIBER AND MATRIX DIRECTIONS			COMPOSITE ELEMENTS (QUAD4)		INTER-LAMINAR SHEAR XZ-MAT	STRAINS PRINCIPAL	STRAINS (ZERO SHEAR)		MAX SHEAR
		NORMAL-1	NORMAL-2	SHEAR-12	SHEAR YZ-MAT	ANGLE			MAJOR	MINOR	
0	84543	1	2.07819E-03	1.53121E-03	5.88836E-03	0.0	0.0	42.35	4.76156E-03	-1.15216E-03	5.91371E-03
0	84543	2	1.52728E-03	2.03183E-03	-5.81733E-03	0.0	0.0	-47.48	4.69914E-03	-1.14004E-03	5.83917E-03
0	84543	3	4.62756E-03	-1.11875E-03	-4.62121E-04	0.0	0.0	-2.30	4.63683E-03	-1.12802E-03	5.76486E-03
0	84543	4	4.56689E-03	-1.10838E-03	-4.19693E-04	0.0	0.0	-2.11	4.57464E-03	-1.11613E-03	5.69077E-03
0	84543	5	1.89274E-03	1.51548E-03	5.60424E-03	0.0	0.0	43.07	4.51257E-03	-1.10436E-03	5.61693E-03
0	84543	6	-1.08765E-03	4.44557E-03	3.34835E-04	0.0	0.0	88.27	4.45063E-03	-1.09271E-03	5.54334E-03
0	84543	7	1.50761E-03	1.80001E-03	-5.46219E-03	0.0	0.0	-46.53	4.38881E-03	-1.08119E-03	5.47001E-03
0	84543	8	4.32424E-03	-1.06692E-03	-2.49978E-04	0.0	0.0	-1.33	4.32714E-03	-1.06981E-03	5.39695E-03
0	84543	9	4.26358E-03	-1.05655E-03	-2.07549E-04	0.0	0.0	-1.12	4.26560E-03	-1.05857E-03	5.32417E-03
0	84543	10	1.49581E-03	1.66093E-03	-5.24910E-03	0.0	0.0	-45.90	4.20421E-03	-1.04748E-03	5.25169E-03
0	84543	11	-1.03582E-03	4.14225E-03	1.22692E-04	0.0	0.0	89.32	4.14298E-03	-1.03654E-03	5.17952E-03
0	84543	12	1.56820E-03	1.48794E-03	5.10704E-03	0.0	0.0	44.55	4.08191E-03	-1.02576E-03	5.10767E-03
0	84543	13	4.02093E-03	-1.01508E-03	-3.78349E-05	0.0	0.0	-0.22	4.02100E-03	-1.01515E-03	5.03615E-03
0	84543	14	3.96027E-03	-1.00471E-03	4.59371E-06	0.0	0.0	0.03	3.96027E-03	-1.00472E-03	4.96498E-03
0	84543	15	1.47614E-03	1.42912E-03	-4.89395E-03	0.0	0.0	-44.72	3.89972E-03	-9.94461E-04	4.89418E-03
0	84543	16	1.38275E-03	1.47220E-03	4.82292E-03	0.0	0.0	45.53	3.83935E-03	-9.84396E-04	4.82375E-03

Figure 40: Lower Skin ϵ_1 Component Tensile Critical Strain Region 1

STRAINS IN LAYERED STRAINS IN FIBER AND MATRIX DIRECTIONS						COMPOSITE ELEMENTS (QUAD4)					MAX SHEAR
ELEMENT ID	PLY ID	NORMAL-1	NORMAL-2	SHEAR-12	INTER-LAMINAR SHEAR XZ-MAT	SHEAR YZ-MAT	ANGLE	STRAINS (ZERO SHEAR) MAJOR	STRAINS (ZERO SHEAR) MINOR		
0	91315	1	4.54853E-03	-6.58130E-04	2.38738E-04	0.0	0.0	1.31	4.55127E-03	-6.60865E-04	5.21213E-03
0	91315	2	1.78171E-03	2.03170E-03	5.07420E-03	0.0	0.0	46.41	4.44688E-03	-6.33474E-04	5.08036E-03
0	91315	3	-6.02664E-04	4.33908E-03	-2.61256E-04	0.0	0.0	-88.49	4.34253E-03	-6.06115E-04	4.94864E-03
0	91315	4	1.96597E-03	1.69345E-03	-4.80928E-03	0.0	0.0	-43.38	4.23821E-03	-5.78789E-04	4.81700E-03
0	91315	5	1.93310E-03	1.64933E-03	-4.67682E-03	0.0	0.0	-43.26	4.13393E-03	-5.51493E-04	4.68543E-03
0	91315	6	-5.19466E-04	4.02490E-03	-2.95032E-04	0.0	0.0	-88.14	4.02969E-03	-5.24249E-04	4.55393E-03
0	91315	7	1.56107E-03	1.86737E-03	4.41191E-03	0.0	0.0	46.99	3.92548E-03	-4.97043E-04	4.42253E-03
0	91315	8	3.81545E-03	-4.64000E-04	3.17550E-04	0.0	0.0	2.12	3.82133E-03	-4.69883E-04	4.29121E-03

Figure 41: Lower Skin ϵ_1 Component Tensile Critical Strain Region 2

ELEMENT ID	PLY ID	STRAINS IN LAYERED STRAINS IN FIBER AND MATRIX DIRECTIONS			COMPOSITE ELEMENTS (QUAD4)		PRINCIPAL ANGLE	STRAINS (ZERO SHEAR)		MAX SHEAR	
		NORMAL-1	NORMAL-2	SHEAR-12	INTER-LAMINAR SHEAR XZ-MAT	SHEAR YZ-MAT		MAJOR	MINOR		
0	88095	1	4.97885E-03	-2.95643E-04	1.70457E-05	0.0	0.0	0.09	4.97886E-03	-2.95657E-04	5.27452E-03
0	88095	2	4.75790E-03	-2.99244E-04	6.77640E-05	0.0	0.0	0.38	4.75812E-03	-2.99471E-04	5.05759E-03
0	88095	3	2.05781E-03	2.17629E-03	4.83979E-03	0.0	0.0	45.70	4.53767E-03	-3.03569E-04	4.84124E-03
0	88095	4	-3.06445E-04	4.31599E-03	-1.69200E-04	0.0	0.0	-88.95	4.31754E-03	-3.07993E-04	4.62553E-03
0	88095	5	2.00246E-03	1.78254E-03	-4.40509E-03	0.0	0.0	-43.57	4.09779E-03	-3.12789E-04	4.41058E-03
0	88095	6	1.91554E-03	1.64490E-03	-4.18774E-03	0.0	0.0	-43.15	3.87846E-03	-3.18014E-04	4.19647E-03
0	88095	7	-3.17247E-04	3.65314E-03	-3.21355E-04	0.0	0.0	-87.69	3.65963E-03	-3.23739E-04	3.98337E-03
0	88095	8	1.36963E-03	1.74171E-03	3.75304E-03	0.0	0.0	47.83	3.44139E-03	-3.30047E-04	3.77144E-03

Figure 42: Lower Skin ϵ_1 Component Tensile Critical Strain Region 3

Figure 42 shows the maximum ϵ_1 component strain of .000498 in the lower skin captured from the results file at region 3. The difference in vectors between the Y global axis and the ϵ_1

material axis are evident here also. The taper of the wing causes these vectors to not be aligned and causes the differences between the two values. The margin of safety for this method of failure is shown below:

$$MS = \frac{\varepsilon_{allowable}}{\varepsilon_{actual}} - 1 = \frac{.0128(in/in)}{.00497885(in/in)} - 1 = 1.571$$

3.2.7.1.3 Secondary Material Axis Tensile Strain

The off axis tensile strain for the upper skin is presented in Figure 43 and the lower skin is shown in Figure 44. The boundary conditions at the root dominate this load condition also. The highest loaded region is in wing region one and is shown in Figure 45. The highest loaded areas in the other regions are presented below

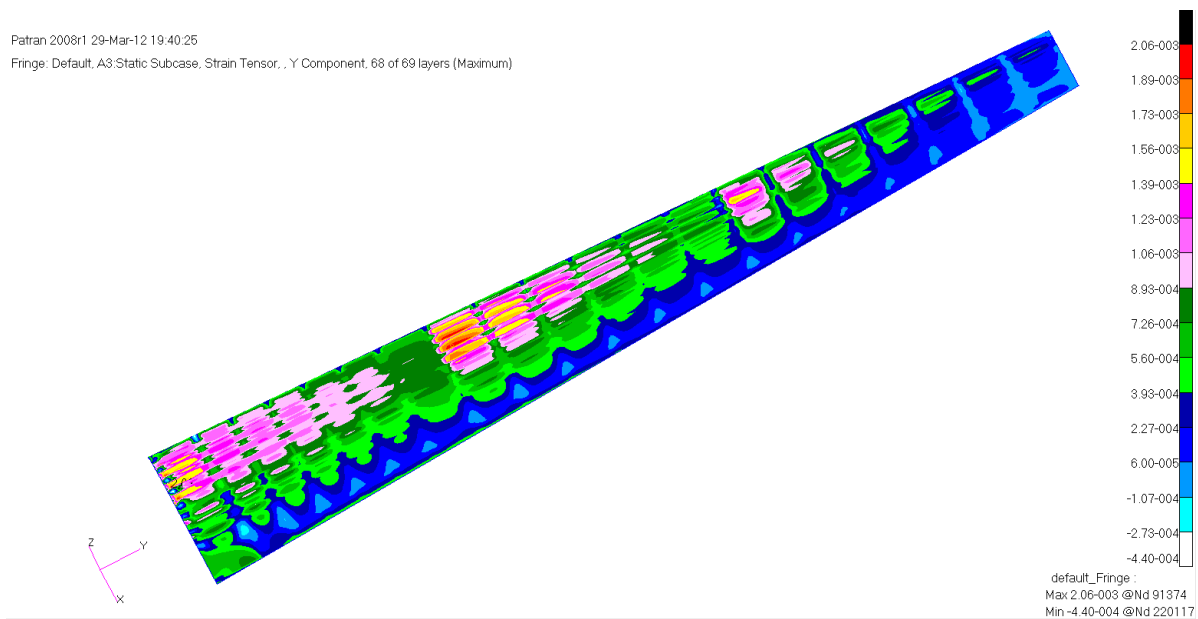


Figure 43: Upper Skin ε_2 Component Tensile Strain

Patran 2008r1 04-Jul-12 16:21:43
 Fringe: Default, A1 Static Subcase, Strain Tensor, Y Component, Maximum, 68 of 69 layers

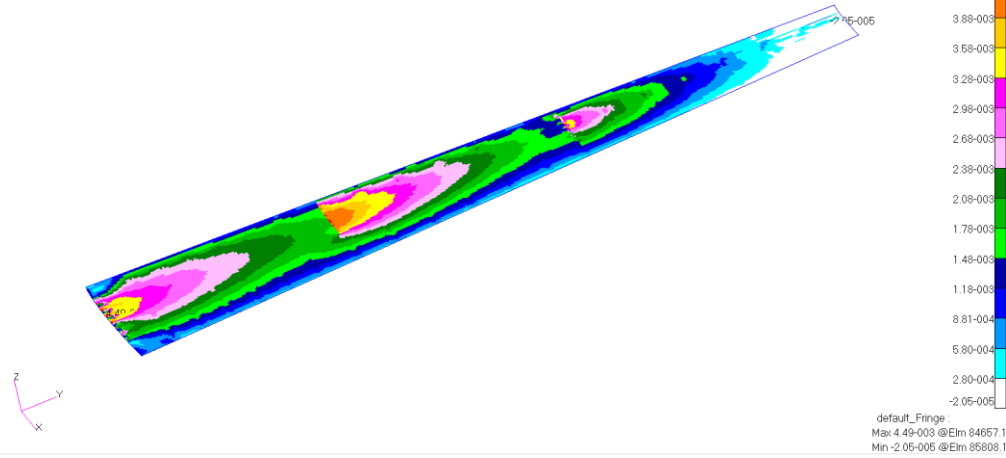


Figure 44: Lower Skin ε_2 Component Tensile Strain

Patran 2008r1 04-Jul-12 16:21:43
 Fringe: Default, A1 Static Subcase, Strain Tensor, Y Component, Maximum, 68 of 69 layers

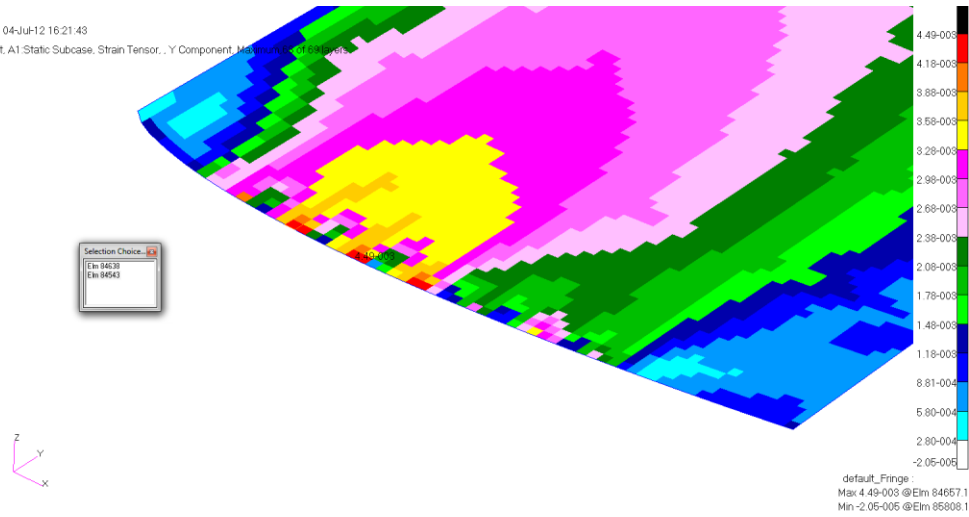


Figure 45: Lower Skin ε_2 Component Tensile Strain Region 1

Patran 2008r1 04-Jul-12 16:21:43
 Fringe: Default, A1 Static Subcase, Strain Tensor, Y Component, Maximum, 68 of 69 layers

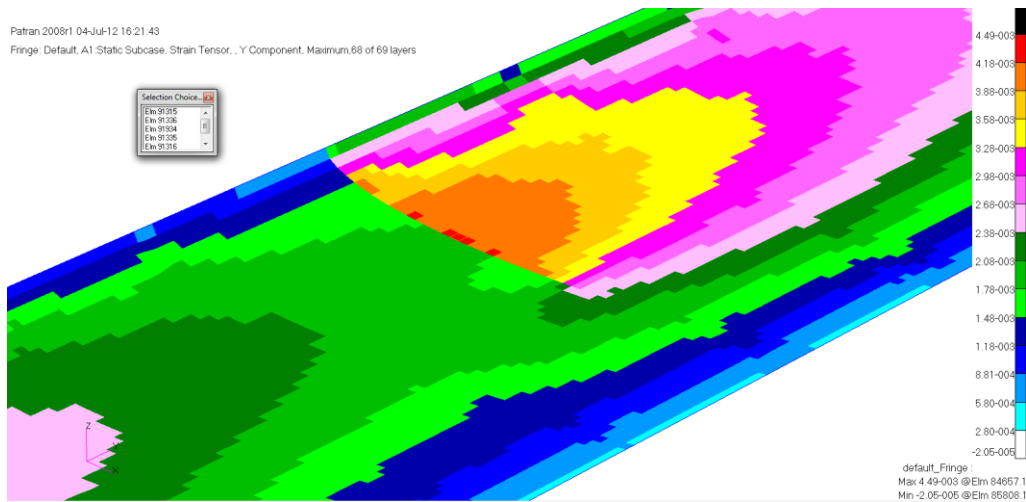


Figure 46: Lower Skin ε_2 Component Tensile Strain Region 2

Patran 2008r1 04-Jul-12 16:21:43

Fringe: Default, A1 Static Subcase, Strain Tensor, Y Component, Maximum,68 of 69 layers

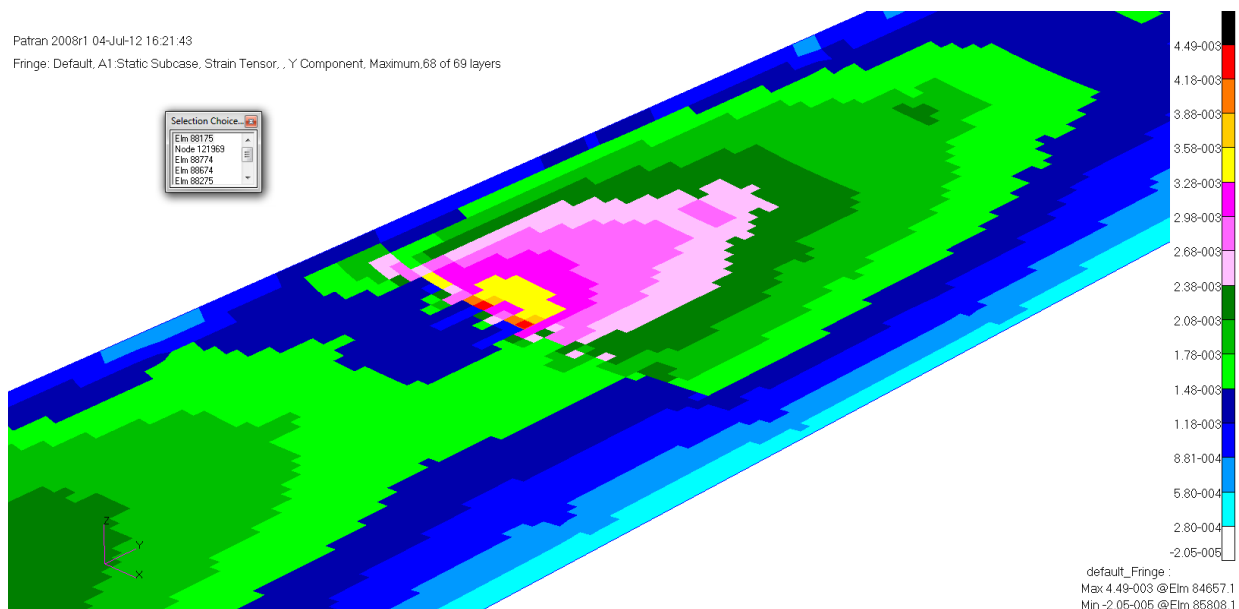


Figure 47: Lower Skin ϵ_2 Component Tensile Strain Region 3

ELEMENT ID	PLY ID	STRAINS IN LAYERED STRAINS IN FIBER AND MATRIX DIRECTIONS			COMPOSITE ELEMENTS (QUAD4) INTER-LAMINAR STRAINS			PRINCIPAL STRAINS (ZERO SHEAR)			MAX SHEAR
		NORMAL-1	NORMAL-2	SHEAR-12	SHEAR XZ-MAT	SHEAR YZ-MAT	ANGLE	MAJOR	MINOR		
0	84543	1	2.07819E-03	1.53121E-03	5.88836E-03	0.0	0.0	42.35	4.76156E-03	-1.15216E-03	5.91371E-03
0	84543	2	1.52728E-03	2.03183E-03	-5.81733E-03	0.0	0.0	-47.48	4.69914E-03	-1.14004E-03	5.83917E-03
0	84543	3	4.62756E-03	-1.11875E-03	-4.62121E-04	0.0	0.0	-2.30	4.63683E-03	-1.12802E-03	5.76486E-03
0	84543	4	4.56689E-03	-1.10838E-03	-4.19693E-04	0.0	0.0	-2.11	4.57464E-03	-1.11613E-03	5.69077E-03
0	84543	5	1.89274E-03	1.51548E-03	5.60424E-03	0.0	0.0	43.07	4.51257E-03	-1.10436E-03	5.61693E-03
0	84543	6	-1.08765E-03	4.44557E-03	3.34835E-04	0.0	0.0	88.27	4.45063E-03	-1.09271E-03	5.54334E-03
0	84543	7	1.50761E-03	1.80001E-03	-5.46219E-03	0.0	0.0	-46.53	4.38881E-03	-1.08119E-03	5.47001E-03
0	84543	8	4.32424E-03	-1.06692E-03	-2.49978E-04	0.0	0.0	-1.33	4.32714E-03	-1.06981E-03	5.39695E-03
0	84543	9	4.26358E-03	-1.05655E-03	-2.07549E-04	0.0	0.0	-1.12	4.26560E-03	-1.05857E-03	5.32417E-03
0	84543	10	1.49581E-03	1.66093E-03	-5.24910E-03	0.0	0.0	-45.90	4.20421E-03	-1.04748E-03	5.25169E-03
0	84543	11	-1.03582E-03	4.14225E-03	1.22692E-04	0.0	0.0	89.32	4.14298E-03	-1.03654E-03	5.17952E-03
0	84543	12	1.56820E-03	1.48794E-03	5.10704E-03	0.0	0.0	44.55	4.08191E-03	-1.02576E-03	5.10767E-03
0	84543	13	4.02093E-03	-1.01508E-03	-3.78349E-05	0.0	0.0	-0.22	4.02100E-03	-1.01515E-03	5.03615E-03
0	84543	14	3.96027E-03	-1.00471E-03	4.59371E-06	0.0	0.0	0.03	3.96027E-03	-1.00472E-03	4.96498E-03
0	84543	15	1.47614E-03	1.42912E-03	-4.89395E-03	0.0	0.0	-44.72	3.89972E-03	-9.94461E-04	4.89418E-03
0	84543	16	1.38275E-03	1.47220E-03	4.82292E-03	0.0	0.0	45.53	3.83935E-03	-9.84396E-04	4.82375E-03

Figure 48: Lower Skin ϵ_2 Component Tensile Strain Critical Stress Region 1

ELEMENT ID	PLY ID	STRAINS IN LAYERED STRAINS IN FIBER AND MATRIX DIRECTIONS			COMPOSITE ELEMENTS (QUAD4) INTER-LAMINAR STRAINS			PRINCIPAL STRAINS (ZERO SHEAR)			MAX SHEAR
		NORMAL-1	NORMAL-2	SHEAR-12	SHEAR XZ-MAT	SHEAR YZ-MAT	ANGLE	MAJOR	MINOR		
0	91315	1	4.54853E-03	-6.58130E-04	2.38738E-04	0.0	0.0	1.31	4.55127E-03	-6.60865E-04	5.21213E-03
0	91315	2	1.78171E-03	2.03170E-03	5.07420E-03	0.0	0.0	46.41	4.44688E-03	-6.33474E-04	5.08036E-03
0	91315	3	-6.02664E-04	4.33908E-03	-2.61256E-04	0.0	0.0	-88.49	4.34253E-03	-6.06115E-04	4.94864E-03
0	91315	4	1.96597E-03	1.69345E-03	-4.80928E-03	0.0	0.0	-43.38	4.23821E-03	-5.78789E-04	4.81700E-03
0	91315	5	1.93310E-03	1.64933E-03	-4.67682E-03	0.0	0.0	-43.26	4.13393E-03	-5.51499E-04	4.68543E-03
0	91315	6	-5.19466E-04	4.02490E-03	-2.95032E-04	0.0	0.0	-88.14	4.02968E-03	-5.24249E-04	4.55393E-03
0	91315	7	1.56107E-03	1.86737E-03	4.41191E-03	0.0	0.0	46.99	3.92548E-03	-4.97043E-04	4.42253E-03
0	91315	8	3.81545E-03	-4.64000E-04	3.17550E-04	0.0	0.0	2.12	3.82133E-03	-4.69883E-04	4.29121E-03

Figure 49: Lower Skin ϵ_2 Component Tensile Strain Critical Stress Region 2

ELEMENT ID	PLY ID	STRAINS IN LAYERED STRAINS IN FIBER AND MATRIX DIRECTIONS			COMPOSITE ELEMENTS (QUAD4) INTER-LAMINAR STRAINS			PRINCIPAL STRAINS (ZERO SHEAR)			MAX SHEAR
		NORMAL-1	NORMAL-2	SHEAR-12	SHEAR XZ-MAT	SHEAR YZ-MAT	ANGLE	MAJOR	MINOR		
0	88175	1	4.81272E-03	-3.86787E-04	-5.04263E-04	0.0	0.0	-2.77	4.82992E-03	-3.98973E-04	5.22889E-03
0	88175	2	4.64552E-03	-3.90334E-04	-5.39720E-04	0.0	0.0	-3.06	4.65994E-03	-4.04754E-04	5.06470E-03
0	88175	3	2.32730E-03	1.75213E-03	4.86719E-03	0.0	0.0	41.63	4.49025E-03	-4.10816E-04	4.90106E-03
0	88175	4	-3.97429E-04	4.63010E-03	6.10635E-04	0.0	0.0	86.30	4.32086E-03	-4.17186E-04	4.73804E-03
0	88175	5	1.54091E-03	2.18700E-03	-4.52986E-03	0.0	0.0	-49.06	4.15181E-03	-4.23899E-04	4.57571E-03
0	88175	6	1.43530E-03	2.11685E-03	-4.36120E-03	0.0	0.0	-49.44	3.98314E-03	-4.30991E-04	4.41413E-03
0	88175	7	-4.08072E-04	3.78446E-03	7.17006E-04	0.0	0.0	85.15	3.81490E-03	-4.38507E-04	4.25341E-03
0	88175	8	1.97655E-03	1.22408E-03	4.02387E-03	0.0	0.0	39.70	3.64713E-03	-4.46495E-04	4.09362E-03
0	88175	9	3.44004E-03	-4.15167E-04	-7.87921E-04	0.0	0.0	-5.78	3.47989E-03	-4.55014E-04	3.93490E-03
0	88175	10	3.26783E-03	-4.18715E-04	-8.23378E-04	0.0	0.0	-6.30	3.31324E-03	-4.64130E-04	3.77737E-03

Figure 50: Lower Skin ϵ_2 Component Tensile Strain Critical Stress Region 3

Figure 48 shows the maximum ε_2 component strain of .00444 in the lower skin captured from the results file in region one. The margin of safety for this method of failure is shown below:

$$MS = \frac{\varepsilon_{allowable}}{\varepsilon_{actual}} - 1 = \frac{.00702(in / in)}{.0044557(in / in)} - 1 = .579$$

3.2.7.1.4 Secondary Material Axis Compressive Strain

The off axis compressive strain for the upper skin is presented in Figure 51 and the lower skin is shown in Figure 52. The critical region for this failure case is in wing region three is shown in Figure 55 and the highest loaded areas in the other regions are presented below.

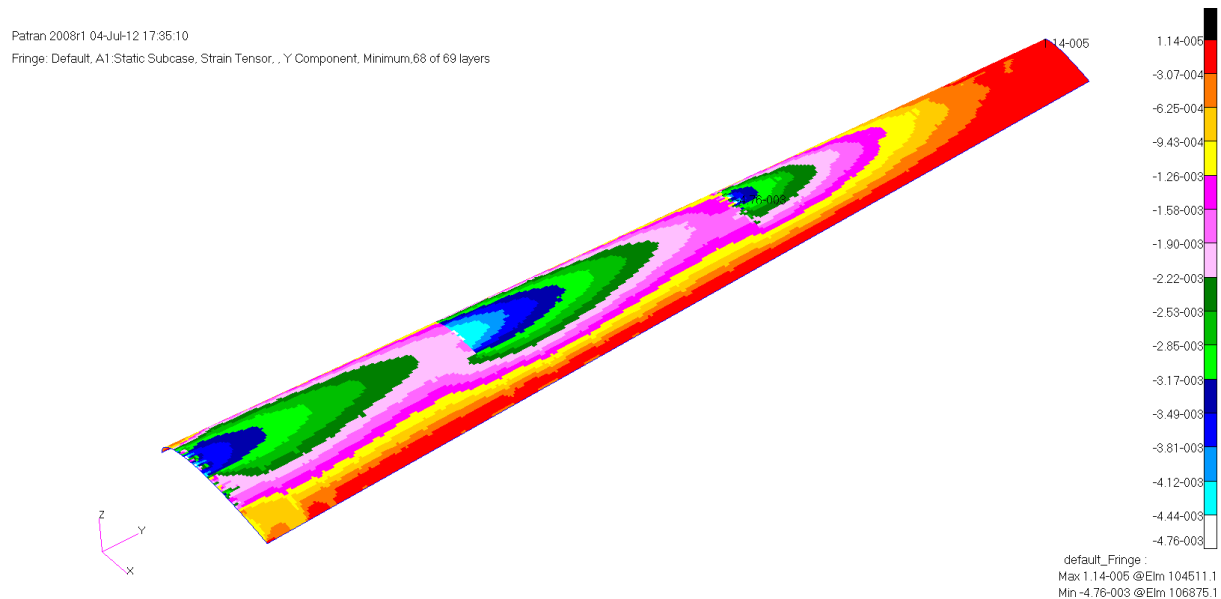


Figure 51: Upper Skin ε_2 Component Compressive Critical Strain

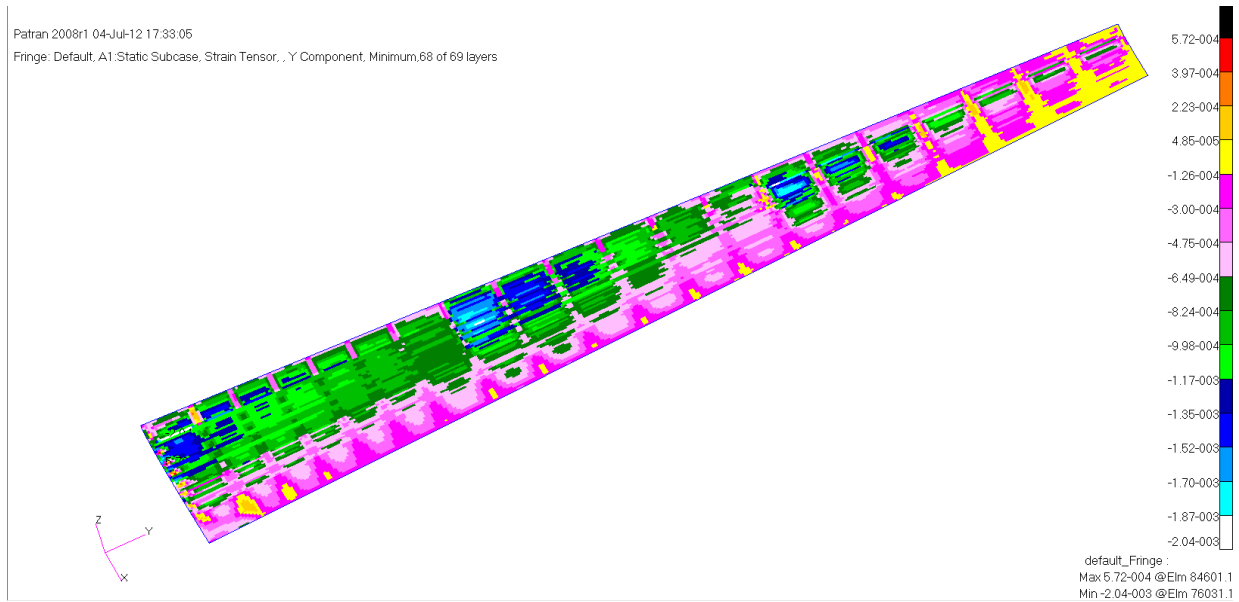


Figure 52: Lower Skin ε_2 Component Compressive Strain Distribution

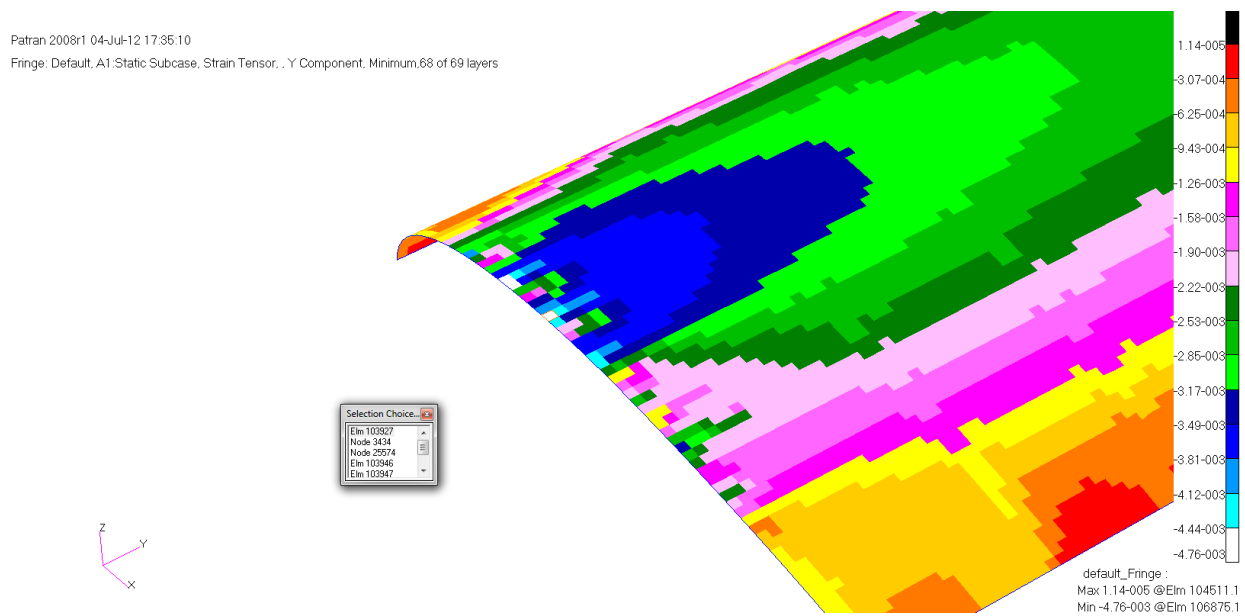


Figure 53: Upper Skin ε_2 Component Compressive Critical Region 1

Patran 2008r1 04-Jul-12 17:35:10
 Fringe: Default, A1:Static Subcase, Strain Tensor, Y Component, Minimum,68 of 69 layers

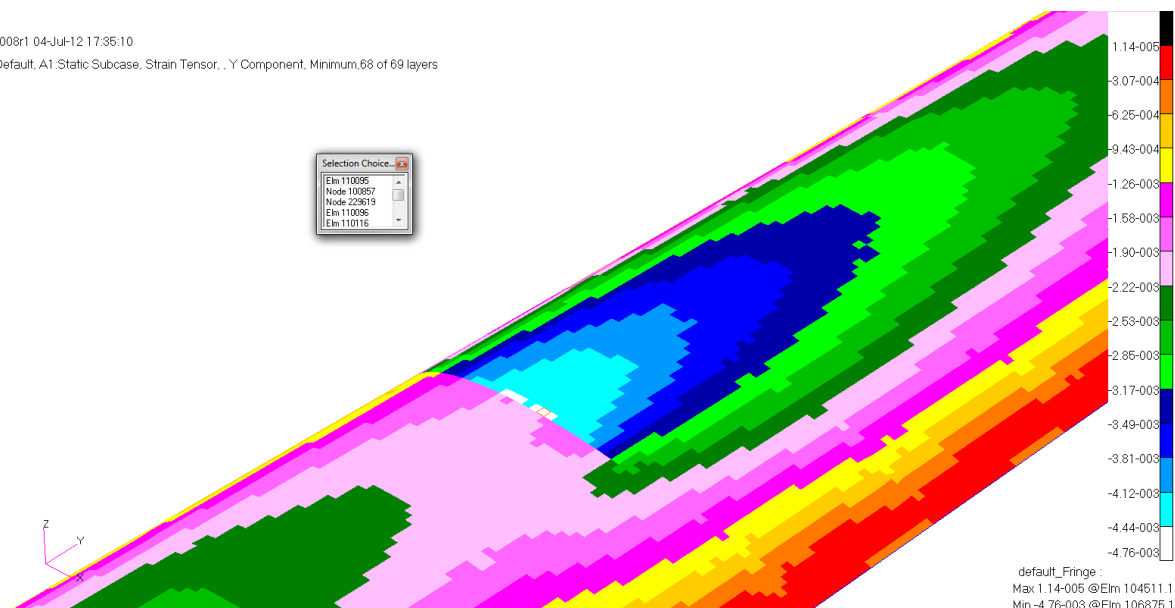


Figure 54: Upper Skin ϵ_2 Component Compressive Critical Region 2

Patran 2008r1 04-Jul-12 17:35:10
 Fringe: Default, A1:Static Subcase, Strain Tensor, Y Component, Minimum,68 of 69 layers

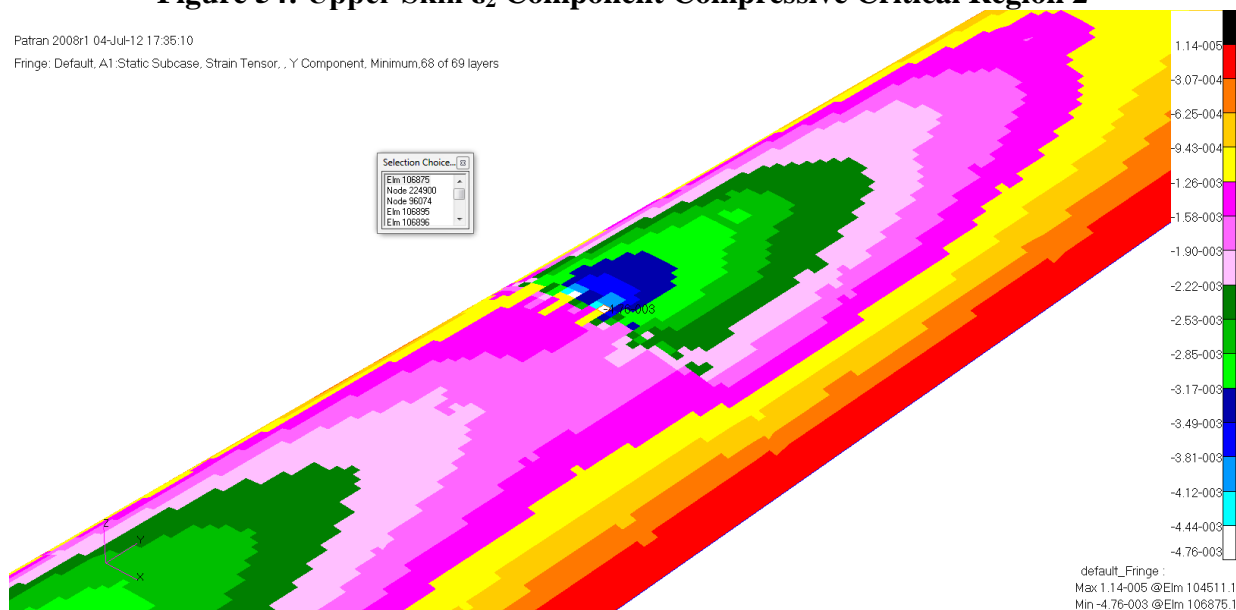


Figure 55: Upper Skin ϵ_2 Component Compressive Critical Region 3

ELEMENT ID	PLY ID	STRAINS IN LAYERED			COMPOSITE ELEMENTS			(QUAD4)			MAX SHEAR
		STRAINS IN FIBER AND MATRIX DIRECTIONS	NORMAL-1	NORMAL-2	SHEAR-12	INTER-LAMINAR	STRAINS	PRINCIPAL	STRAINS (ZERO SHEAR)	MINOR	
0	103927	1	-1.31639E-03	-1.67025E-03	-4.92441E-03	0.0	0.0	-42.94	9.75235E-04	-3.96187E-03	4.93711E-03
0	103927	2	-1.67650E-03	-1.35724E-03	4.99111E-03	0.0	0.0	46.83	9.83785E-04	-4.01752E-03	5.00131E-03
0	103927	3	-4.06933E-03	9.88482E-04	-2.84674E-04	0.0	0.0	-88.39	9.92485E-04	-4.07333E-03	5.06581E-03
0	103927	4	-4.12623E-03	9.98280E-04	-2.50082E-04	0.0	0.0	-88.60	1.00133E-03	-4.12928E-03	5.13061E-03
0	103927	5	-1.47978E-03	-1.69527E-03	-5.19121E-03	0.0	0.0	-43.81	1.01031E-03	-4.18536E-03	5.19568E-03
0	103927	6	1.01788E-03	-4.24003E-03	1.80897E-04	0.0	0.0	0.99	1.01943E-03	-4.24159E-03	5.26102E-03
0	103927	7	-1.70778E-03	-1.56148E-03	5.32461E-03	0.0	0.0	45.79	1.02868E-03	-4.29794E-03	5.32662E-03
0	103927	8	-4.35383E-03	1.03747E-03	-1.11712E-04	0.0	0.0	-89.41	1.03805E-03	-4.35441E-03	5.39246E-03
0	103927	9	-4.41074E-03	1.04727E-03	-7.71190E-05	0.0	0.0	-89.60	1.04754E-03	-4.41101E-03	5.45855E-03
0	103927	10	-1.72655E-03	-1.68402E-03	5.52471E-03	0.0	0.0	45.22	1.05715E-03	-4.46772E-03	5.52487E-03
0	103927	11	1.06687E-03	-4.52454E-03	7.93388E-06	0.0	0.0	0.04	1.06687E-03	-4.52454E-03	5.59141E-03
0	103927	12	-1.76572E-03	-1.73906E-03	-5.65810E-03	0.0	0.0	-45.13	1.07669E-03	-4.58147E-03	5.65817E-03
0	103927	13	-4.63834E-03	1.08646E-03	6.12512E-05	0.0	0.0	89.69	1.08663E-03	-4.63851E-03	5.72513E-03
0	103927	14	-4.69524E-03	1.09626E-03	9.58438E-05	0.0	0.0	89.53	1.09666E-03	-4.69564E-03	5.79230E-03
0	103927	15	-1.75783E-03	-1.88826E-03	5.85820E-03	0.0	0.0	44.36	1.10678E-03	-4.75287E-03	5.85966E-03
0	103927	16	-1.92911E-03	-1.76408E-03	-5.92490E-03	0.0	0.0	-45.80	1.11700E-03	-4.81020E-03	5.92720E-03

Figure 56: Upper Skin ϵ_2 Component Compressive Critical Strain Region 1

ELEMENT ID	PLY ID	STRAINS IN LAYERED FIBER AND MATRIX DIRECTIONS			COMPOSITE ELEMENTS (QUAD4)					MAX SHEAR	
		STRAINS IN FIBER AND MATRIX DIRECTIONS			INTER-LAMINAR STRAINS		PRINCIPAL STRAINS (ZERO SHEAR)				
		NORMAL-1	NORMAL-2	SHEAR-12	SHEAR XZ-MAT	SHEAR YZ-MAT	ANGLE	MAJOR	MINOR		
0	110095	1	-4.30583E-03	6.85225E-04	-9.64294E-04	0.0	0.0	-84.53	7.31375E-04	-4.35198E-03	5.08336E-03
0	110095	2	-1.37540E-03	-2.29427E-03	-5.02776E-03	0.0	0.0	-39.82	7.20686E-04	-4.39035E-03	5.11104E-03
0	110095	3	6.72872E-04	-4.39160E-03	8.73442E-04	0.0	0.0	4.89	7.10255E-04	-4.42898E-03	5.13924E-03
0	110095	4	-2.29790E-03	-1.46988E-03	5.10117E-03	0.0	0.0	49.61	7.00078E-04	-4.46786E-03	5.16794E-03
0	110095	5	-2.29972E-03	-1.51713E-03	5.13788E-03	0.0	0.0	49.33	6.90149E-04	-4.50699E-03	5.19714E-03
0	110095	6	6.54343E-04	-4.52024E-03	7.37163E-04	0.0	0.0	4.05	6.80464E-04	-4.54637E-03	5.22683E-03
0	110095	7	-1.61161E-03	-2.30335E-03	-5.21129E-03	0.0	0.0	-41.22	6.71021E-04	-4.58598E-03	5.25700E-03
0	110095	8	-4.60601E-03	6.41990E-04	-6.46311E-04	0.0	0.0	-86.49	6.61814E-04	-4.62583E-03	5.28765E-03

Figure 57: Upper Skin ε_2 Component Compressive Critical Strain Region 2

ELEMENT ID	PLY ID	STRAINS IN LAYERED FIBER AND MATRIX DIRECTIONS				COMPOSITE ELEMENTS (QUAD4)					MAX SHEAR
		STRAINS IN FIBER AND MATRIX DIRECTIONS			INTER-LAMINAR STRAINS		STRAINS (ZERO SHEAR)				
		NORMAL-1	NORMAL-2	SHEAR-12	SHEAR XZ-MAT	SHEAR YZ-MAT	ANGLE	MAJOR	MINOR		
0106875	1	-3.94581E-03	5.63129E-04	5.63834E-04	0.0	0.0	86.44	5.80687E-04	-3.96337E-03	4.54406E-03	
0106875	2	-4.08149E-03	5.56954E-04	5.56001E-04	0.0	0.0	86.58	5.73556E-04	-4.09810E-03	4.67165E-03	
0106875	3	-2.10728E-03	-1.55912E-03	-4.76796E-03	0.0	0.0	-48.28	5.66484E-04	-4.23288E-03	4.79937E-03	
0106875	4	5.44606E-04	-4.35286E-03	-5.40333E-04	0.0	0.0	-3.15	5.59464E-04	-4.36772E-03	4.92719E-03	
0106875	5	-1.70881E-03	-2.24131E-03	5.02698E-03	0.0	0.0	41.98	5.52494E-04	-4.50261E-03	5.05510E-03	
0106875	6	-1.78365E-03	-2.30832E-03	5.15649E-03	0.0	0.0	42.10	5.45569E-04	-4.63754E-03	5.18311E-03	
0106875	7	5.26083E-04	-4.75992E-03	-5.16833E-04	0.0	0.0	-2.79	5.38686E-04	-4.77252E-03	5.31121E-03	
0106875	8	-2.44235E-03	-1.93335E-03	-5.41551E-03	0.0	0.0	-47.68	5.31842E-04	-4.90753E-03	5.43938E-03	

Figure 58: Upper Skin ε_2 Component Compressive Critical Strain Region 3

Figure 56 shows the maximum ε_2 component strain of .00452 in the upper skin captured from the results file. The margin of safety for this method of failure is shown below:

$$MS = \frac{\gamma_{allowable}}{\gamma_{actual}} - 1 = \frac{.005(in/in)}{.00452454(in/in)} - 1 = .105$$

3.2.7.1.5 Shear Stress

The shear strains for the upper skin is presented in Figure 59 and the lower skin is shown in Figure 60. The critical region is found in the second bay in the lower skin and is shown in Figure 62 and the highest loaded areas in the other regions are presented below.

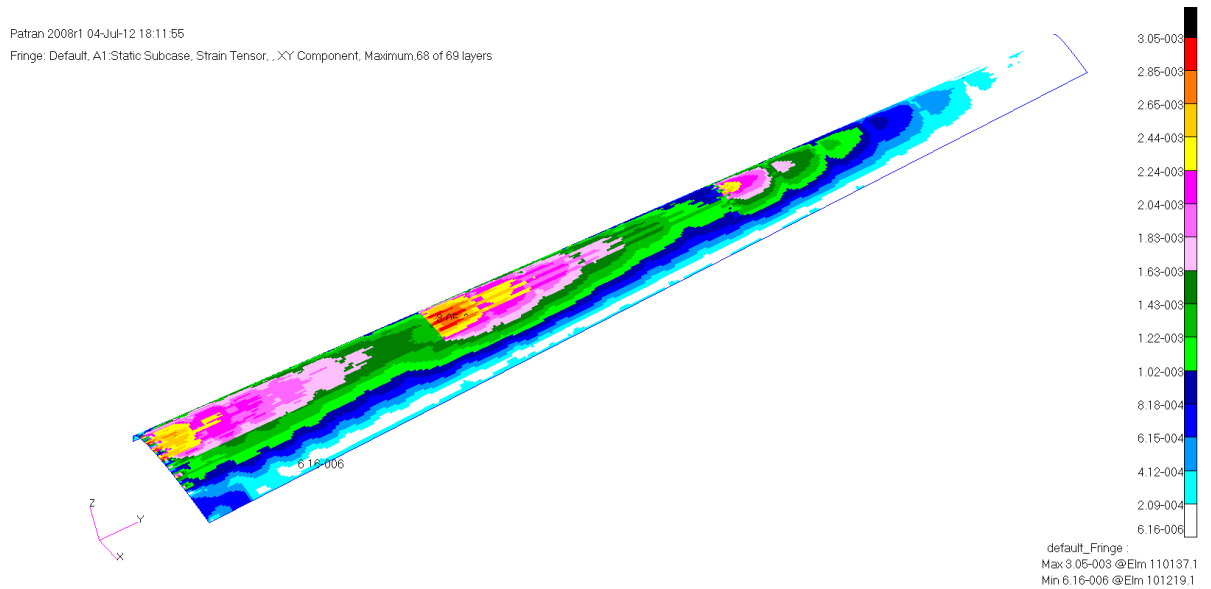


Figure 59: Upper Skin γ_{12} Component Shear Strain Distribution

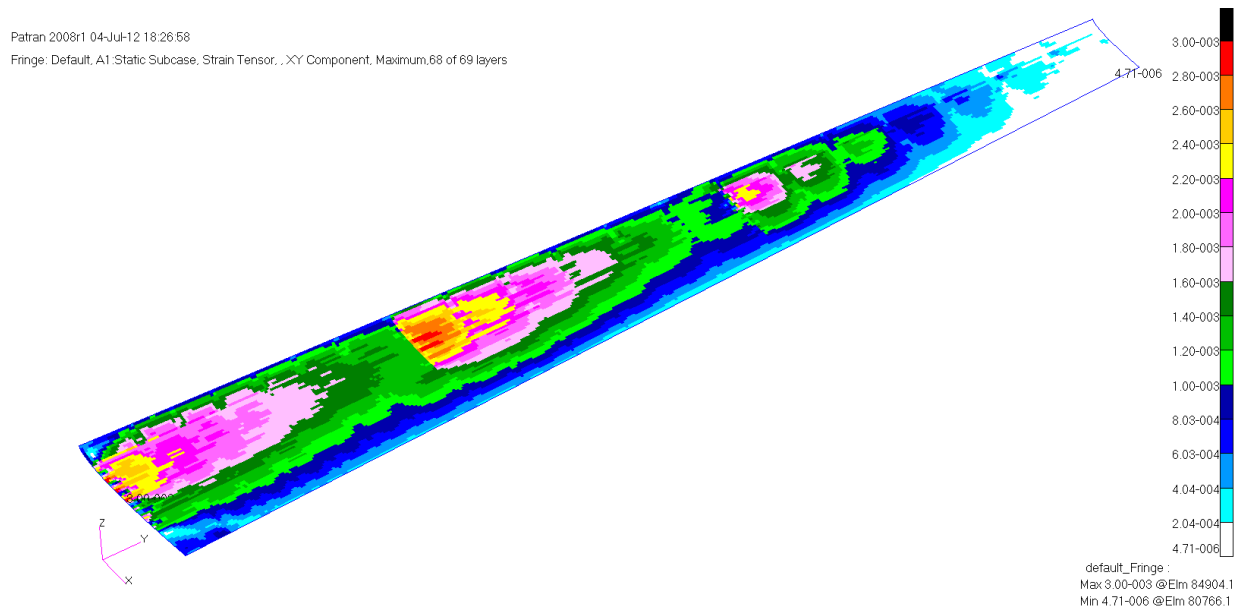


Figure 60: Lower Skin γ_{12} Component Shear Strain Distribution

Patran 2008r1 04-Jul-12 18:26:58
 Fringe: Default, A1-Static Subcase, Strain Tensor, .XY Component, Maximum:68 of 69 layers

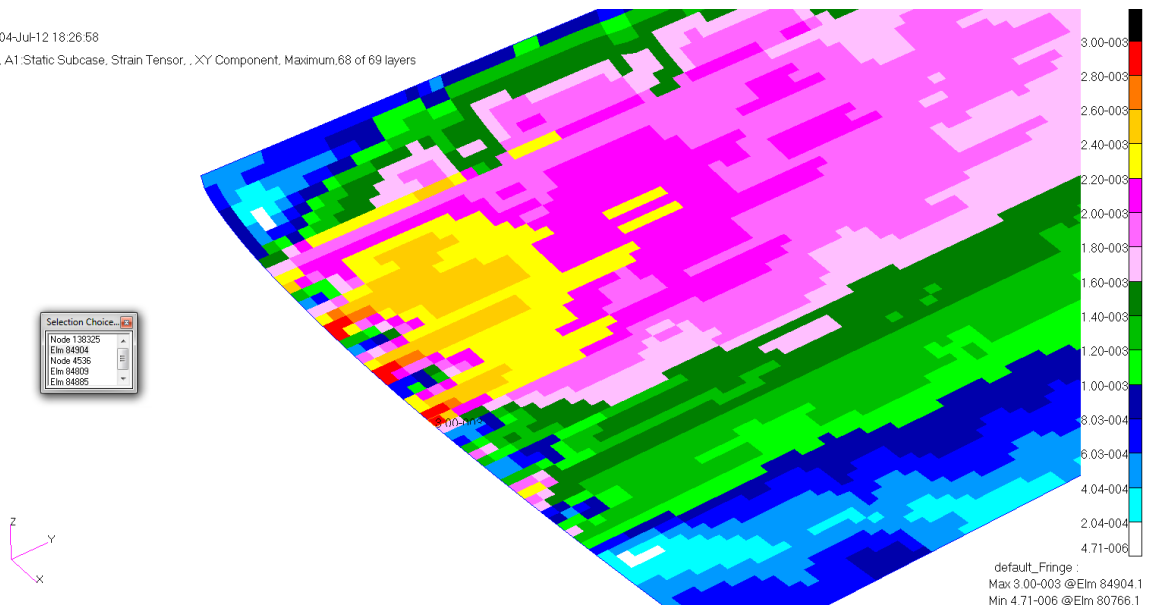


Figure 61: Lower Skin γ_{12} Component Shear Strain Distribution Region 1

Patran 2008r1 04-Jul-12 18:26:58
 Fringe: Default, A1-Static Subcase, Strain Tensor, .XY Component, Maximum:68 of 69 layers

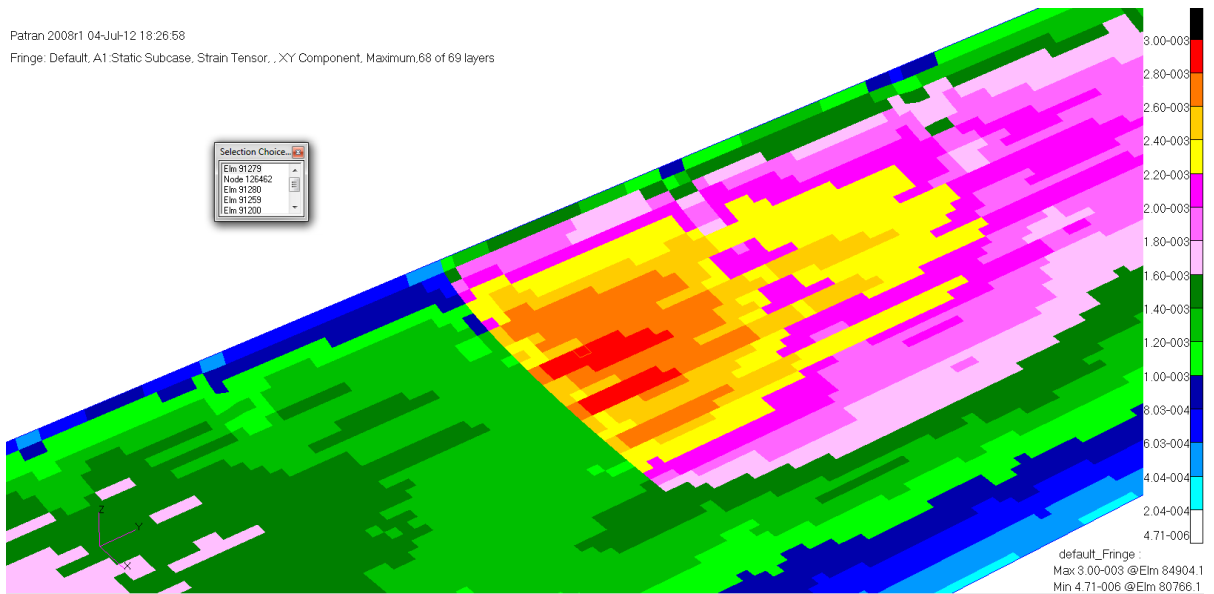


Figure 62: Lower Skin γ_{12} Component Shear Strain Distribution Region 2

Patran 2008r1 04-Jul-12 18:26:58

Fringe: Default, A1:Static Subcase, Strain Tensor, ,XY Component, Maximum,68 of 69 layers

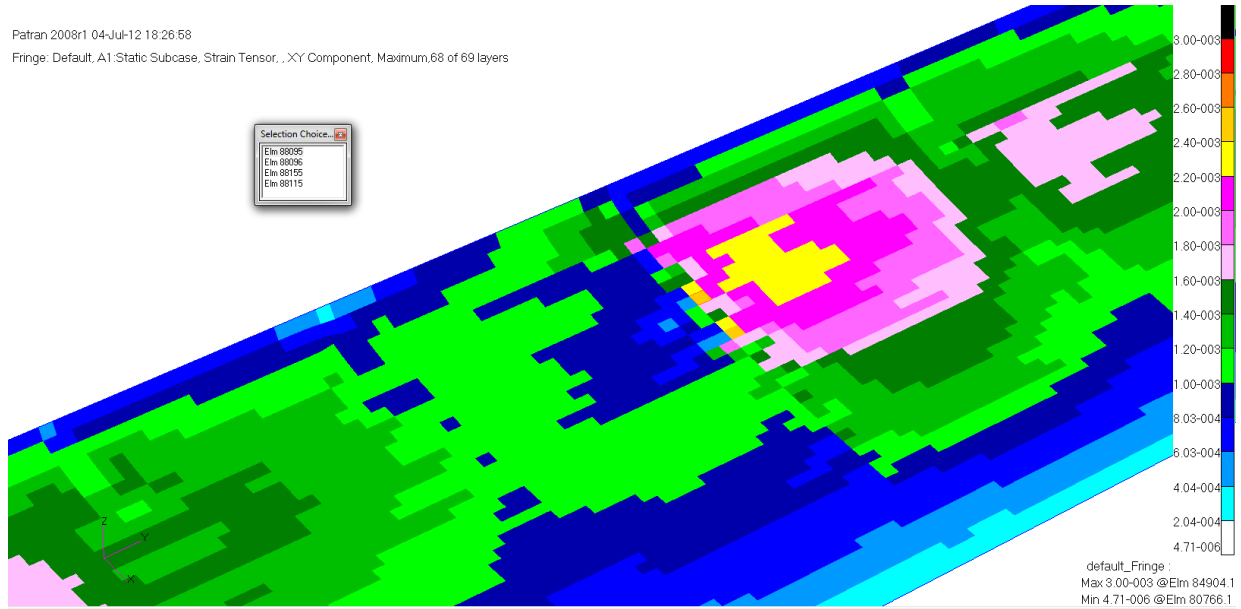


Figure 63: Lower Skin γ_{12} Component Shear Strain Distribution Region 3

ELEMENT ID	PLY ID	STRAINS IN LAYERED STRAINS IN FIBER AND MATRIX DIRECTIONS			COMPOSITE ELEMENTS (QUAD4)		PRINCIPAL ANGLE	STRAINS (ZERO SHEAR)		MAX SHEAR
		NORMAL-1	NORMAL-2	SHEAR-12	INTER-LAMINAR SHEAR XZ-MAT	STRAINS SHEAR YZ-MAT		MAJOR	MINOR	
0	84904	1	4.35813E-03	-1.26622E-03	4.16028E-03	0.0	18.24	5.04386E-03	-1.95194E-03	6.99580E-03
0	84904	2	-1.31358E-03	4.34780E-03	-4.01244E-03	0.0	-72.34	4.98666E-03	-1.95243E-03	6.93909E-03
0	84904	3	3.42057E-03	-4.44037E-04	-5.69842E-03	0.0	-27.93	4.93091E-03	-1.95438E-03	6.88529E-03
0	84904	4	3.31781E-03	-3.98966E-04	-5.73546E-03	0.0	-28.53	4.87666E-03	-1.95781E-03	6.83447E-03
0	84904	5	4.31683E-03	-1.45567E-03	3.56894E-03	0.0	15.86	4.82392E-03	-1.96276E-03	6.78668E-03
0	84904	6	-3.08822E-04	3.11229E-03	5.80953E-03	0.0	60.25	4.77274E-03	-1.96927E-03	6.74201E-03
0	84904	7	-1.55040E-03	4.29617E-03	-3.27328E-03	0.0	-75.38	4.72314E-03	-1.97736E-03	6.70050E-03
0	84904	8	2.90677E-03	-2.18679E-04	-5.88360E-03	0.0	-31.01	4.67516E-03	-1.98707E-03	6.66222E-03
0	84904	9	2.80401E-03	-1.73607E-04	-5.92064E-03	0.0	-31.65	4.62881E-03	-1.99842E-03	6.62723E-03
0	84904	10	-1.63240E-03	4.26519E-03	-2.82978E-03	0.0	-77.30	4.58414E-03	-2.01143E-03	6.59557E-03
0	84904	11	-8.34638E-05	2.59848E-03	6.89374E-03	0.0	57.05	4.54116E-03	-2.02614E-03	6.56730E-03
0	84904	12	4.24454E-03	-1.78721E-03	2.53411E-03	0.0	11.39	4.49989E-03	-2.04256E-03	6.54246E-03
0	84904	13	2.39296E-03	6.67957E-06	-6.06879E-03	0.0	-34.27	4.46036E-03	-2.06072E-03	6.52108E-03
0	84904	14	2.29020E-03	5.17512E-05	-6.10582E-03	0.0	-34.93	4.42258E-03	-2.08063E-03	6.50321E-03
0	84904	15	-1.92930E-03	4.21356E-03	-2.09062E-03	0.0	-80.60	4.38656E-03	-2.10230E-03	6.48887E-03
0	84904	16	4.20323E-03	-1.97666E-03	1.94278E-03	0.0	8.73	4.35233E-03	-2.12575E-03	6.47808E-03

Figure 64: Lower Skin γ_{12} Component Critical Shear Strain Region 1

ELEMENT ID	PLY ID	STRAINS IN LAYERED STRAINS IN FIBER AND MATRIX DIRECTIONS			COMPOSITE ELEMENTS (QUAD4)		PRINCIPAL ANGLE	STRAINS (ZERO SHEAR)		MAX SHEAR
		NORMAL-1	NORMAL-2	SHEAR-12	INTER-LAMINAR SHEAR XZ-MAT	STRAINS SHEAR YZ-MAT		MAJOR	MINOR	
0	91279	1	4.03899E-03	-1.56741E-03	-3.54750E-04	0.0	-1.81	4.04459E-03	-1.57301E-03	5.61761E-03
0	91279	2	1.41710E-03	1.04517E-03	5.62012E-03	0.0	43.11	4.04735E-03	-1.58507E-03	5.63242E-03
0	91279	3	-1.59044E-03	4.04341E-03	3.89109E-04	0.0	88.02	4.05012E-03	-1.59715E-03	5.64727E-03
0	91279	4	1.01869E-03	1.42498E-03	-5.64758E-03	0.0	-47.06	4.05292E-03	-1.60925E-03	5.66218E-03
0	91279	5	1.00545E-03	1.42892E-03	-5.66131E-03	0.0	-47.14	4.05574E-03	-1.62138E-03	5.67713E-03
0	91279	6	-1.62499E-03	4.05005E-03	4.40646E-04	0.0	87.78	4.05859E-03	-1.63353E-03	5.69212E-03
0	91279	7	1.43679E-03	9.78964E-04	6.8877E-03	0.0	42.70	4.06146E-03	-1.64570E-03	5.70716E-03
0	91279	8	4.05447E-03	-1.64802E-03	-4.75005E-04	0.0	-2.38	4.06435E-03	-1.65790E-03	5.72225E-03

Figure 65: Lower Skin γ_{12} Component Critical Shear Strain Region 2

ELEMENT ID	PLY ID	STRAINS IN LAYERED STRAINS IN FIBER AND MATRIX DIRECTIONS			COMPOSITE ELEMENTS (QUAD4)		PRINCIPAL ANGLE	STRAINS (ZERO SHEAR)		MAX SHEAR
		NORMAL-1	NORMAL-2	SHEAR-12	INTER-LAMINAR SHEAR XZ-MAT	STRAINS SHEAR YZ-MAT		MAJOR	MINOR	
0	88095	1	4.97885E-03	-2.95643E-04	1.70457E-05	0.0	0.09	4.97886E-03	-2.95657E-04	5.27452E-03
0	88095	2	4.75790E-03	-2.99244E-04	6.77640E-05	0.0	0.38	4.75812E-03	-2.99471E-04	5.05759E-03
0	88095	3	2.05781E-03	2.17629E-03	4.83979E-03	0.0	45.70	4.53767E-03	-3.03569E-04	4.84124E-03
0	88095	4	-3.06445E-04	4.31599E-03	-1.69200E-04	0.0	-88.95	4.31754E-03	-3.07993E-04	4.62553E-03
0	88095	5	2.00246E-03	1.78254E-03	-4.40509E-03	0.0	-43.57	4.09779E-03	-3.12789E-04	4.41058E-03
0	88095	6	1.91554E-03	1.64490E-03	-4.18774E-03	0.0	-43.15	3.87846E-03	-3.18014E-04	4.19647E-03
0	88095	7	-3.17247E-04	3.65314E-03	-3.21355E-04	0.0	-87.69	3.65963E-03	-3.23739E-04	3.98337E-03
0	88095	8	1.36963E-03	1.74171E-03	3.75304E-03	0.0	47.83	3.44139E-03	-3.30047E-04	3.77144E-03
0	88095	9	3.21124E-03	-3.24448E-04	4.22792E-04	0.0	3.41	3.22383E-03	-3.37042E-04	3.56088E-03
0	88095	10	2.99029E-03	-3.28049E-04	4.73510E-04	0.0	4.06	3.00710E-03	-3.44855E-04	3.35195E-03

Figure 66: Lower Skin γ_{12} Component Critical Shear Strain Region 3

Figure 65 shows the maximum shear strain of .0057 in the lower skin captured from the results file. The margin of safety for this method of failure is shown below:

$$MS = \frac{\varepsilon_{allowable}}{\varepsilon_{actual}} - 1 = \frac{.0292(in/in)}{.00568877(in/in)} - 1 = 4.133$$

3.2.7.2 Spars

In this section the charts are all presented in material coordinate systems. The material is defined by the global Y vector which goes down the wing. The margins of safety for the failure methods examined for the spars are presented in Table 20. The critical margin of safety has been highlighted orange.

Table 20: Curvature Spar Critical Strains

	Region 1	Region 2	Region 3
ε_1^C	0.00629	0.00456	0.00329
ε_1^T	0.00633	0.00430	0.00325
γ_{12}	0.00372	0.00606	0.00394
ε_2^C	0.00487	0.00444	0.00313
ε_2^T	0.00517	0.00417	0.00317

Table 21: Curvature Spar Critical Margins

	Region 1	Region 2	Region 3
ε_1^C	0.765	1.436	2.372
ε_1^T	1.022	1.977	2.938
γ_{12}	6.841	5.580	8.343
ε_2^C	1.713	1.975	3.223
ε_2^T	0.357	0.683	1.215

Each of these failure methods will be examined and the strains for each failure method will be presented next.

3.2.7.2.1 Primary Material Axis Tensile Stress

The on-axis tensile strains for the spars are presented in Figure 67. The lower spar cap experiences the highest strain in wing region one and the critical region is shown in Figure 68.

The highest loaded areas in the other regions are also presented below.

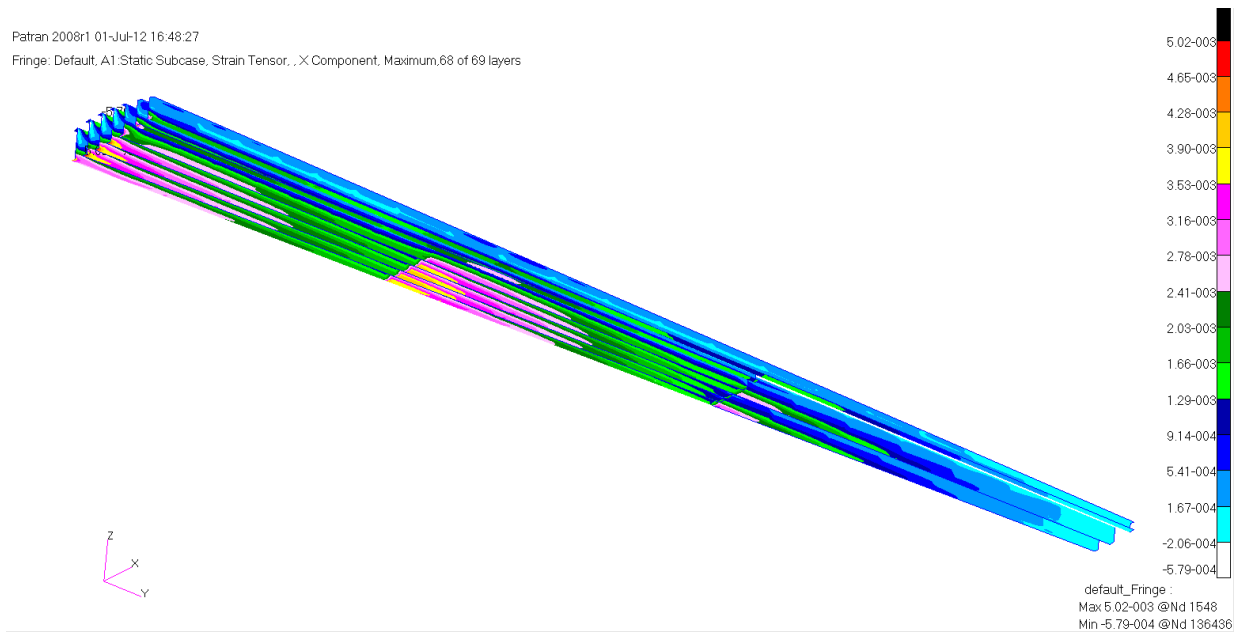


Figure 67: Spars ϵ_1 Component Tensile Strain Distribution

Patran 2008r1 01-Jul-12 16:48:27
 Fringe: Default, A1 Static Subcase, Strain Tensor, X Component, Maximum, 68 of 69 layers

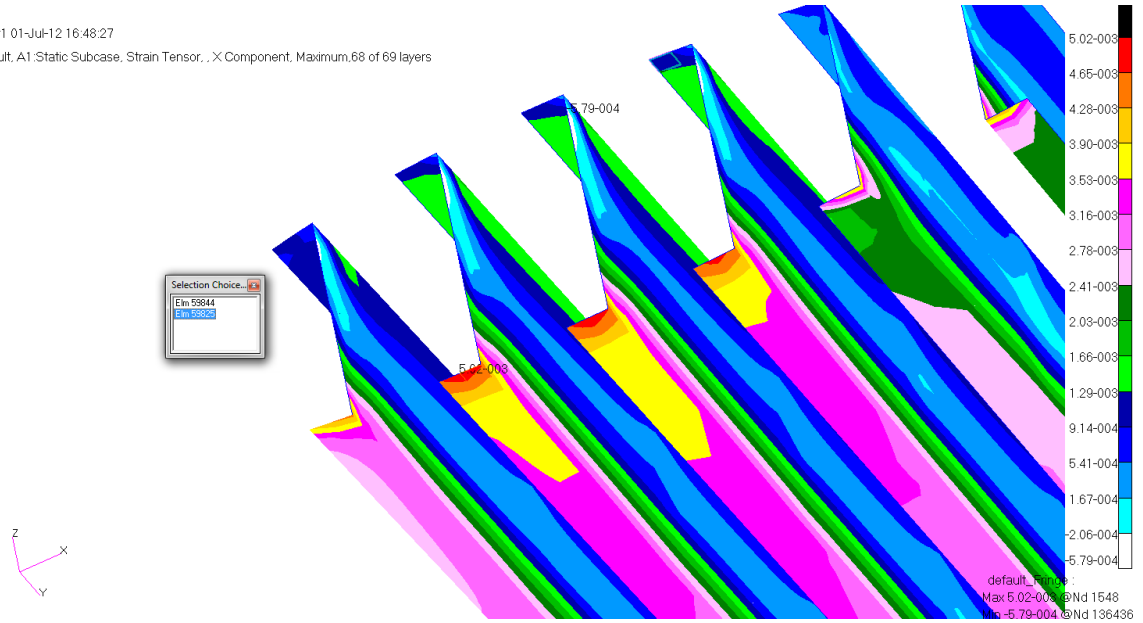


Figure 68: Spars ϵ_1 Component Tensile Strain Critical Region 1

Patran 2008r1 01-Jul-12 16:48:27
 Fringe: Default, A1 Static Subcase, Strain Tensor, X Component, Maximum, 68 of 69 layers

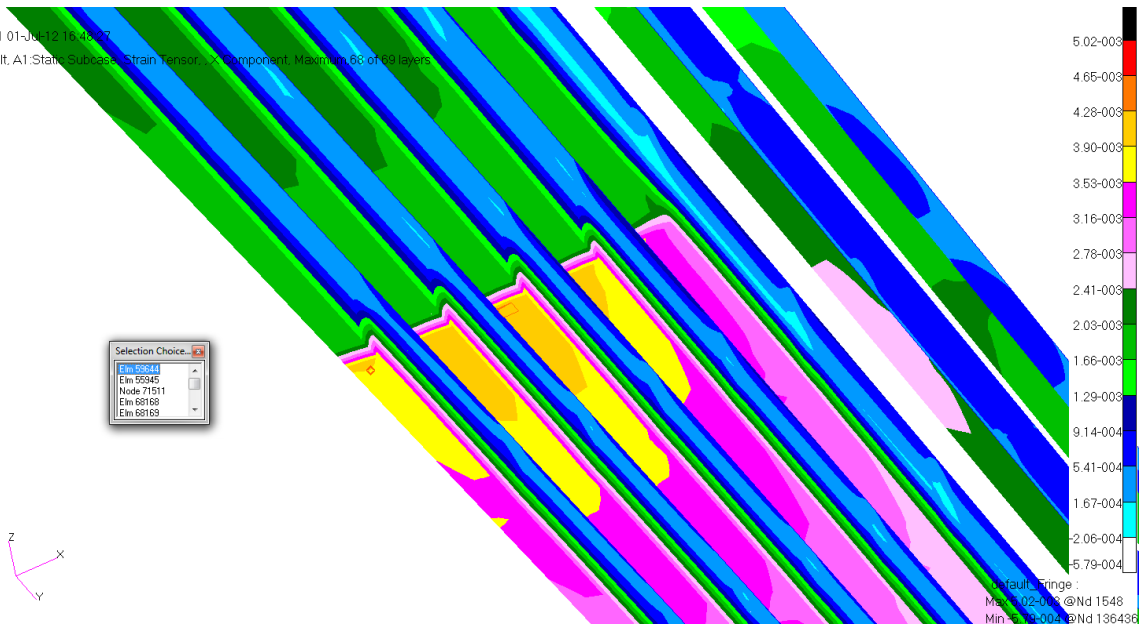


Figure 69: Spars ϵ_1 Component Tensile Strain Critical Region 2

Patran 2008r1 01-Jul-12 16:48:27

Fringe: Default, A1 Static Subcase, Strain Tensor, X Component, Maximum, 63 of 63 layers

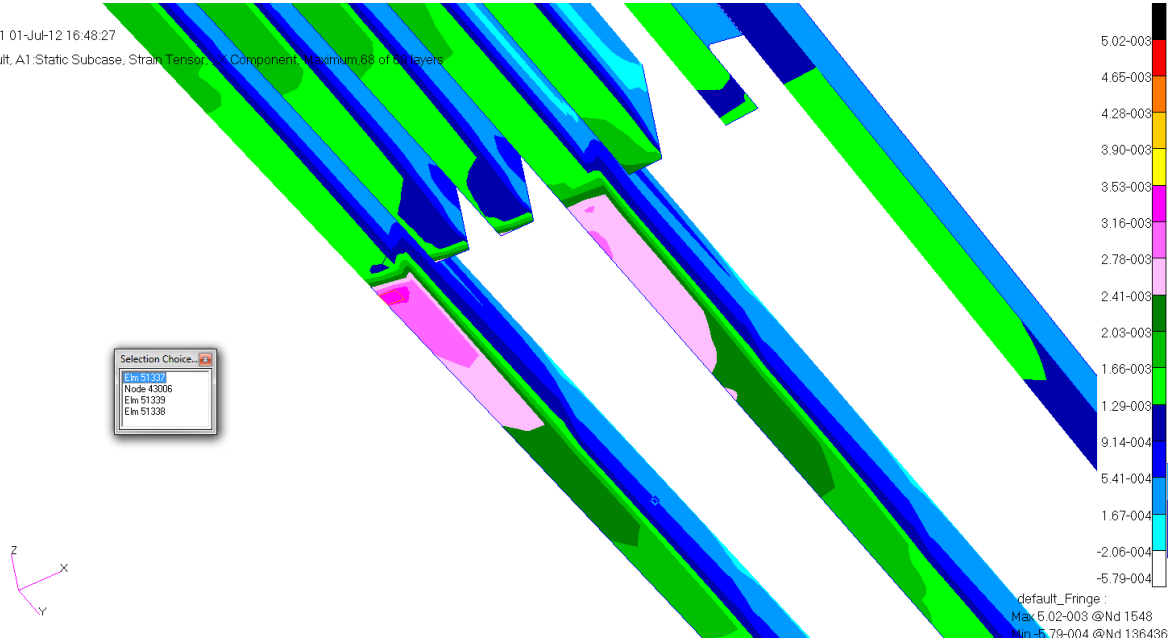


Figure 70: Spars ε_1 Component Tensile Strain Critical Region 3

ELEMENT ID	PLY ID	STRAINS IN LAYERED STRAINS IN FIBER AND MATRIX DIRECTIONS			COMPOSITE ELEMENTS (QUAD4)		PRINCIPAL ANGLE	STRAINS (ZERO SHEAR)		MAX SHEAR	
		NORMAL-1	NORMAL-2	SHEAR-12	INTER-LAMINAR SHEAR XZ-MAT	STRAINS SHEAR YZ-MAT		MAJOR	MINOR		
0	59825	1	6.32611E-03	-1.40902E-03	-1.65012E-03	0.0	0.0	-6.02	6.41314E-03	-1.49604E-03	7.90918E-03
0	59825	2	6.26545E-03	-1.39865E-03	-1.60769E-03	0.0	0.0	-5.92	6.34885E-03	-1.48205E-03	7.83090E-03
0	59825	3	6.20478E-03	-1.38828E-03	-1.56527E-03	0.0	0.0	-5.82	6.28461E-03	-1.46811E-03	7.75272E-03
0	59825	4	6.14452E-03	-1.37788E-03	-1.52204E-03	0.0	0.0	-5.72	6.22042E-03	-1.45422E-03	7.67464E-03
0	59825	5	6.17775E-03	-1.39816E-03	-7.45101E-03	0.0	0.0	-50.62	6.15628E-03	-1.44037E-03	7.59665E-03
0	59825	6	6.02280E-03	-1.35718E-03	-1.43798E-03	0.0	0.0	-5.51	6.09219E-03	-1.42658E-03	7.51877E-03
0	59825	7	5.96213E-03	-1.34682E-03	-1.39555E-03	0.0	0.0	-5.40	6.02815E-03	-1.41284E-03	7.44099E-03
0	59825	8	5.90147E-03	-1.33645E-03	-1.35312E-03	0.0	0.0	-5.29	5.96417E-03	-1.39915E-03	7.36332E-03
0	59825	9	5.84020E-03	-1.32127E-03	-7.16689E-03	0.0	0.0	-50.18	5.90024E-03	-1.38552E-03	7.28576E-03
0	59825	10	5.86635E-03	-1.59808E-03	-7.9586E-03	0.0	0.0	-39.93	5.83637E-03	-1.37194E-03	7.20831E-03
0	59825	11	5.71948E-03	-1.30535E-03	-1.22584E-03	0.0	0.0	-4.95	5.77256E-03	-1.35843E-03	7.13099E-03
0	59825	12	5.65882E-03	-1.29498E-03	-1.18341E-03	0.0	0.0	-4.83	5.70881E-03	-1.34497E-03	7.05378E-03
0	59825	13	5.59816E-03	-1.28462E-03	-1.14098E-03	0.0	0.0	-4.71	5.64512E-03	-1.33158E-03	6.97671E-03

Figure 71: Spars ε_1 Component Tensile Critical Strain Region 1

ELEMENT ID	PLY ID	STRAINS IN LAYERED STRAINS IN FIBER AND MATRIX DIRECTIONS			COMPOSITE ELEMENTS (QUAD4)				MAX SHEAR		
		NORMAL-1		NORMAL-2	INTER-LAMINAR STRAINS		PRINCIPAL STRAINS (ZERO SHEAR)				
		NORMAL-1	NORMAL-2	SHEAR-12	SHEAR XZ-MAT	SHEAR YZ-MAT	ANGLE	MAJOR		MINOR	
0	59644	1	4.30172E-03	-1.41766E-03	4.96902E-04	0.0	0.0	2.48	4.31249E-03	-1.42843E-03	5.74092E-03
0	59644	2	4.24106E-03	-1.40655E-03	4.92619E-03	0.0	0.0	47.28	4.29995E-03	-1.43375E-03	5.73370E-03
0	59644	3	4.18040E-03	-1.39082E-03	4.88336E-03	0.0	0.0	-42.93	4.28757E-03	-1.43922E-03	5.72678E-03
0	59644	4	4.26929E-03	-1.43879E-03	3.71494E-04	0.0	0.0	1.86	4.27533E-03	-1.44483E-03	5.72016E-03
0	59644	5	4.25848E-03	-1.44584E-03	3.29691E-04	0.0	0.0	1.65	4.26324E-03	-1.45060E-03	5.71384E-03
0	59644	6	4.24767E-03	-1.45289E-03	2.87888E-04	0.0	0.0	1.45	4.25130E-03	-1.45652E-03	5.70782E-03
0	59644	7	4.51150E-03	-1.26542E-03	-5.69679E-03	0.0	0.0	-43.76	4.39515E-03	-1.46259E-03	5.70210E-03
0	59644	8	4.27739E-03	-1.48168E-03	5.69302E-03	0.0	0.0	46.03	4.22788E-03	-1.46881E-03	5.69668E-03
0	59644	9	4.21523E-03	-1.47402E-03	1.62480E-04	0.0	0.0	0.82	4.21639E-03	-1.47518E-03	5.69157E-03
0	59644	10	4.20442E-03	-1.48107E-03	1.20677E-04	0.0	0.0	0.61	4.20506E-03	-1.48171E-03	5.68677E-03
0	59644	11	4.19361E-03	-1.48811E-03	7.88746E-05	0.0	0.0	0.40	4.19388E-03	-1.48839E-03	5.68227E-03
0	59644	12	4.32529E-03	-1.36236E-03	5.67796E-03	0.0	0.0	45.19	4.18286E-03	-1.49522E-03	5.67808E-03
0	59644	13	-1.50220E-03	4.17199E-03	4.73095E-06	0.0	0.0	89.98	4.17199E-03	-1.50222E-03	5.67419E-03
0	59644	14	4.30270E-03	-1.34923E-03	-5.67043E-03	0.0	0.0	-45.24	4.16127E-03	-1.50934E-03	5.67062E-03
0	59644	15	4.15037E-03	-1.51629E-03	-8.83365E-05	0.0	0.0	-0.45	4.15071E-03	-1.51664E-03	5.66735E-03
0	59644	16	4.13956E-03	-1.52334E-03	-1.30139E-04	0.0	0.0	-0.66	4.14030E-03	-1.52409E-03	5.66439E-03
0	59644	17	4.21321E-03	-1.38515E-03	-5.65913E-03	0.0	0.0	-45.87	4.13005E-03	-1.53169E-03	5.66174E-03
0	59644	18	-1.53743E-03	4.17193E-03	2.3745E-04	0.0	0.0	88.92	4.11995E-03	-1.53945E-03	5.65940E-03
0	59644	19	4.40910E-03	-1.15355E-03	5.65160E-03	0.0	0.0	43.71	4.11010E-03	-1.54736E-03	5.65737E-03
0	59644	20	4.09631E-03	-1.55152E-03	-2.97350E-04	0.0	0.0	-1.51	4.0022E-03	-1.55543E-03	5.65503E-03
0	59644	21	4.08505E-03	-1.55957E-03	3.9153E-04	0.0	0.0	-1.72	3.90563E-03	-1.5636E-03	5.64825E-03
0	59644	22	4.07469E-03	-1.56561E-03	-3.80956E-04	0.0	0.0	-1.93	3.08111E-03	-1.57204E-03	5.63515E-03
0	59644	23	4.45699E-03	-1.03423E-03	5.63653E-03	0.0	0.0	42.86	4.07179E-03	-1.58057E-03	5.65237E-03
0	59644	24	4.00440E-03	-1.46896E-03	-5.63277E-03	0.0	0.0	-47.36	4.06263E-03	-1.58926E-03	5.65189E-03
0	59644	25	4.04226E-03	-1.58675E-03	-5.06364E-04	0.0	0.0	-2.57	4.05362E-03	-1.59811E-03	5.65173E-03
0	59644	26	4.03144E-03	-1.59379E-03	-5.48167E-04	0.0	0.0	-2.78	4.04477E-03	-1.60712E-03	5.65188E-03
0	59644	27	4.02063E-03	-1.60084E-03	-5.89970E-04	0.0	0.0	-3.00	4.03607E-03	-1.61627E-03	5.65235E-03
0	59644	28	8.85084E-04	-1.51686E-03	-5.61771E-03	0.0	0.0	-48.21	4.02753E-03	-1.62559E-03	5.65312E-03
0	59644	29	1.52883E-03	8.55254E-04	5.61394E-03	0.0	0.0	41.58	4.01914E-03	-1.63506E-03	5.65420E-03
0	59644	30	3.98820E-03	-1.62197E-03	-7.15378E-04	0.0	0.0	-3.63	4.01091E-03	-1.64469E-03	5.65560E-03

Figure 72: Spars ε_1 Component Tensile Critical Strain Region 2

S T R A I N S I N L A Y E R E D C O M P O S I T E E L E M E N T S (Q U A D 4)											
ELEMENT	PLY	STRAINS IN FIBER AND MATRIX DIRECTIONS			INTER-LAMINAR		STRAINS	PRINCIPAL	STRAINS (ZERO SHEAR)		MAX
ID	ID	NORMAL-1	NORMAL-2	SHEAR-12	SHEAR XZ-MAT	SHEAR YZ-MAT	ANGLE	MAJOR	MINOR		SHEAR
0	51337	1	3.12388E-03	-7.79056E-04	3.74165E-04	0.0	0.0	2.74	3.13283E-03	-7.88003E-04	3.92083E-03
0	51337	2	3.13541E-03	-8.07863E-04	3.42373E-04	0.0	0.0	2.48	3.14283E-03	-8.15280E-04	3.95811E-03
0	51337	3	3.14694E-03	-8.36670E-04	3.10580E-04	0.0	0.0	2.23	3.15298E-03	-8.42714E-04	3.99570E-03
0	51337	4	1.00710E-03	1.28589E-03	4.02394E-03	0.0	0.0	46.98	3.16329E-03	-8.70300E-04	4.03359E-03
0	51337	5	-8.94284E-04	3.16999E-03	-2.46996E-04	0.0	0.0	-88.26	3.17374E-03	-8.98033E-04	4.07177E-03
0	51337	6	1.23681E-03	1.02161E-03	-4.10461E-03	0.0	0.0	-43.50	3.18434E-03	-9.25910E-04	4.11025E-03
0	51337	7	1.21228E-03	1.02887E-03	-4.14494E-03	0.0	0.0	-43.73	3.19507E-03	-9.53926E-04	4.14900E-03
0	51337	8	-9.80705E-04	3.20457E-03	-1.51620E-04	0.0	0.0	-88.96	3.20594E-03	-9.82078E-04	4.18802E-03
0	51337	9	1.04338E-03	1.16321E-03	4.22561E-03	0.0	0.0	45.81	3.21695E-03	-1.01036E-03	4.22731E-03
0	51337	10	3.22762E-03	-1.03832E-03	8.80353E-05	0.0	0.0	0.59	3.22808E-03	-1.03877E-03	4.26685E-03
0	51337	11	3.23915E-03	-1.06713E-03	5.62432E-05	0.0	0.0	0.37	3.23933E-03	-1.06731E-03	4.30665E-03
0	51337	12	3.25068E-03	-1.09593E-03	2.44511E-05	0.0	0.0	0.16	3.25071E-03	-1.09597E-03	4.34668E-03

Figure 73: Spars ϵ_1 Component Tensile Critical Strain Region 3

Figure 71 shows the maximum ϵ_1 component strain of .006326 in the spar captured from the results file. The margin of safety for this method of failure is shown below:

$$MS = \frac{\epsilon_{allowable}}{\epsilon_{actual}} - 1 = \frac{.0128(in/in)}{.00632611(in/in)} - 1 = 1.023$$

3.2.7.2.2 Secondary Material Axis Tensile Strain

The off axis tensile strains for the spars are presented in Figure 74. The lower spar cap experiences the highest strain in region one and the critical region is shown in Figure 75. The highest loaded areas in the other regions are also presented below.

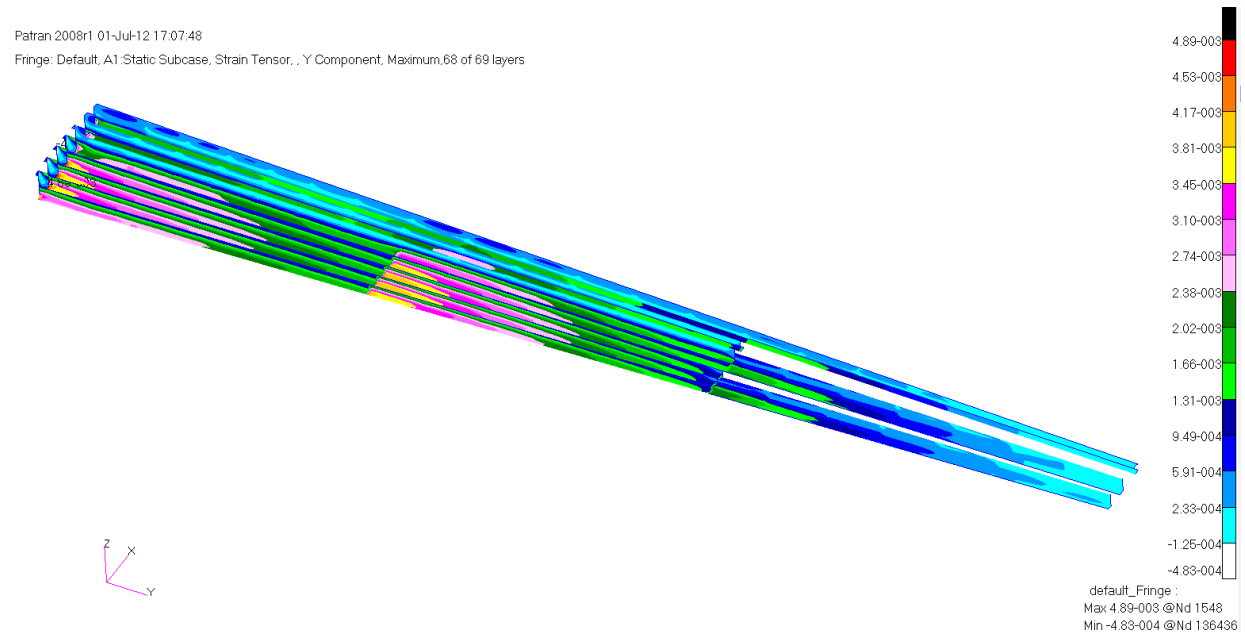


Figure 74: Spars ϵ_2 Component Tensile Strain Distribution

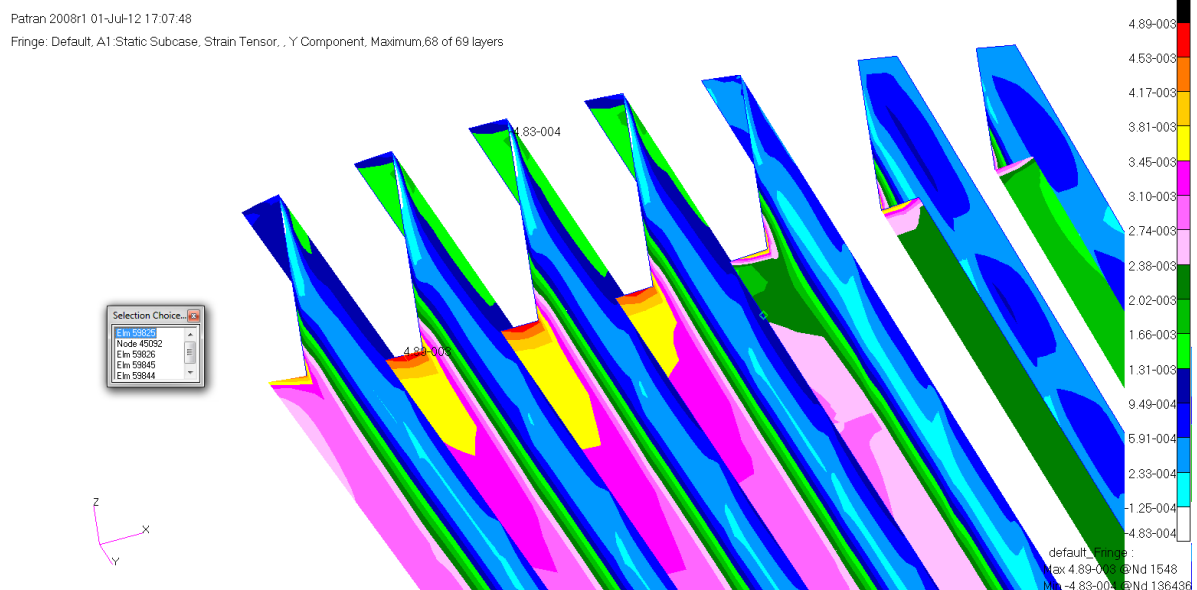


Figure 75: Spars ϵ_2 Component Tensile Strain Critical Region 1

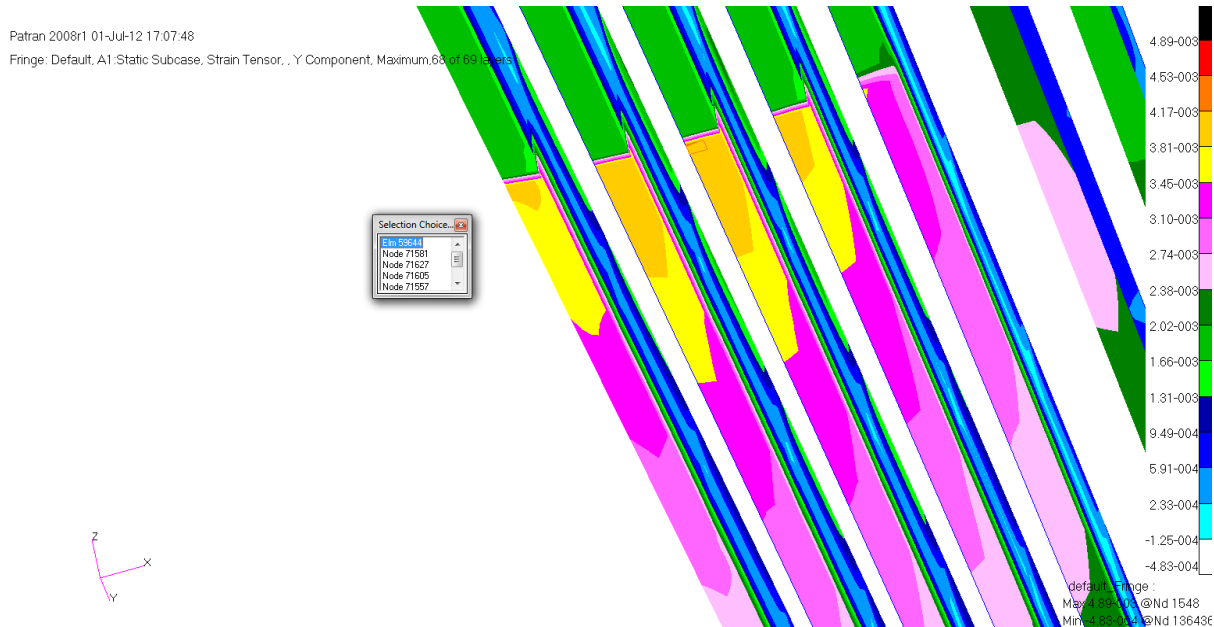


Figure 76: Spars ε_2 Component Tensile Strain Critical Region 2

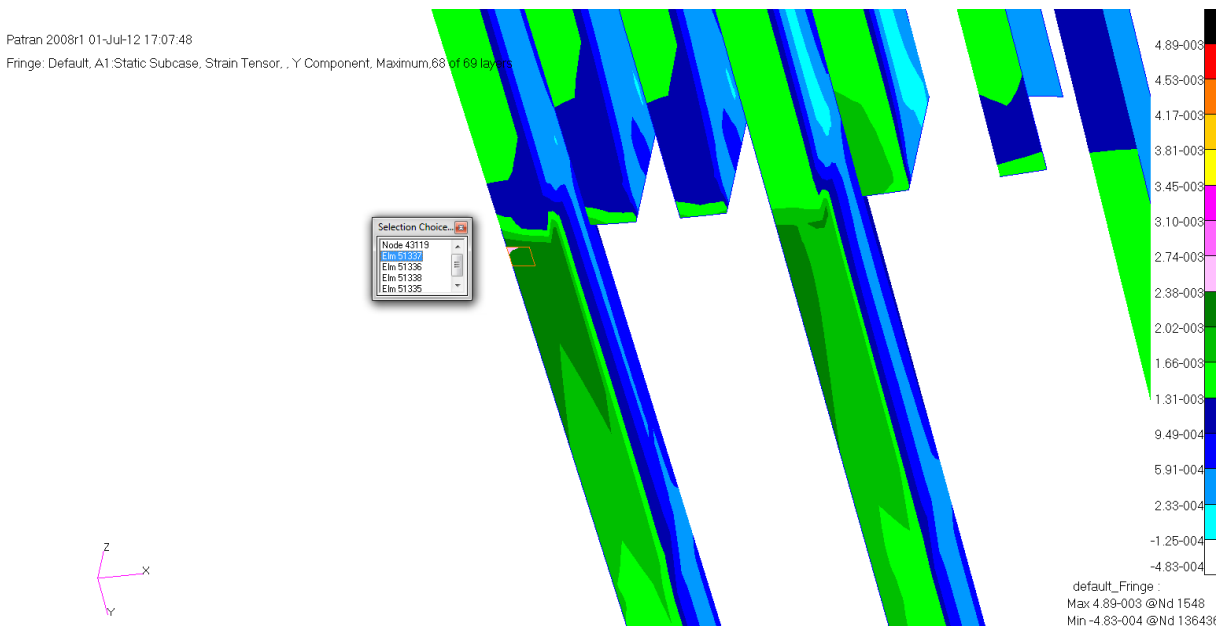


Figure 77: Spars ε_2 Component Tensile Strain Critical Region 3

STRAINS IN LAYERED						COMPOSITE ELEMENTS						(QUAD4)			
ELEMENT		STRAINS IN FIBER AND MATRIX DIRECTIONS				INTER-LAMINAR		STRAINS		PRINCIPAL		STRAINS (ZERO SHEAR)		MAX	
ID	ID	NORMAL-1	NORMAL-2	SHEAR-12		SHEAR XZ-MAT	SHEAR YZ-MAT	ANGLE	MAJOR	MINOR	SHEAR		SHEAR		
0	59825	14	2.68090E-03	1.58235E-03	6.81174E-03	0.0	0.0	40.42	5.58150E-03	-1.31826E-03	6.89976E-03	0	59825	14	2.68090E-03
0	59825	15	1.57841E-03	2.63454E-03	-6.74072E-03	0.0	0.0	-49.45	5.51795E-03	-1.30500E-03	6.82295E-03	0	59825	15	1.57841E-03
0	59825	16	5.41617E-03	-1.25352E-03	-1.01369E-03	0.0	0.0	-4.32	5.45447E-03	-1.29181E-03	6.74628E-03	0	59825	16	5.41617E-03
0	59825	17	5.35551E-03	-1.24315E-03	-9.71265E-04	0.0	0.0	-4.19	5.39106E-03	-1.27870E-03	6.6975E-03	0	59825	17	5.35551E-03
0	59825	18	5.29484E-03	-1.23278E-03	-9.28836E-04	0.0	0.0	-4.05	5.32772E-03	-1.26566E-03	6.59338E-03	0	59825	18	5.29484E-03
0	59825	19	1.56268E-03	2.44909E-03	-6.45660E-03	0.0	0.0	-48.91	5.26446E-03	-1.25270E-03	6.51716E-03	0	59825	19	1.56268E-03
0	59825	20	-1.21205E-03	5.17352E-03	8.43979E-04	0.0	0.0	86.24	5.20129E-03	-1.23982E-03	6.44110E-03	0	59825	20	-1.21205E-03
0	59825	21	2.35636E-03	1.55481E-03	6.31454E-03	0.0	0.0	41.38	5.13819E-03	-1.22702E-03	6.36521E-03	0	59825	21	2.35636E-03
0	59825	22	5.05219E-03	-1.19132E-03	-7.59122E-04	0.0	0.0	-3.47	5.07518E-03	-1.21431E-03	6.28949E-03	0	59825	22	5.05219E-03
0	59825	23	4.99153E-03	-1.18095E-03	-7.16693E-04	0.0	0.0	-3.31	5.01227E-03	-1.20168E-03	6.21395E-03	0	59825	23	4.99153E-03
0	59825	24	4.93087E-03	-1.17058E-03	-6.74264E-04	0.0	0.0	-3.15	4.94944E-03	-1.18915E-03	6.13859E-03	0	59825	24	4.93087E-03
0	59825	25	2.17091E-03	1.53908E-03	6.03042E-03	0.0	0.0	42.01	4.88671E-03	-1.17672E-03	6.06343E-03	0	59825	25	2.17091E-03
0	59825	26	-1.14985E-03	4.80954E-03	5.89407E-04	0.0	0.0	87.18	4.82408E-03	-1.16439E-03	5.98847E-03	0	59825	26	-1.14985E-03
0	59825	27	1.53121E-03	2.07819E-03	-5.88836E-03	0.0	0.0	-47.65	4.76156E-03	-1.15216E-03	5.91371E-03	0	59825	27	1.53121E-03
0	59825	28	4.68822E-03	-1.12912E-03	-5.04550E-04	0.0	0.0	-2.48	4.69914E-03	-1.14004E-03	5.83917E-03	0	59825	28	4.68822E-03
0	59825	29	4.62756E-03	-1.11875E-03	-4.62121E-04	0.0	0.0	-2.30	4.63683E-03	-1.12802E-03	5.76486E-03	0	59825	29	4.62756E-03
0	59825	30	4.56689E-03	-1.10838E-03	-4.19693E-04	0.0	0.0	-2.11	4.5746E-03	-1.11613E-03	5.69077E-03	0	59825	30	4.56689E-03
0	59825	31	1.51548E-03	1.89274E-03	-5.60425E-03	0.0	0.0	-46.93	4.51257E-03	-1.10436E-03	5.61693E-03	0	59825	31	1.51548E-03
0	59825	32	-1.08765E-03	4.44557E-03	3.34835E-04	0.0	0.0	88.27	4.45063E-03	-1.09271E-03	5.54334E-03	0	59825	32	-1.08765E-03
0	59825	33	1.80001E-03	1.50761E-03	5.46219E-03	0.0	0.0	43.47	4.38881E-03	-1.08119E-03	5.47001E-03	0	59825	33	1.80001E-03
0	59825	34	4.32424E-03	-1.06692E-03	-2.49978E-04	0.0	0.0	-1.33	4.32714E-03	-1.06981E-03	5.39695E-03	0	59825	34	4.32424E-03
0	59825	35	4.26358E-03	-1.05655E-03	-2.07549E-04	0.0	0.0	-1.12	4.26560E-03	-1.05875E-03	5.32417E-03	0	59825	35	4.26358E-03
0	59825	36	1.66093E-03	1.49581E-03	5.24910E-03	0.0	0.0	44.10	4.20421E-03	-1.04748E-03	5.25169E-03	0	59825	36	1.66093E-03
0	59825	37	-1.03582E-03	4.14225E-03	1.22692E-04	0.0	0.0	89.32	4.14298E-03	-1.03654E-03	5.17952E-03	0	59825	37	-1.03582E-03
0	59825	38	1.48794E-03	1.56820E-03	-5.10704E-03	0.0	0.0	-45.45	4.08191E-03	-1.02576E-03	5.10767E-03	0	59825	38	1.48794E-03

Figure 78: Spars ε_2 Component Tensile Critical Strain Region 1

ELEMENT ID	PLY ID	STRAINS IN LAYERED			COMPOSITE ELEMENTS			(QUAD4)			MAX SHEAR
		STRAINS IN FIBER AND MATRIX DIRECTIONS			INTER-LAMINAR STRAINS			STRAINS PRINCIPAL (ZERO SHEAR)			
		NORMAL-1	NORMAL-2	SHEAR-12	SHEAR XZ-MAT	SHEAR YZ-MAT	ANGLE	MAJOR	MINOR		
0	59644	1	4.30172E-03	-1.41766E-03	4.96902E-04	0.0	0.0	2.48	4.31249E-03	-1.42843E-03	5.74092E-03
0	59644	2	1.20555E-03	1.66065E-03	5.71561E-03	0.0	0.0	47.28	4.29995E-03	-1.43375E-03	5.73370E-03
0	59644	3	1.63082E-03	1.21753E-03	-5.71185E-03	0.0	0.0	-42.93	4.28757E-03	-1.43922E-03	5.72678E-03
0	59644	4	4.26929E-03	-1.43879E-03	3.71494E-04	0.0	0.0	1.86	4.27533E-03	-1.44483E-03	5.72016E-03
0	59644	5	4.25848E-03	-1.44584E-03	3.29691E-04	0.0	0.0	1.65	4.26324E-03	-1.45060E-03	5.71384E-03
0	59644	6	4.24767E-03	-1.45289E-03	2.87888E-04	0.0	0.0	1.45	4.25130E-03	-1.45652E-03	5.70782E-03
0	59644	7	1.51150E-03	1.26542E-03	-5.69679E-03	0.0	0.0	-43.76	4.23951E-03	-1.46259E-03	5.70210E-03
0	59644	8	1.27739E-03	1.48168E-03	5.69302E-03	0.0	0.0	46.03	4.22788E-03	-1.46881E-03	5.69668E-03
0	59644	9	4.21523E-03	-1.47402E-03	1.62480E-04	0.0	0.0	0.82	4.21639E-03	-1.47518E-03	5.69157E-03
0	59644	10	4.20442E-03	-1.48107E-03	1.20677E-04	0.0	0.0	0.61	4.20506E-03	-1.48171E-03	5.68677E-03
0	59644	11	4.19361E-03	-1.48811E-03	7.88746E-05	0.0	0.0	0.40	4.19388E-03	-1.48839E-03	5.68227E-03
0	59644	12	1.32529E-03	1.36236E-03	5.67796E-03	0.0	0.0	45.19	4.18286E-03	-1.49522E-03	5.67808E-03
0	59644	13	-1.50220E-03	4.17199E-03	4.73095E-06	0.0	0.0	89.98	4.17199E-03	-1.50220E-03	5.67419E-03
0	59644	14	1.30270E-03	1.34923E-03	-5.67043E-03	0.0	0.0	-45.24	4.16127E-03	-1.50934E-03	5.67062E-03
0	59644	15	4.15037E-03	-1.51629E-03	-8.83365E-05	0.0	0.0	-0.45	4.15071E-03	-1.51664E-03	5.66735E-03
0	59644	16	4.13956E-03	-1.52334E-03	-1.30139E-04	0.0	0.0	-0.66	4.14030E-03	-1.52409E-03	5.66439E-03
0	59644	17	1.21321E-03	1.38515E-03	-5.65913E-03	0.0	0.0	-45.87	4.13005E-03	-1.53169E-03	5.66174E-03
0	59644	18	-1.53743E-03	4.11793E-03	2.13745E-04	0.0	0.0	88.92	4.11995E-03	-1.53945E-03	5.65940E-03
0	59644	19	1.40910E-03	1.15355E-03	5.65160E-03	0.0	0.0	43.71	4.11001E-03	-1.54736E-03	5.65737E-03
0	59644	20	4.09631E-03	-1.55152E-03	-2.97350E-04	0.0	0.0	-1.51	4.10022E-03	-1.55543E-03	5.65565E-03
0	59644	21	4.08550E-03	-1.55857E-03	-3.39153E-04	0.0	0.0	-1.72	4.09059E-03	-1.56366E-03	5.65425E-03
0	59644	22	4.07469E-03	-1.56561E-03	-3.80956E-04	0.0	0.0	-1.93	4.08111E-03	-1.57204E-03	5.65315E-03
0	59644	23	1.45699E-03	1.03423E-03	5.63653E-03	0.0	0.0	42.86	4.07179E-03	-1.58057E-03	5.65237E-03
0	59644	24	1.00440E-03	1.46896E-03	-5.63277E-03	0.0	0.0	-47.36	4.06263E-03	-1.58926E-03	5.65189E-03
0	59644	25	4.04226E-03	-1.58675E-03	-5.06364E-04	0.0	0.0	-2.57	4.05362E-03	-1.59811E-03	5.65173E-03
0	59644	26	4.03144E-03	-1.59379E-03	-5.48167E-04	0.0	0.0	-2.78	4.04477E-03	-1.60712E-03	5.65188E-03
0	59644	27	4.02063E-03	-1.60084E-03	-5.89970E-04	0.0	0.0	-3.00	4.03607E-03	-1.61627E-03	5.65235E-03
0	59644	28	8.85084E-04	1.51686E-03	-5.61771E-03	0.0	0.0	-48.21	4.02753E-03	-1.62559E-03	5.65312E-03
0	59644	29	1.52883E-03	8.55254E-04	5.61394E-03	0.0	0.0	41.58	4.01914E-03	-1.63506E-03	5.65420E-03
0	59644	30	3.98820E-03	-1.62197E-03	-7.15378E-04	0.0	0.0	-3.63	4.01091E-03	-1.64469E-03	5.65560E-03

Figure 79: Spars ε_2 Component Tensile Critical Strain Region 2

STRAINS IN LAYERED						COMPOSITE ELEMENTS (QUAD4)									
		STRAINS IN FIBER AND MATRIX DIRECTIONS				INTER-LAMINAR		STRAINS		PRINCIPAL		STRAINS (ZERO SHEAR)		MAX	
ELEMENT	PLY	NORMAL-1		NORMAL-2		SHEAR-12		SHEAR XZ-MAT		SHEAR YZ-MAT		ANGLE	MAJOR	MINOR	SHEAR
ID	ID														
0	51337	1	3.12388E-03	-7.79056E-04	3.74165E-04	0.0	0.0	2.74	3.13283E-03	-7.88003E-04	3.92083E-03				
0	51337	2	3.13541E-03	-8.07863E-04	3.42373E-04	0.0	0.0	2.48	3.14283E-03	-8.15280E-04	3.95811E-03				
0	51337	3	3.14694E-03	-8.36670E-04	3.10580E-04	0.0	0.0	2.23	3.15298E-03	-8.42714E-04	3.99570E-03				
0	51337	4	1.00710E-03	1.28589E-03	4.02394E-03	0.0	0.0	46.98	3.16329E-03	-8.70300E-04	4.03359E-03				
0	51337	5	-8.94284E-04	3.16399E-03	-2.46996E-04	0.0	0.0	-88.26	3.17374E-03	-8.98033E-04	4.07117E-03				
0	51337	6	1.23681E-03	1.02161E-03	-4.10461E-03	0.0	0.0	-43.50	3.18434E-03	-9.25910E-04	4.11025E-03				
0	51337	7	1.21228E-03	1.02887E-03	-4.14494E-03	0.0	0.0	-43.73	3.19507E-03	-9.53926E-04	4.14900E-03				
0	51337	8	-9.80705E-04	3.20457E-03	-1.51620E-04	0.0	0.0	-88.96	3.20594E-03	-9.82078E-04	4.18802E-03				
0	51337	9	1.04338E-03	1.16321E-03	4.22561E-03	0.0	0.0	45.81	3.21695E-03	-1.01036E-03	4.22731E-03				
0	51337	10	3.22762E-03	-1.03832E-03	8.80353E-05	0.0	0.0	0.59	3.22808E-03	-1.03877E-03	4.26685E-03				
0	51337	11	3.23915E-03	-1.06713E-03	5.62432E-05	0.0	0.0	0.37	3.23933E-03	-1.06731E-03	4.30665E-03				
0	51337	12	3.25068E-03	-1.09593E-03	2.44511E-05	0.0	0.0	0.16	3.25071E-03	-1.09597E-03	4.34668E-03				

Figure 80: Spars ε_2 Component Tensile Critical Strain Region 3

Figure 78 shows the maximum ε_2 component strain of .00517 in the spar captured from the results file. The margin of safety for this method of failure is shown below:

$$MS = \frac{\varepsilon_{allowable}}{\varepsilon_{actual}} - 1 = \frac{.00702(in/in)}{.00517352(in/in)} - 1 = .357$$

3.2.7.2.3 Secondary Material Axis Compressive Strain

The off axis compressive strains for the spars are presented in Figure 81. The upper spar cap experiences the highest strain in wing region one and the critical region is shown in Figure 82. The highest loaded areas in the other regions are also presented below.

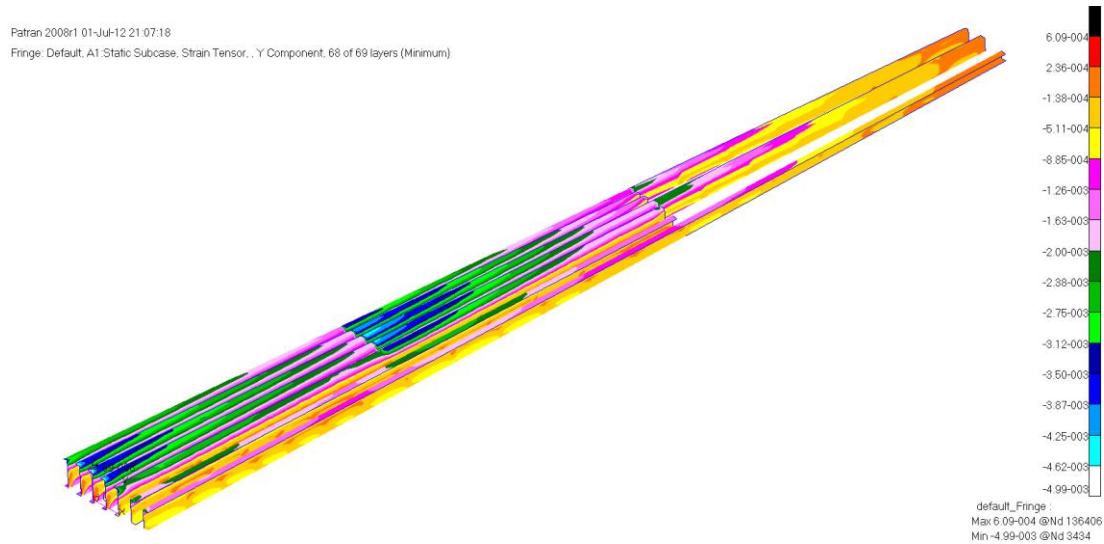


Figure 81: Spars ϵ_2 Component Compressive Strain Distribution

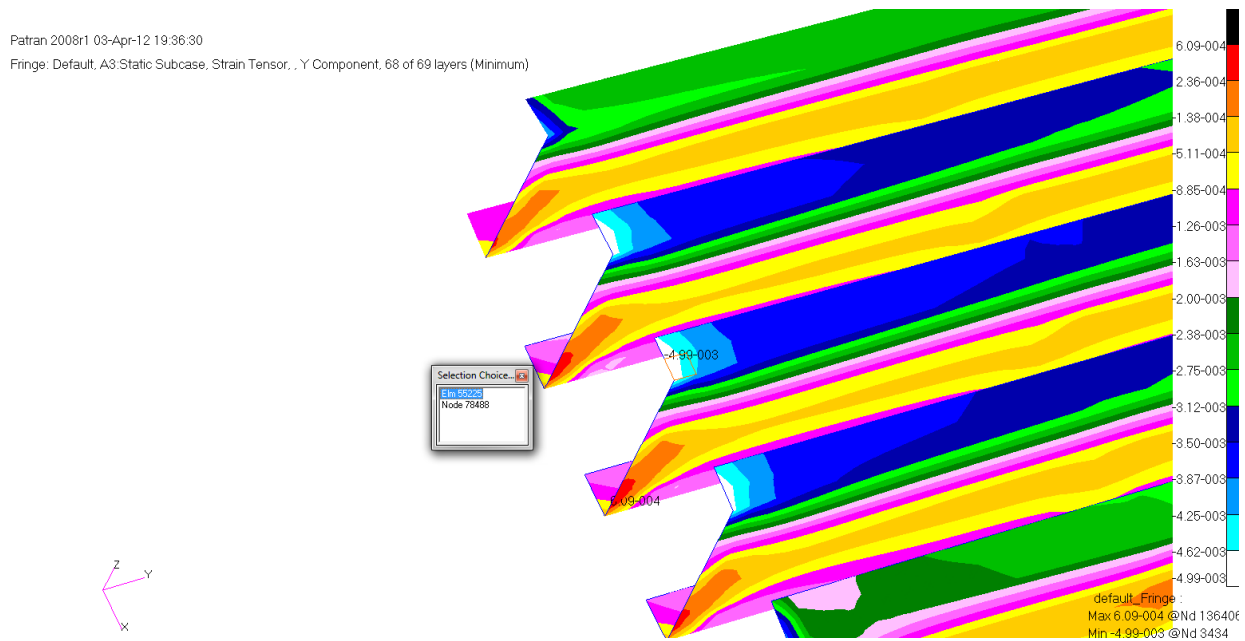


Figure 82: Spars ϵ_2 Component Compressive Strain Critical Region 1

Patran 2008r1 01-Jul-12 21:07:18
 Fringe: Default, A1 Static Subcase, Strain Tensor, Y Component, 68 of 69 layers (Minimum)

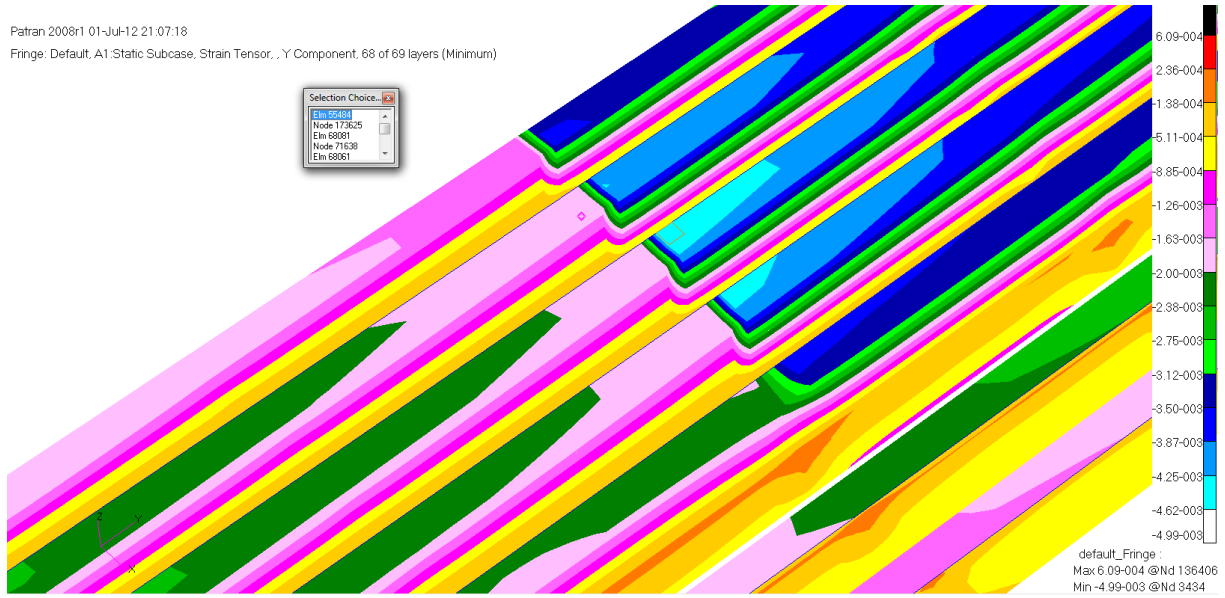


Figure 83: Spars ϵ_2 Component Compressive Strain Critical Region 2

Patran 2008r1 01-Jul-12 21:07:18
 Fringe: Default, A1 Static Subcase, Strain Tensor, Y Component, 68 of 69 layers (Minimum)

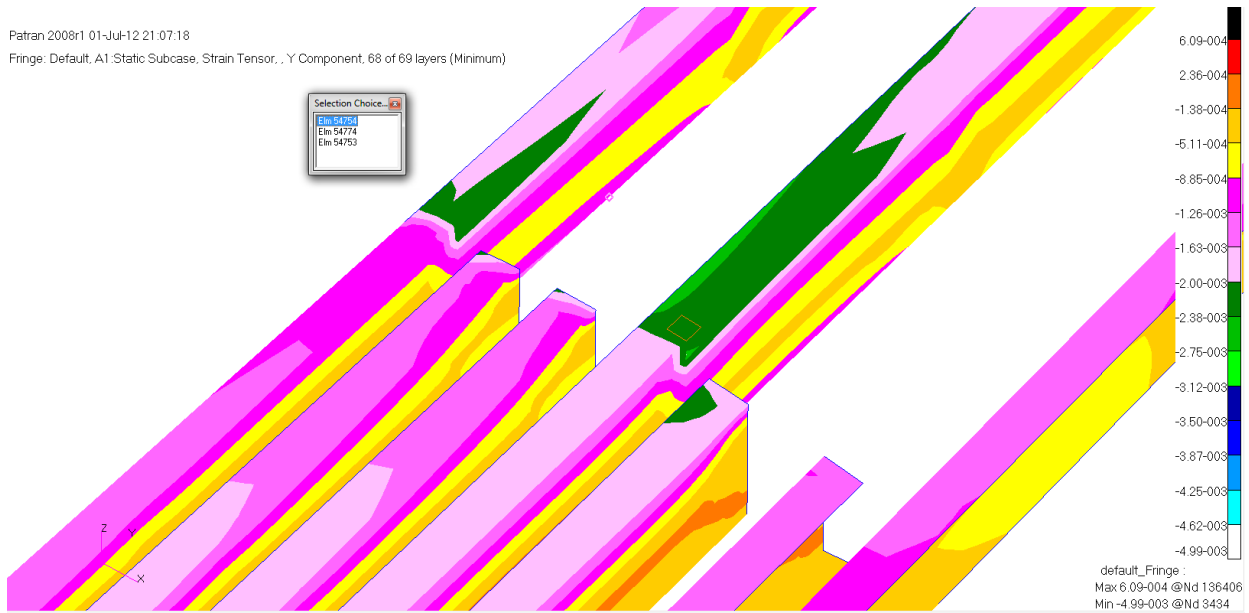


Figure 84: Spars ϵ_2 Component Compressive Strain Critical Region 3

ELEMENT ID	PLY ID	STRAINS IN LAYERED STRAINS IN FIBER AND MATRIX DIRECTIONS			COMPOSITE ELEMENTS (QUAD4)					MAX SHEAR	
		NORMAL-1	NORMAL-2	SHEAR-12	INTER-LAMINAR STRAINS		PRINCIPAL ANGLE	STRAINS (ZERO SHEAR)			
					SHEAR XZ-MAT	SHEAR YZ-MAT		MAJOR	MINOR		
0	55225	29	-4.06933E-03	9.88482E-04	-2.84674E-04	0.0	0.0	-88.39	9.92485E-04	-4.07333E-03	5.06581E-03
0	55225	30	-4.12623E-03	9.98280E-04	-2.50082E-04	0.0	0.0	-88.60	1.00133E-03	-4.12928E-03	5.13061E-03
0	55225	31	-1.69527E-03	-1.47978E-03	5.19121E-03	0.0	0.0	46.19	1.01031E-03	-4.18536E-03	5.19568E-03
0	55225	32	1.01788E-03	-4.24003E-03	1.80897E-04	0.0	0.0	0.99	1.01943E-03	-4.24159E-03	5.26102E-03
0	55225	33	-1.56148E-03	-1.70778E-03	-5.32461E-03	0.0	0.0	-44.21	1.02868E-03	-4.29794E-03	5.32662E-03
0	55225	34	-4.35383E-03	1.03747E-03	-1.11712E-04	0.0	0.0	-89.41	1.03805E-03	-4.35441E-03	5.39246E-03
0	55225	35	-4.41074E-03	1.04727E-03	-7.71190E-05	0.0	0.0	-89.60	1.04754E-03	-4.41101E-03	5.45855E-03
0	55225	36	-1.68402E-03	-1.72655E-03	-5.52471E-03	0.0	0.0	-44.78	1.05715E-03	-4.46772E-03	5.52487E-03
0	55225	37	1.06687E-03	-4.52454E-03	7.93392E-06	0.0	0.0	0.04	1.06687E-03	-4.52454E-03	5.59141E-03
0	55225	38	-1.73906E-03	-1.76572E-03	5.65810E-03	0.0	0.0	44.87	1.07669E-03	-4.58147E-03	5.65817E-03
0	55225	39	-4.63834E-03	1.08646E-03	6.12512E-05	0.0	0.0	89.69	1.08663E-03	-4.63851E-03	5.72513E-03
0	55225	40	-4.69524E-03	1.09626E-03	9.58437E-05	0.0	0.0	89.53	1.09666E-03	-4.69564E-03	5.79230E-03
0	55225	41	-4.75215E-03	1.10606E-03	1.30436E-04	0.0	0.0	89.36	1.10678E-03	-4.75287E-03	5.85966E-03
0	55225	42	-1.76408E-03	-1.92911E-03	5.92490E-03	0.0	0.0	44.20	1.11700E-03	-4.81020E-03	5.92720E-03
0	55225	43	1.12565E-03	-4.86595E-03	-1.99621E-04	0.0	0.0	-0.95	1.12731E-03	-4.86761E-03	5.99493E-03
0	55225	44	-2.01081E-03	-1.77659E-03	-6.05830E-03	0.0	0.0	-46.11	1.13771E-03	-4.92511E-03	6.06283E-03
0	55225	45	-4.97975E-03	1.14525E-03	2.68806E-04	0.0	0.0	88.74	1.14820E-03	-4.98270E-03	6.13090E-03
0	55225	46	-5.03666E-03	1.15505E-03	3.03399E-04	0.0	0.0	88.60	1.15876E-03	-5.04037E-03	6.19913E-03
0	55225	47	-5.09356E-03	1.16484E-03	3.37992E-04	0.0	0.0	88.45	1.16940E-03	-5.09812E-03	6.26752E-03
0	55225	48	-2.17420E-03	-1.80162E-03	-6.32510E-03	0.0	0.0	-46.69	1.18012E-03	-5.15594E-03	6.33607E-03
0	55225	49	1.18444E-03	-5.20736E-03	-4.07177E-04	0.0	0.0	-1.82	1.19092E-03	-5.21384E-03	6.40476E-03
0	55225	50	-1.81413E-03	-2.25590E-03	6.45850E-03	0.0	0.0	43.04	1.20178E-03	-5.27181E-03	6.47359E-03
0	55225	51	-5.32116E-03	1.20404E-03	4.76362E-04	0.0	0.0	87.91	1.21272E-03	-5.32985E-03	6.54256E-03
0	55225	52	-5.37807E-03	1.21383E-03	5.10954E-04	0.0	0.0	87.78	1.22372E-03	-5.38795E-03	6.61167E-03
0	55225	53	-5.43497E-03	1.22363E-03	5.45547E-04	0.0	0.0	87.66	1.23479E-03	-5.44612E-03	6.68091E-03

Figure 85: Spars ε_2 Component Compressive Critical Strain Region 1

ELEMENT ID	PLY ID	STRAINS IN LAYERED STRAINS IN FIBER AND MATRIX DIRECTIONS			COMPOSITE ELEMENTS (QUAD4)					MAX SHEAR	
		NORMAL-1	NORMAL-2	SHEAR-12	INTER-LAMINAR STRAINS		PRINCIPAL ANGLE	STRAINS (ZERO SHEAR)			
					SHEAR XZ-MAT	SHEAR YZ-MAT		MAJOR	MINOR		
0	55484	15	-4.40778E-03	1.63780E-03	1.61163E-04	0.0	0.0	89.24	1.63887E-03	-4.40886E-03	6.04773E-03
0	55484	16	-4.41768E-03	1.62864E-03	1.12233E-04	0.0	0.0	89.47	1.62916E-03	-4.41820E-03	6.04736E-03
0	55484	17	-1.37240E-03	-1.43570E-03	6.04705E-03	0.0	0.0	44.70	1.61964E-03	-4.42774E-03	6.04738E-03
0	55484	18	1.61031E-03	-4.43747E-03	-1.43741E-05	0.0	0.0	-0.07	1.61032E-03	-4.43748E-03	6.04780E-03
0	55484	19	-1.40583E-03	-1.44038E-03	-6.04852E-03	0.0	0.0	-44.84	1.60120E-03	-4.44742E-03	6.04862E-03
0	55484	20	-4.45726E-03	1.59199E-03	-8.34853E-05	0.0	0.0	-89.60	1.59228E-03	-4.45755E-03	6.04983E-03
0	55484	21	-4.46716E-03	1.58283E-03	-1.32415E-04	0.0	0.0	-89.37	1.58356E-03	-4.46789E-03	6.05144E-03
0	55484	22	-4.47706E-03	1.57367E-03	-1.81345E-04	0.0	0.0	-89.14	1.57503E-03	-4.47842E-03	6.05345E-03
0	55484	23	-1.34608E-03	-1.57636E-03	-6.05147E-03	0.0	0.0	-43.91	1.56670E-03	-4.48914E-03	6.05585E-03
0	55484	24	-1.61035E-03	-1.33115E-03	6.05220E-03	0.0	0.0	46.32	1.55857E-03	-4.50007E-03	6.05864E-03
0	55484	25	-4.50675E-03	1.54619E-03	-3.28134E-04	0.0	0.0	-88.45	1.55064E-03	-4.51119E-03	6.06183E-03
0	55484	26	-4.51664E-03	1.53703E-03	-3.77063E-04	0.0	0.0	-88.22	1.54290E-03	-4.52251E-03	6.06541E-03
0	55484	27	-4.52654E-03	1.52787E-03	-4.25993E-04	0.0	0.0	-87.99	1.53536E-03	-4.53402E-03	6.06938E-03
0	55484	28	-1.74632E-03	-1.27140E-03	6.05515E-03	0.0	0.0	47.24	1.52801E-03	-4.54573E-03	6.07374E-03
0	55484	29	-1.25646E-03	-1.78032E-03	-6.05588E-03	0.0	0.0	-42.53	1.52086E-03	-4.55764E-03	6.07850E-03
0	55484	30	-4.55623E-03	1.50039E-03	-5.72782E-04	0.0	0.0	-87.30	1.51390E-03	-4.56974E-03	6.08364E-03

Figure 86: Spars ε_2 Component Compressive Critical Strain Region 2

ELEMENT ID	PLY ID	STRAINS IN LAYERED STRAINS IN FIBER AND MATRIX DIRECTIONS			COMPOSITE ELEMENTS (QUAD4)					MAX SHEAR	
		NORMAL-1	NORMAL-2	SHEAR-12	INTER-LAMINAR STRAINS		PRINCIPAL ANGLE	STRAINS (ZERO SHEAR)			
					SHEAR XZ-MAT	SHEAR YZ-MAT		MAJOR	MINOR		
0	54754	1	-3.10637E-03	1.03805E-03	7.14412E-04	0.0	0.0	85.11	1.06861E-03	-3.13693E-03	4.20554E-03
0	54754	2	-3.10910E-03	9.97578E-04	6.83566E-04	0.0	0.0	85.27	1.02583E-03	-3.13735E-03	4.16318E-03
0	54754	3	-3.11183E-03	9.57105E-04	6.52720E-04	0.0	0.0	85.44	9.83115E-04	-3.13784E-03	4.12095E-03
0	54754	4	-1.40990E-03	-7.88028E-04	-4.03119E-03	0.0	0.0	-49.38	9.40474E-04	-3.13840E-03	4.07888E-03
0	54754	5	8.76158E-04	-3.11729E-03	-5.91027E-04	0.0	0.0	-4.21	8.97907E-04	-3.13904E-03	4.03695E-03
0	54754	6	-8.62079E-04	-1.42226E-03	3.95571E-03	0.0	0.0	40.97	8.55418E-04	-3.13976E-03	3.99517E-03
0	54754	7	-8.99104E-04	-1.42844E-03	3.91796E-03	0.0	0.0	41.15	8.13009E-04	-3.14055E-03	3.95356E-03
0	54754	8	7.54737E-04	-3.12549E-03	-4.98488E-04	0.0	0.0	-3.66	7.70682E-04	-3.14143E-03	3.91211E-03
0	54754	9	-1.44080E-03	-9.73155E-04	-3.84248E-03	0.0	0.0	-48.47	7.28440E-04	-3.14239E-03	3.87083E-03
0	54754	10	-3.13095E-03	6.73790E-04	4.36796E-04	0.0	0.0	86.73	6.86286E-04	-3.14344E-03	3.82973E-03
0	54754	11	-3.13368E-03	6.33317E-04	4.05950E-04	0.0	0.0	86.92	6.44222E-04	-3.14458E-03	3.78881E-03
0	54754	12	-3.13641E-03	5.92843E-04	3.75103E-04	0.0	0.0	87.13	6.02252E-04	-3.14582E-03	3.74807E-03

Figure 87: Spars ε_2 Component Compressive Critical Strain Region 3

Figure 85 shows the maximum ε_2 component strain of .00487 in the spar captured from the results file. The margin of safety for this method of failure is shown below:

$$MS = \frac{\varepsilon_{allowable}}{\varepsilon_{actual}} - 1 = \frac{.0132(in/in)}{.00486595(in/in)} - 1 = 1.713$$

3.2.7.2.4 Primary Material Axis Compressive Strain

The on-axis tensile strain for the spars are presented in Figure 88. The upper spar cap experiences the highest strain in region one and the critical region is shown in Figure 89. The highest loaded areas in the other regions are also presented below. Since this structure is within the skins of the aircraft it was not limited to a strain of .005 since it is protected from damage with the aircraft, and is not expected to tolerate a bolted repair.

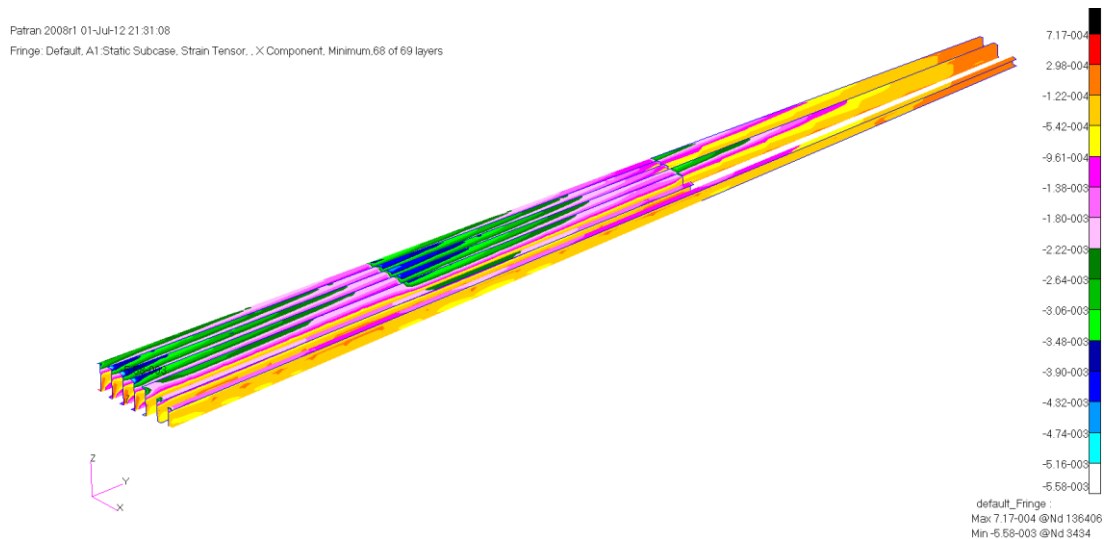


Figure 88: Spars ϵ_1 Component Compressive Strain Distribution

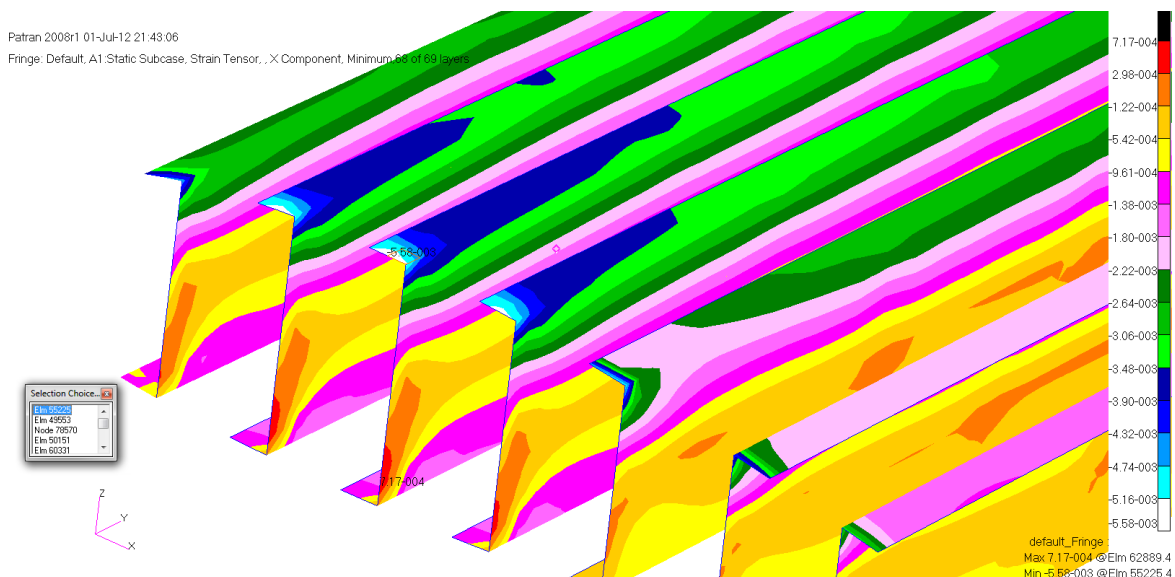


Figure 89: Spars ϵ_1 Component Compressive Strain Critical Region 1

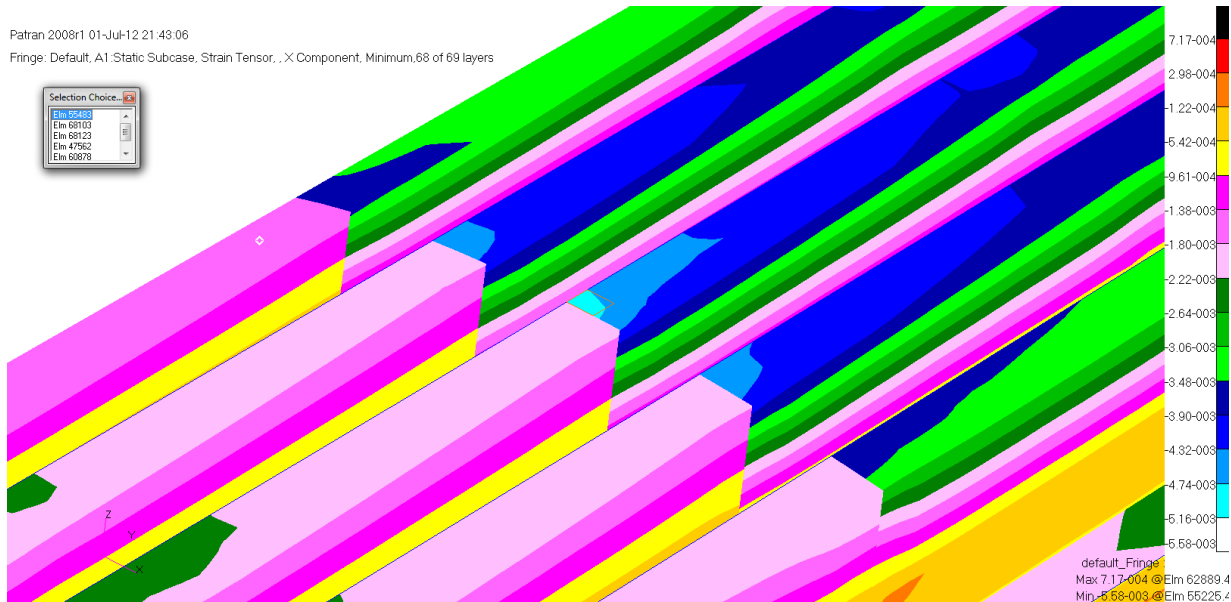


Figure 90: Spars ϵ_1 Component Compressive Strain Critical Region 2

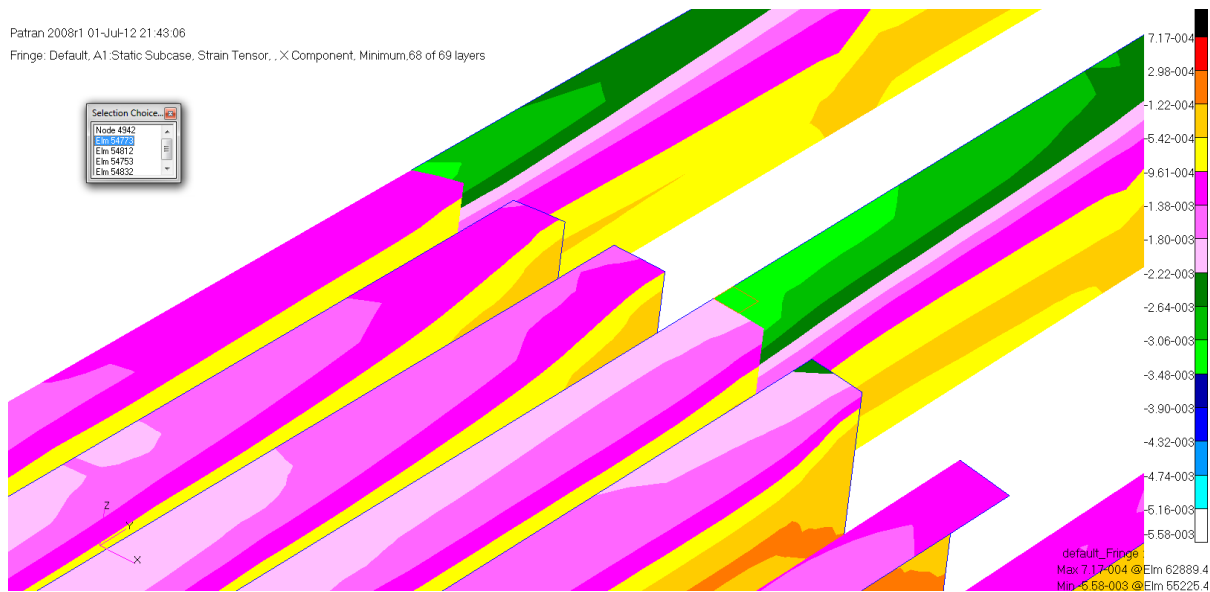


Figure 91: Spars ϵ_1 Component Compressive Strain Critical Region 3

STRAINS IN LAYERED				COMPOSITE ELEMENTS (QUAD4)				PRINCIPAL STRAINS (ZERO SHEAR)				MAX SHEAR
ELEMENT ID	PLY ID	STRAINS IN FIBER AND MATRIX DIRECTIONS	INTER-LAMINAR	STRAINS	ANGLE	MAJOR	MINOR					
		NORMAL-1	NORMAL-2	SHEAR-12	SHEAR XZ-MAT	SHEAR YZ-MAT						
0	55225	54	-1.83915E-03	-2.41929E-03	6.72530E-03	0.0	42.53	1.24592E-03	-5.50436E-03	6.75027E-03		
0	55225	55	-2.46014E-03	-1.84541E-03	-6.79200E-03	0.0	-47.59	1.25711E-03	-5.56265E-03	6.81976E-03		
0	55225	56	-5.60567E-03	1.25303E-03	6.49324E-04	0.0	87.30	1.26836E-03	-5.62101E-03	6.88937E-03		
0	55225	57	-5.66257E-03	1.26282E-03	6.83917E-04	0.0	87.18	1.27967E-03	-5.67942E-03	6.95909E-03		
0	55225	58	-5.71948E-03	1.27262E-03	7.18510E-04	0.0	87.07	1.29103E-03	-5.73789E-03	7.02892E-03		
0	55225	59	-2.62353E-03	-1.87043E-03	-7.05880E-03	0.0	-48.04	1.30245E-03	-5.79641E-03	7.09886E-03		
0	55225	60	-1.87668E-03	-2.66438E-03	7.12550E-03	0.0	41.85	1.31392E-03	-5.85498E-03	7.16890E-03		
0	55225	61	-5.89018E-03	1.30202E-03	8.22287E-04	0.0	86.74	1.32544E-03	-5.91361E-03	7.23905E-03		
0	55225	62	-5.94708E-03	1.31181E-03	8.56880E-04	0.0	86.63	1.33701E-03	-5.97228E-03	7.30930E-03		
0	55225	63	-6.00399E-03	1.32161E-03	8.91472E-04	0.0	86.53	1.34863E-03	-6.03101E-03	7.37964E-03		
0	55225	64	-1.90171E-03	-2.82777E-03	7.39230E-03	0.0	41.43	1.36030E-03	-6.08978E-03	7.45008E-03		
0	55225	65	-2.86862E-03	-1.90796E-03	-7.45900E-03	0.0	-48.67	1.37201E-03	-6.14859E-03	7.52106E-03		
0	55225	66	-6.17459E-03	1.35100E-03	9.95250E-04	0.0	86.23	1.38377E-03	-6.20745E-03	7.59122E-03		
0	55225	67	-6.23159E-03	1.36080E-03	1.02984E-03	0.0	86.14	1.39557E-03	-6.26636E-03	7.66192E-03		
0	55225	68	-6.28849E-03	1.37060E-03	1.06443E-03	0.0	86.04	1.40741E-03	-6.32530E-03	7.73271E-03		

Figure 92: Spars ϵ_1 Component Compressive Critical Strain Region 1

STRAINS IN LAYERED COMPOSITE ELEMENTS (QUAD4)											
ELEMENT ID	PLY ID	STRAINS IN FIBER AND MATRIX DIRECTIONS			INTER-LAMINAR STRAINS			PRINCIPAL STRAINS (ZERO SHEAR)			MAX SHEAR
		NORMAL-1	NORMAL-2	SHEAR-12	SHEAR XZ-MAT	SHEAR YZ-MAT	ANGLE	MAJOR	MINOR		
0	55484	15	-4.40778E-03	1.63780E-03	1.61163E-04	0.0	0.0	89.24	1.63887E-03	-4.40886E-03	6.04773E-03
0	55484	16	-4.41768E-03	1.62864E-03	1.12233E-04	0.0	0.0	89.47	1.62916E-03	-4.41820E-03	6.04736E-03
0	55484	17	-1.37240E-03	-1.43570E-03	6.04705E-03	0.0	0.0	44.70	1.61964E-03	-4.42774E-03	6.04738E-03
0	55484	18	1.61031E-03	-4.43747E-03	-1.43741E-05	0.0	0.0	-0.07	1.61032E-03	-4.43748E-03	6.04780E-03
0	55484	19	-1.40583E-03	-1.44038E-03	-6.04852E-03	0.0	0.0	-44.84	1.60120E-03	-4.44742E-03	6.04862E-03
0	55484	20	-4.45726E-03	1.59199E-03	-8.34853E-05	0.0	0.0	-89.60	1.59228E-03	-4.45755E-03	6.04983E-03
0	55484	21	-4.46716E-03	1.58283E-03	-1.32415E-04	0.0	0.0	-89.37	1.58356E-03	-4.46789E-03	6.05144E-03
0	55484	22	-4.47706E-03	1.57367E-03	-1.81345E-04	0.0	0.0	-89.14	1.57503E-03	-4.47842E-03	6.05345E-03
0	55484	23	-1.34608E-03	-1.57636E-03	-6.05147E-03	0.0	0.0	-43.91	1.56670E-03	-4.48914E-03	6.05585E-03
0	55484	24	-1.61035E-03	-1.33115E-03	6.05220E-03	0.0	0.0	46.32	1.55857E-03	-4.50007E-03	6.05864E-03
0	55484	25	-4.50675E-03	1.54619E-03	-3.28134E-04	0.0	0.0	-88.45	1.55064E-03	-4.51119E-03	6.06183E-03
0	55484	26	-4.51664E-03	1.53703E-03	-3.77063E-04	0.0	0.0	-88.22	1.54290E-03	-4.52251E-03	6.06541E-03
0	55484	27	-4.52654E-03	1.52787E-03	-4.25993E-04	0.0	0.0	-87.99	1.53536E-03	-4.53402E-03	6.06938E-03
0	55484	28	-1.74632E-03	-1.27140E-03	6.05515E-03	0.0	0.0	47.24	1.52801E-03	-4.54573E-03	6.07374E-03
0	55484	29	-1.25646E-03	-1.78032E-03	-6.05588E-03	0.0	0.0	-42.53	1.52086E-03	-4.55764E-03	6.07850E-03
0	55484	30	-3.29134E-03	1.50039E-03	-5.72782E-04	0.0	0.0	-87.30	1.51390E-03	-4.56974E-03	6.08364E-03

Figure 93: Spars ϵ_1 Component Compressive Critical Strain Region 2

STRAINS IN LAYERED COMPOSITE ELEMENTS (QUAD4)											
ELEMENT ID	PLY ID	STRAINS IN FIBER AND MATRIX DIRECTIONS			INTER-LAMINAR STRAINS			PRINCIPAL STRAINS (ZERO SHEAR)			MAX SHEAR
		NORMAL-1	NORMAL-2	SHEAR-12	SHEAR XZ-MAT	SHEAR YZ-MAT	ANGLE	MAJOR	MINOR		
0	54773	1	-2.73036E-03	6.01791E-04	3.16379E-04	0.0	0.0	87.29	6.09284E-04	-2.73785E-03	3.34713E-03
0	54773	2	-2.78136E-03	5.85692E-04	2.65410E-04	0.0	0.0	87.75	5.90915E-04	-2.78658E-03	3.37749E-03
0	54773	3	-2.83235E-03	5.69594E-04	2.14442E-04	0.0	0.0	88.20	5.72970E-04	-2.83573E-03	3.40870E-03
0	54773	4	-1.24667E-03	-1.08319E-03	-3.43685E-03	0.0	0.0	-46.36	5.55438E-04	-2.88530E-03	3.44073E-03
0	54773	5	5.37396E-04	-2.93435E-03	-1.12505E-04	0.0	0.0	-0.93	5.38307E-04	-2.93526E-03	3.47357E-03
0	54773	6	-1.20126E-03	-1.26279E-03	3.50665E-03	0.0	0.0	44.50	5.21567E-04	-2.98562E-03	3.50719E-03
0	54773	7	-1.26029E-03	-1.27086E-03	3.54155E-03	0.0	0.0	44.91	5.05206E-04	-3.03636E-03	3.54156E-03
0	54773	8	4.89100E-04	-3.08735E-03	4.04007E-05	0.0	0.0	0.32	4.89214E-04	-3.08746E-03	3.57668E-03
0	54773	9	-1.28699E-03	-1.37836E-03	-3.61135E-03	0.0	0.0	-44.28	4.73579E-04	-3.13893E-03	3.61250E-03
0	54773	10	-3.18935E-03	4.56902E-04	-1.42338E-04	0.0	0.0	-88.88	4.58291E-04	-3.19074E-03	3.64903E-03
0	54773	11	-3.24035E-03	4.40803E-04	-1.93306E-04	0.0	0.0	-88.50	4.43339E-04	-3.24288E-03	3.68622E-03
0	54773	12	-3.29134E-03	4.24705E-04	-2.44275E-04	0.0	0.0	-88.12	4.28715E-04	-3.29535E-03	3.72407E-03

Figure 94: Spars ϵ_1 Component Compressive Critical Strain Region 3

Figure 92 shows the maximum X component strain of .0063 in the upper skin captured from the results file. In this case the difference between the plot and the .f06 file comes from the averaging definition within the plotter. The margin of safety for this method of failure is shown below:

$$MS = \frac{\epsilon_{allowable}}{\epsilon_{actual}} - 1 = \frac{.0111(in/in)}{.00628848(in/in)} - 1 = .765$$

3.2.7.2.5 Shear

The shear strains for the spars are presented in Figure 95. The lower spar cap experiences the highest strain in region two and the critical region is shown in Figure 96. The highest loaded areas in the other regions are also presented below.

Patran 2008r1 01-Jul-12 21:51:49
 Fringe: Default, A1:Static Subcase, Strain Tensor, ,XY Component, Maximum,68 of 69 layers

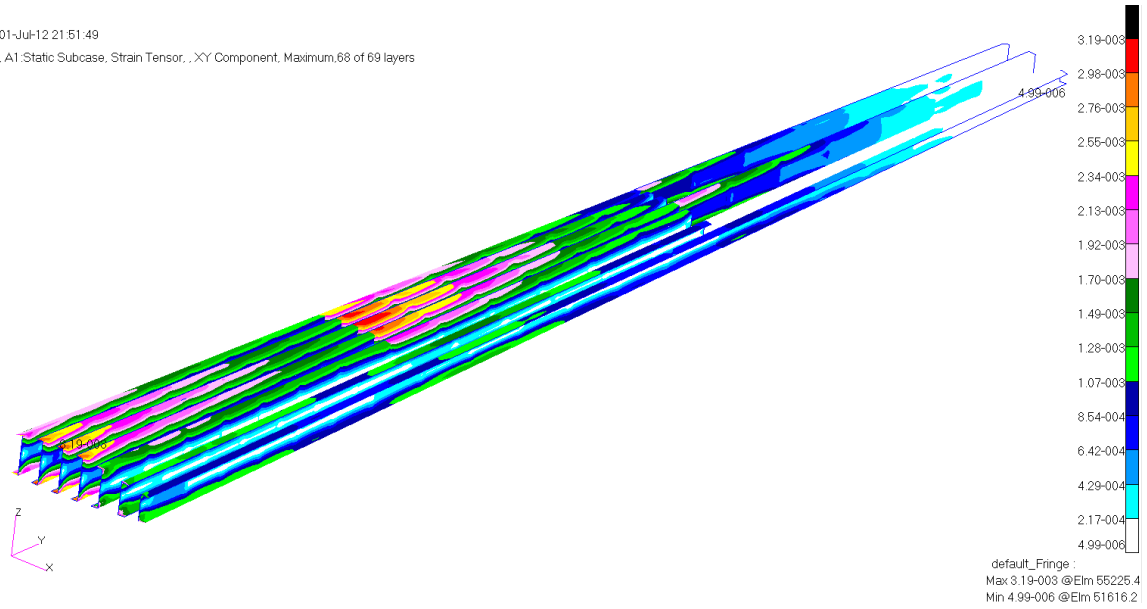


Figure 95: Spars γ_{12} Component Shear Strain Distribution

Patran 2008r1 01-Jul-12 22:02:13
 Fringe: Default, A1:Static Subcase, Strain Tensor, ,XY Component, Maximum,68 of 69 layers

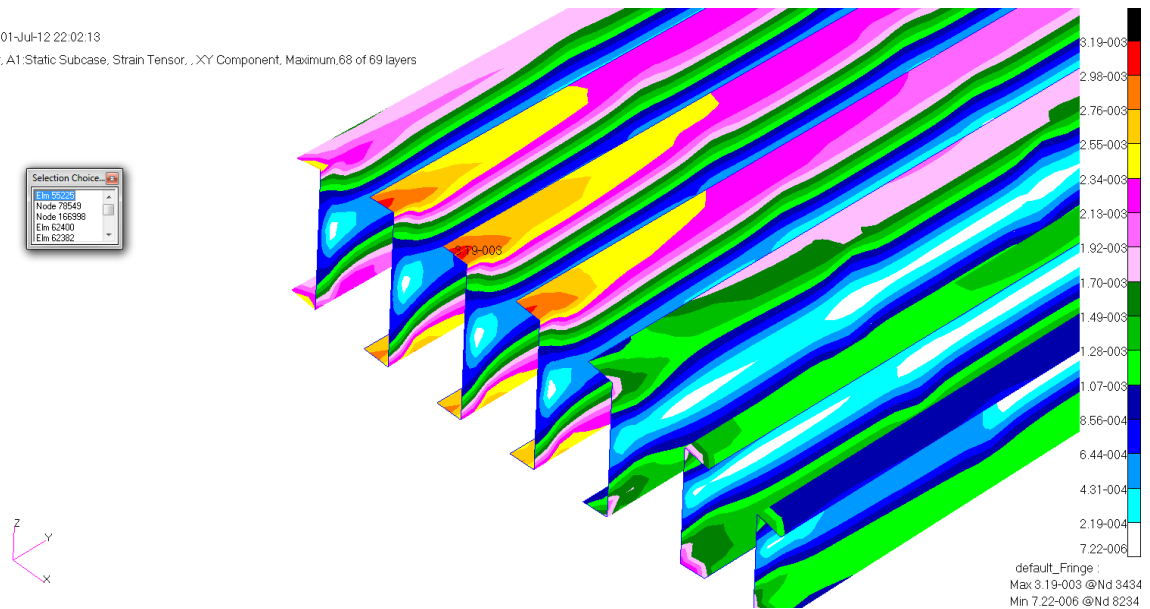


Figure 96: Spars γ_{12} Component Shear Strain Critical Region 1

Patran 2008r1 01-Jul-12 22:02:13
Fringe: Default, A1 Static Subcase, Strain Tensor, .XY Component, Maximum, 68 of 69 layers

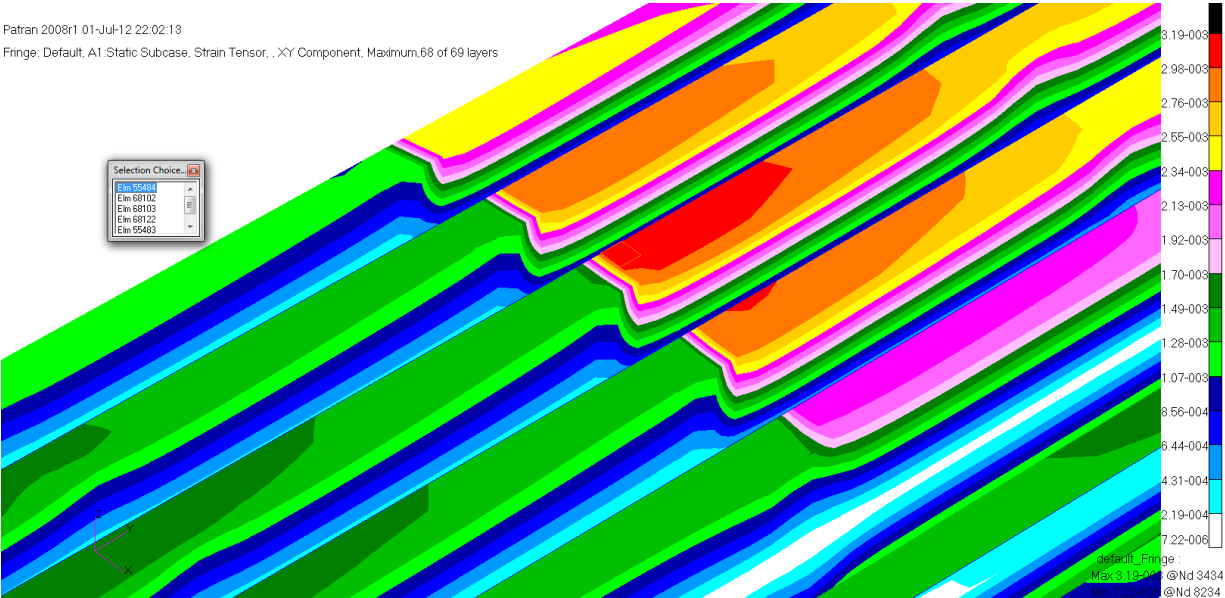


Figure 97: Spars γ_{12} Component Shear Strain Critical Region 2

Patran 2008r1 01-Jul-12 22:02:13
Fringe: Default, A1 Static Subcase, Strain Tensor, .XY Component, Maximum, 68 of 69 layers

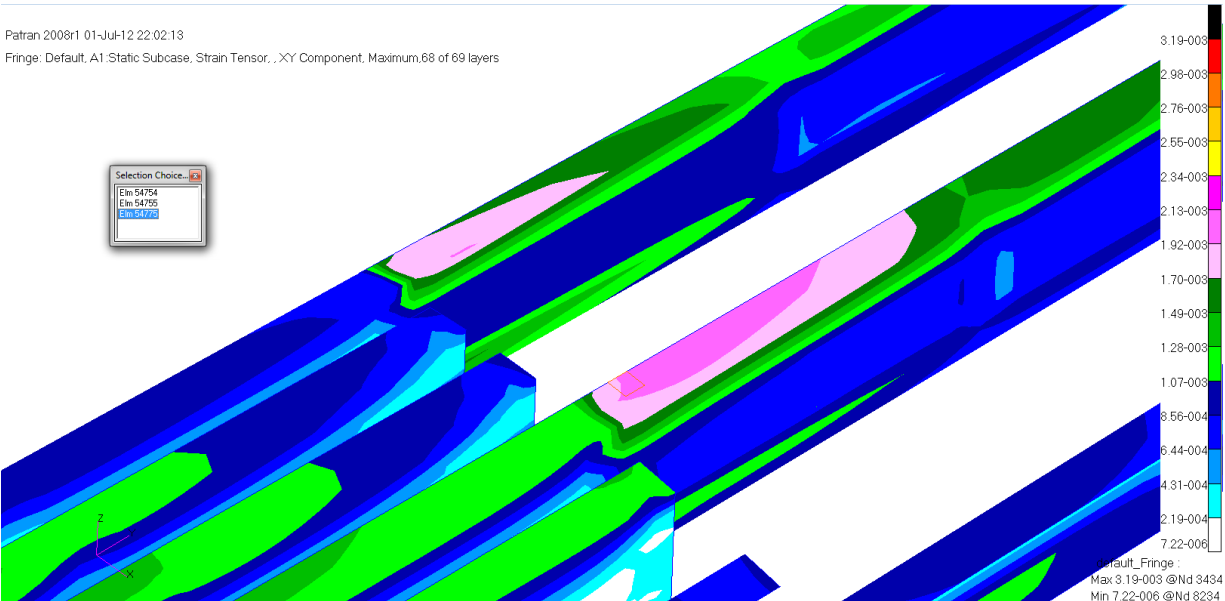


Figure 98: Spars γ_{12} Component Shear Strain Critical Region 3

ELEMENT ID	PLY ID	STRAINS IN LAYERED STRAINS IN FIBER AND MATRIX DIRECTIONS			COMPOSITE ELEMENTS (QUAD4)		PRINCIPAL ANGLE	STRAINS (ZERO SHEAR)		MAX SHEAR	
		NORMAL-1	NORMAL-2	SHEAR-12	INTER-LAMINAR SHEAR XZ-MAT	STRAINS SHEAR YZ-MAT		MAJOR	MINOR		
0	55225	4	-3.76879E-04	-1.52637E-03	-3.39032E-03	0.0	0.0	-35.64	8.38318E-04	-2.74157E-03	3.57988E-03
0	55225	5	-1.53262E-03	-4.17728E-04	3.45702E-03	0.0	0.0	53.94	8.40999E-04	-2.79135E-03	3.63235E-03
0	55225	6	-2.76058E-03	7.63131E-04	-1.08030E-03	0.0	0.0	-81.48	8.44071E-04	-2.84153E-03	3.68560E-03
0	55225	7	-2.81749E-03	7.72928E-04	-1.04571E-03	0.0	0.0	-81.88	8.47520E-04	-2.89208E-03	3.73960E-03
0	55225	8	-2.87439E-03	7.82726E-04	-1.01112E-03	0.0	0.0	-82.27	8.51328E-04	-2.94299E-03	3.79432E-03
0	55225	9	-1.55765E-03	-5.81120E-04	3.72301E-03	0.0	0.0	52.35	8.55480E-04	-2.99425E-03	3.84973E-03

Figure 99: Spars γ_{12} Component Shear Critical Strain Region 1

STRAINS IN LAYERED					COMPOSITE ELEMENTS (QUAD4)						
STRAINS IN FIBER AND MATRIX DIRECTIONS					INTER-LAMINAR		STRAINS PRINCIPAL		STRAINS (ZERO SHEAR)		MAX
ELEMENT	PLY	NORMAL-1	NORMAL-2	SHEAR-12	SHEAR XZ-MAT	SHEAR YZ-MAT	ANGLE	MAJOR	MINOR	SHEAR	
ID	ID										
0	55484	15	-4.40778E-03	1.63780E-03	1.61163E-04	0.0	0.0	89.24	1.63887E-03	-4.40886E-03	6.04773E-03
0	55484	16	-4.41768E-03	1.62864E-03	1.12233E-04	0.0	0.0	89.47	1.62916E-03	-4.41820E-03	6.04736E-03
0	55484	17	-1.37240E-03	-1.43570E-03	6.04705E-03	0.0	0.0	44.70	1.61964E-03	-4.42774E-03	6.04738E-03
0	55484	18	1.61031E-03	-4.43747E-03	-1.43741E-05	0.0	0.0	-0.07	1.61032E-03	-4.43748E-03	6.04780E-03
0	55484	19	-1.40583E-03	-1.44038E-03	-6.04852E-03	0.0	0.0	-44.84	1.60120E-03	-4.44742E-03	6.04862E-03
0	55484	20	-4.45726E-03	1.59199E-03	-8.34853E-05	0.0	0.0	-89.60	1.59228E-03	-4.45755E-03	6.04983E-03
0	55484	21	-4.46716E-03	1.58283E-03	-1.32415E-04	0.0	0.0	-89.37	1.58356E-03	-4.46789E-03	6.05144E-03
0	55484	22	-4.47706E-03	1.57367E-03	-1.81345E-04	0.0	0.0	-89.14	1.57503E-03	-4.47842E-03	6.05345E-03
0	55484	23	-1.34608E-03	-1.57636E-03	-6.05147E-03	0.0	0.0	-43.91	1.56670E-03	-4.48914E-03	6.05585E-03
0	55484	24	-1.61035E-03	-1.33115E-03	6.05220E-03	0.0	0.0	46.32	1.55857E-03	-4.50007E-03	6.05864E-03
0	55484	25	-4.50675E-03	1.54619E-03	-3.28134E-04	0.0	0.0	-88.45	1.55064E-03	-4.51119E-03	6.06183E-03
0	55484	26	-4.51664E-03	1.53703E-03	-3.77063E-04	0.0	0.0	-88.22	1.54290E-03	-4.52251E-03	6.06541E-03
0	55484	27	-4.52654E-03	1.52787E-03	-4.25993E-04	0.0	0.0	-87.99	1.53536E-03	-4.53402E-03	6.06938E-03
0	55484	28	-1.74632E-03	-1.27140E-03	6.05515E-03	0.0	0.0	47.24	1.52801E-03	-4.54573E-03	6.07374E-03
0	55484	29	-1.25646E-03	-1.78032E-03	-6.05588E-03	0.0	0.0	-42.53	1.52086E-03	-4.55764E-03	6.07850E-03
0	55484	30	-4.55623E-03	1.50039E-03	-5.72782E-04	0.0	0.0	-87.30	1.51390E-03	-4.56974E-03	6.08364E-03

Figure 100: Spars γ_{12} Component Shear Critical Strain Region 2

STRAINS IN LAYERED					COMPOSITE ELEMENTS (QUAD4)								
		STRAINS IN FIBER AND MATRIX DIRECTIONS			INTER-LAMINAR		STRAINS	PRINCIPAL	STRAINS (ZERO SHEAR)		MAX		
ELEMENT	PLY	NORMAL-1	NORMAL-2	SHEAR-12	SHEAR XZ-MAT	SHEAR YZ-MAT	ANGLE	MAJOR	MINOR				
0	54775	1	-3.19499E-03	9.36539E-04	6.64355E-04	0.0	0.0	85.43	9.63076E-04	-3.22152E-03	4.18460E-03		
0	54775	2	-3.17675E-03	9.15636E-04	6.39135E-04	0.0	0.0	85.56	9.40440E-04	-3.20155E-03	4.14199E-03		
0	54775	3	-3.15851E-03	8.94733E-04	6.13915E-04	0.0	0.0	85.69	9.17847E-04	-3.18162E-03	4.09947E-03		
0	54775	4	-1.42757E-03	-8.38871E-04	-4.01410E-03	0.0	0.0	-49.17	8.95299E-04	-3.16174E-03	4.05703E-03		
0	54775	5	8.52926E-04	-3.12203E-03	-5.63476E-04	0.0	0.0	-4.03	8.72796E-04	-3.14190E-03	4.01469E-03		
0	54775	6	-8.66754E-04	-1.40501E-03	8.93581E-03	0.0	0.0	41.11	8.50341E-04	-3.12211E-03	3.97245E-03		
0	54775	7	-8.80696E-04	-1.39373E-03	3.89667E-03	0.0	0.0	41.25	8.27934E-04	-3.10236E-03	3.93030E-03		
0	54775	8	7.90217E-04	-3.06731E-03	-4.87816E-04	0.0	0.0	-3.60	8.05578E-04	-3.08267E-03	3.88825E-03		
0	54775	9	-1.37118E-03	-9.08579E-04	-3.81838E-03	0.0	0.0	-48.45	7.83273E-04	-3.06303E-03	3.84630E-03		
0	54775	10	-3.03083E-03	7.48410E-04	4.37376E-04	0.0	0.0	86.70	7.61023E-04	-3.04344E-03	3.80446E-03		
0	54775	11	-3.01259E-03	7.27507E-04	4.12157E-04	0.0	0.0	86.86	7.38828E-04	-3.02391E-03	3.76274E-03		
0	54775	12	-2.99435E-03	7.06604E-04	3.86937E-04	0.0	0.0	87.02	7.16690E-04	-3.00444E-03	3.72113E-03		

Figure 101: Spars γ_{12} Component Shear Critical Strain Region 3

Figure 99 shows the maximum γ_{12} shear strain of .00372 in the upper skin captured from the results file. The margin of safety for this method of failure is shown below:

$$MS = \frac{\gamma_{allowable}}{\gamma_{actual}} - 1 = \frac{.0292(in/in)}{.00606(in/in)} - 1 = 5.580$$

3.2.8 Summary of problem

In summary a representative UAV was imagined and design characteristics of the aircraft were selected. The selection of an aircraft also resulted in cruise altitude and airspeeds being selected. These airspeeds were used to adjust and scale previous aerodynamic pressure distributions for a similar fairing such that they are applicable to the proposed array and aircraft. A fairing mounted below the wing, such as that shown in Figure 102, will extend and flex as the wing curves under positive G's. Thus to size the fairing structure, which is the primary focus of this thesis, it was necessary to model and develop a range of deflections and curvatures for the representative aircraft wing. Three wing designs were investigated and the design with the largest curvature was used to size the fairing structure. This approach recognizes a limitation in the preliminary wing sizing, with the likely outcome of an artificially high stiffness resulting from structures with high positive margins of safety. Optimal wing structures would have low margins of safety, and thus the wing curvatures would be higher. Curvatures and displacements presented in this section however, are believed to be a reasonable approximation in the root section of the representative aircraft, where the fairing is assumed to be located. In addition, overall tip displacements appear to agree with those referenced for the representative aircraft [20]. Next in Section 3.3 the geometry of the fairing is introduced. Section 3.4 details the finite element model and also introduces the glass composite and metallic materials used. Section 3.5 details the stress and critical margins in each of the designed structures as well as the buckling characteristics of the structure. Section 3.6 shows the fasteners required to hold the structure together. Section 3.7 shows a modal analysis of the structure and compares it to hypothetical sources of vibration.

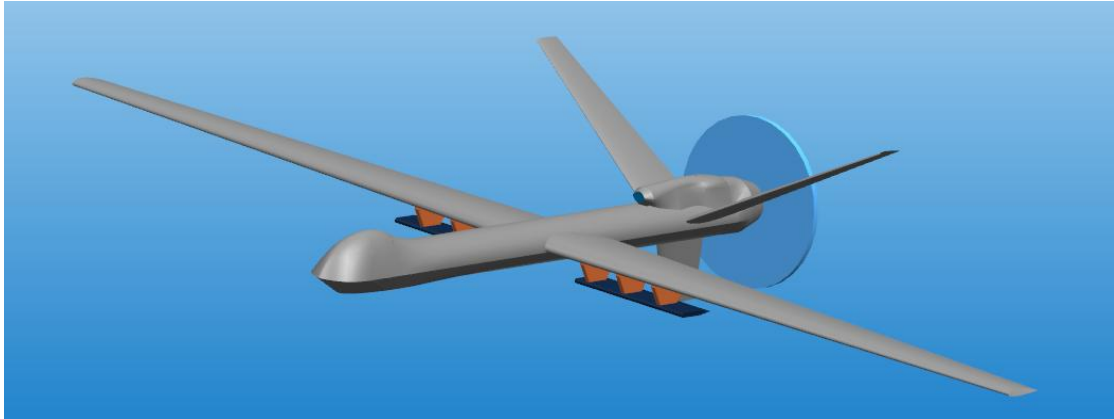


Figure 102: Array on Representative UAV

3.3 Geometry

This section details the geometry of the fairing used to carry the MCoRDs array for the representative UAV. Each component of the array is presented separately for clarity. A view of the design with transparent upper skins is shown in Figure 103. The three antennas it is designed to carry can be seen in red. The total weight of the pylon and fairing structure was found to be 85.7 lbs. Two are mounted on the aircraft for a total added weight of 171.4 lbs.

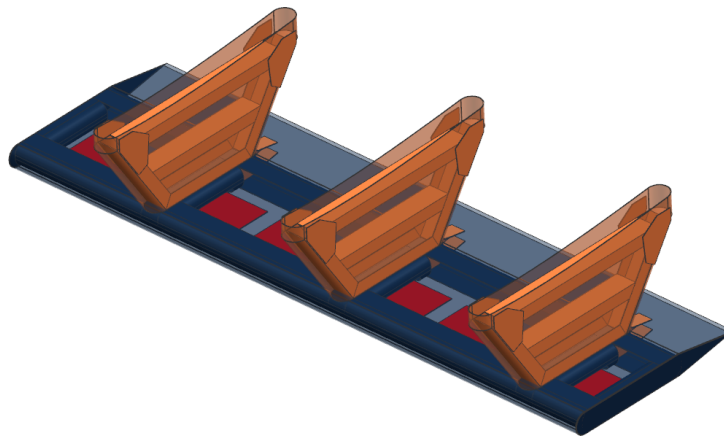


Figure 103: Transparent Upper Skin Reveals Internal Antenna Elements and Ribs

Figure 104 shows the skins for the fairing structure. The images in this section are color coded so that metallic structure is orange and composite structure is blue. The pylon skins are made of 2024-T3 aluminum that is .032" thick.

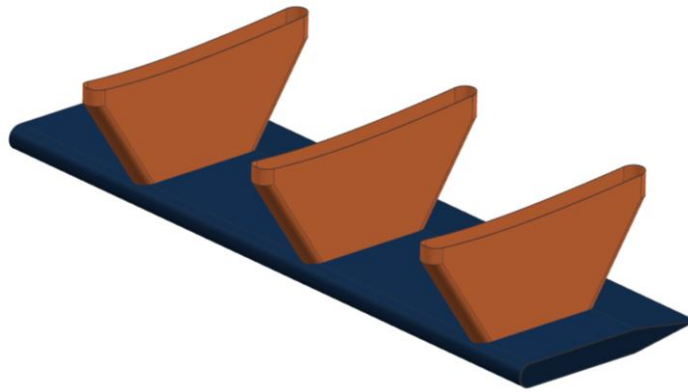


Figure 104: Fairing Skins

The fairing skins are glass composite and are split into four sections. These skin sections are identified in Figure 105.

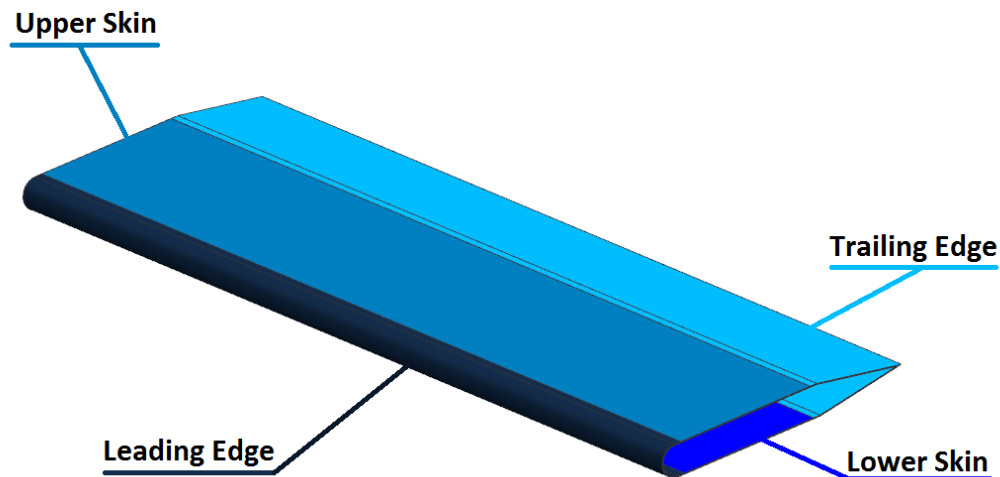


Figure 105: Fairing Skin Sections

The composite layups emphasize damage tolerance in the leading edge which is the surface most likely to be hit during flight. The upper, lower, and trailing edge skins emphasized getting as much bending stiffness as possible out of the skin at the expense of damage tolerance. This was deemed acceptable since they are protected by the leading edge. If the an array was to be fielded with a crew more likely to drop tools and other items on the array the design philosophy of these skins would need to change and additional layers of composite would be needed to

protect the structure. The leading edge of the fairing is made of 8 layers of ACG 6781 S-2 glass composite. This makes the structure 0.081 inches thick. The layup for the composite is $[-45, 0, 0, 45]_s$. The design for the leading edge is a circular leading edge that flattens to allow it to be fastened to the forward spar. The trailing edge is made of 13 layers of ACG 6781 S-2 glass composite which makes the part 0.131 inches thick. The layup for the trailing edge is $[0, 0, 0, -45, 45, 0, 0]_{os}$. This skin is fastened into the aft spar. The upper skin is made of 8 layers of ACG 6781 S-2 glass composite resulting in a skin that is 0.081 inches thick. The layup for the composite is $[-45, 0, 0, 45]_s$. In between the pylons Rohacell 71 core is used increase the flexural stiffness of the skins. The skin is fastened to the forward and aft spars. The lower skin is made of 10 layers of ACG 6781 S-2 glass composite resulting in a skin that is 0.101 inches thick. At the rib attachment points additional bearing strength is needed so the structure is padded up to 17 layers. The layup for the skin is $[0\ 0\ -45\ 45\ 0]_s$ which then pads up to $[0\ 0\ -45\ 45\ 0\ 0\ 45\ -45\ 0]_s$. The order of the ply drops is shown in Table 22.

Table 22: Lower Skin Ply Drops from Pad Up

Pad Up	Ply Drops							Lower Skin	Drop Order
0	0	0	0	0	0	0	0	0	
0	0	0	0	0	0	0	0	0	
-45	-45	-45	-45	-45	-45	-45	-45	-45	
+45	+45	+45	+45	+45	+45	+45	+45	+45	
0	0	0	0	0	0				5
0	0	0	0	0	0	0	0	0	
+45	+45								1
-45	-45	-45	-45	-45					4
0	0	0	0	0	0	0	0		7
-45	-45	-45	-45						3
+45	+45	+45							2
0	0	0	0	0	0	0	0	0	
0	0	0	0	0	0	0			6
+45	+45	+45	+45	+45	+45	+45	+45	+45	
-45	-45	-45	-45	-45	-45	-45	-45	-45	
0	0	0	0	0	0	0	0	0	
0	0	0	0	0	0	0	0	0	

The substructure of the pylons and array are shown in Figure 106. This provides the primary load paths throughout the array. The loads along the array are transferred into the two spars. One runs down the front and one down the back of the array. Loads are transferred into the ribs through the rib inserts. The ribs are located beneath all three pylons, but must bridge the center area of the lower skin in order to cross the antenna elements. The ribs transfer their load into the pylon substructures which are attached to the aircraft via 12 attachment plates.

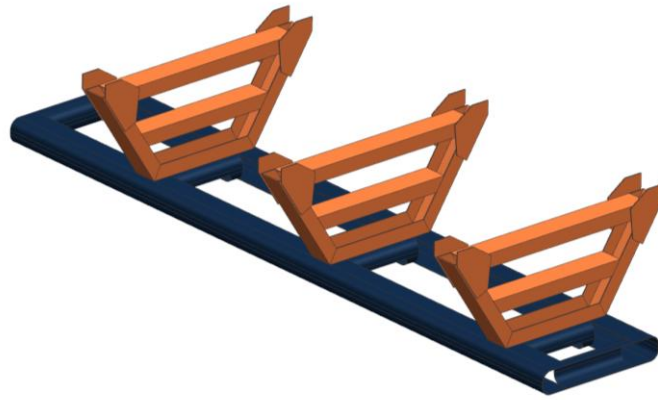


Figure 106: Fairing Structure

To attach the fairing to the aircraft attachment plates are used as can be seen in Figure 107. These interface directly into the rib and spar structure of the metallic pylons. These are made of 0.125 inch thick 7075-T6 Aluminum. At each of the hardpoint locations there are two forward and two aft attachment points for a total of 12 attachment locations. This is consistent with an assumption that existing hardpoints on these aircraft are likely to be single clevis pins to which the fairings will attach via the double clevis formed by each pair of attachment plates.

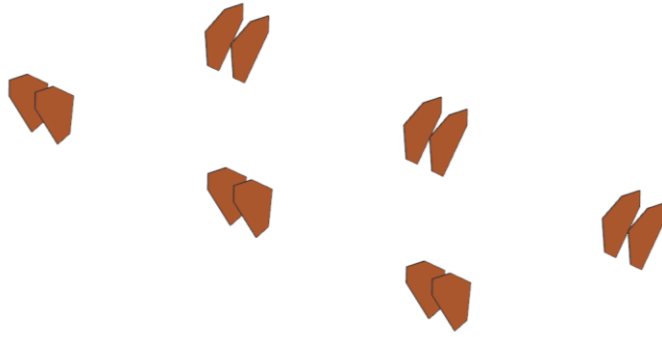


Figure 107: Attachment Plates

The pylons consist of two aluminum closeout ribs with an additional center rib to prevent the aluminum skins from buckling. Forward and aft spars extend the full span of the pylon to connect to the fairing structure. All of these components are made of 0.063 2024 T-3 extrusions. 0.063 2024 T3 aluminum gussets connect the bottom closeout rib and the spars. The rib and spar structure are U-channel structures attached via plates bolted on the inside of the structure. The structure is shown in Figure 108.

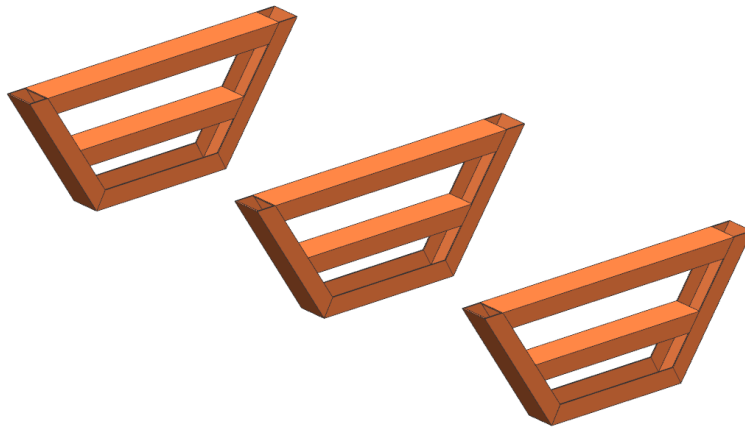


Figure 108: Pylon Substructure

Three of the fairing ribs sit right below the pylon substructure. The others are at the ends of the array and are used to attach the upper and lower skins. To conserve the cost of tooling these will have an identical cross-sectional geometry as spars, but will have a lower cap section cut out to allow antennas to slide underneath. The curved cross section of these ribs make them

unsuitable to be an aerodynamic close out rib. To leave room for an aerodynamic closeout the ribs on the end of the fairing are positioned with the C facing inward. These act as the structural ribs but a closeout rib will be needed for aerodynamic reasons. They are made of 15 layers of ACG 6781 S-2 glass composite resulting in a rib that is 0.152 inches thick. They layup for the ribs is $[-45, 0, 0, 45, 0, 0, -45, 0]_{os}$.

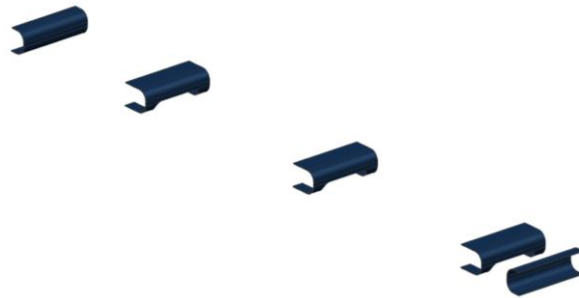


Figure 109: Fairing Ribs

The fairing rib inserts rest inside the ribs and extend forward into the spars. The inserts can be seen in Figure 110 and their interaction with the spars and ribs can be seen in Figure 111. These are made of 0.25 inch thick 6061-T651 square tubing. These are fastened and form a connection between the spars, ribs, and pylon substructure. Although full metallic ribs would disrupt the antenna array performance since they bridge the antenna elements, these metallic inserts are required to carry the fairing-pylon interaction loads. The inserts are forward and aft of the antenna element, and only the glass/epoxy rib crosses the antenna element.

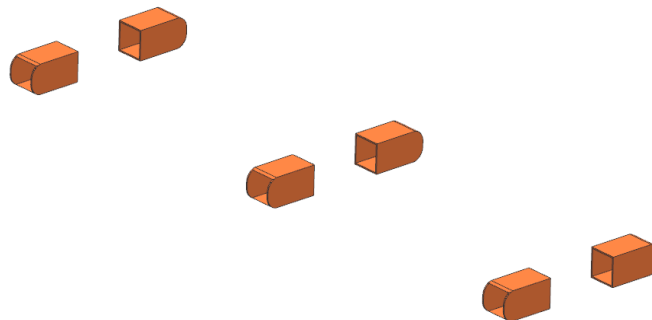


Figure 110: Fairing Rib Inserts

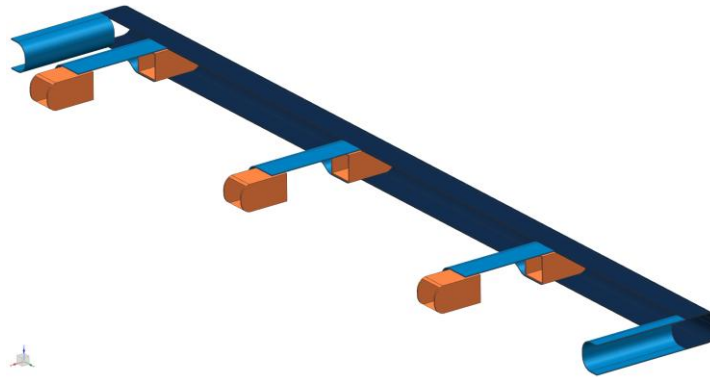


Figure 111: Rib Insert, Spar, and Rib Interaction

The spars are shown in Figure 112 and are made of 15 layers of ACG 6781 S-2 glass composite resulting in a spar that is 0.152 inches thick. These are fastened to the upper and lower skins and the fairing rib inserts.



Figure 112: Fairing Spars

The last structures presented are the trailing edge ribs which can be seen in Figure 113. These are located at the same wing station as the ribs which are at the pylon locations. These prevent the trailing edge skin from buckling and are made of 0.072 thick 2024 T-3 aluminum. These ribs are extremely thick for buckling reasons. Dropping thickness here results in buckling before the desired load. An alternative approach would be to add thickness to the trailing edge

fairing skin. Doing so would likely add weight to the structure but the thickness added could be a protective angled ply which would improve the damage tolerance.

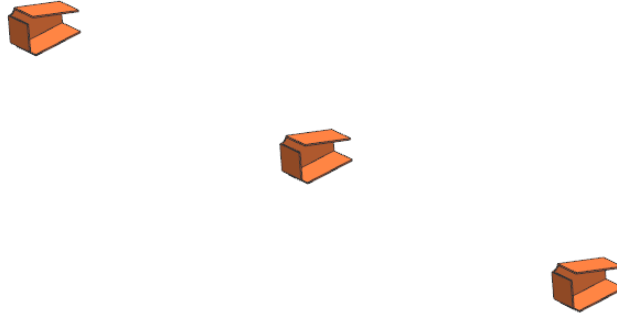


Figure 113: Trailing Edge Ribs

3.4 **FEM Model**

3.4.1 **External Loads**

There are three primary external loads applied to the fairing. The first is the aerodynamic loads. These are applied as local pressures. At an angle of attack of zero this structure would result in a predominately global drag load since the structure is symmetric and generates no lift at. The load case tested includes a five degree angle of attack so the structure generates lift. These loads were defined by the aerodynamic study in reference 22 and as previously stated these loads were then reduced based on the dynamic pressure at the flight conditions of the array. To apply the load 17 pressure regions were developed for load boundaries. These are shown in Figure 264 through Figure 280 in Appendix A. An additional total load was applied uniformly to the entire model to adjust the total applied load to the expected values in Table 23. This correction is necessary because of the slight variations between the orientations of the discretized geometry and finite element model versus the 3D solid geometry used to develop the pressure distributions. The loads applied in this section differ from the curvature model in that they are now limit loads instead of ultimate loads. This means that the factor of safety must now be applied in the safety calculation. The reason for this change is that margin is not the same across all of the structures due to the NASA guidelines. A margin of safety of 3.0 was applied to composite structures and 2.25 was applied to metallic structures.

Table 23: Aerodynamic Loads for Each Array

Aerodynamic Loads	
Side Force	200 lbs
Lift	1820 lbs
Drag	660 lbs

The second primary external load is the induced load from the wing flexure. As the wing flexes under load it extends and flexes the attached array beneath it, and also flexes the pylon mounts. This load has been greatly discussed above and the amount of curvature was based on the 7 spar representative wing in Section 3.2.

The third external load was the thermally induced load. In cyrospheric climates the air temperature can be extremely cold and this affects the structure. The assumed zero strain condition for the wing is the standard atmosphere ground temperature of 77°F. The applied temperature to the aircraft was -75°F. This is a total temperature change of 152°F. This shrinks the structure and directly opposes the wing curvature which is attempting to stretch out the structure. The structure must also endure a high temperature environment if it is to survive flying from the NASA Dryden flight facility in the California desert. Fortunately the expansion effect on the structure should be a reliving force in the air. It is worth noting that the material properties of the structure also are very different at different temperatures. The lower temperature properties of the material have a higher specific strength and stiffness. Conversely the high temperature and high moisture properties are much poorer than the room temperature properties. These reduced properties at high temperature could easily have a larger effect than the relieving strains from thermal expansion. The analysis presented applied the standard room temperature properties and did not take advantage of the higher strength at lower temperature but it is recommended to examine the effects temperature has in greater detail before installing a real world fairing.

Another load considered was an inertial load but this load was found to reduce stress in the primary structure. The inertial load pulls the structure down and back together. This opposes the curve of the wing. In future final sizing its recommended to look at this load again

for some of the attachment structure but for all of the skins examined this load was found to be relieving. If a 3.95g dive maneuver was performed and then pulled out of the inertial load would drop off faster than the wing curvature. This lag would cause the structure to see the load case presented and for this reason the inertial load was not included.

3.4.2 Material Properties

The material properties used in the structure are presented in Tables 22-28. The structures for which these materials are used can be found in Section 3.3. The properties for the S-2 glass have been reduced to account for the inclusion of fasteners, countersinks, and edge distances in the same way that was applied in previous NASA fairing installations [22].

Table 24: 2024-T351 Aluminum Extrusion [22]

E	10800	ksi
E^C	11000	ksi
G	4100	ksi
ρ	0.1	lb/in ³
ν	0.33	~
F_{tu}	61	ksi
F_{su}	31	ksi

Table 25: 2024-T3 Aluminum Sheet, RT, QQ-A-250/4 [22]

E	10500	ksi
E^C	10700	ksi
G	4000	ksi
ρ	0.1	lb/in ³
ν	0.33	~
F_{tu}	65	ksi
F_{su}	40	ksi

Table 26: 6061-T6 Aluminum Extrusion, RT, QQ-A-200/3 [22]

E	9900	ksi
E^C	10100	ksi
G	3800	ksi
ρ	0.1	lb/in ³
ν	0.33	~
F_{tu}	41	ksi
F_{ty}	38	ksi
F_{cy}	37	ksi
F_{su}	26	ksi

Table 27: ACG S-2 Glass 6781/MTM45-1 [22]

	-64F, Dry	75F, RTD	180F, Wet	
E_1^T	4320	4220	3900	ksi
E_1^C	4350	4220	4090	ksi
E_2^T	4140	4070	3770	ksi
E_2^C	4240	4020	3940	ksi
G_{12}	710	550	340	ksi
ν_{12}	0.14	0.14	0.12	~
t_{nom}	0.0101	0.0101	0.0101	in
α_1	0.000009	0.000009	0.000009	in / in / °F
α_2	0.000009	0.000009	0.000009	in / in / °F
ρ	0.0650	0.0650	0.0650	lb _f / in ³
F_1^T	38.9	32.1	24.4	ksi
F_1^C	37.0	37.0	26.3	ksi
F_2^T	38.0	30.8	20.1	ksi
F_2^C	31.6	31.6	20.1	ksi
F_{12}	12.3	9.2	5.6	ksi

Table 28: Rohacell 71 IG Properties [22]

E	13.34	ksi
G	4.205	ksi
ρ	0.0027	lb/in ³
F_{tu}	0.406	ksi
F_{cu}	0.218	ksi
F_{su}	0.189	ksi

Table 29: 7075-T651 Aluminum Plate [22]

E	10300	ksi
E^C	10600	ksi
G	3900	ksi
ρ	0.101	lb/in ³
ν	0.33	~
F_{tu}	79	ksi
F_{ty}	70	ksi
F_{cy}	70	ksi
F_{su}	45	ksi

Table 30: AN Bolt Allowables [22]

	AN3	AN4	
Ultimate Tensile Strength	2210	4080	lbs
Single Lap Shear Strength	2125	3680	lbs

3.4.3 Elements and Boundary Conditions

The pylon and fairing skins, spars and attachment plates are expected to undergo axial, shear and flexural stress so these were modeled as 2D shell elements. All of these elements were modeled as quad elements when possible while paying attention to element angles and aspect ratios. If necessary, triangular elements were used. The attachment bolts to the aircraft skins were modeled as 1D beam elements since they are expected to undergo axial and flexural loads.

The only bolted that were simulated like this were the ones which connect the fairing to the simulated wing. This does induce extreme stress concentrations on the node where the beam is attached but it also simulates the way the fairing interacts with the wing attachments. The false stress concentrations that this method induced are known and accounted for. The model contains 58,820 CQUAD4 elements, 64 CTRIA3 elements, and 12 CBAR elements. This results in an estimated 244,590 degrees of freedom.

The boundary conditions for the fairing are shown in Figure 114. To simulate the attachment to the wing a dummy wing was created above the pylon. This dummy wing is used to simulate actual boundary conditions by imposing local displacements and rotations consistent with those discovered from the wing curvature model. The stiffness of this dummy wing was based upon the wing in reference 22. Since the wing of the representative aircraft is assumed to be a composite wing this stiffness was increased.

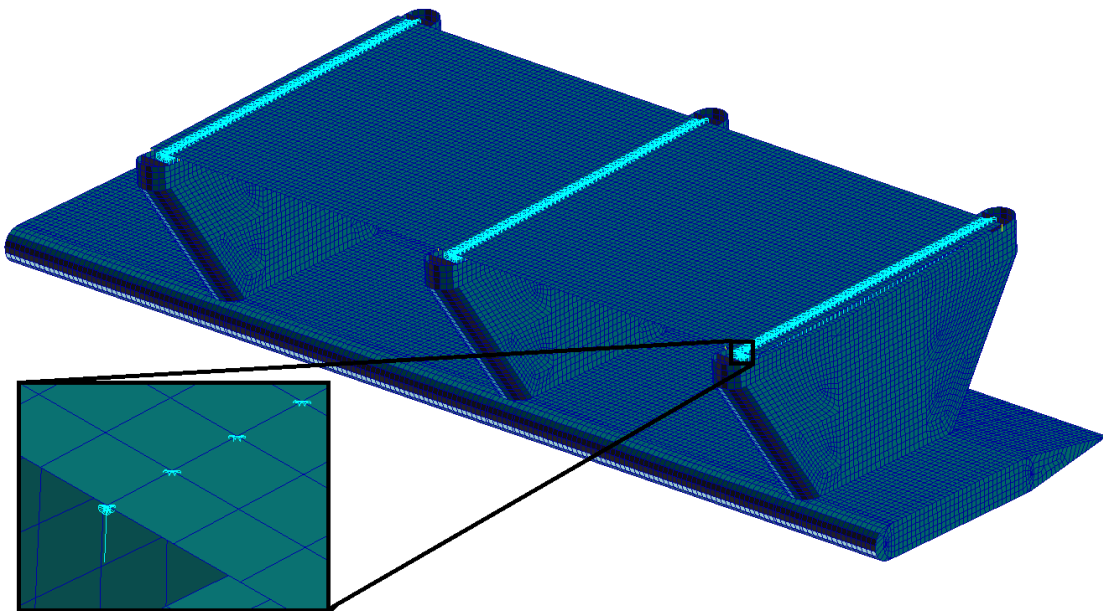


Figure 114: Fairing Boundary Conditions

3.4.4 Model Verification

Before sizing each of the fairing components it is important to verify the accuracy of the FEM model. The first thing checked is that the loads match the expected applied loads. The applied loads are shown in Figure 115. These match the aerodynamic loads from Table 23 nearly exactly.

```

*** USER INFORMATION MESSAGE 7310 (VECPRN)
    ORIGIN OF SUPERELEMENT BASIC COORDINATE SYSTEM WILL BE USED AS REFERENCE LOCATION.
    RESULTANTS ABOUT ORIGIN OF SUPERELEMENT BASIC COORDINATE SYSTEM IN SUPERELEMENT BASIC SYSTEM COORDINATES.
0
SUBCASE/   LOAD      T1      T2      T3      R1      R2      R3
DAREA ID  TYPE
0          1      FX      FY      FZ      MX      MY      MZ
              6.600001E+02  -2.000000E+02  -1.820000E+03  -1.319100E+05  5.079887E+05  -5.570593E+04
              0.000000E+00  0.000000E+00  0.000000E+00  0.000000E+00  0.000000E+00  0.000000E+00
              TOTALS  6.600001E+02  -2.000000E+02  -1.820000E+03  -1.232251E+05  5.310419E+05  -1.050574E+05
1  MSC.NASTRAN JOB CREATED ON 18-OCT-11 AT 17:06:04  MARCH 4, 2012  HD NASTRAN 5/ 9/08  PAGE 9

```

Figure 115: Applied Loads

Next the displacements of the structure were checked. This is plotted in Figure 116. The forced deflection of the wing dominates the displacement results as expected. The results fall within the expectations for the structure and add credibility to the model. A unit displacement check was also done and no errors were found. The results are shown in Figure 117 through Figure 119.

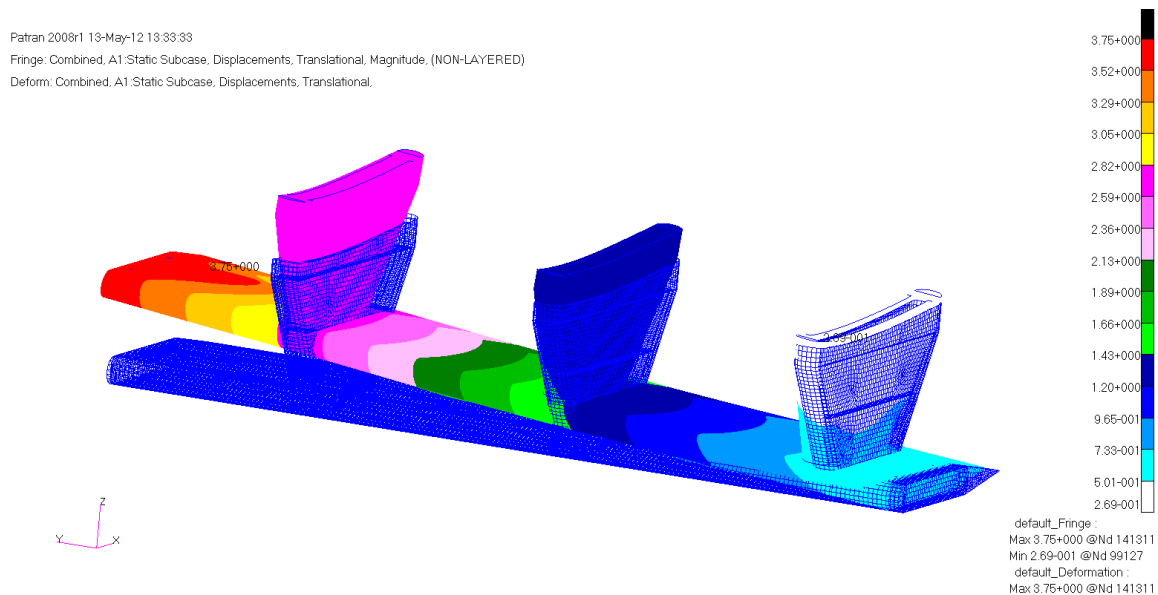


Figure 116: Displacement of the Fairing and Pylons

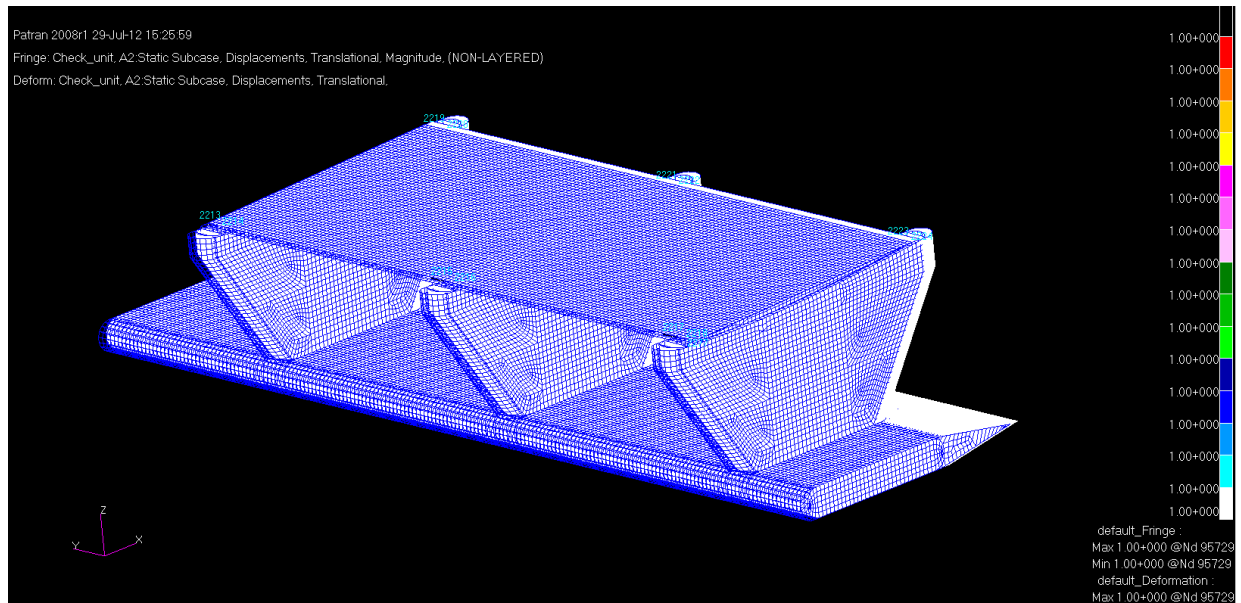


Figure 117: Fairing X Unit Displacement Check

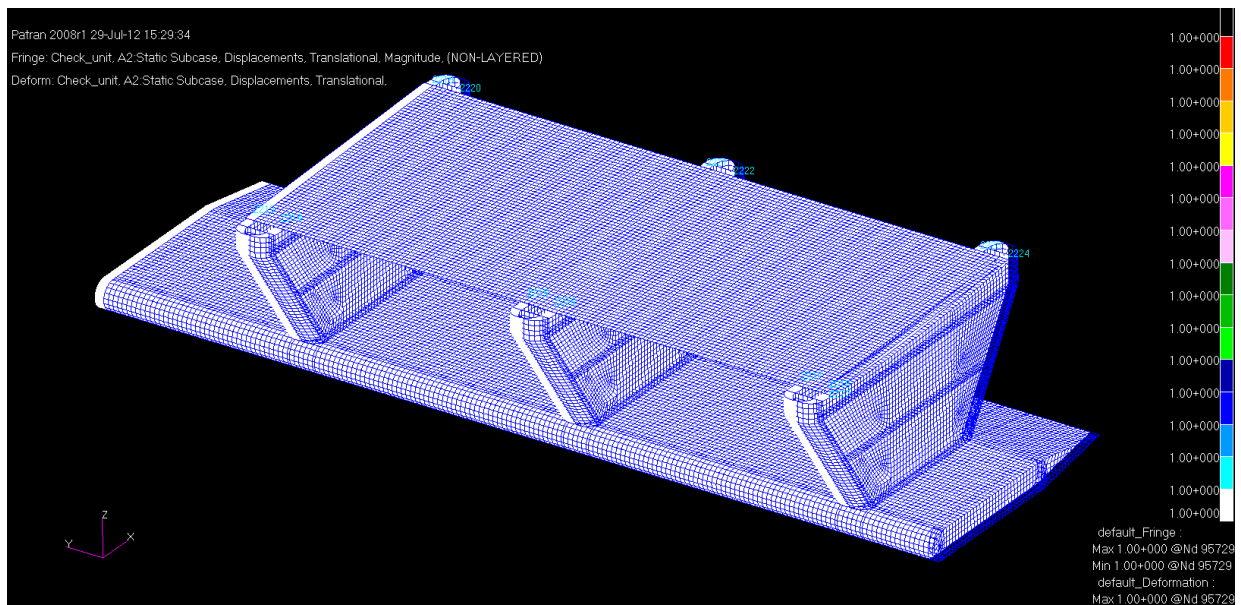


Figure 118: Fairing Y Unit Displacement Check

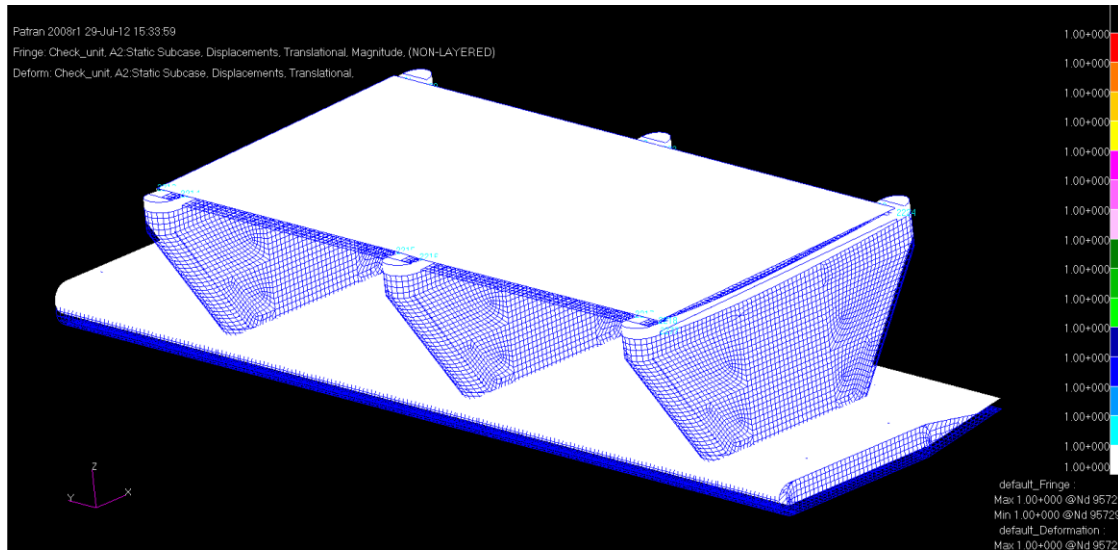


Figure 119: Fairing Z Unit Displacement Check

Next the epsilon value for the FEA model was checked. This value is the error in strain energy norm of the finite element model. This error should be small and any values greater than 0.001 should bring the results of the model into question. Since this value shown in Figure 120 is low this verification check is passed.

```

*** USER INFORMATION MESSAGE 5293 (SSG3A)
FOR DATA BLOCK KLL
LOAD SEQ. NO. 1
Epsilon -1.4205370E-15
EXTERNAL WORK 1.2266966E+08
EPSILONS LARGER THAN 0.001 ARE FLAGGED WITH ASTERISKS
1 MSC.NASTRAN JOB CREATED ON 18-OCT-11 AT 17:06:04
MARCH 4, 2012 MD NASTRAN 5/ 9/08 PAGE 18

```

Figure 120: Epsilon Verification

The model contains 244,590 degrees of freedom which for its size indicates that the model is properly discretized. This judgment is based upon my previous experience with FEA models of this size. However a convergence study would add value to the model since several of the stress concentrations are due to local effects induced by the pylon-fairing interactions. More information on the convergence of this concentrations would be beneficial but the current model is more than sufficient. With that in mind the finite element model is well-behaved and passes all of verification checks.

3.5 Sizing

The results of the sizing analysis are presented component by component with the exception of the buckling results which are presented first. The critical margins for all of the components are presented in Table 31.

Table 31: Critical Margins by Component

Structure	Failure Type	Margin
Upper Skin	Buckling	0.277
Lower Skin	Tensile on Axis	0.026
Ribs	Tensile on Axis	.715
Spars	Tensile off Axis	0.085
Rib Inserts	Tensile	0.279
Pylon Spars/ Ribs	Tensile	0.071
Pylon Skin	Buckling	0.089
Trailing Edge	Buckling	0.007
Pylon Plate	Shear	0.221
Trailing Edge Ribs	Tensile	.797

3.5.1 Buckling Analysis

Figure 121 through Figure 126 show the first six buckling locations in order of load factor.

Metallic structures were not allowed to buckle until a load factor of 2.25 and composite structures were limited to a load factor of 3.0. These values were based upon the NASA requirements for the previous array which can be found in reference 22. These requirements resulted in the trailing edge ribs being added and were the critical margins of safety for the upper skin of the fairing, the trailing edge skin, and the pylon skins of the structure.

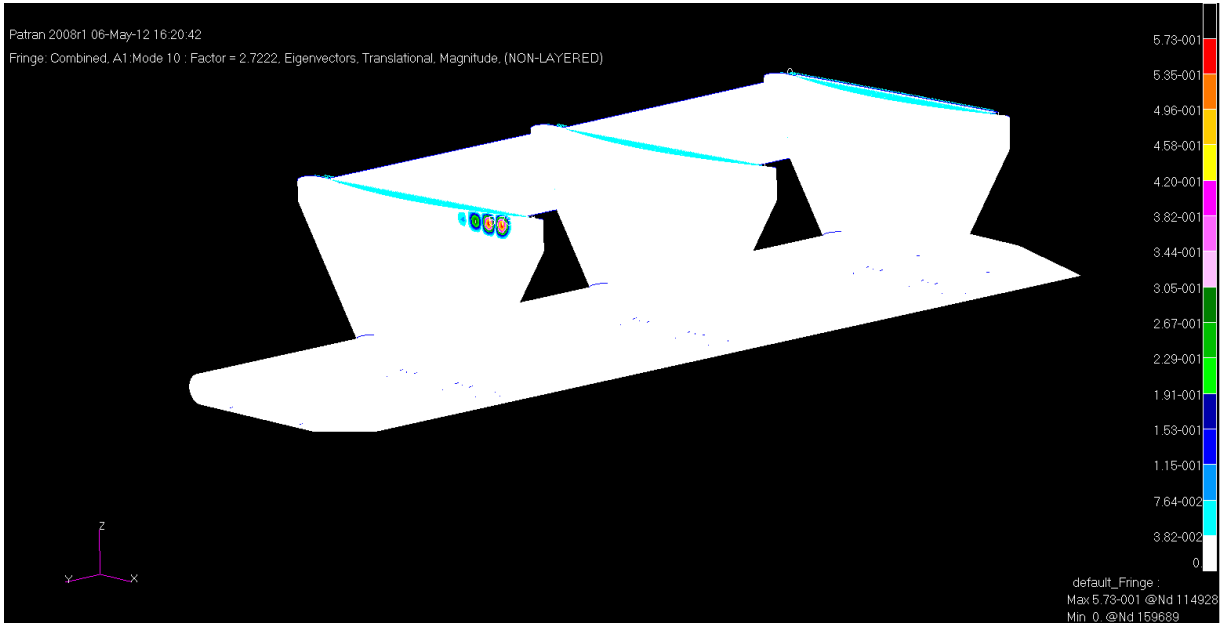


Figure 121: First Mode Buckling at Buckling Factor of 2.72

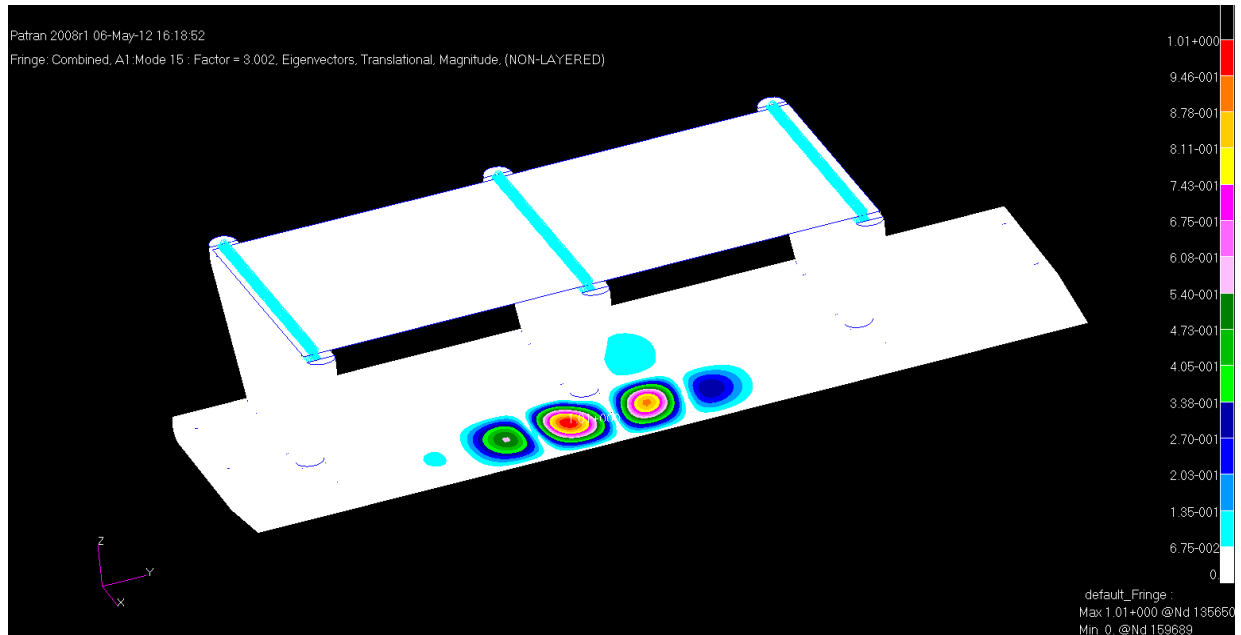


Figure 122: Second Mode Buckling at Load Factor of 3.002

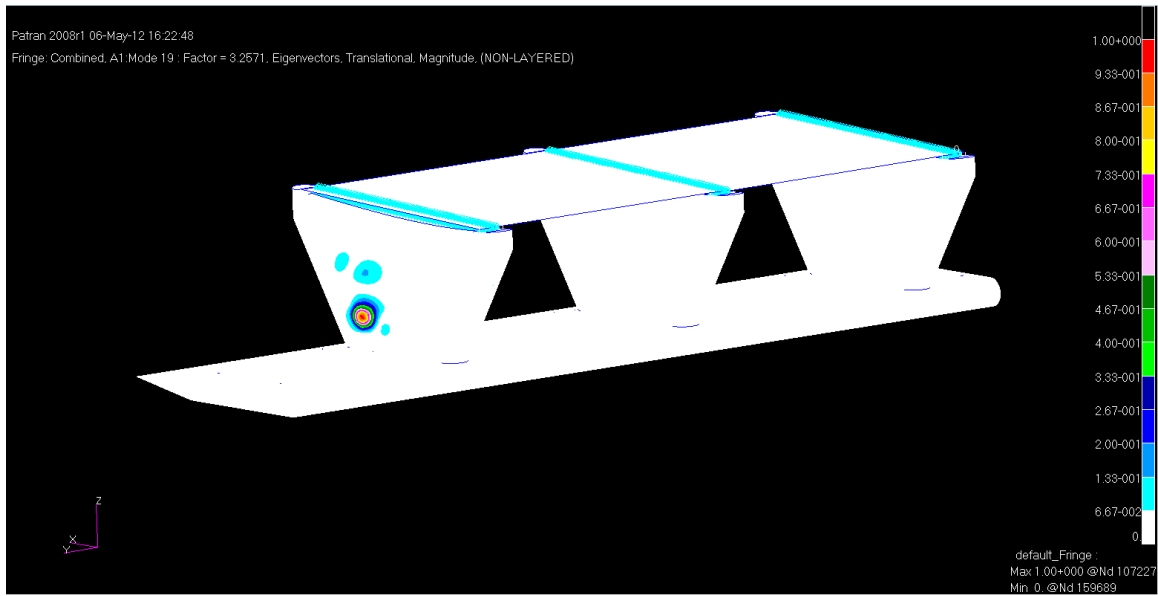


Figure 123: Third Mode Buckling at Load Factor of 3.2571

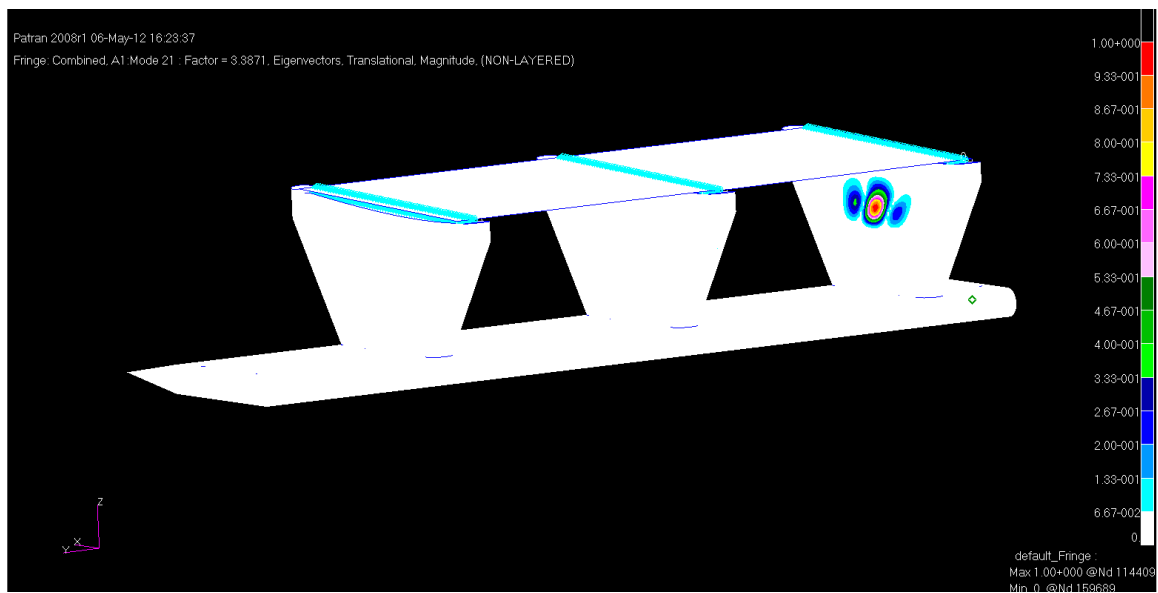


Figure 124: Fourth Mode Buckling at Load Factor of 3.387

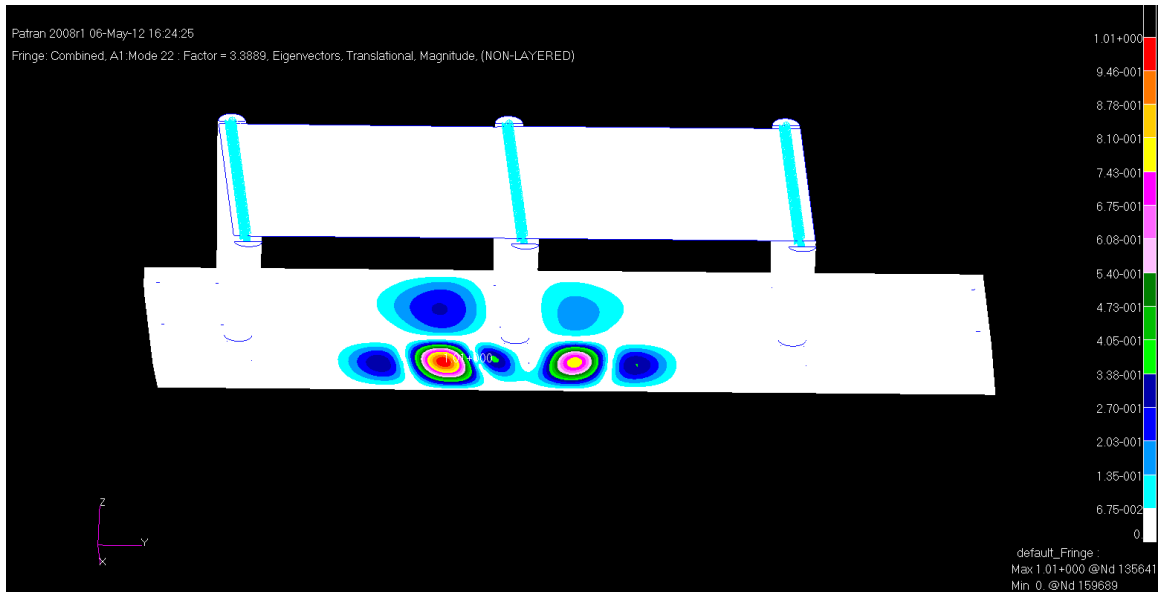


Figure 125: Fifth Mode Buckling at Load Factor of 3.389

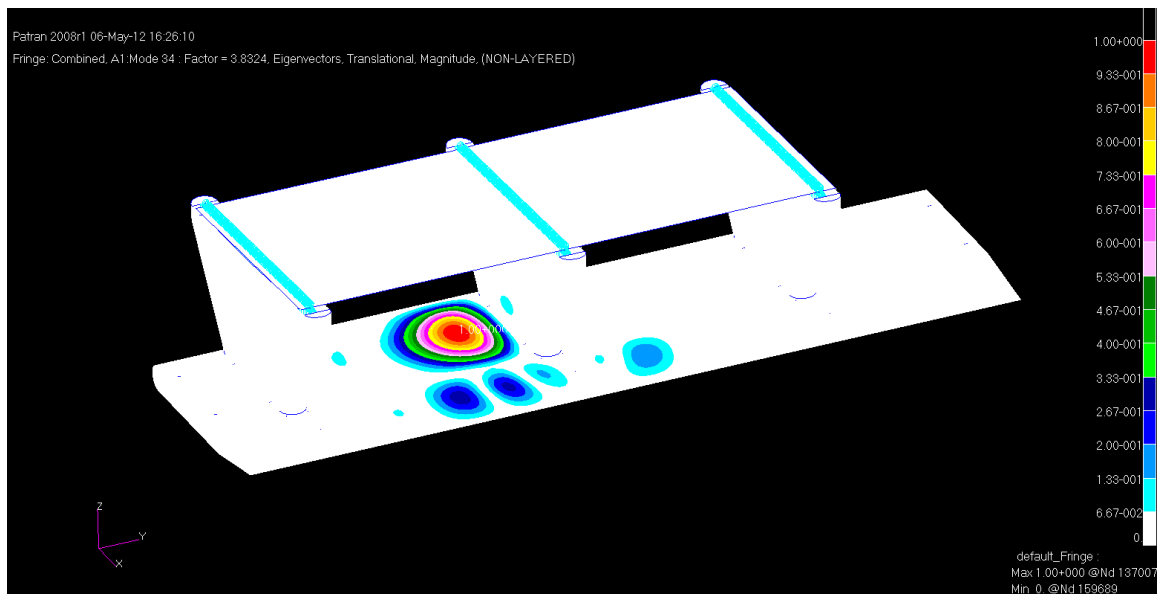


Figure 126: Sixth Mode Buckling at Load Factor of 3.8324

3.5.2 Lower Skins

The most critical margin of safety for the lower skin is the tensile on-axis failure method as seen in Table 32. All of the failure cases are presented with the overall stress distribution first, then the critical region is shown, then the results from the NASTRAN output file are presented and lastly that result is turned into a margin of safety.

Table 32: Lower Skin Failure Methods

Stress Type	Stress	Margin	Allowable	Load Case
Compressive on Axis	-9.79 (ksi)	0.259	-12.3 (ksi)	No Thermal
Tensile on Axis	10.43 (ksi)	0.026	10.7 (ksi)	Thermal
Shear	0.92 (ksi)	2.353	3.1 (ksi)	No Thermal
Compressive off Axis	-8.67 (ksi)	0.214	-10.5 (ksi)	Thermal
Tensile off Axis	9.08 (ksi)	0.131	10.3 (ksi)	No Thermal

3.5.2.1 Tensile Stress

The lower skin's most critical region in tension on the material x axis is near the center rib attachment point. Figure 127 shows the overall stress distribution in the lower skin and Figure 128 shows the region in the skin found to be the most critical with the critical element highlighted. The plots in this section are plotted on the material axes. The materials in the skins are aligned down the fairing heading outboard which is at a slight angle from the global y axis. This angle is due to the dihedral and the reduction in the chord along the wing of the representative aircraft.

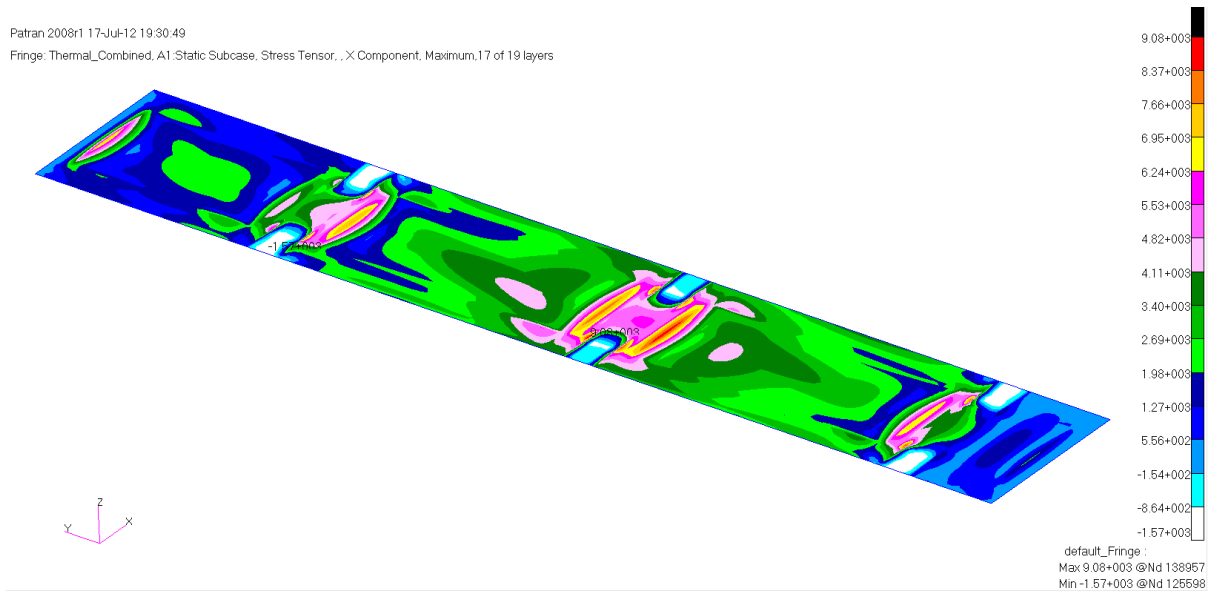


Figure 127: Lower Skins σ_1 Component Tensile Stress

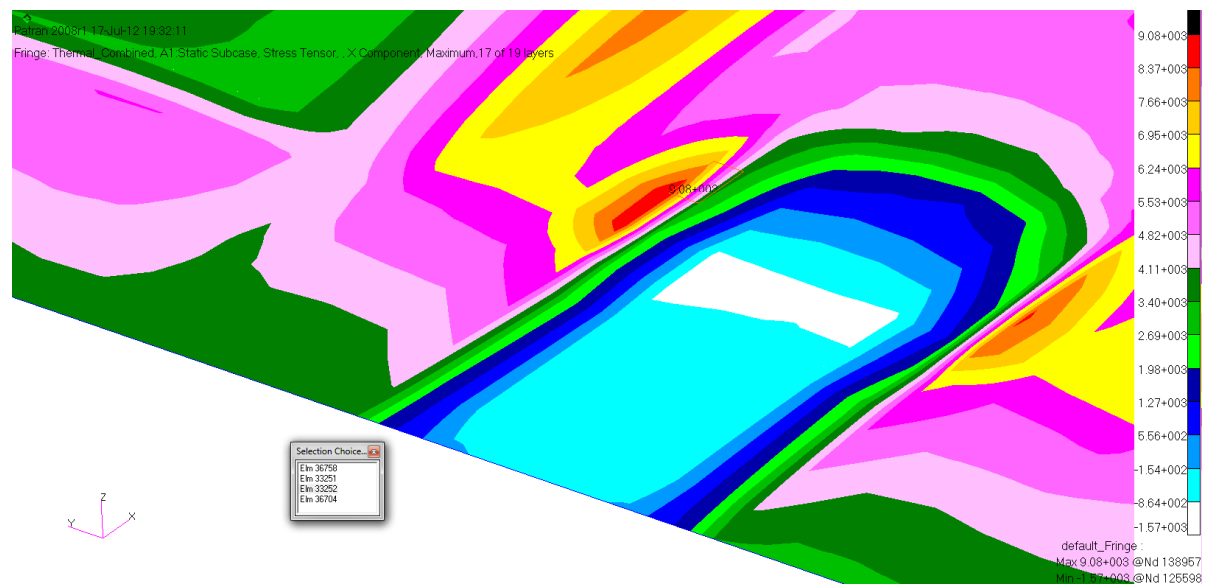


Figure 128: Lower Skins σ_1 Component Tensile Critical Region

Figure 129 shows the maximum σ_1 component stress of 10.04 ksi in the lower skin captured from the results file. The stress peaks at the discontinuity from the lower skin pad up to the lower skin standard layup. This stress is artificially high since when produced there would be a taper region as these plies dropped. This is also in the region where the center rib attaches. This

attachment causes a stress concentration as it transfers the load from the wing curvature to the fairing.

STRESSES IN LAYERED COMPOSITE ELEMENTS (QUAD4)						STRESSES IN FIBER AND MATRIX DIRECTIONS						INTER-LAMINAR STRESSES						PRINCIPAL STRESSES (ZERO SHEAR)						MAX SHEAR	
ELEMENT ID	PLY ID	NORMAL-1		NORMAL-2		SHEAR-12		SHEAR XZ-MAT		SHEAR YZ-MAT		ANGLE		MAJOR		MINOR									
0	33252	1	1.04321E+04	5.84058E+03	1.15344E+03	9.61899E+01	4.60431E+01	13.34	1.07055E+04	5.56711E+03	2.56922E+03	2.56922E+03													
0	33252	2	9.30250E+03	5.19890E+03	1.07174E+03	1.80356E+02	8.63308E+01	13.79	9.56555E+03	4.93585E+03	2.31485E+03	2.31485E+03													
0	33252	3	2.68026E+03	9.78957E+03	4.41691E+02	2.24975E+02	1.08751E+02	86.46	9.81691E+03	2.65292E+03	3.58199E+03	3.58199E+03													
0	33252	4	9.06161E+03	1.99293E+03	-3.82263E+02	2.62158E+02	1.27435E+02	-3.09	9.08222E+03	1.97232E+03	3.55495E+03	3.55495E+03													
0	33252	5	5.91377E+03	3.27387E+03	8.26656E+02	3.10252E+02	1.50456E+02	16.03	6.15126E+03	3.03638E+03	1.55744E+03	1.55744E+03													
0	33252	6	4.78420E+03	2.63219E+03	7.44962E+02	3.46324E+02	1.67722E+02	17.35	5.01691E+03	2.39947E+03	1.30872E+03	1.30872E+03													
0	33252	7	5.41661E+03	3.12026E+02	-2.03979E+02	3.61197E+02	1.75196E+02	-2.28	5.42475E+03	3.03888E+02	2.56043E+03	2.56043E+03													
0	33252	8	-2.60628E+02	4.00249E+03	1.44551E+02	3.68633E+02	1.78932E+02	88.06	4.00738E+03	-2.65523E+02	2.13645E+03	2.13645E+03													
0	33252	9	1.39547E+03	7.07160E+02	4.99877E+02	3.68633E+02	1.78932E+02	27.73	1.65821E+03	4.4421E+02	6.06893E+02	6.06893E+02													
0	33252	10	-1.43698E+03	1.68765E+03	2.56950E+01	3.61197E+02	1.75196E+02	89.53	1.68786E+03	-1.43719E+03	1.56253E+03	1.56253E+03													
0	33252	11	5.56614E+02	-1.92918E+03	3.37330E+01	3.46324E+02	1.67722E+02	0.78	5.57072E+02	-1.92964E+03	1.24336E+03	1.24336E+03													
0	33252	12	-1.99326E+03	-1.21787E+03	2.54792E+02	3.10252E+02	1.50456E+02	73.34	-1.14164E+03	-2.06949E+03	4.63925E+02	4.63925E+02													
0	33252	13	-3.12284E+03	-1.85955E+03	1.73097E+02	2.62158E+02	1.27435E+02	82.34	-1.83626E+03	-3.14613E+03	6.54933E+02	6.54933E+02													
0	33252	14	-3.08839E+03	-3.61009E+03	2.12017E+02	2.24975E+02	1.08751E+02	19.55	-3.01309E+03	-3.68538E+03	3.36146E+02	3.36146E+02													
0	33252	15	-4.37787E+03	-4.09943E+03	-2.71445E+02	1.80356E+02	8.63308E+01	-58.58	-3.93359E+03	-4.54371E+03	3.05064E+02	3.05064E+02													
0	33252	16	-6.51157E+03	-3.78458E+03	-7.19872E+01	9.61899E+01	4.60431E+01	-88.49	-3.78268E+03	-6.51346E+03	1.36539E+03	1.36539E+03													
0	33252	17	-7.64114E+03	-4.42626E+03	-1.53682E+02	3.46751E-12	3.31879E-13	-87.27	-4.41893E+03	-7.64847E+03	1.61477E+03	1.61477E+03													

Figure 129: Lower Skins σ_1 Component Tensile Critical Stress

The margin of safety for this method of failure is shown below:

$$MS = \frac{\sigma_{allowable}}{FS \bullet \sigma_{actual}} - 1 = \frac{32100 \text{ psi}}{3 \bullet 10432.1 \text{ psi}} - 1 = .026$$

The lower skin's most critical region in tension on the σ_2 axis is in one of the center bays

between the pylons. Figure 130 shows the overall stress distribution in the lower skin and

Figure 131 shows the region in the skin found to be the most critical with the critical element highlighted.

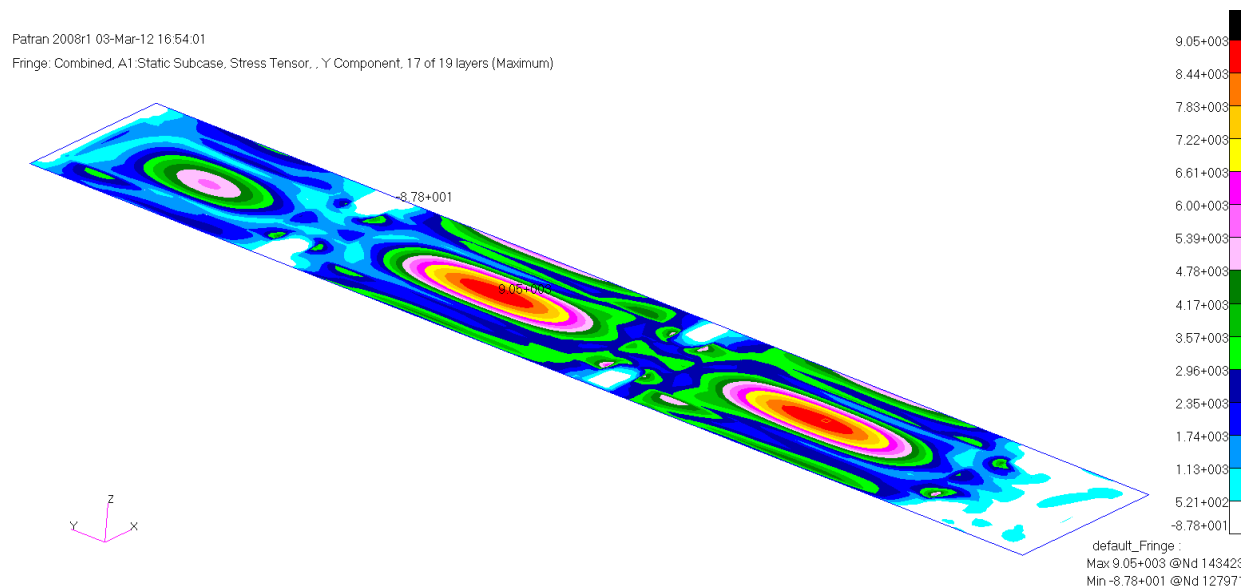


Figure 130: Lower Skins σ_2 Component Tensile Stress

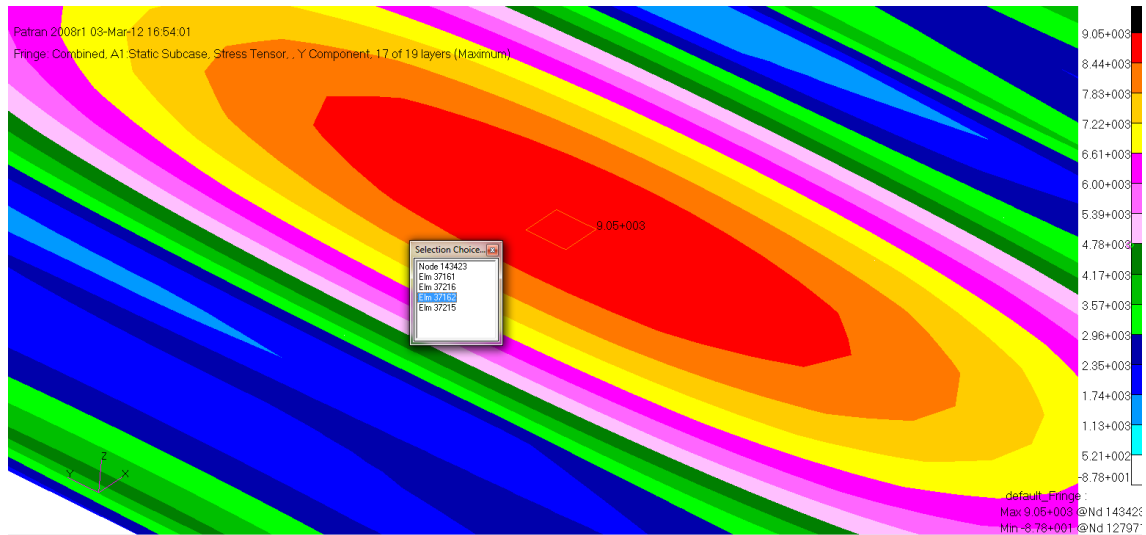


Figure 131: Lower Skins σ_2 Component Tensile Critical Region

Figure 132 shows the maximum σ_2 component stress of 9.08 ksi in the lower skin captured from the results file.

STRESSES IN LAYERED					COMPOSITE ELEMENTS (QUAD4)						
ELEMENT	PLY	STRESSES IN FIBER AND MATRIX DIRECTIONS			INTER-LAMINAR STRESSES			PRINCIPAL STRESSES (ZERO SHEAR)		MAX	
ID	ID	NORMAL-1	NORMAL-2	SHEAR-12	SHEAR XZ-MAT	SHEAR YZ-MAT	ANGLE	MAJOR	MINOR	SHEAR	
0	37162	1	-3.76089E+02	-8.63262E+03	-4.71444E+01	-9.93218E-03	1.70663E+00	-0.33	-3.75820E+02	-8.63289E+03	4.12854E+03
0	37162	2	-1.13846E+01	-6.66476E+03	-4.75265E+01	-1.76572E-02	3.03400E+00	-0.41	-1.10451E+01	-6.66510E+03	3.32703E+03
0	37162	3	-2.10483E+03	-2.35524E+03	6.88658E+02	-2.10699E-02	3.64958E+00	39.85	-1.53009E+03	-2.92998E+03	6.99947E+02
0	37162	4	-1.25865E+03	-8.46033E+02	-4.66955E+02	-2.31176E-02	4.01892E+00	-56.92	-5.41840E+02	-1.56284E+03	5.10499E+02
0	37162	5	1.08273E+03	-7.61154E+02	-4.86729E+01	-2.42211E-02	4.20855E+00	-1.51	1.08401E+03	-7.62438E+02	9.23225E+02
0	37162	6	1.44743E+03	1.20671E+03	-4.90551E+01	-2.31176E-02	4.01892E+00	-11.09	1.45705E+03	1.19710E+03	1.29973E+02
0	37162	7	2.38267E+03	2.63109E+03	1.98154E+02	-2.10699E-02	3.64958E+00	61.04	2.74074E+03	2.27301E+03	2.33865E+02
0	37162	8	3.97869E+03	3.42599E+03	-4.19857E+02	-1.76572E-02	3.03400E+00	-28.32	4.20498E+03	3.19970E+03	5.02642E+02
0	37162	9	2.54155E+03	7.11032E+03	-5.02015E+01	-9.93218E-03	1.70663E+00	-89.37	7.11087E+03	2.54099E+03	2.28494E+03
0	37162	10	2.90625E+03	9.07818E+03	-5.05837E+01	2.33156E-18	0.0	-89.53	9.07860E+03	2.90584E+03	3.08638E+03

Figure 132: Lower Skins σ_2 Component Tensile Critical Stress

The margin of safety for this method of failure is shown below:

$$MS = \frac{\sigma_{allowable}}{FS \bullet \sigma_{actual}} - 1 = \frac{30810 \text{ psi}}{3 \bullet 9078.2 \text{ psi}} - 1 = .131$$

3.5.2.2 Compressive stress

The lower skin's most critical region in compression on the σ_1 axis is near the inboard rib attachment point. Figure 133 shows the overall stress distribution in the lower skin and Figure 134 shows the region in the skin found to be the most critical with the critical element highlighted. The stress in this region rises dramatically for several reasons. The first is that the lower skin is primarily a structure in tension so most of the skin should not see compressive stress at all. The ribs provide sources for local compressive effects but some of these effects are artificial from the modeling. Fortunately it is not critical to determine the percentage of the stress that is real since it is not a sizing failure condition.

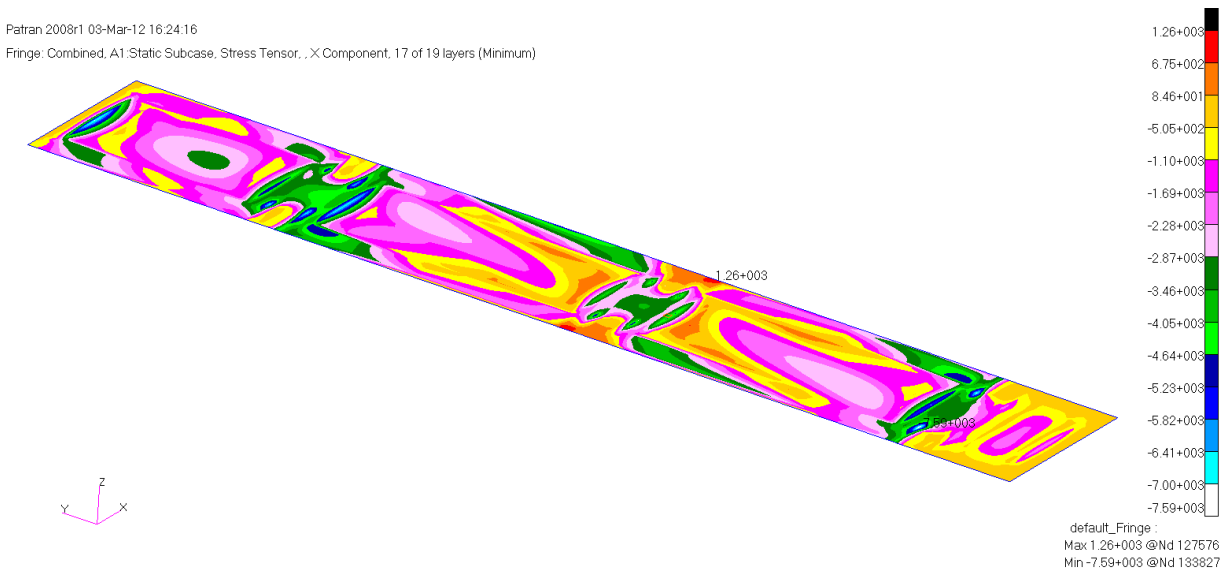


Figure 133: Lower Skins σ_1 Component Compressive Stress

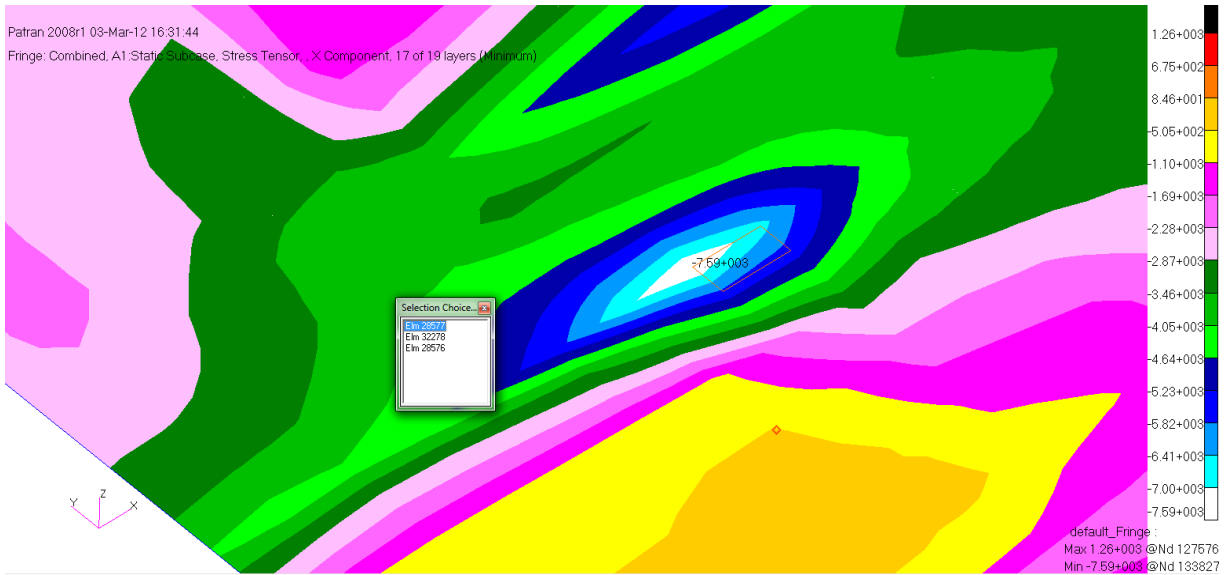


Figure 134: Lower Skins σ_1 Component Compressive Critical Region

0	28577	1	1.05595E+04	5.67217E+03	7.25107E+02	1.10054E+02	5.82244E+01	8.26	1.06648E+04	5.56686E+03	2.54899E+03
0	28577	2	9.28770E+03	4.88816E+03	6.42327E+02	2.06350E+02	1.09171E+02	8.14	9.37956E+03	4.79630E+03	2.29163E+03
0	28577	3	4.01548E+03	7.91496E+03	4.83210E+02	2.57400E+02	1.37522E+02	83.04	7.97394E+03	3.95649E+03	2.00872E+03
0	28577	4	6.94375E+03	3.12992E+03	-4.24716E+02	2.99942E+02	1.61149E+02	-6.28	6.99047E+03	3.08319E+03	1.95364E+03
0	28577	5	5.47224E+03	2.53614E+03	3.93988E+02	3.54968E+02	1.90261E+02	7.51	5.52419E+03	2.48419E+03	1.52000E+03
0	28577	6	4.20042E+03	1.75213E+03	3.11209E+02	3.96238E+02	2.12095E+02	7.13	4.23936E+03	1.71319E+03	1.26308E+03
0	28577	7	2.84878E+03	1.04416E+03	-2.49235E+02	4.13255E+02	2.21546E+02	-7.72	2.88257E+03	1.01037E+03	9.36100E+02
0	28577	8	3.66260E+02	1.41347E+03	1.90741E+02	4.21763E+02	2.26271E+02	79.99	1.44713E+03	3.32600E+02	5.57264E+02
0	28577	9	3.84956E+02	-5.99893E+02	6.28701E+01	4.21763E+02	2.26271E+02	3.64	3.88953E+02	-6.03891E+02	4.96422E+02
0	28577	10	-1.09343E+03	-1.18713E+03	7.37530E+01	4.13255E+02	2.21546E+02	28.79	-1.05290E+03	-1.22765E+03	8.73751E+01
0	28577	11	-2.61118E+03	-1.73686E+03	-1.52591E+02	3.96238E+02	2.12095E+02	-89.00	-1.73659E+03	-2.61144E+03	4.37424E+02
0	28577	12	-3.43051E+03	-2.95192E+03	-1.85469E+02	3.54968E+02	1.90261E+02	-71.11	-2.88846E+03	-3.49397E+03	3.02755E+02
0	28577	13	-4.70233E+03	-3.73592E+03	-2.68248E+02	2.99942E+02	1.61149E+02	-75.48	-3.66646E+03	-4.77179E+03	5.52667E+02
1	THIS IS A DEFAULT SUBCASE.										
						MARCH		3, 2012	MD NASTRAN	5/ 9/08	PAGE 4990
0	SUBCASE 1										
	STRESSES IN LAYERED COMPOSITE ELEMENTS (QUAD4)										
	ELEMENT	PLY	STRESSES IN FIBER AND MATRIX DIRECTIONS			INTER-LAMINAR STRESSES			PRINCIPAL STRESSES (ZERO SHEAR)		
	ID	ID	NORMAL-1	NORMAL-2	SHEAR-12	SHEAR XZ-MAT	SHEAR YZ-MAT	ANGLE	MAJOR	MINOR	MAX SHEAR
0	28577	14	-6.70614E+03	-3.82262E+03	1.60223E+02	2.57400E+02	1.37522E+02	86.83	-3.81375E+03	-6.71502E+03	1.45064E+03
0	28577	15	-4.74265E+03	-7.68862E+03	-2.18717E+02	2.06350E+02	1.09171E+02	-4.22	-4.72650E+03	-7.70476E+03	1.48913E+03
0	28577	16	-8.51779E+03	-6.08795E+03	-5.16587E+02	1.10054E+02	5.82244E+01	-78.48	-5.98268E+03	-8.62305E+03	1.32019E+03
0	28577	17	-9.78961E+03	-6.87195E+03	-5.99367E+02	3.96272E-12	4.19681E-13	-78.83	-6.75362E+03	-9.90794E+03	1.57716E+03

Figure 135: Lower Skins σ_1 Component Compressive Critical Stress

Figure 135 shows the maximum σ_1 compressive stress of 9.79 ksi in the lower skin captured from the results file at the critical region. The margin of safety for this method of failure is shown below:

$$MS = \frac{\sigma_{allowable}}{FS \cdot \sigma_{actual}} - 1 = \frac{-37000 \text{ psi}}{3 \cdot -9789.6 \text{ psi}} - 1 = .259$$

The lower skin's most critical region in compression on the material σ_2 axis is in the center of the bay between the two inboard attachment pylons. Figure 136 shows the overall stress distribution in the lower skin and Figure 137 shows the region in the skin found to be the most critical with the critical element highlighted.

Patran 2008r1 17-Jul-12 19:45:25

Fringe: Thermal_Combined, A1 Static Subcase, Stress Tensor, Y Component, Minimum, 17 of 19 layers

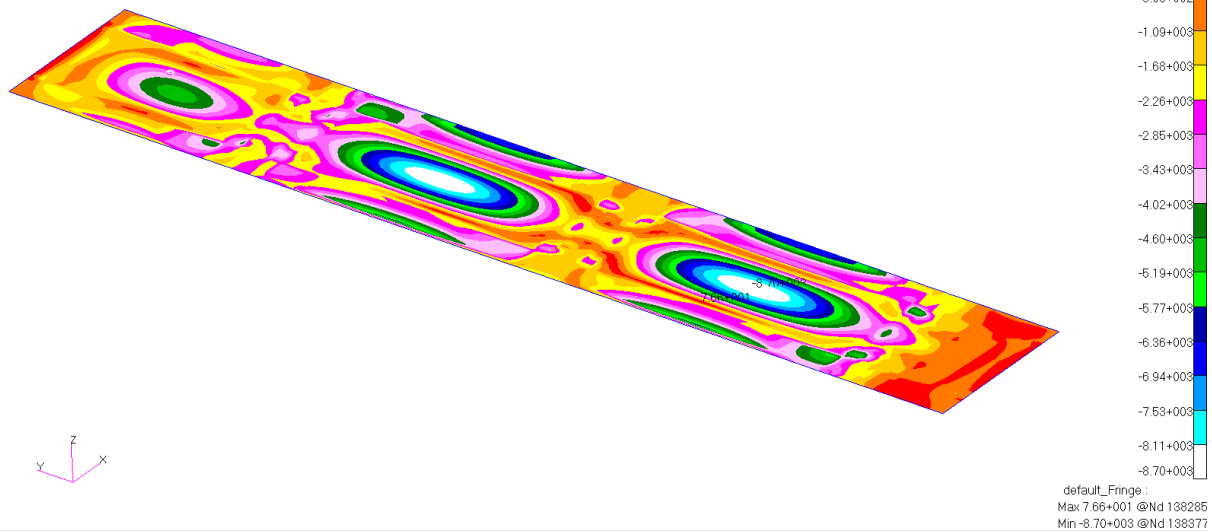


Figure 136: Lower Skins σ_2 Component Compressive Stress

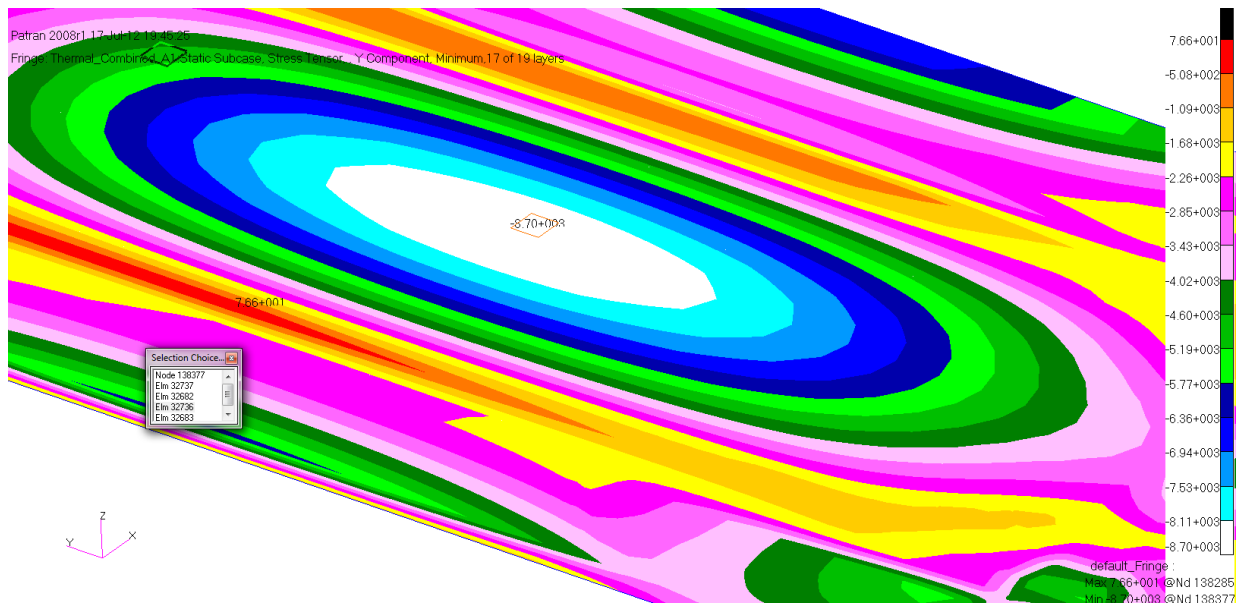


Figure 137: Lower Skins σ_2 Component Compressive Critical Region

ELEMENT ID	PLY ID	STRESSES IN LAYERED COMPOSITE ELEMENTS (QUAD4)			INTER-LAMINAR STRESSES			PRINCIPAL STRESSES (ZERO SHEAR)			MAX SHEAR
		NORMAL-1	NORMAL-2	SHEAR-12	SHEAR XZ-MAT	SHEAR YZ-MAT	ANGLE	MAJOR	MINOR		
0 32736	1	-3.92641E+02	-8.67220E+03	1.51123E+01	1.21653E-01	-4.33178E+00	0.10	-3.92613E+02	-8.67222E+03	4.13981E+03	
0 32736	2	-3.18386E+01	-6.71194E+03	1.64623E+01	2.16272E-01	-7.70094E+00	0.14	-3.17980E+01	-6.71198E+03	3.34009E+03	
0 32736	3	-2.39790E+03	-2.15406E+03	6.92981E+02	2.58072E-01	-9.26340E+00	49.99	-1.57236E+03	-2.97960E+03	7.03624E+02	
0 32736	4	-1.04676E+03	-1.13721E+03	-4.71812E+02	2.83152E-01	-1.02009E+01	-42.26	-6.18012E+02	-1.56596E+03	4.73974E+02	
0 32736	5	1.05057E+03	-8.31186E+02	2.05123E+01	2.96669E-01	-1.06822E+01	0.62	1.05079E+03	-8.31409E+02	9.41101E+02	
0 32736	6	1.41137E+03	1.12907E+03	2.18624E+01	2.83152E-01	-1.02009E+01	4.40	1.41305E+03	1.12738E+03	1.42835E+02	
0 32736	7	2.59665E+03	2.30392E+03	1.91698E+02	2.58072E-01	-9.26340E+00	26.32	2.69147E+03	2.20910E+03	2.41184E+02	
0 32736	8	3.62265E+03	3.63049E+03	-4.12867E+02	2.16272E-01	-7.70094E+00	-45.27	4.03946E+03	3.21369E+03	4.12886E+02	
0 32736	9	2.49378E+03	7.00982E+03	2.59124E+01	1.21653E-01	-4.33178E+00	89.67	7.00937E+03	2.49363E+03	2.25817E+03	
0 32736	10	2.85458E+03	8.97008E+03	2.72624E+01	-2.85578E-17	0.0	89.74	8.97020E+03	2.85446E+03	3.05787E+03	

Figure 138: Lower Skins σ_2 Component Compressive Critical Stress

Figure 138 shows the maximum σ_2 component compressive stress of 8.67 ksi in the lower skin captured from the results file at the critical region. The margin of safety for this method of failure is shown below:

$$MS = \frac{\sigma_{allowable}}{FS \bullet \sigma_{actual}} - 1 = \frac{-31590 psi}{3 \bullet -8616.7 psi} - 1 = .214$$

3.5.2.3 Shear Stress

The lower skin's most critical region in τ_{12} shear is near the outboard rib. To help determine the exact element where the stress peaked no averaging was used in the plots which makes them look more pixelated. Figure 139 shows the overall stress distribution in the lower skin and Figure 140 shows the region in the skin found to be the most critical with the critical element highlighted.

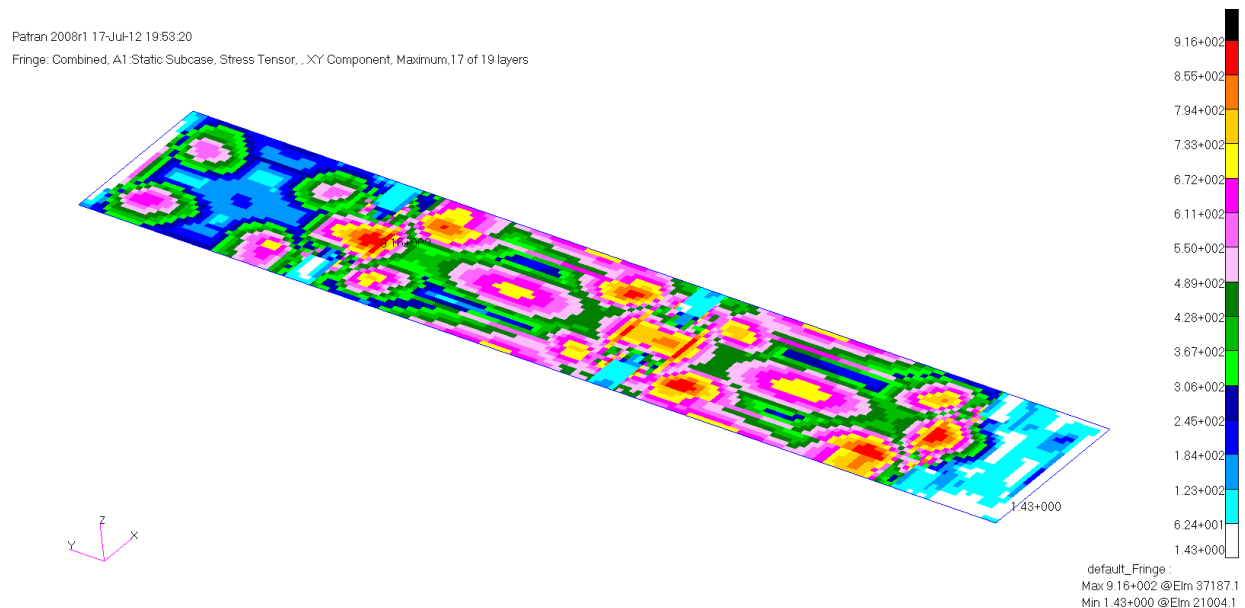


Figure 139: Lower Skins τ_{12} Component Shear Stress

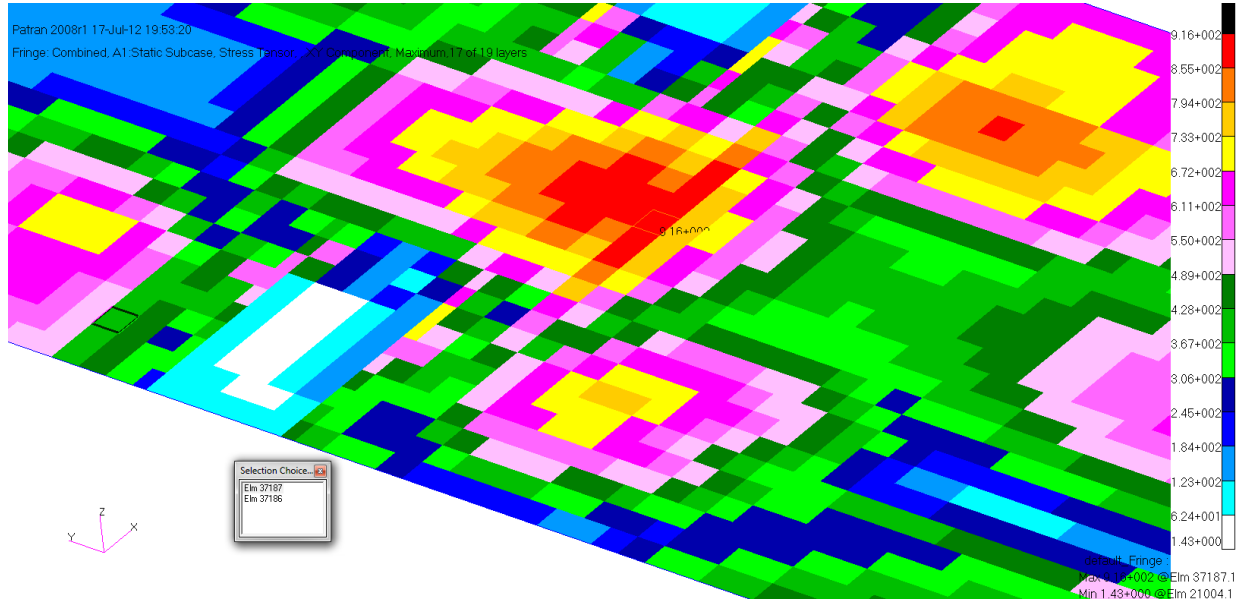


Figure 140: Lower Skins τ_{12} Component Shear Stress Critical Region

ELEMENT ID	PLY ID	STRESSES IN LAYERED COMPOSITE ELEMENTS (QUAD4)			INTER-LAMINAR STRESSES			PRINCIPAL STRESSES (ZERO SHEAR)			MAX SHEAR
		NORMAL-1	NORMAL-2	SHEAR-12	SHEAR XZ-MAT	SHEAR YZ-MAT	ANGLE	MAJOR	MINOR		
0	37187	1	8.69154E+03	-2.73213E+03	-4.05648E+01	-4.32377E+01	1.82682E+00	-0.20	8.69168E+03	-2.73227E+03	5.71198E+03
0	37187	2	6.87078E+03	-2.30659E+03	-3.99283E+01	-7.68670E+01	3.24768E+00	-0.25	6.87095E+03	-2.30676E+03	4.58886E+03
0	37187	3	1.68843E+03	1.32122E+03	9.15531E+02	-9.17235E+01	3.90661E+00	39.33	2.43859E+03	5.71065E+02	9.33763E+02
0	37187	4	7.02376E+02	9.51624E+02	-6.20011E+02	-1.00637E+02	4.30197E+00	-50.68	1.45941E+03	1.94588E+02	6.32411E+02
0	37187	5	1.40850E+03	-1.02996E+03	-3.80188E+01	-1.05442E+02	4.50495E+00	-0.89	1.40909E+03	-1.03055E+03	1.21982E+03
0	37187	6	-4.12261E+02	-6.04415E+02	-3.73823E+01	-1.00637E+02	4.30197E+00	-10.63	-4.05245E+02	-6.11432E+02	1.03094E+02
0	37187	7	-1.35137E+03	-1.01874E+03	2.66561E+02	-9.17235E+01	3.90661E+00	60.98	-3.70866E+02	-1.49924E+03	3.14189E+02
0	37187	8	-1.75989E+03	-1.93946E+03	-5.62085E+02	-7.68670E+01	3.24768E+00	-40.44	-1.27988E+03	-2.41846E+03	5.69289E+02
0	37187	9	-5.87454E+03	6.72214E+02	-3.54728E+01	-4.32377E+01	1.82682E+00	-89.69	6.72406E+02	-5.87473E+03	3.27357E+03
0	37187	10	-7.69530E+03	1.09776E+03	-3.48363E+01	1.01500E-14	0.0	-89.77	1.09789E+03	-7.69544E+03	4.39667E+03

Figure 141: Lower Skins τ_{12} Component Shear Critical Stress

Figure 141 shows the maximum shear stress of .916 ksi in the lower skin captured from the results file at the critical region. The margin of safety for this method of failure is shown below:

$$MS = \frac{\tau_{allowable}}{FS \bullet \tau_{actual}} - 1 = \frac{9210 \text{ psi}}{3 \bullet 915.5 \text{ psi}} - 1 = 2.353$$

3.5.3 Upper Skins

The most critical margin of safety for the upper skin is in buckling as seen in Table 32. The results are presented in the same order as the previous section. The outboard section of this component lacks a core insert so in several of the static sizing it looks like this region dominates the sizing since its a less effective structure. This is not the case since the structure is sized by buckling in the center bays which does not come into play with the outboard section of the array which is why it is possible to drop the core in this region.

Table 33: Upper Skin Failure Methods

Stress Type	Stress	Margin	Allowable	Load Case
Compressive on Axis	-7.74 (ksi)	0.593	-12.33 (ksi)	Thermal
Tensile on Axis	7.62 (ksi)	0.405	10.7 (ksi)	No Thermal
Shear	1.38 (ksi)	1.225	3.07 (ksi)	No Thermal
Compressive off Axis	-4.66 (ksi)	1.258	-10.53 (ksi)	Thermal
Tensile off Axis	5.83 (ksi)	0.760	10.27 (ksi)	Thermal
Buckling	3.83 (ksi)	0.277	3	

3.5.3.1 Tensile Stress

The upper skin's most critical region in tensile stress on the σ_1 axis at the attachment point to the outboard pylon. This region has a higher stress distribution since it lacks core like the other skin regions. Figure 142 shows the overall stress distribution in the upper skin and Figure 143 shows the region in the skin found to be the most critical with the critical element highlighted.

Patran 2008r1 17-Jul-12 20:15:14
Fringe: Thermal_Combined, A1 Static Subcase, Stress Tensor, , X Component, Maximum, 17 of 19 layers

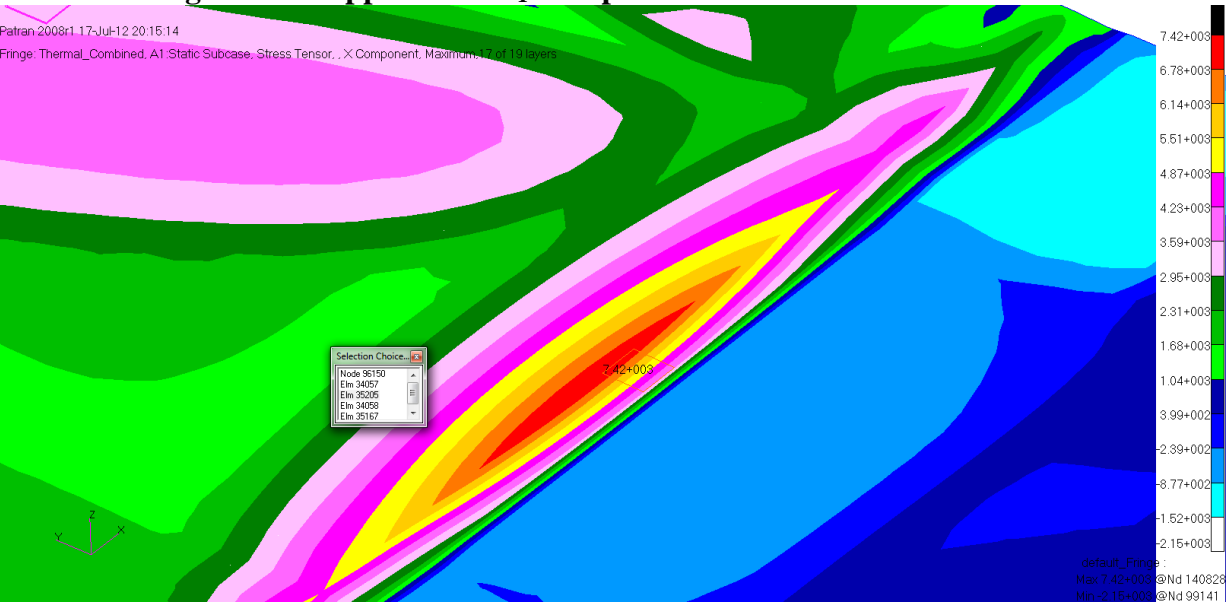
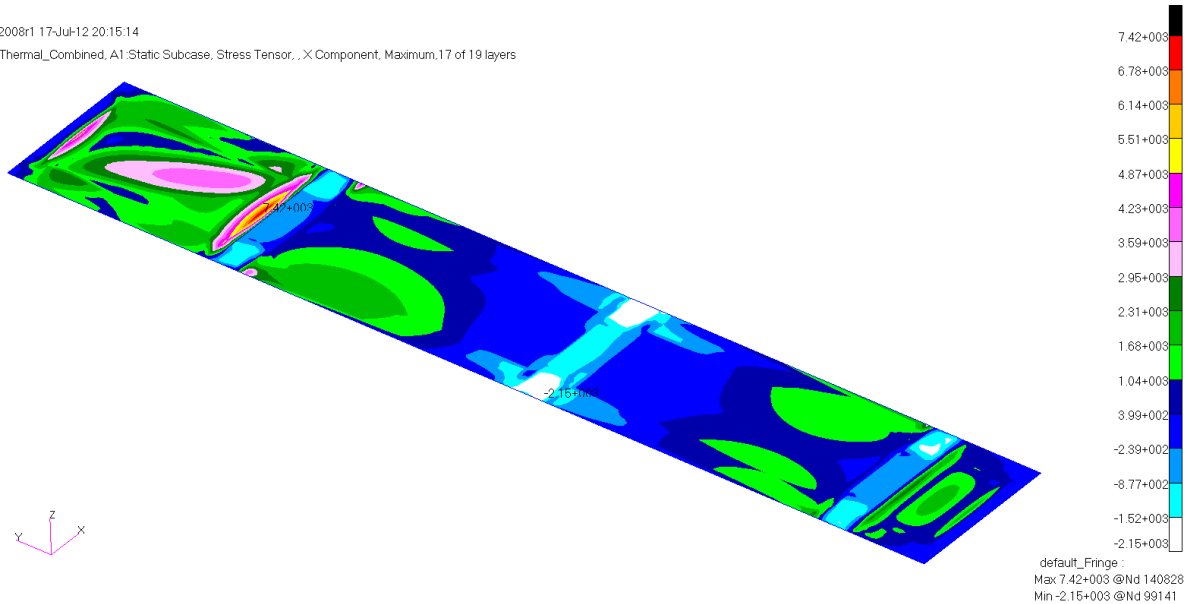


Figure 144: Upper Skins σ_1 Component Tensile Critical Stress

ELEMENT ID	PLY ID	STRESSES IN LAYERED			COMPOSITE ELEMENTS (QUAD4)				PRINCIPAL STRESSES (ZERO SHEAR)		MAX SHEAR
		NORMAL-1	NORMAL-2	SHEAR-12	INTER-LAMINAR STRESSES	SHEAR XZ-MAT	SHEAR YZ-MAT	ANGLE	MAJOR	MINOR	
0	35205	1	4.84189E+03	4.66795E+03	1.61779E+03	2.74733E+01	-4.89300E-01	43.46	6.37505E+03	3.13479E+03	1.62013E+03
0	35205	2	8.29408E+03	-1.25804E+03	2.28570E+00	5.92022E+01	-1.02761E+00	0.01	8.29408E+03	-1.25804E+03	4.77606E+03
0	35205	3	5.51068E+03	-1.24395E+03	-3.02659E+00	7.82395E+01	-1.35060E+00	-0.03	5.51068E+03	-1.24395E+03	3.37732E+03
0	35205	4	6.86125E+02	7.14557E+02	-5.23716E+02	8.21642E+01	-1.42050E+00	-45.78	1.22425E+03	1.76433E+02	5.23909E+02
0	35205	5	-7.18561E+02	-5.84728E+02	-1.59023E+02	7.82395E+01	-1.35060E+00	-56.41	-4.79116E+02	-8.24173E+02	1.72528E+02
0	35205	6	-2.83952E+03	-1.20168E+03	-1.89634E+01	5.92022E+01	-1.02761E+00	-89.34	-1.20146E+03	-2.83974E+03	8.19139E+02
0	35205	7	-5.62292E+03	-1.18760E+03	-2.42757E+01	2.74733E+01	-4.89300E-01	-89.69	-1.18746E+03	-5.62306E+03	2.21780E+03
0	35205	8	-4.70560E+03	-4.69885E+03	-9.35056E+02	0.0	0.0	-45.10	-3.76716E+03	-5.63728E+03	9.35063E+02

Figure 144 shows the maximum σ_1 component tensile stress of 8.29 ksi in the upper skin captured from the results file at the critical region. The margin of safety for this method of failure is shown below:

$$MS = \frac{\sigma_{allowable}}{FS \bullet \sigma_{actual}} - 1 = \frac{32100 psi}{3 \bullet 7616 psi} - 1 = .290$$

The upper skin's most critical region in tensile stress on the σ_2 axis at the attachment point to the outboard pylon. This region has a higher stress distribution since it lacks core that is at the center of the other skin regions. Figure 145 shows the overall stress distribution in the upper skin and Figure 146 shows the region in the skin found to be the most critical with the critical element highlighted.

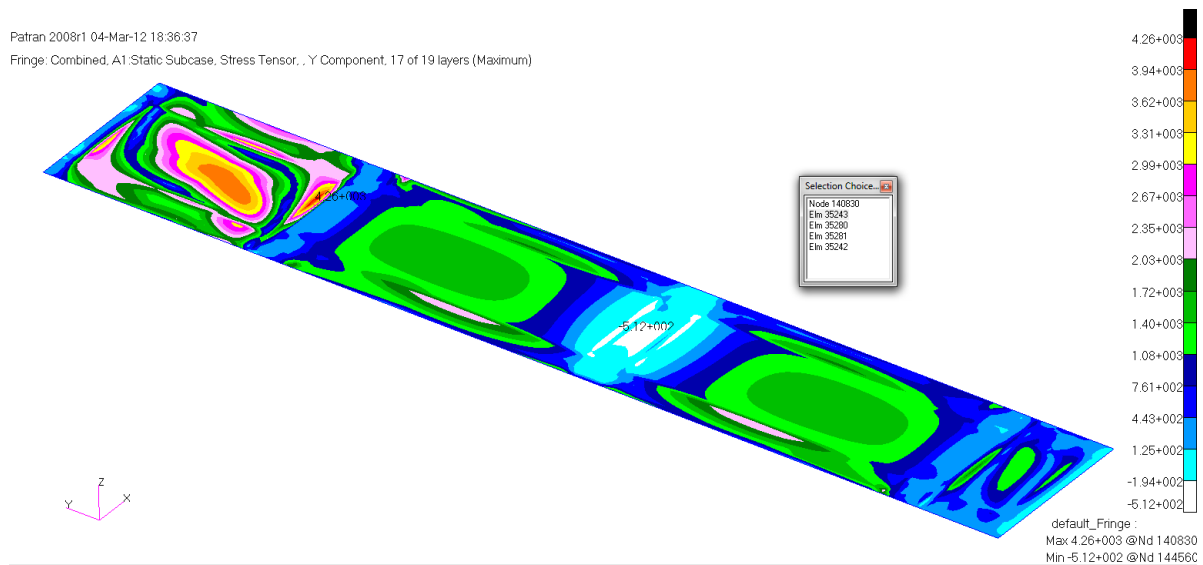


Figure 145: Upper Skins σ_2 Component Tensile Stress Distribution

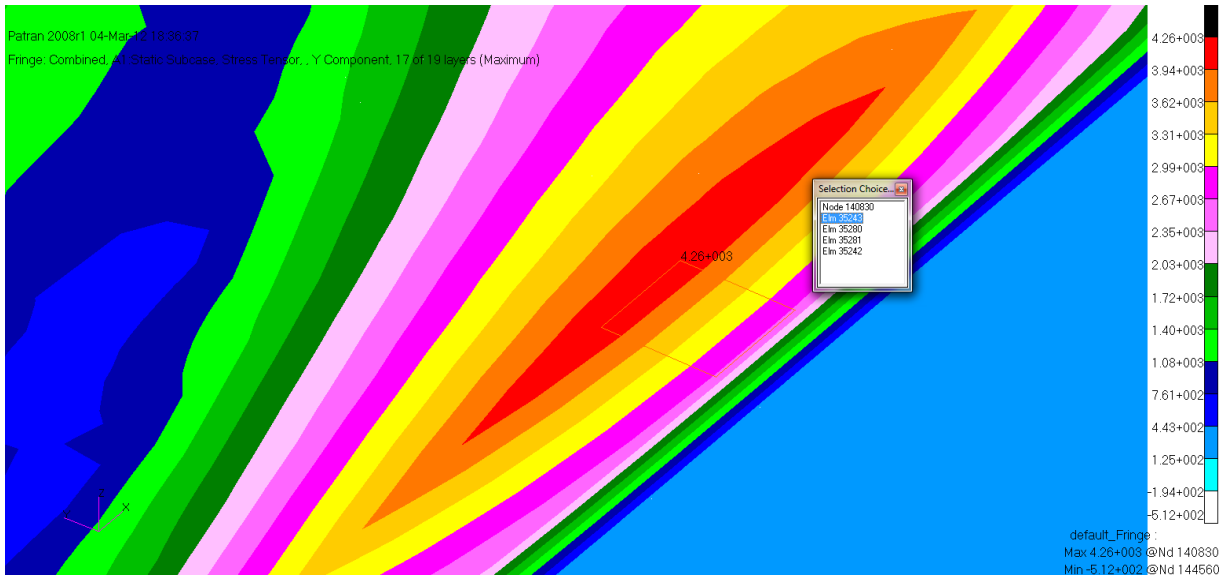


Figure 146: Upper Skins σ_2 Component Tensile Stress Critical Region

STRESSES IN LAYERED					COMPOSITE ELEMENTS (QUAD4)								
ELEMENT ID	PLY ID	STRESSES IN FIBER AND MATRIX DIRECTIONS			INTER-LAMINAR STRESSES			PRINCIPAL STRESSES (ZERO SHEAR)			MAX SHEAR		
		NORMAL-1	NORMAL-2	SHEAR-12	SHEAR XZ-MAT	SHEAR YZ-MAT	ANGLE	MAJOR	MINOR				
0	35243	1	4.97089E+03	4.80473E+03	1.34033E+03	3.09254E+01	-9.99362E-01	43.23	6.23072E+03	3.54490E+03	1.34291E+03		
0	35243	2	7.44766E+03	-1.13371E+02	-4.29082E+00	6.66411E+01	-2.09882E+00	-0.03	7.44766E+03	-1.13374E+02	3.78052E+03		
0	35243	3	4.74597E+03	-9.84449E+01	-1.80814E+01	8.80705E+01	-2.75850E+00	-0.21	4.74603E+03	-9.85124E+01	2.42227E+03		
0	35243	4	8.56028E+02	1.04841E+03	-2.77861E+02	9.24884E+01	-2.90127E+00	-54.55	1.24626E+03	6.58181E+02	2.94040E+02		
0	35243	5	-5.39888E+02	-1.80550E+02	7.62976E+01	8.80705E+01	-2.75850E+00	78.50	-1.65021E+02	-5.55417E+02	1.95198E+02		
0	35243	6	-3.35911E+03	-5.36662E+01	-5.94530E+01	6.66411E+01	-2.09882E+00	-88.97	-5.25972E+01	-3.36017E+03	1.65379E+03		
0	35243	7	-6.06080E+03	-3.87399E+01	-7.32436E+01	3.09254E+01	-9.99362E-01	-89.30	-3.78492E+01	-6.06169E+03	3.01192E+03		
0	35243	8	-4.05985E+03	-4.50358E+03	-1.13877E+03	0.0	0.0	-39.49	-3.12153E+03	-5.44190E+03	1.16018E+03		

Figure 147: Upper Skins σ_2 Component Tensile Critical Stress

Figure 147 shows the maximum σ_2 component stress of 4.80 ksi in the upper skin captured from the results file at the critical region. The margin of safety for this method of failure is shown below:

$$MS = \frac{\sigma_{allowable}}{FS \cdot \sigma_{actual}} - 1 = \frac{30810 \text{ psi}}{3 \cdot 4804.7 \text{ psi}} - 1 = 1.137$$

3.5.3.2 Compressive Stress

The upper skin's most critical region in compressive stress on the σ_1 axis at the attachment point to the center pylon. Figure 148 shows the overall stress distribution in the upper skin and Figure 149 shows the region in the skin found to be the most critical with the critical element highlighted.

Patran 2008r1 17-Jul-12 20:59:55
 Fringe: Thermal_Combined, A1 Static Subcase, Stress Tensor, , X Component, Minimum, 17 of 19 layers

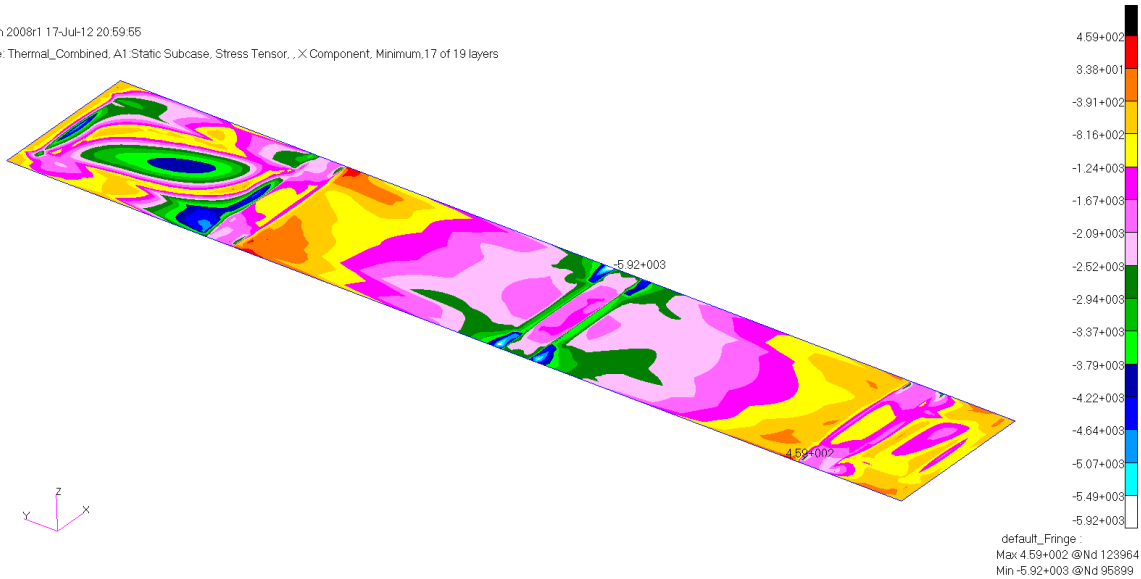


Figure 148: Upper Skins σ_1 Component Compressive Stress Distribution

Patran 2008r1 17-Jul-12 20:59:55
 Fringe: Thermal_Combined, A1 Static Subcase, Stress Tensor, , X Component, Minimum, 17 of 19 layers

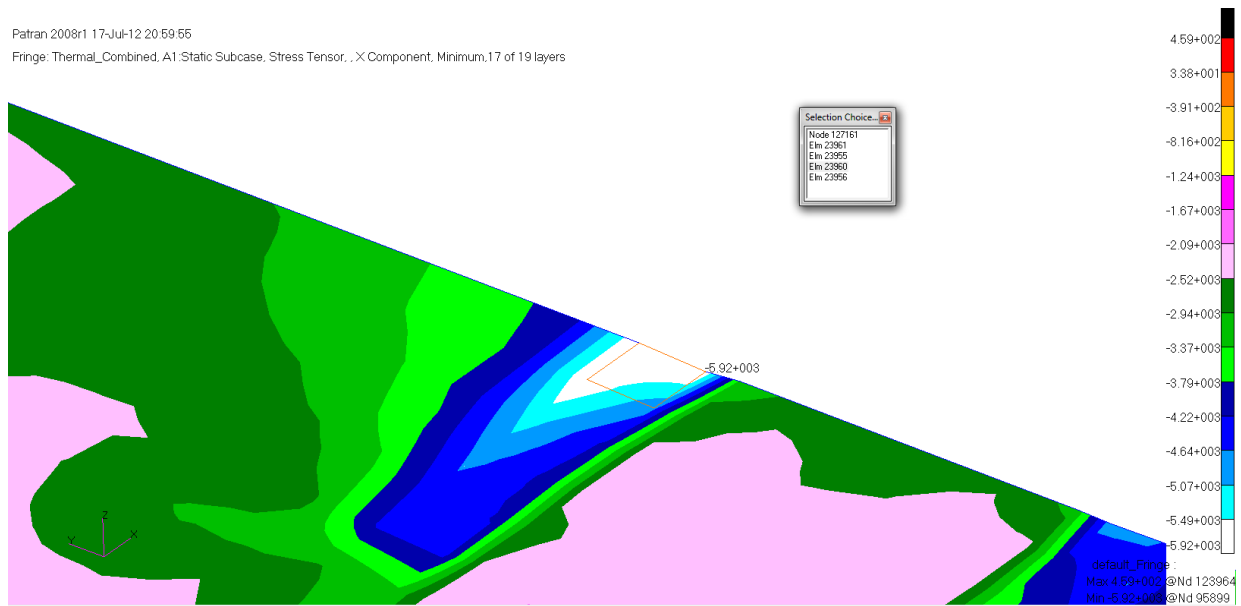


Figure 149: Upper Skins σ_1 Component Compressive Stress Critical Region

STRESSES IN LAYERED					COMPOSITE ELEMENTS (QUAD4)							
ELEMENT	PLY	STRESSES IN FIBER AND MATRIX DIRECTIONS			INTER-LAMINAR STRESSES			PRINCIPAL STRESSES (ZERO SHEAR)				MAX
ID	ID	NORMAL-1	NORMAL-2	SHEAR-12	SHEAR XZ-MAT	SHEAR YZ-MAT	ANGLE	MAJOR	MINOR		SHEAR	
0	23960	1	1.62267E+02	-2.23349E+03	-1.43655E+02	3.64893E+01	7.40530E+00	-3.42	1.70850E+02	-2.24207E+03	1.20646E+03	
0	23960	2	-2.37754E+03	-6.93923E+02	-3.09360E+02	7.86306E+01	1.55524E+01	-79.91	-6.38878E+02	-2.43258E+03	8.96852E+02	
0	23960	3	-3.11279E+03	-8.73384E+02	-2.91995E+02	1.03915E+02	2.04406E+01	-82.69	-8.35937E+02	-3.15024E+03	1.15715E+03	
0	23960	4	-3.53021E+03	-1.35561E+03	3.57476E+02	1.09128E+02	2.14985E+01	80.90	-1.29835E+03	-3.58747E+03	1.14456E+03	
0	23960	5	-3.92541E+03	-1.85901E+03	4.28750E+02	1.03915E+02	2.04406E+01	78.73	-1.77358E+03	-4.01084E+03	1.11863E+03	
0	23960	6	-5.31855E+03	-1.41177E+03	-2.39899E+02	7.86306E+01	1.55524E+01	-86.50	-1.39709E+03	-5.33322E+03	1.96807E+03	
0	23960	7	-6.05380E+03	-1.59123E+03	-2.22534E+02	3.64893E+01	7.40530E+00	-87.15	-1.58016E+03	-6.06487E+03	2.24235E+03	
0	23960	8	-3.53682E+03	-4.86879E+03	-6.42570E+02	0.0	0.0	-21.99	-3.27736E+03	-5.12824E+03	9.25438E+02	

Figure 150: Upper Skins σ_1 Component Compressive Critical Stress

Figure 150 shows the maximum compressive stress of 6.05 ksi in the upper skin captured from the results file at the critical region. The margin of safety for this method of failure is shown below:

$$MS = \frac{\sigma_{allowable}}{FS \bullet \sigma_{actual}} - 1 = \frac{-36990\,psi}{3 \bullet -6053.8\,psi} - 1 = 1.037$$

The upper skin's most critical region in compressive stress on the material σ_2 axis at the attachment point to the middle pylon Figure 151 shows the overall stress distribution in the upper skin and Figure 152 shows the region in the skin found to be the most critical with the critical element highlighted.

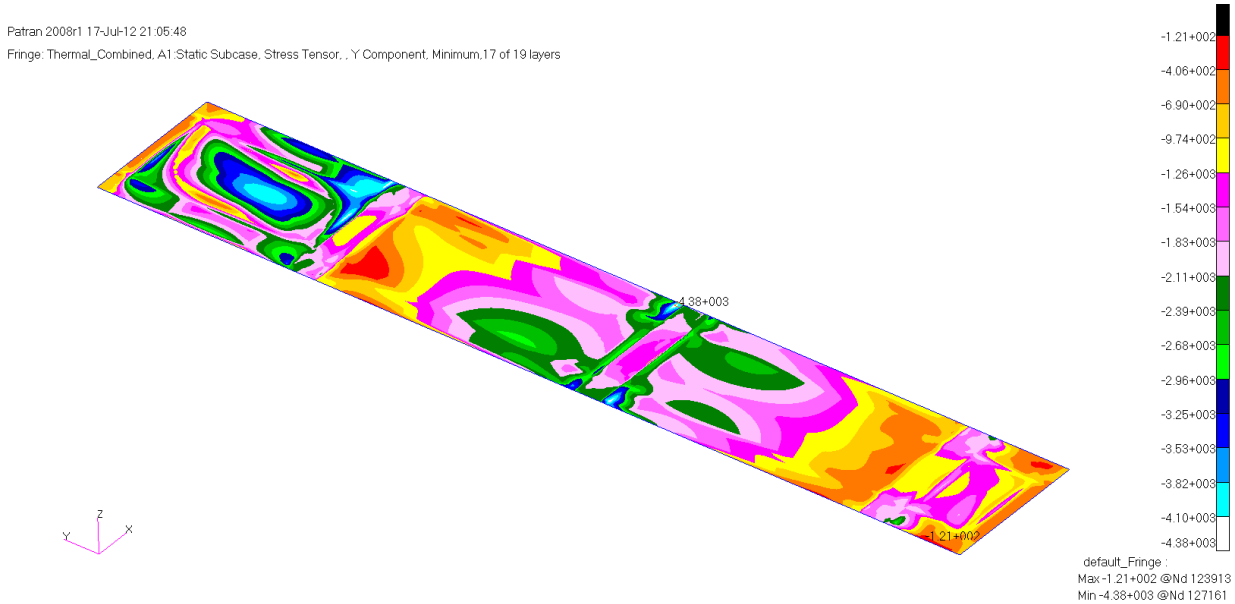


Figure 151: Upper Skins σ_2 Component Compressive Stress Distribution

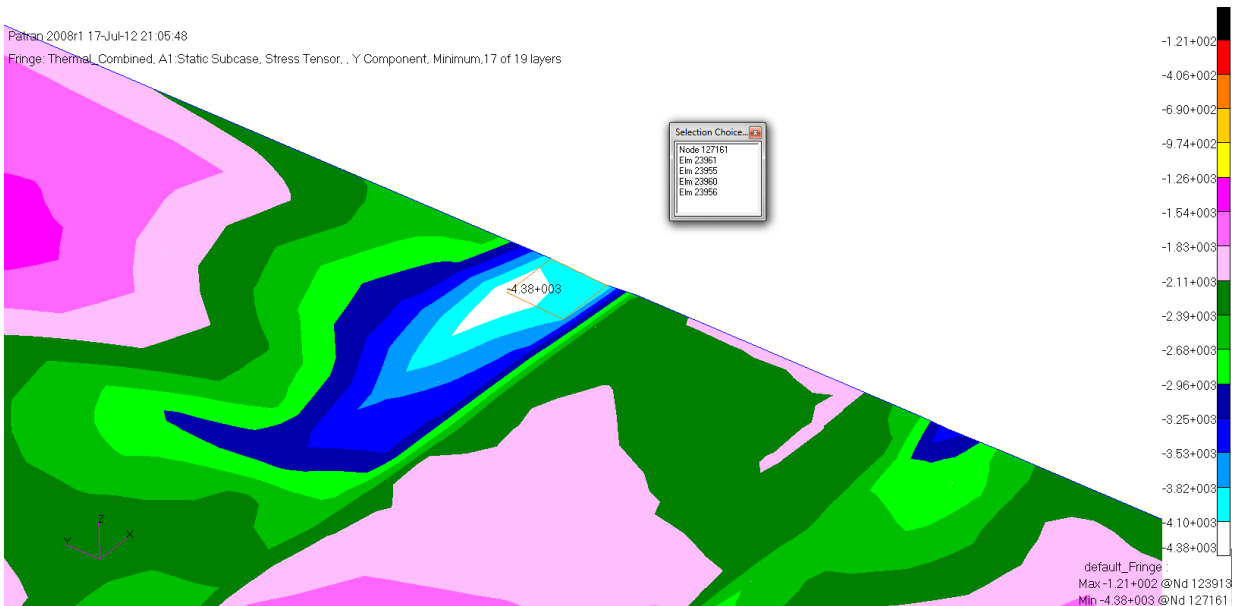


Figure 152: Upper Skins σ_2 Component Compressive Stress Critical Region

STRESSES IN LAYERED						COMPOSITE ELEMENTS (QUAD4)					
ELEMENT ID	PLY ID	STRESSES IN FIBER AND MATRIX DIRECTIONS			INTER-LAMINAR STRESSES			PRINCIPAL STRESSES (ZERO SHEAR)			MAX SHEAR
		NORMAL-1	NORMAL-2	SHEAR-12	SHEAR YZ-MAT	SHEAR YZ-MAT	ANGLE	MAJOR	MINOR		SHEAR
0	23960	1	6.12267E+02	-2.23349E+03	-1.43655E+02	3.64893E+01	7.40530E+00	-3.42	1.70850E+02	-2.24207E+03	1.20646E+03
0	23960	2	-2.37754E+03	-6.93923E+02	-3.09360E+02	7.86306E+01	1.55524E+01	-79.91	-6.38878E+02	-2.43258E+03	8.96852E+02
0	23960	3	-3.11279E+03	-8.73384E+02	-2.91995E+02	1.03915E+02	2.04406E+01	-82.69	-8.35937E+02	-3.15024E+03	1.15715E+03
0	23960	4	-3.53021E+03	-1.35561E+03	3.57476E+02	1.09128E+02	2.14985E+01	80.90	-1.29835E+03	-3.58747E+03	1.14456E+03
0	23960	5	-3.92541E+03	-1.85901E+03	4.28750E+02	1.03915E+02	2.04406E+01	78.73	-1.77358E+03	-4.01084E+03	1.11863E+03
0	23960	6	-5.31855E+03	-1.41177E+03	-2.39899E+02	7.86306E+01	1.55524E+01	-86.50	-1.39709E+03	-5.33322E+03	1.96807E+03
0	23960	7	-6.05380E+03	-1.59123E+03	-2.22534E+02	3.64893E+01	7.40530E+00	-87.15	-1.58016E+03	-6.06487E+03	2.24235E+03
0	23960	8	-3.53682E+03	-4.86879E+03	-6.42570E+02	0.0	0.0	-21.99	-3.27736E+03	-5.12824E+03	9.25438E+02

Figure 153: Upper Skins σ_2 Component Compressive Critical Stress

Figure 153 shows the maximum σ_2 compressive stress of 4.87 ksi in the upper skin captured from the results file at the critical region. The margin of safety for this method of failure is shown below:

$$MS = \frac{\sigma_{allowable}}{FS \bullet \sigma_{actual}} - 1 = \frac{-31590 psi}{3 \bullet -4868.8 psi} - 1 = 1.163$$

3.5.3.3 Shear Stress

The upper skin's most critical region in τ_{12} shear is at the attachment point to the outboard pylon. This region has a higher stress distribution since it lacks core like the other skin regions. Figure 154 shows the overall stress distribution in the upper skin and Figure 155 shows the region in the skin found to be the most critical with the critical element highlighted.

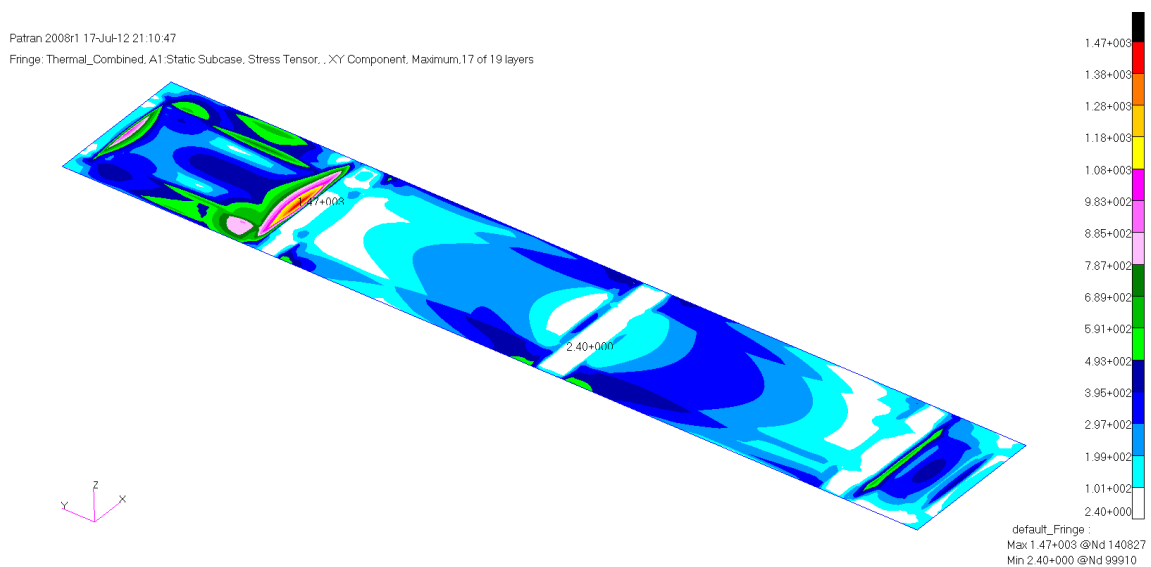


Figure 154: Upper Skins τ_{12} Component Shear Stress Distribution

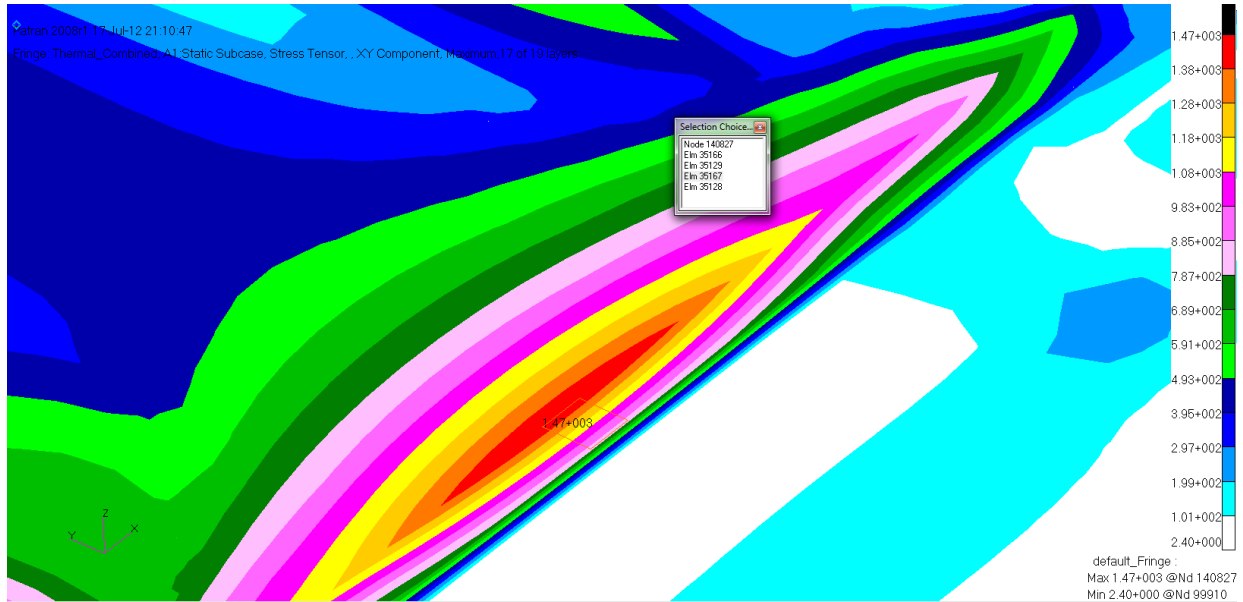


Figure 155: Upper Skins τ_{12} Component Shear Critical Region

ELEMENT ID	PLY ID	STRESSES IN FIBER AND MATRIX DIRECTIONS			COMPOSITE ELEMENTS (QUAD4)			INTER-LAMINAR STRESSES			PRINCIPAL STRESSES (ZERO SHEAR)			MAX SHEAR
		NORMAL-1	NORMAL-2	SHEAR-12	SHEAR XZ-MAT	SHEAR YZ-MAT	ANGLE	MAJOR	MINOR		MAJOR	MINOR		
0	35167	1	4.96236E+03	4.61417E+03	1.632821E+03	2.75651E+01	7.34918E-02	41.95	6.42586E+03	3.15067E+03	1.63759E+03			1.63759E+03
0	35167	2	8.34951E+03	-1.26596E+03	-1.30567E+01	5.94001E+01	1.54345E-01	-0.08	8.34953E+03	-1.26598E+03	4.80775E+03			4.80775E+03
0	35167	3	5.54917E+03	-1.25186E+03	-1.06519E+01	7.85010E+01	2.02857E-01	-0.09	5.54919E+03	-1.25187E+03	3.40053E+03			3.40053E+03
0	35167	4	6.93113E+02	7.20543E+02	-5.27605E+02	8.24389E+01	2.13355E-01	-45.74	1.23461E+03	1.79045E+02	5.27783E+02			5.27783E+02
0	35167	5	-6.90426E+02	-6.15003E+02	-1.60702E+02	7.85010E+01	2.02857E-01	-51.60	-4.87646E+02	-8.17782E+02	1.65068E+02			1.65068E+02
0	35167	6	-2.85184E+03	-1.20954E+03	-3.43741E+00	5.94001E+01	1.54345E-01	-89.88	-1.20954E+03	-2.85184E+03	8.21154E+02			8.21154E+02
0	35167	7	-5.65217E+03	-1.19544E+03	-1.03259E+00	2.75651E+01	7.34918E-02	-89.99	-1.19544E+03	-5.65217E+03	2.22837E+03			2.22837E+03
0	35167	8	-4.85157E+03	-4.61161E+03	-9.40005E+02	0.0	0.0	-48.64	-3.78396E+03	-5.67922E+03	9.47631E+02			9.47631E+02

Figure 156: Upper Skins τ_{12} Component Shear Critical Stress

Figure 156 shows the maximum τ_{12} shear stress of 1.63 ksi in the upper skin captured from the results file at the critical region. The margin of safety for this method of failure is shown below:

$$MS = \frac{\tau_{allowable}}{FS \bullet \tau_{actual}} - 1 = \frac{9210 psi}{3 \bullet 1628.3 psi} - 1 = .885$$

3.5.4 Trailing Edge Skin

The most critical margin of safety for the trailing edge skin is in buckling as seen in Table 34.

The plots in this section are presented in material space. The materials in the trailing edge skin are aligned down the fairing heading outboard which is at a slight angle from the global y axis.

The results are presented in the same order as the previous section.

Table 34: Trailing Edge Skin Failure Methods

Stress Type	Stress	Margin	Allowable	Load Case
Compressive on Axis	-6.48 (ksi)	0.902	-12.3 (ksi)	Thermal
Tensile on Axis	4.11 (ksi)	1.602	10.7 (ksi)	Thermal
Shear	0.70 (ksi)	3.416	3.1 (ksi)	No Thermal
Compressive off Axis	-6.41 (ksi)	0.642	-10.5 (ksi)	No Thermal
Tensile off Axis	6.18 (ksi)	0.661	10.3 (ksi)	No Thermal
Buckling (Load Factor)	3.02	0.007	3.0	No Thermal

3.5.4.1 Tensile Stress

The trailing edge skin's most critical region in tensile stress on the σ_1 axis is in the inboard bay between the inboard and mid attachment points. Figure 157 shows the overall stress distribution in the trailing edge and Figure 158 shows the region in the skin found to be the most critical with the critical element highlighted.

Patran 2008r1 22-Jul-12 18:57:49
Fringe: Thermal_Combined, A1 Static Subcase, Stress Tensor, X Component, Maximum, 17 of 19 layers

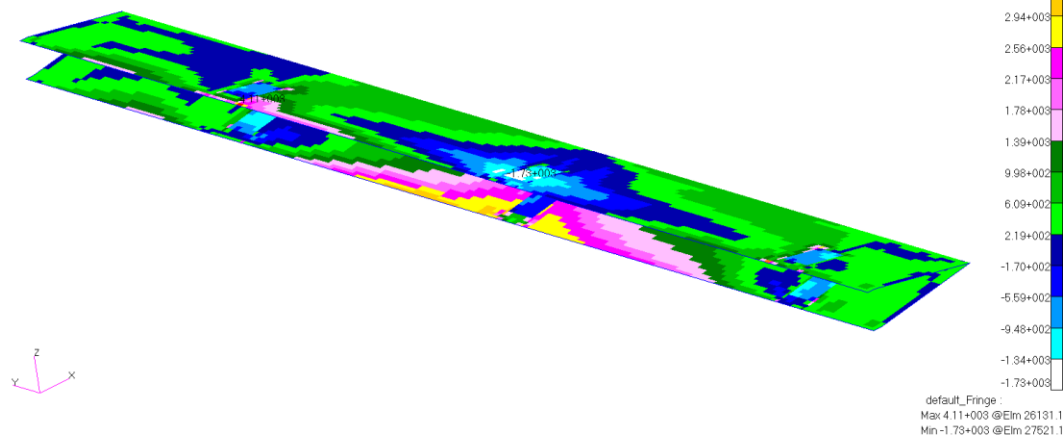


Figure 157: Trailing Edge σ_1 Component Tensile Stress Distribution

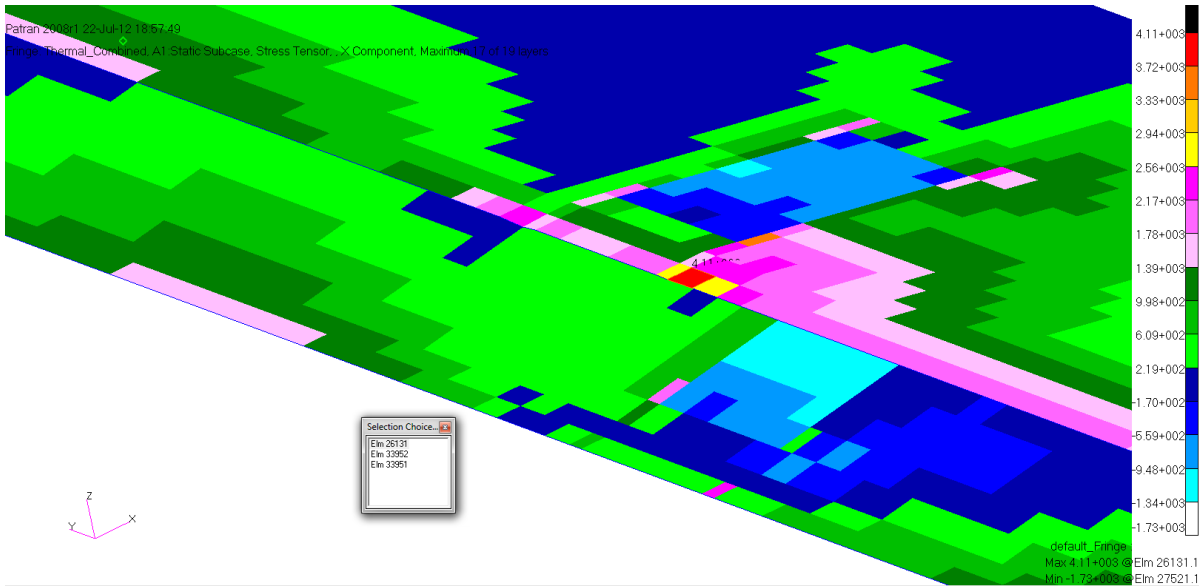


Figure 158: Trailing Edge σ_1 Component Tensile Stress Critical Region

ELEMENT ID	PLY ID	STRESSES IN FIBER AND MATRIX DIRECTIONS			COMPOSITE ELEMENTS (QUAD4)			PRINCIPAL STRESSES (ZERO SHEAR)			MAX SHEAR
		NORMAL-1	NORMAL-2	SHEAR-12	SHEAR XZ-MAT	SHEAR YZ-MAT	ANGLE	MAJOR	MINOR		
0	26131	1	-2.26020E+03	1.46443E+03	3.39288E+02	1.71511E+01	4.47944E+00	84.84	1.49508E+03	-2.29086E+03	1.89297E+03
0	26131	2	1.46887E+03	-1.48758E+03	5.25436E+02	3.69590E+01	9.40756E+00	9.78	1.55947E+03	-1.57819E+03	1.56883E+03
0	26131	3	1.99756E+03	-1.39089E+03	5.55938E+02	4.88437E+01	1.23644E+01	9.08	2.08644E+03	-1.47977E+03	1.78311E+03
0	26131	4	2.83363E+03	-1.58701E+03	-5.06318E+02	5.12939E+01	1.30044E+01	-6.45	2.89088E+03	-1.64426E+03	2.26757E+03
0	26131	5	3.26574E+03	-1.39832E+03	-5.61995E+02	4.88437E+01	1.23644E+01	-6.77	3.33251E+03	-1.46508E+03	2.39879E+03
0	26131	6	3.58364E+03	-1.10082E+03	-6.47445E+02	3.69590E+01	9.40756E+00	7.73	3.67148E+03	-1.18866E+03	2.43007E+03
0	26131	7	4.11233E+03	-1.00413E+03	-6.77947E+02	1.71511E+01	4.47944E+00	7.42	4.20064E+03	-1.09244E+03	2.64654E+03
0	26131	8	-8.73650E+02	4.34587E+03	7.29026E+02	0.0	0.0	82.20	4.44579E+03	-9.73563E+02	2.70967E+03

Figure 159: Trailing Edge σ_1 Component Tensile Critical Stress

Figure 159 shows the maximum σ_1 component stress of 5.06 ksi in the trailing edge skin captured from the results file at the critical region. This is an extreme jump in stress which questions its validity. The trailing edge ribs, aft spar, and pylons all interact at this point which

should cause a local jump in stress. If this were a sizing condition the validity of the stress should be investigated but since buckling comes well before this region would fail it was not investigated. The margin of safety for this method of failure is shown below:

$$MS = \frac{\sigma_{allowable}}{FS \bullet \sigma_{actual}} - 1 = \frac{32100\text{psi}}{3 \bullet 4112.3\text{psi}} - 1 = 1.602$$

The trailing edge skin's most critical region in tensile stress on the material σ_2 axis is in the inboard bay between the inboard and mid attachment points. Figure 160 shows the overall stress distribution in the trailing edge skin and Figure 161 shows the region in the skin found to be the most critical with the critical element highlighted.

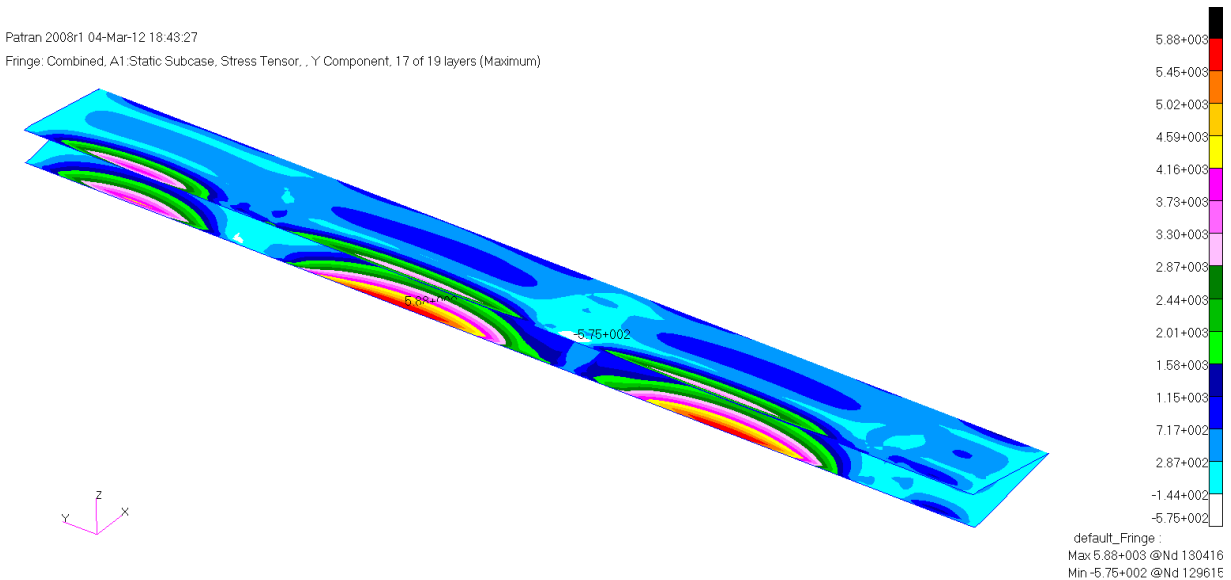


Figure 160: Trailing Edge σ_2 Component Tensile Stress Distribution

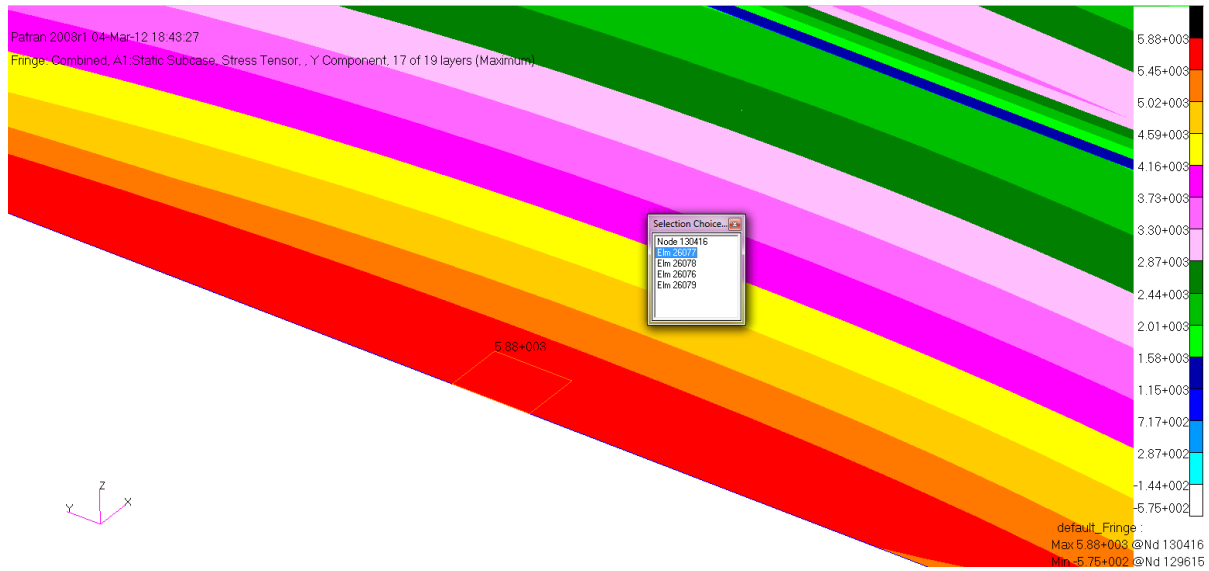


Figure 161: Trailing Edge σ_2 Component Tensile Stress Critical Region

ELEMENT ID	PLY ID	STRESSES IN LAYERED COMPOSITE ELEMENTS (QUAD4)			INTER-LAMINAR STRESSES			PRINCIPAL STRESSES (ZERO SHEAR)			MAX SHEAR
		NORMAL-1	NORMAL-2	SHEAR-12	SHEAR XZ-MAT	SHEAR YZ-MAT	ANGLE	MAJOR	MINOR		
0	26077	1.30344E+03	6.18135E+03	-1.05767E+02	-9.06731E+00	1.67210E+01	-88.76	6.18365E+03	1.30115E+03	2.44125E+03	
0	26077	1.33370E+03	5.13039E+03	-1.09343E+02	-1.66234E+01	3.06552E+01	-88.35	5.13354E+03	1.33055E+03	1.90150E+03	
0	26077	1.36395E+03	4.07943E+03	-1.12920E+02	-2.26683E+01	4.18025E+01	-87.62	4.08411E+03	1.35926E+03	1.36243E+03	
0	26077	2.73359E+03	1.75255E+03	-2.32633E+02	-2.54723E+01	4.72306E+01	-12.69	2.78596E+03	1.70018E+03	5.42888E+02	
0	26077	1.28952E+03	2.10603E+03	8.49011E+01	-2.73416E+01	5.08493E+01	84.13	2.11477E+03	1.28079E+03	4.16991E+02	
0	26077	1.45471E+03	9.26531E+02	-1.23650E+02	-2.88528E+01	5.36361E+01	-12.54	1.48222E+03	8.99017E+02	2.91603E+02	
0	26077	1.48496E+03	-1.24435E+02	-1.27227E+02	-2.88528E+01	5.36361E+01	-4.49	1.49496E+03	-1.34431E+02	8.14694E+02	
0	26077	1.51522E+03	-1.17540E+03	-1.30803E+02	-2.73416E+01	5.08493E+01	-2.78	1.52156E+03	-1.18174E+03	1.35165E+03	
0	26077	-9.11361E+02	1.14027E+02	-5.06026E+02	-2.54723E+01	4.72306E+01	-67.69	3.21692E+02	-1.11903E+03	7.20359E+02	
0	26077	-4.03078E+02	-1.39231E+03	6.53758E+02	-2.26683E+01	4.18025E+01	26.44	-7.79118E+01	-1.71748E+03	8.19784E+02	
0	26077	1.60598E+03	-4.32830E+03	-1.41533E+02	-1.66234E+01	3.06552E+01	-1.37	1.60935E+03	-4.33167E+03	2.97051E+03	
0	26077	1.63623E+03	-5.37926E+03	-1.45110E+02	-9.06731E+00	1.67210E+01	-1.18	1.63923E+03	-5.38226E+03	3.51075E+03	
0	26077	1.66648E+03	-6.43023E+03	-1.48687E+02	-3.89522E-13	8.65307E-13	-1.05	1.66921E+03	-6.43296E+03	4.05109E+03	

Figure 162: Trailing Edge σ_2 Component Tensile Critical Stress

Figure 162 shows the maximum tensile stress of 6.18 ksi in the trailing edge skin captured from the results file at the critical region. The margin of safety for this method of failure is shown below:

$$MS = \frac{\sigma_{allowable}}{FS \bullet \sigma_{actual}} - 1 = \frac{30810 \text{ psi}}{3 \bullet 6181 \text{ psi}} - 1 = .661$$

3.5.4.2 Compressive Stress

The trailing edge skin's most critical region in compression on the material σ_2 axis is in the inboard bay between the inboard and mid attachment points. Figure 163 shows the overall stress distribution in the trailing edge skin and Figure 164 shows the region in the skin found to be the most critical with the critical element highlighted.

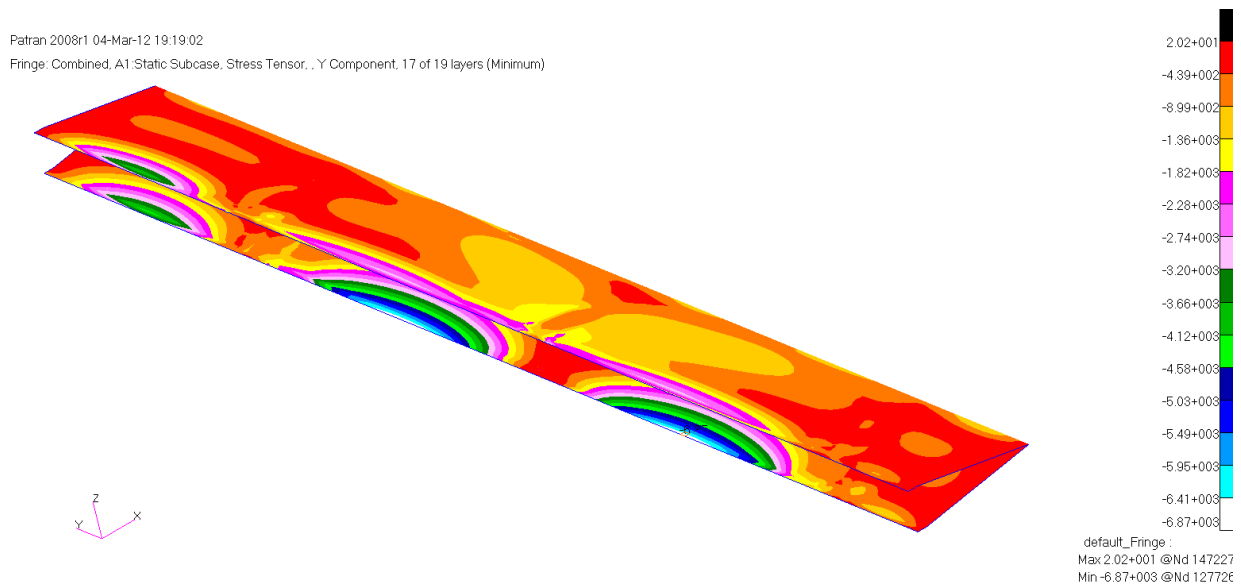


Figure 163: Trailing Edge σ_2 Component Compressive Stress Distribution

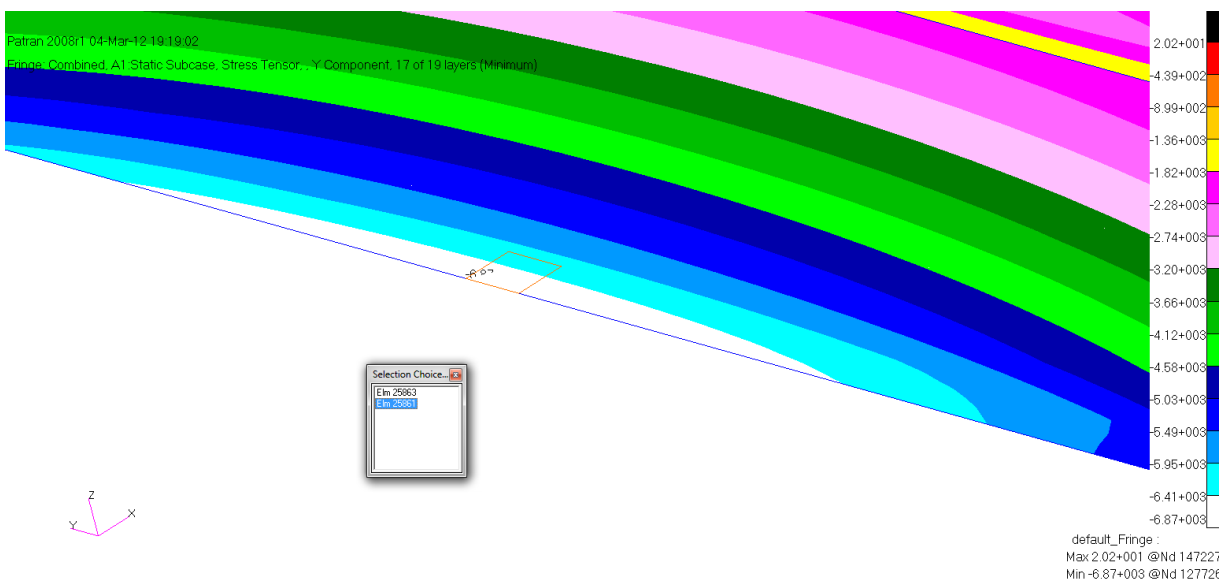


Figure 164: Trailing Edge σ_2 Component Compressive Stress Critical Region

		STRESSES IN LAYERED			COMPOSITE ELEMENTS (QUAD4)							
ELEMENT	PLY	STRESSES IN FIBER AND MATRIX DIRECTIONS			INTER-LAMINAR STRESSES			PRINCIPAL STRESSES (ZERO SHEAR)			MAX	
ID	ID	NORMAL-1	NORMAL-2	SHEAR-12	SHEAR XZ-MAT	SHEAR YZ-MAT	ANGLE	MAJOR	MINOR		SHEAR	
0	25860	7	1.66623E+03	-1.29319E+02	8.70578E+01	1.59191E+01	4.25342E+01	2.77	1.67044E+03	-1.33530E+02	9.01984E+02	
0	25860	8	1.68684E+03	-1.08069E+03	8.60930E+01	1.50853E+01	4.03242E+01	1.78	1.68951E+03	-1.08337E+03	1.38644E+03	
0	25860	9	1.13725E+02	-5.13874E+02	-5.00554E+02	1.40539E+01	3.74545E+01	-28.96	3.90708E+02	-7.90858E+02	5.90783E+02	
0	25860	10	-1.02479E+03	-3.61061E+02	6.33404E+02	1.25069E+01	3.31500E+01	58.83	2.21516E+01	-1.40800E+03	7.15075E+02	
0	25860	11	1.74867E+03	-3.93482E+03	8.31984E+01	9.17170E+00	2.43100E+01	0.84	1.74989E+03	-3.93604E+03	2.84296E+03	
0	25860	12	1.76928E+03	-4.88619E+03	8.22336E+01	5.00275E+00	1.32600E+01	0.71	1.77030E+03	-4.88721E+03	3.32875E+03	
0	25860	13	1.78990E+03	-5.83757E+03	8.12688E+01	2.14913E-13	6.86202E-13	0.61	1.79076E+03	-5.83843E+03	3.81460E+03	
0	25861	1	1.48502E+03	6.14530E+03	1.20458E+02	8.06660E+00	1.60195E+01	88.52	6.14841E+03	1.48191E+03	2.33325E+03	
0	25861	2	1.51659E+03	5.09868E+03	1.18775E+02	1.47888E+01	2.93692E+01	88.10	5.10261E+03	1.51265E+03	1.79498E+03	
0	25861	3	1.54815E+03	4.05206E+03	1.17092E+02	2.01665E+01	4.00489E+01	87.33	4.05752E+03	1.54269E+03	1.25742E+03	
0	25861	4	1.92459E+03	2.67691E+03	-2.05305E+02	2.26610E+01	4.52492E+01	-75.69	2.72929E+03	1.87221E+03	4.28543E+02	
0	25861	5	2.27007E+03	1.33125E+03	5.79976E+01	2.43240E+01	4.87161E+01	3.52	2.27364E+03	1.32768E+03	4.72982E+02	
0	25861	6	1.64284E+03	9.12204E+02	1.12044E+02	2.56685E+01	5.13861E+01	8.53	1.65964E+03	8.95408E+02	3.82114E+02	
0	25861	7	1.67440E+03	-1.34414E+02	1.10361E+02	2.56685E+01	5.13861E+01	3.48	1.68111E+03	-1.41123E+02	9.11118E+02	
0	25861	8	1.70597E+03	-1.18103E+03	1.08679E+02	2.43240E+01	4.87161E+01	2.15	1.71005E+03	-1.18512E+03	1.44759E+03	
0	25861	9	1.10001E+02	-6.77254E+02	-5.31234E+02	2.26610E+01	4.52492E+01	-26.73	3.77548E+02	-9.44801E+02	6.61175E+02	
0	25861	10	-1.23806E+03	-4.09638E+02	6.78542E+02	2.01665E+01	4.00489E+01	60.70	-2.88700E+01	-1.61882E+03	7.94976E+02	
0	25861	11	1.80066E+03	-4.32089E+03	1.03630E+02	1.47888E+01	2.93692E+01	0.97	1.80241E+03	-4.32264E+03	3.06253E+03	
0	25861	12	1.83222E+03	-5.36751E+03	1.01947E+02	8.06660E+00	1.60195E+01	0.81	1.83367E+03	-5.36895E+03	3.60131E+03	
0	25861	13	1.86379E+03	-5.92146E+03	1.00265E+02	3.46532E-13	8.29007E-13	0.69	1.86500E+03	-6.41534E+03	4.14017E+03	

Figure 165: Trailing Edge σ_2 Component Compressive Critical Stress

Figure 165 shows the maximum σ_2 component compressive stress of 6.41 ksi in the trailing edge captured from the results file at the critical region. The margin of safety for this method of failure is shown below:

$$MS = \frac{\sigma_{allowable}}{FS \bullet \sigma_{actual}} - 1 = \frac{-31590 psi}{3 \bullet -6414 psi} - 1 = .642$$

The trailing edge skin's most critical region in compression on the σ_1 axis is near the mid attachment points. Figure 166 shows the overall stress distribution in the trailing edge skin and Figure 167 shows the region in the skin found to be the most critical with the critical element highlighted.

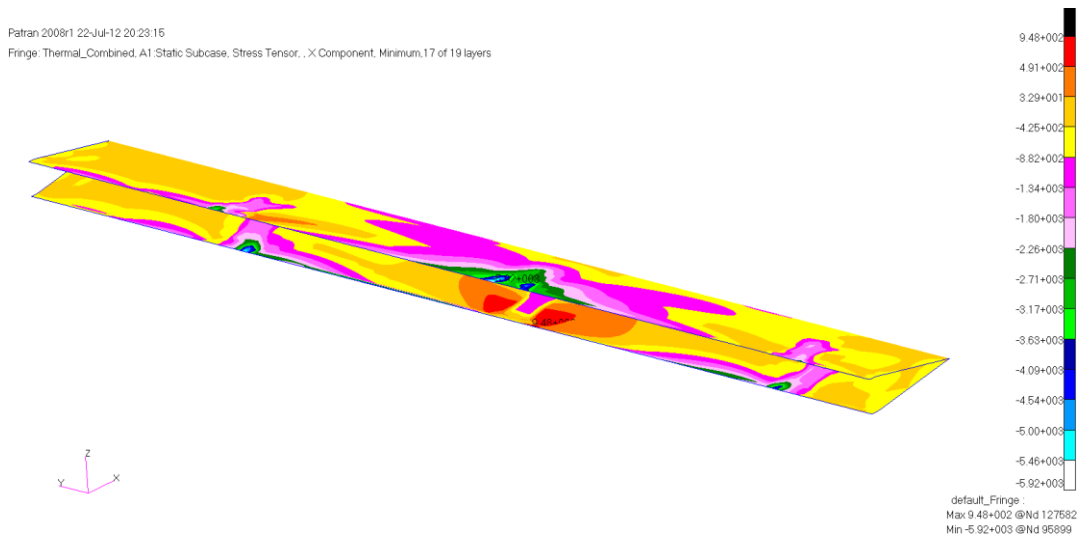


Figure 166: Trailing Edge σ_1 Component Compressive Stress Distribution

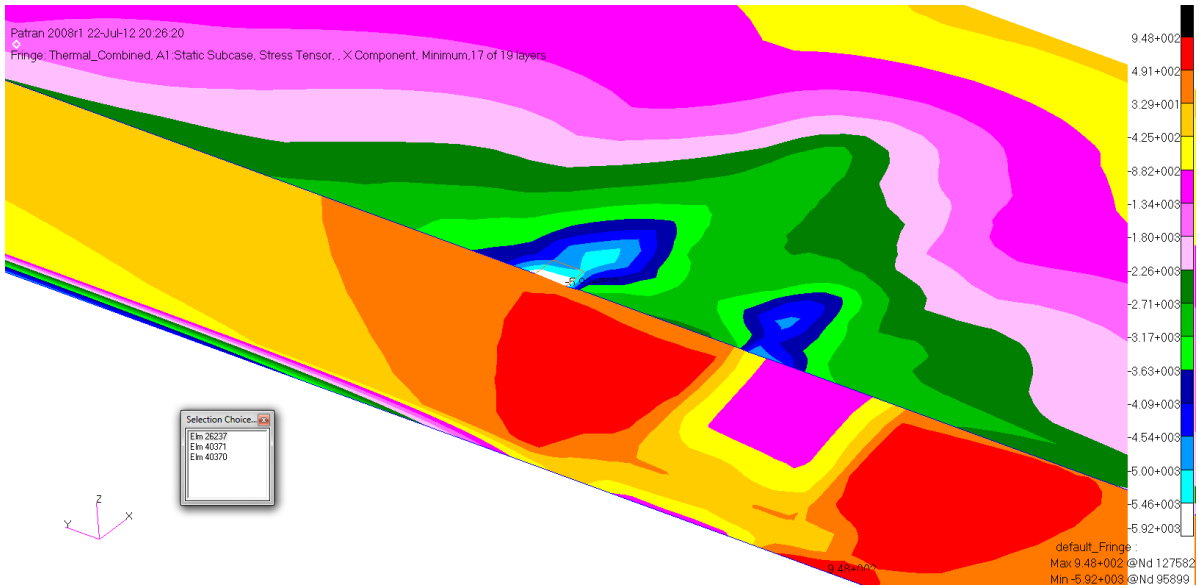


Figure 167: Trailing Edge σ_1 Component Compressive Stress Critical Region

STRESSES IN LAYERED					COMPOSITE ELEMENTS (QUAD4)							
STRESSES IN FIBER AND MATRIX DIRECTIONS					INTER-LAMINAR STRESSES			PRINCIPAL STRESSES (ZERO SHEAR)				MAX
ELEMENT	PLY	NORMAL-1	NORMAL-2	SHEAR-12	SHEAR XZ-MAT	SHEAR YZ-MAT	ANGLE	MAJOR	MINOR	SHEAR		
0	26236	10	-1.52595E+03	-2.61038E+03	-7.87464E+02	9.68003E+01	-1.36026E+01	-27.73	-1.11208E+03	-3.02425E+03	9.56082E+02	
0	26236	11	-5.41921E+03	9.41667E+02	-1.65171E+02	7.09869E+01	-9.97521E+00	-88.51	9.45953E+02	-5.42350E+03	3.18473E+03	
0	26236	12	-5.68433E+03	1.03751E+03	-1.72082E+02	3.87201E+01	-5.44102E+00	-88.53	1.04192E+03	-5.68873E+03	3.36532E+03	
0	26236	13	-5.94944E+03	1.13336E+03	-1.78993E+02	1.66338E-12	-2.81572E-13	-88.55	1.13788E+03	-5.95396E+03	3.54592E+03	
0	26237	1	1.84328E+02	-1.37211E+03	-6.20681E+02	2.71936E+01	-4.04899E+00	-19.29	4.01533E+02	-1.58932E+03	9.95426E+02	
0	26237	2	-3.58783E+03	1.63556E+03	-2.05546E+02	5.85994E+01	-8.50354E+00	-87.75	1.64363E+03	-3.59590E+03	2.61977E+03	
0	26237	3	-4.16647E+03	1.60106E+03	-1.99342E+02	7.74429E+01	-1.11763E+01	-88.02	1.60795E+03	-4.17335E+03	2.89065E+03	
0	26237	4	-2.29125E+03	-7.71001E+02	8.32771E+02	8.13277E+01	-1.17547E+01	66.19	-4.03606E+02	-2.65864E+03	1.12752E+03	
0	26237	5	-2.57487E+03	-1.08653E+03	9.03468E+02	7.74429E+01	-1.11763E+01	64.74	-6.60213E+02	-3.00119E+03	1.17049E+03	
0	26237	6	-5.90240E+03	1.49759E+03	-1.80728E+02	5.85994E+01	-8.50354E+00	-88.60	1.50200E+03	-5.90681E+03	3.70441E+03	
0	26237	7	-6.48105E+03	1.46310E+03	-1.74523E+02	2.71936E+01	-4.04899E+00	-88.74	1.46693E+03	-6.48488E+03	3.97590E+03	
0	26237	8	-2.13428E+03	-3.26338E+03	-1.11556E+03	0.0	0.0	-31.58	-1.44855E+03	-3.94910E+03	1.25027E+03	

Figure 168: Trailing Edge σ_1 Component Compressive Critical Stress

Figure 168 shows the maximum σ_1 compressive stress of 6.48 ksi in the trailing edge skin captured from the results file at the critical region. This again is a questionable stress concentration but since it is above the sizing condition it was conservatively assumed to be real. The margin of safety for this method of failure is shown below:

$$MS = \frac{\sigma_{allowable}}{FS \bullet \sigma_{actual}} - 1 = \frac{-36990 \text{ psi}}{3 \bullet -6481.1 \text{ psi}} - 1 = .902$$

3.5.4.3 Shear

The trailing edge skin's most critical region in τ_{12} shear is in the inboard bay between the inboard and mid attachment points. Figure 169 shows the overall stress distribution in the trailing edge skin and Figure 170 shows the region in the skin found to be the most critical with the critical element highlighted.

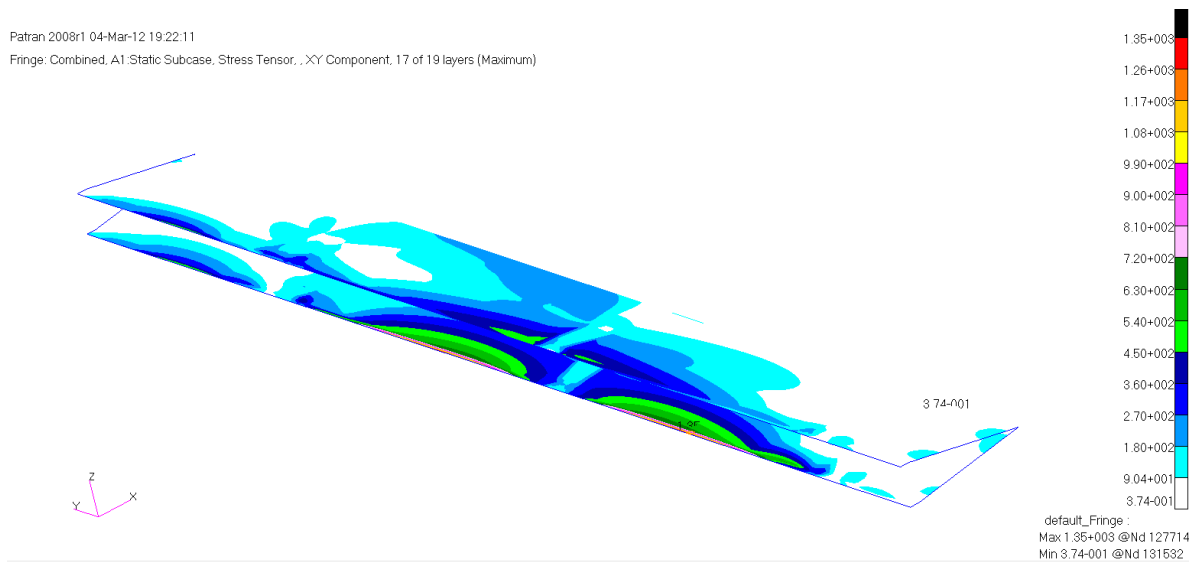


Figure 169: Trailing Edge τ_{12} Shear Stress Distribution

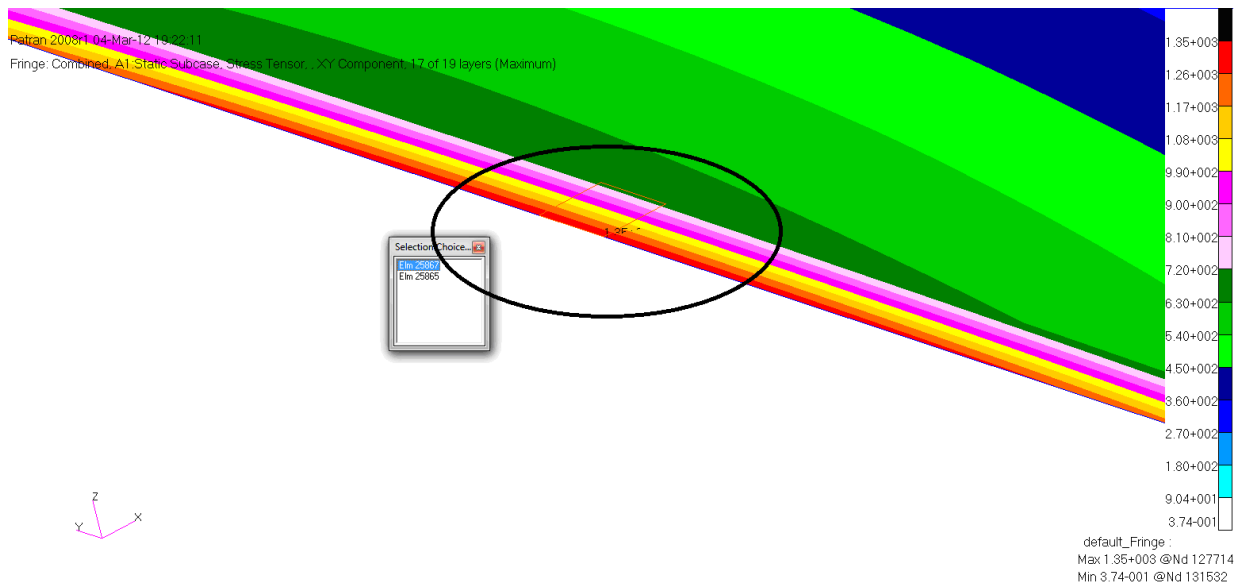


Figure 170: Trailing Edge τ_{12} Shear Stress Critical Region

STRESSES IN LAYERED COMPOSITE ELEMENTS (QUAD4)												
STRESSES IN FIBER AND MATRIX DIRECTIONS				INTER-LAMINAR STRESSES				PRINCIPAL STRESSES (ZERO SHEAR)				MAX
ELEMENT ID	PLY ID	NORMAL-1	NORMAL-2	SHEAR-12	SHEAR XZ-MAT	SHEAR YZ-MAT	ANGLE	MAJOR	MINOR			SHEAR
0	25867	1	1.65817E+03	6.01248E+03	1.84920E+02	8.18046E+00	1.48458E+01	87.57	6.02032E+03	1.65033E+03	2.18499E+03	
0	25867	2	1.69117E+03	4.98681E+03	1.71111E+02	1.49975E+01	2.72173E+01	87.04	4.99567E+03	1.68231E+03	1.65668E+03	
0	25867	3	1.72417E+03	3.96114E+03	1.57302E+02	2.04511E+01	3.71145E+01	86.00	3.97215E+03	1.71316E+03	1.12949E+03	
0	25867	4	1.86885E+03	2.82908E+03	-1.72605E+02	2.29809E+01	4.19339E+01	-80.11	2.85916E+03	1.83876E+03	5.10199E+02	
0	25867	5	2.39500E+03	1.33362E+03	2.79758E+01	2.46674E+01	4.51468E+01	1.51	2.39573E+03	1.33288E+03	5.31425E+02	
0	25867	6	1.82316E+03	8.84124E+02	1.15875E+02	2.60308E+01	4.76211E+01	6.93	1.83724E+03	8.70037E+02	4.83604E+02	
0	25867	7	1.85615E+03	-1.41548E+02	1.02066E+02	2.60308E+01	4.76211E+01	2.92	1.86135E+03	-1.46749E+02	1.00405E+03	
0	25867	8	1.88915E+03	-1.16722E+03	8.82568E+01	2.46674E+01	4.51468E+01	1.65	1.89170E+03	-1.16977E+03	1.53073E+03	
0	25867	9	9.56879E+01	-4.52993E+02	-5.50539E+02	2.29809E+01	4.19339E+01	-31.76	4.36454E+02	-7.93759E+02	6.15106E+02	
0	25867	10	-9.44405E+02	-4.56432E+02	6.95168E+02	2.04511E+01	3.71145E+01	54.67	3.63229E+01	-1.43716E+03	7.36741E+02	
0	25867	11	1.98814E+03	-4.24423E+03	4.68299E+01	1.49975E+01	2.72173E+01	0.43	1.98849E+03	-4.24459E+03	3.11654E+03	
0	25867	12	2.02114E+03	-5.26991E+03	3.30210E+01	8.18046E+00	1.48458E+01	0.26	2.02129E+03	-5.27005E+03	3.64567E+03	
0	25867	13	2.05414E+03	-6.29558E+03	1.92120E+01	3.51424E-13	7.68267E-13	0.13	2.05418E+03	-6.29562E+03	4.17490E+03	

Figure 171: Trailing Edge τ_{12} Shear Critical Stress

Figure 171 shows the maximum shear stress of .70 ksi in the trailing edge skin captured from the results file at the critical region. The discrepancy between the fringe plot due to the plotter averaging method which is looking at nodes in the upper skin. In addition there is a bend in the skin and the spar affects the skin in this area. Despite these local stress effects the skin can take all of the real and artificial load. The margin of safety for this method of failure is shown below:

$$MS = \frac{\tau_{allowable}}{FS \bullet \tau_{actual}} - 1 = \frac{9210psi}{3 \bullet 695.2psi} - 1 = 3.416$$

3.5.5 Spars

The most critical margin of safety for the upper skin is in tensile off axis failure as seen in Table 35. The figures are all presented in material coordinate systems. The materials in the spar are aligned down the fairing heading outboard which is at a slight angle from the global y axis. The results are presented in the same method as the previous section.

Table 35: Spar Failure Methods

Stress Type	Stress	Margin	Allowable	Load Case
Compressive on Axis	-7.45 (ksi)	0.655	-12.3 (ksi)	Thermal
Tensile on Axis	8.25 (ksi)	0.297	10.7 (ksi)	Thermal
Shear	1.66 (ksi)	0.846	3.1 (ksi)	No Thermal
Compressive off Axis	-9.42 (ksi)	0.118	-10.5 (ksi)	Thermal
Tensile off Axis	9.47 (ksi)	0.085	10.3 (ksi)	Thermal
Crippling	-9.42 (ksi)	0.093	-10.3 (ksi)	Thermal

3.5.5.1 Compressive Stress

The spar's most critical region in compressive stress on the σ_1 axis is on the forward spar between the mid and outboard attachment points. Figure 172 shows the overall stress distribution in the spar and Figure 173 shows the region in the spar found to be the most critical with the critical element highlighted.

Patran 2008r1 23-Jul-12 17:40:00
Fringe: Thermal_Combined, A1 Static Subcase, Stress Tensor, , X Component, Minimum, 17 of 19 layers

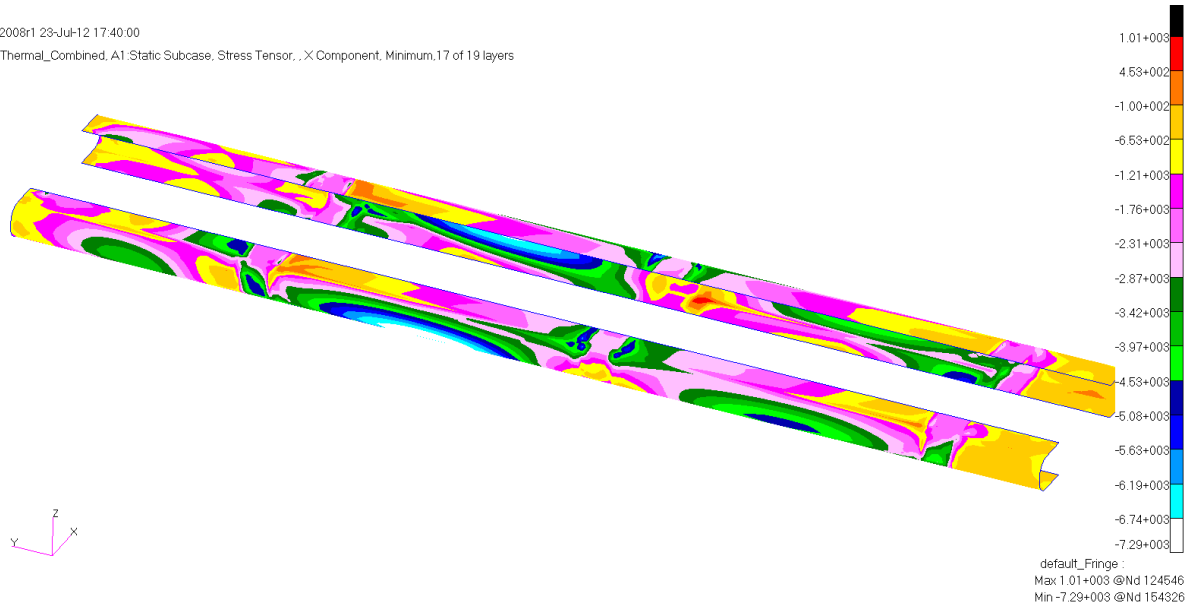


Figure 172: Spars σ_1 Component Compressive Stress Distribution

Patran 2008r1 23-Jul-12 17:40:00
Fringe: Thermal_Combined, A1 Static Subcase, Stress Tensor, , X Component, Minimum, 17 of 19 layers

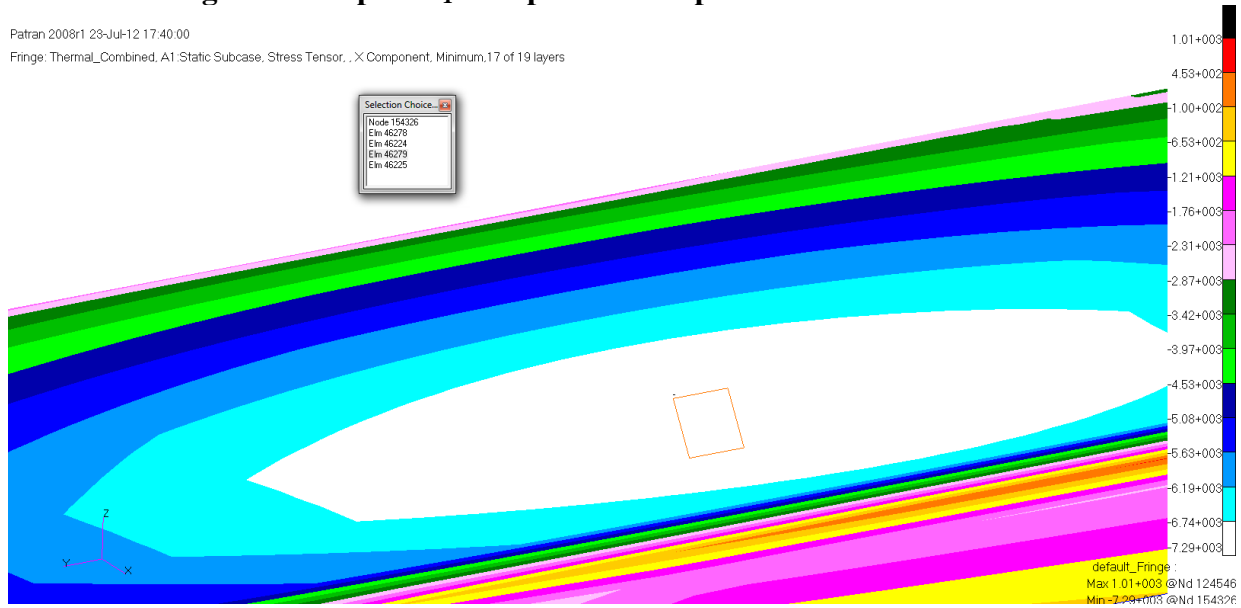


Figure 173: Spars σ_1 Component Compressive Stress Distribution

ELEMENT ID	PLY ID	STRESSES IN LAYERED			COMPOSITE ELEMENTS (QUAD4)			PRINCIPAL STRESSES (ZERO SHEAR)			MAX SHEAR
		NORMAL-1	NORMAL-2	SHEAR-12	SHEAR XZ-MAT	SHEAR YZ-MAT	ANGLE	MAJOR	MINOR		
0	46279	1	-7.45119E+03	-3.42880E+03	1.49606E+03	5.00114E-01	-9.71321E+00	71.68	-2.93339E+03	-7.94660E+03	2.50661E+03
0	46279	2	2.18316E+02	-9.17683E+03	5.04908E+02	1.19321E+00	-2.25366E+01	3.07	2.45372E+02	-9.20388E+03	4.72463E+03
0	46279	3	2.22503E+02	-7.62281E+03	5.07804E+02	1.77079E+00	-3.32227E+01	3.69	2.55235E+02	-7.65555E+03	3.95539E+03
0	46279	4	-1.11279E+03	-4.79280E+03	-8.59854E+02	2.05657E+00	-3.87731E+01	-12.52	-9.21794E+02	-4.98380E+03	2.03100E+03
0	46279	5	2.30878E+02	-4.51479E+03	5.13596E+02	2.40312E+00	-4.51848E+01	6.11	2.85826E+02	-4.56974E+03	2.42778E+03
0	46279	6	2.35066E+02	-2.96078E+03	5.16492E+02	2.63415E+00	-4.94592E+01	8.96	3.16465E+02	-3.04218E+03	1.67932E+03
0	46279	7	-2.61131E+03	1.30870E+03	2.23651E+02	2.70560E+00	-5.08468E+01	86.75	1.32142E+03	-2.62403E+03	1.97273E+03
0	46279	8	2.43441E+02	1.47241E+02	5.22284E+02	2.70560E+00	-5.08468E+01	42.37	7.19835E+02	-3.29153E+02	5.24494E+02
0	46279	9	-9.98022E+02	2.88787E+03	-2.00484E+02	2.63415E+00	-4.94592E+01	-87.05	2.89818E+03	-1.00834E+03	1.95326E+03
0	46279	10	2.51816E+02	3.25526E+03	5.28076E+02	2.40312E+00	-4.51848E+01	80.31	3.34541E+03	1.61673E+02	1.59187E+03
0	46279	11	2.56003E+02	4.80927E+03	5.30972E+02	2.05657E+00	-3.87731E+01	83.44	4.87037E+03	1.94905E+02	2.33773E+03
0	46279	12	5.51814E+03	1.35453E+03	8.36687E+02	1.77079E+00	-3.32227E+01	10.95	5.67998E+03	1.19268E+03	2.24365E+03
0	46279	13	2.64379E+02	7.91730E+03	5.36764E+02	1.19321E+00	-2.25366E+01	86.01	7.95476E+03	2.26914E+02	3.86392E+03
0	46279	14	2.68566E+02	9.47131E+03	5.39660E+02	5.00114E-01	-9.71321E+00	86.66	9.50285E+03	2.37028E+02	4.63291E+03
0	46279	15	3.84185E+03	7.62537E+03	-1.47289E+03	3.45338E-14	-6.42275E-13	-71.05	8.13114E+03	3.33608E+03	2.39753E+03

Figure 174: Spars σ_1 Component Compressive Critical Stress

Figure 174 shows the maximum σ_1 component compressive stress of 7.45 ksi in the spar captured from the results file at the critical region. The margin of safety for this method of failure is shown below:

$$MS = \frac{\sigma_{allowable}}{FS \bullet \sigma_{actual}} - 1 = \frac{-36990 psi}{3 \bullet -7451.2 psi} - 1 = .655$$

The spar's most critical region in compressive stress on the σ_2 axis is on the forward spar between the mid and outboard attachment points. Figure 175 shows the overall stress distribution in the spar and Figure 176 shows the region in the spar found to be the most critical with the critical element highlighted.

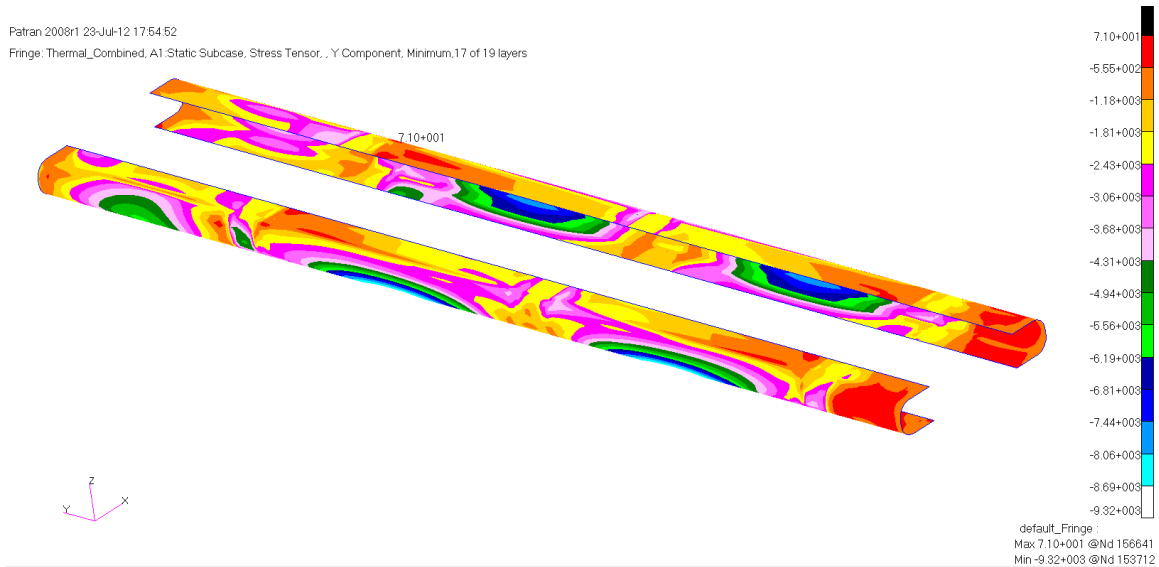


Figure 175: Spars σ_2 Component Compressive Stress Distribution

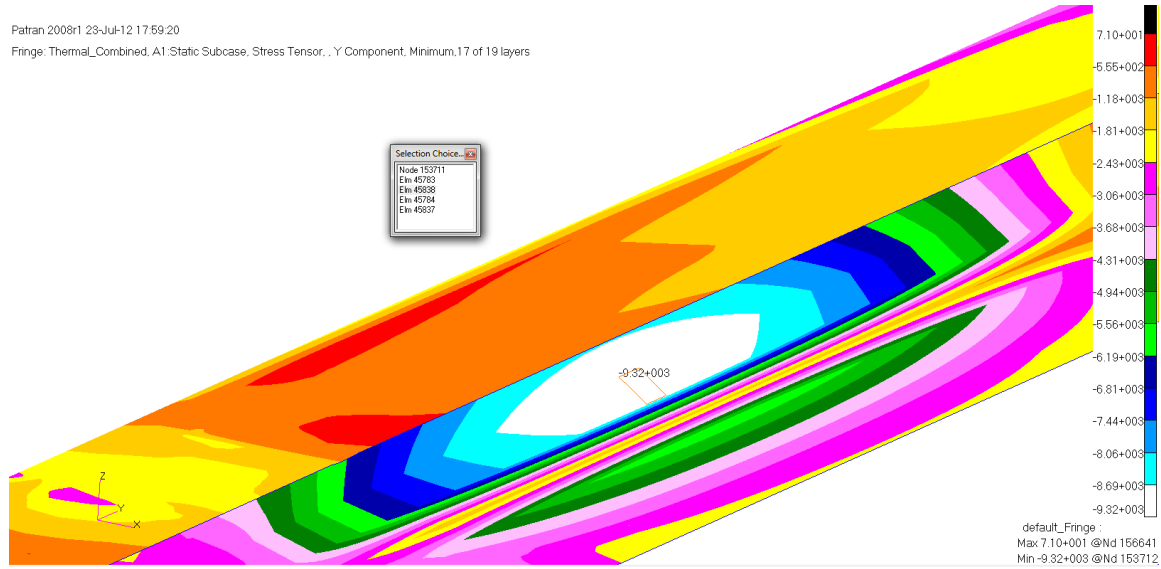


Figure 176: Spars σ_2 Component Compressive Stress Critical Region

ELEMENT ID	PLY ID	STRESSES IN LAYERED COMPOSITE ELEMENTS (QUAD4)			INTER-LAMINAR STRESSES			PRINCIPAL STRESSES (ZERO SHEAR)			MAX SHEAR
		NORMAL-1	NORMAL-2	SHEAR-12	SHEAR XZ-MAT	SHEAR YZ-MAT	ANGLE	MAJOR	MINOR		
0	45838	1	-3.52672E+03	-6.45598E+03	1.66466E+03	-4.36645E+00	8.59435E+00	24.33	-2.77408E+03	-7.20861E+03	2.21726E+03
0	45838	2	1.22084E+03	-9.42042E+03	-4.23511E+02	-1.04178E+01	1.99406E+01	-2.28	1.23766E+03	-9.43725E+03	5.33746E+03
0	45838	3	1.20735E+03	-7.84947E+03	-4.23386E+02	-1.54606E+01	2.93958E+01	-2.67	1.22710E+03	-7.86922E+03	4.54816E+03
0	45838	4	-4.32228E+03	-1.02379E+03	-1.01460E+03	-1.79558E+01	3.43069E+01	-74.20	-7.36693E+02	-4.60938E+03	1.93634E+03
0	45838	5	1.18039E+03	-4.70757E+03	-4.23134E+02	-2.09814E+01	3.99800E+01	-4.09	1.21065E+03	-4.73782E+03	2.97423E+03
0	45838	6	1.16691E+03	-3.13662E+03	-4.23008E+02	-2.29986E+01	4.37621E+01	-5.56	1.20810E+03	-3.17780E+03	2.19295E+03
0	45838	7	1.37727E+03	-1.77889E+03	3.64536E+02	-2.36223E+01	4.49898E+01	6.50	1.41882E+03	-1.82045E+03	1.61963E+03
0	45838	8	1.13995E+03	5.28683E+00	-4.22756E+02	-2.36223E+01	4.49898E+01	-18.35	1.28014E+03	-1.34904E+02	7.07523E+02
0	45838	9	3.01193E+03	-2.19860E+02	-6.88396E+01	-2.29986E+01	4.37621E+01	-1.22	3.01339E+03	-2.21325E+02	1.61736E+03
0	45838	10	1.11299E+03	3.14719E+03	-4.22504E+02	-2.09814E+01	3.99800E+01	-78.72	3.23145E+03	1.02873E+03	1.10136E+03
0	45838	11	1.09951E+03	4.71814E+03	-4.22378E+02	-1.79558E+01	3.43069E+01	-83.43	4.76679E+03	1.05086E+03	1.85796E+03
0	45838	12	2.22409E+03	5.20496E+03	7.18904E+02	-1.54606E+01	2.93958E+01	77.12	5.36928E+03	2.05977E+03	1.65476E+03
0	45838	13	1.07255E+03	7.86004E+03	-4.22126E+02	-1.04178E+01	1.99406E+01	-86.45	7.88619E+03	1.04640E+03	3.41990E+03
0	45838	14	1.05907E+03	9.43099E+03	-4.22000E+02	-4.36645E+00	8.59435E+00	-87.12	9.45221E+03	1.03785E+03	4.20718E+03
0	45838	15	7.91591E+03	4.45723E+03	-1.36897E+03	-3.01512E-13	5.68292E-13	-19.18	8.39217E+03	3.98096E+03	2.20560E+03

Figure 177: Spars σ_2 Component Compressive Critical Stress

Figure 177 shows the maximum compressive stress of 9.42 ksi in the spars captured from the results file at the critical region. The margin of safety for this method of failure is shown below:

$$MS = \frac{\sigma_{allowable}}{FS \bullet \sigma_{actual}} - 1 = \frac{-31590 \text{ psi}}{3 \bullet -9420.4 \text{ psi}} - 1 = .118$$

To determine the crippling failure point of the spars the equation below from Reference 23 was used. This equation is typically used on metallic spar caps and stiffeners but since the laminate is not an extreme family and contains a balanced amount of angled plies it was deemed to be sufficient. The values for the equation and their sources are shown in Table 36.

$$\sigma_{cc} = \alpha \sigma_c \left[\frac{\pi^2 C}{12(1-\nu^2) \left(\sqrt{\frac{\sigma_c}{E}} \frac{b}{t} \right)^2} \right]^{1-n}$$

Table 36: Spar Crippling Terms

Item	Value	Reference	Item	Value	Reference
α	0.8	[23]	E	4220 ksi	Table 27
n	0.6	[23]	t	0.152 in	Section 3.6
ν	0.14	Table 27	b	2.5 in	Section 3.6
σ_c	31.6 ksi	Table 27			

$$\sigma_{cc} = .8 \cdot (31.6 \text{ ksi}) \left[\frac{\pi^2 (4)}{12(1-.14^2) \left(\sqrt{\frac{31.6 \text{ ksi}}{4220 \text{ ksi}}} \frac{2.5 \text{ in}}{.152 \text{ in}} \right)^2} \right]^{1-.6} = 30.9 \text{ ksi}$$

The results for the crippling equation are shown above. They take very little off of the compressive allowable for the spar. A margin of safety for crippling is shown below.

$$MS = \frac{\sigma_{allowable}}{FS \bullet \sigma_{actual}} - 1 = \frac{-30900 \text{ psi}}{3 \bullet -9364 \text{ psi}} - 1 = .1012$$

3.5.5.2 Tensile Stress

The spar's most critical region in tensile stress on the σ_1 axis is on the forward spar between the mid and inboard attachment points. Figure 178 shows the overall stress distribution in the spar and Figure 179 shows the region in the spar found to be the most critical with the critical element highlighted.

Patran 2008r1 04-Mar-12 20:01:09
 Fringe: Combined, A1 Static Subcase, Stress Tensor, X Component, 17 of 19 layers (Maximum)

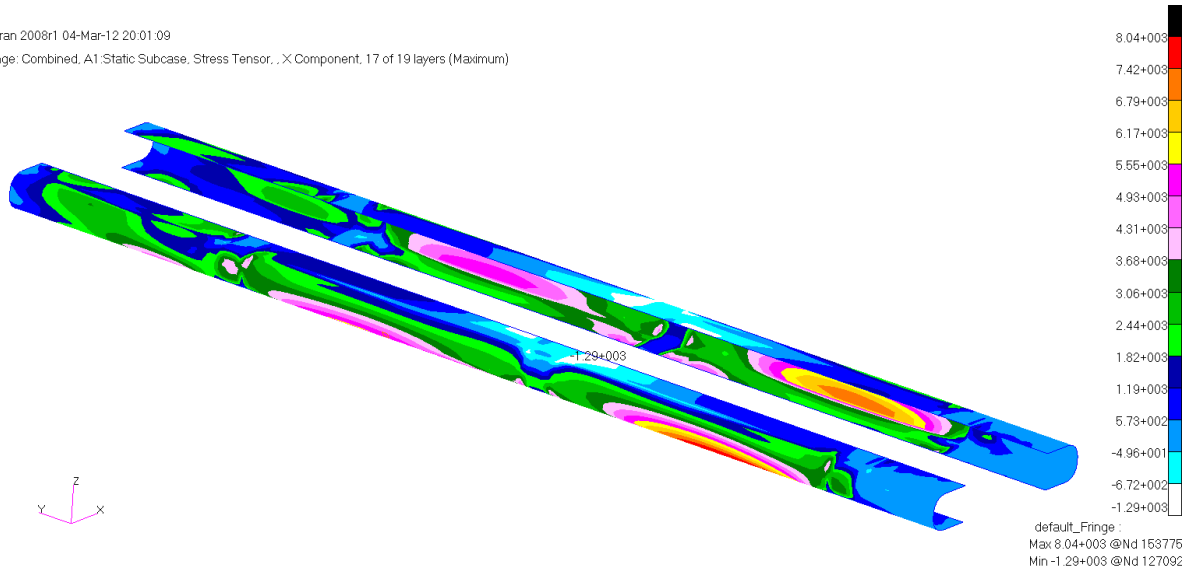


Figure 178: Spars σ_1 Component Tensile Stress Distribution

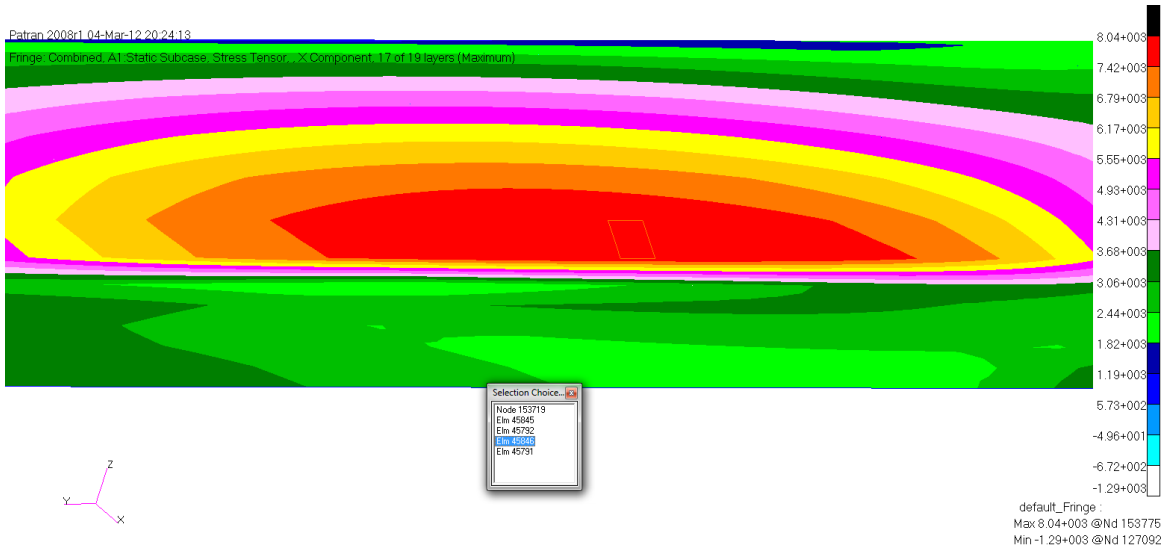


Figure 179: Spars σ_1 Component Tensile Stress Critical Region

0	45846	1	-3.66899E+03	-5.18765E+03	1.44753E+03	-2.25857E+00	7.20902E+00	27.35	-2.92026E+03	-6.46750E+03	1.77362E+03	
0	45846	2	7.06185E+02	-8.47084E+03	-3.31820E+02	-5.38868E+00	1.67263E+01	-2.07	7.18167E+02	-8.48282E+03	4.60049E+03	
0	45846	3	6.95258E+02	-7.04468E+03	-3.59408E+02	-7.99711E+00	2.46574E+01	-2.65	7.11911E+02	-7.06133E+03	3.88662E+03	
0	45846	4	-4.09152E+03	-1.06902E+03	-8.57893E+02	-9.28772E+00	2.87769E+01	-75.21	-8.42493E+02	-4.31804E+03	1.73777E+03	
0	45846	5	6.73404E+02	-4.19237E+03	-4.14585E+02	-1.08528E+01	3.35355E+01	-4.84	7.08475E+02	-4.22744E+03	2.46796E+03	
0	45846	6	6.62477E+02	-2.76621E+03	-4.42173E+02	-1.18961E+01	3.67080E+01	-7.23	7.18582E+02	-2.82232E+03	1.77045E+03	
0	45846	7	1.42459E+03	-2.07646E+03	2.68258E+02	-1.22188E+01	3.77378E+01	4.36	1.44502E+03	-2.09689E+03	1.77096E+03	
1	THIS IS A DEFAULT SUBCASE.							MARCH	4, 2012	MD NASTRAN	5/ 9/08	PAGE 13226
SUBCASE 1												
STRESSES IN LAYERED COMPOSITE ELEMENTS (QUAD4)												
ELEMENT	PLY	STRESSES IN FIBER AND MATRIX DIRECTIONS			INTER-LAMINAR STRESSES			PRINCIPAL STRESSES (ZERO SHEAR)			MAX	
ID	ID	NORMAL-1	NORMAL-2	SHEAR-12	SHEAR XZ-MAT	SHEAR YZ-MAT	ANGLE	MAJOR	MINOR	SHEAR		
0	45846	8	6.40622E+02	8.61029E+01	-4.97350E+02	-1.22188E+01	3.77378E+01	-30.43	9.32774E+02	-2.06049E+02	5.63412E+02	
0	45846	9	3.12245E+03	-8.62354E+02	-1.24832E+02	-1.18961E+01	3.67080E+01	-1.79	3.12635E+03	-8.66261E+02	1.99631E+03	
0	45846	10	6.18768E+02	2.93842E+03	-5.52526E+02	-1.08528E+01	3.35355E+01	-77.26	3.06330E+03	4.93883E+02	1.28471E+03	
0	45846	11	6.07841E+02	4.36457E+03	-5.80115E+02	-9.28772E+00	2.87769E+01	-81.42	4.45211E+03	5.20300E+02	1.96591E+03	
0	45846	12	1.00650E+03	5.40055E+03	7.14467E+02	-7.99711E+00	2.46574E+01	80.99	5.51381E+03	8.93247E+02	2.31028E+03	
0	45846	13	5.85987E+02	7.21689E+03	-6.35291E+02	-5.38868E+00	1.67263E+01	-84.58	7.27720E+03	5.25670E+02	3.37577E+03	
0	45846	14	5.75060E+02	8.64304E+03	-6.62880E+02	-2.25857E+00	7.20902E+00	-85.33	8.69714E+03	5.20959E+02	4.08809E+03	
0	45846	15	8.21603E+02	2.77995E+03	-1.30410E+03	-1.55959E-13	4.76688E-13	-12.82	8.51269E+03	2.48329E+03	3.01470E+03	

Figure 180: Spars σ_1 Component Tensile Critical Stress

Figure 180 shows the maximum σ_1 component tensile stress of 8.22 ksi in the spars captured from the results file at the critical region. The margin of safety for this method of failure is shown below:

$$MS = \frac{\sigma_{allowable}}{FS \bullet \sigma_{actual}} - 1 = \frac{32100 psi}{3 \bullet 8216 psi} - 1 = .302$$

The spar's most critical region in tensile stress on the material σ_2 axis is on the forward spar between the mid and inboard attachment points. Figure 181 shows the overall stress distribution in the spar and Figure 182 shows the region in the spar found to be the most critical with the critical element highlighted.

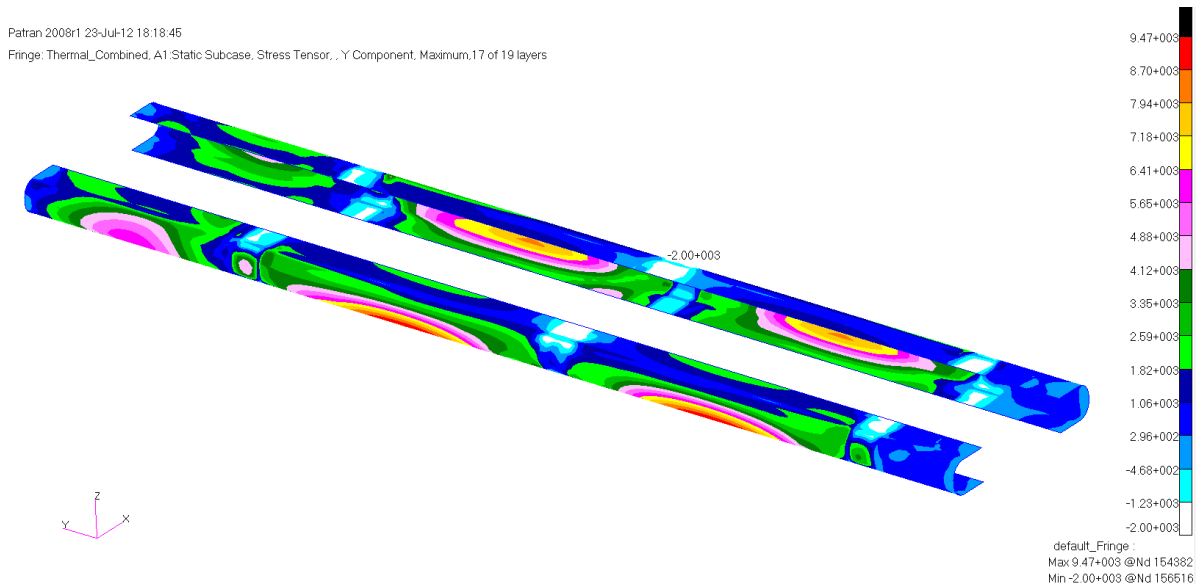


Figure 181: Spars σ_2 Component Tensile Stress Distribution

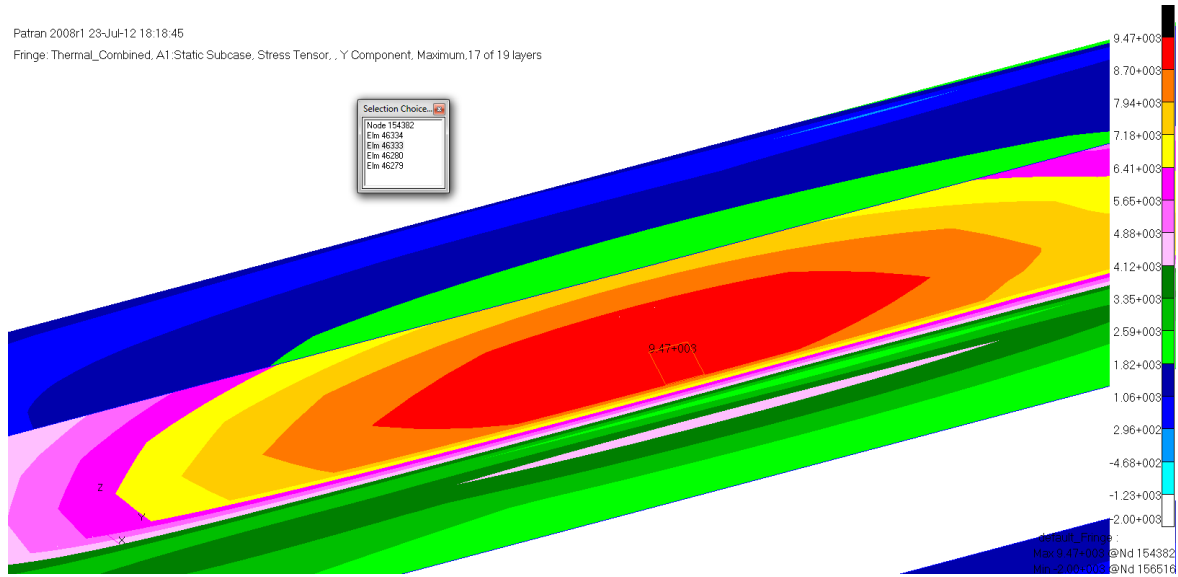


Figure 182: Spars σ_2 Component Tensile Critical Stress

ELEMENT		STRESSES IN LAYERED			COMPOSITE ELEMENTS (QUAD4)			PRINCIPAL STRESSES (ZERO SHEAR)			MAX
ID	PLY	NORMAL-1	NORMAL-2	SHEAR-12	SHEAR XZ-MAT	SHEAR YZ-MAT	ANGLE	MAJOR	MINOR	SHEAR	
0	46333	1	-7.05720E+03	-3.25473E+03	1.62090E+03	4.63470E+00	8.90101E+00	69.78	-2.65757E+03	-7.65436E+03	2.49840E+03
0	46333	2	9.69961E+02	-9.34487E+03	4.78230E+02	1.10578E+01	2.06521E+01	2.65	9.92086E+02	-9.36699E+03	5.17954E+03
0	46333	3	9.58502E+02	-7.77736E+03	4.81981E+02	1.64105E+01	3.04447E+01	3.15	9.85014E+02	-7.80387E+03	4.39444E+03
0	46333	4	-9.22431E+02	-4.42897E+03	-9.73035E+02	1.90589E+01	3.55310E+01	-14.51	-6.70519E+02	-4.68088E+03	2.00518E+03
0	46333	5	9.35584E+02	-4.64233E+03	4.89483E+02	2.22704E+01	4.14065E+01	4.98	9.78212E+02	-4.68496E+03	2.83159E+03
0	46333	6	9.24125E+02	-3.07482E+03	4.93234E+02	2.44115E+01	4.53235E+01	6.93	9.84063E+02	-3.13476E+03	2.05941E+03
0	46333	7	-2.24143E+03	1.49730E+03	3.25174E+02	2.50736E+01	4.65951E+01	85.07	1.52537E+03	-2.26951E+03	1.89744E+03
0	46333	8	9.01207E+02	6.01959E+01	5.00736E+02	2.50736E+01	4.65951E+01	24.99	1.13458E+03	-1.73180E+02	6.53882E+02
0	46333	9	-6.36179E+02	3.08131E+03	-1.06734E+02	2.44115E+01	4.53235E+01	-88.36	3.08438E+03	-6.39241E+02	1.86181E+03
0	46333	10	8.78289E+02	3.19522E+03	5.08238E+02	2.22704E+01	4.14065E+01	78.16	3.30180E+03	7.71705E+02	1.26505E+03
0	46333	11	8.66830E+02	4.76273E+03	5.11989E+02	1.90589E+01	3.55310E+01	82.64	4.82889E+03	8.00669E+02	2.01411E+03
0	46333	12	5.72884E+03	1.68774E+03	7.54595E+02	1.64105E+01	3.04447E+01	10.24	5.86515E+03	1.55143E+03	2.15686E+03
0	46333	13	8.43912E+02	7.89775E+03	5.19492E+02	1.10578E+01	2.06521E+01	85.81	7.93580E+03	8.05858E+02	3.56497E+03
0	46333	14	8.32453E+02	9.46526E+03	5.23243E+02	4.63470E+00	8.90101E+00	86.54	9.49686E+03	8.00854E+02	4.34800E+03
0	46333	15	4.17959E+03	7.83335E+03	-1.40246E+03	3.20035E-13	5.88569E-13	-71.24	8.30959E+03	3.70334E+03	2.30312E+03

Figure 183: Spars σ_2 Component Tensile Critical Stress

Figure 183 shows the maximum σ_2 component tensile stress of 9.4 ksi in the spars captured from the results file at the critical region. The margin of safety for this method of failure is shown below:

$$MS = \frac{\sigma_{allowable}}{FS \cdot \sigma_{actual}} - 1 = \frac{30810 \text{ psi}}{3 \cdot 9399 \text{ psi}} - 1 = .093$$

3.5.5.3 Shear

The spar's most critical region in τ_{12} shear stress is on the forward spar between the mid and inboard attachment points. Figure 184 shows the overall stress distribution in the spar and

Figure 185 shows the region in the spar found to be the most critical with the critical element highlighted.

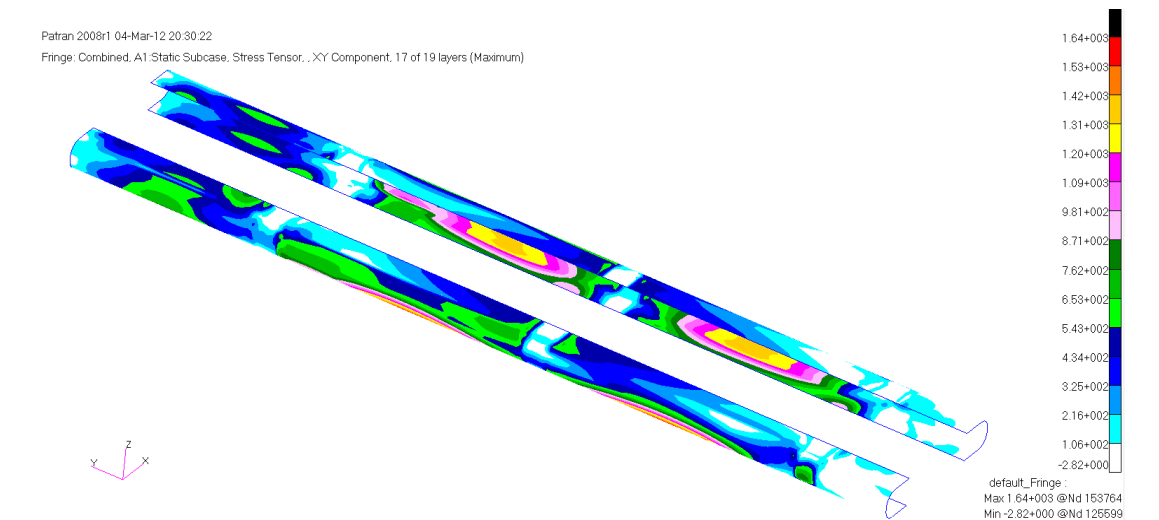


Figure 184: Spars τ_{12} Shear Stress Distribution

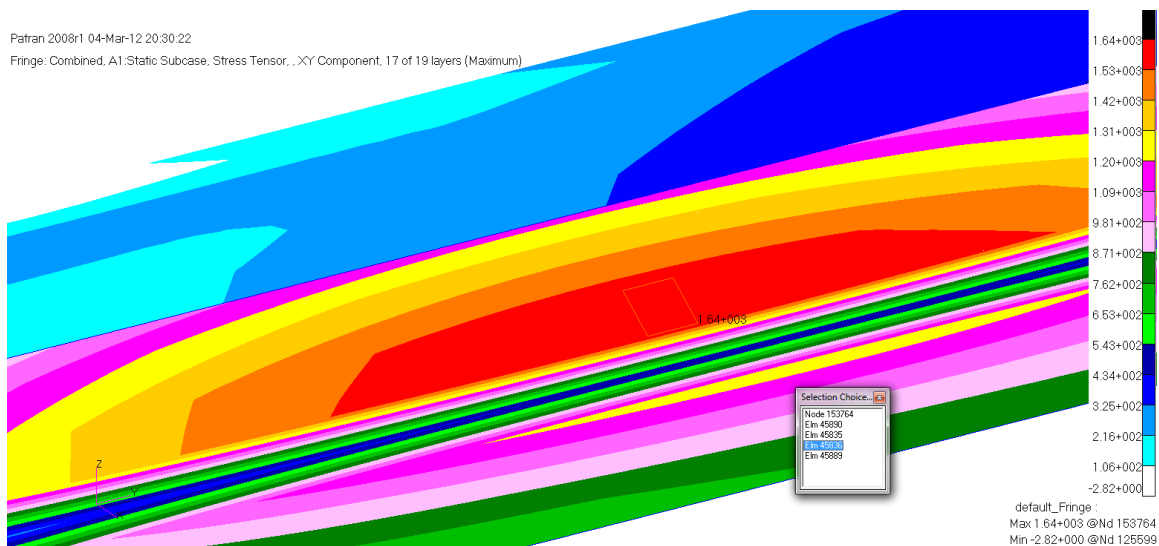


Figure 185: Spars τ_{12} Shear Stress Distribution

0	45836	1	-3.32695E+03	-6.41450E+03	1.66303E+03	-4.79975E+00	7.54122E+00	23.56	-2.60160E+03	-7.13985E+03	2.26912E+03				
0	45836	2	1.33446E+03	-9.31871E+03	-4.36817E+02	-1.14516E+01	1.74971E+01	-2.34	1.35234E+03	-9.33659E+03	5.34446E+03				
0	45836	3	1.31921E+03	-7.76790E+03	-4.29636E+02	-1.69949E+01	2.57937E+01	-2.70	1.33948E+03	-7.78817E+03	4.56382E+03				
0	45836	4	-4.23191E+03	-9.43580E+02	-1.02055E+03	-1.97376E+01	3.01030E+01	-74.09	-6.52599E+02	-4.52289E+03	1.93514E+03				
0	45836	5	1.28872E+03	-4.66628E+03	-4.15274E+02	-2.30635E+01	3.50809E+01	-3.97	1.31754E+03	-4.69510E+03	3.00632E+03				
0	45836	6	1.27348E+03	-3.11548E+03	-4.08093E+02	-2.52808E+01	3.83995E+01	-5.27	1.31110E+03	-3.15310E+03	2.23210E+03				
0	45836	7	1.34590E+03	-1.64818E+03	3.78059E+02	-2.59665E+01	3.94769E+01	7.09	1.39290E+03	-1.69518E+03	1.54404E+03				
1	THIS IS A DEFAULT SUBCASE.										MARCH	4, 2012	MD NASTRAN	5/ 9/08	PAGE 13220
0															
SUBCASE 1															
STRESSES IN LAYERED COMPOSITE ELEMENTS (QUAD4)															
STRESSES IN FIBER AND MATRIX DIRECTIONS INTER-LAMINAR STRESSES PRINCIPAL STRESSES (ZERO SHEAR) MAX															
ELEMENT	PLY	NORMAL-1	NORMAL-2	SHEAR-12	SHEAR XZ-MAT	SHEAR YZ-MAT	ANGLE	MAJOR	MINOR	SHEAR					
ID	ID														
0	45836	8	1.24299E+03	-1.38602E+01	-3.93731E+02	-2.59665E+01	3.94769E+01	-16.03	1.35614E+03	-1.27016E+02	7.41579E+02				
0	45836	9	2.90352E+03	-5.94127E+01	-5.02654E+01	-2.52808E+01	3.83995E+01	-0.97	2.90437E+03	-6.02652E+01	1.48232E+03				
0	45836	10	1.21249E+03	3.08776E+03	-3.79368E+02	-2.30635E+01	3.50809E+01	-78.99	3.16160E+03	1.13865E+03	1.01147E+03				
0	45836	11	1.19725E+03	4.63856E+03	-3.72187E+02	-1.97376E+01	3.01030E+01	-83.90	4.67836E+03	1.15746E+03	1.76045E+03				
0	45836	12	2.43935E+03	4.99161E+03	6.92752E+02	-1.69949E+01	2.57937E+01	75.75	5.16752E+03	2.26345E+03	1.45204E+03				
0	45836	13	1.16676E+03	7.74018E+03	-3.57825E+02	-1.14516E+01	1.74971E+01	-86.89	7.75960E+03	1.14734E+03	3.30613E+03				
0	45836	14	1.15151E+03	9.29099E+03	-3.50644E+02	-4.79975E+00	7.54122E+00	-87.54	9.30607E+03	1.13643E+03	4.08482E+03				
0	45836	15	7.57637E+03	4.70690E+03	-1.33524E+03	-3.31432E-13	4.98655E-13	-21.47	8.10157E+03	4.18171E+03	1.95993E+03				

Figure 186: Spars τ_{12} Shear Critical Stress

Figure 186 shows the maximum shear stress of 1.66 ksi in the spars captured from the results file at the critical region. The margin of safety for this method of failure is shown below:

$$MS = \frac{\tau_{allowable}}{FS \bullet \tau_{actual}} - 1 = \frac{9210psi}{3 \bullet 1663psi} - 1 = .846$$

3.5.6 Ribs

The most critical margin of safety for the ribs is in tensile failure as seen in Table 37. The figures are all presented in material coordinate systems. The materials in the ribs are aligned down the global x axis which goes down the fuselage stations of the fairing. The results are presented in the same order as the previous section. As previously mentioned to simplify tooling and reduce costs the ribs are made from spar cross sections which have been cut down. This made the ribs quite a bit stronger than what was required. This helped speed the analysis since the ribs are a complex structure with many local stress influences and instead of having to size for these complex interactions a thicker solution was chosen to cut time and save cost. For these reasons the margins of safety are quite high despite very conservative methods.

Table 37: Rib Failure Methods

Stress Type	Stress	Margin	Allowable	Load Case
Compressive on Axis	-5.85 (ksi)	1.107	-12.3 (ksi)	No Thermal
Tensile on Axis	6.24 (ksi)	0.715	10.7 (ksi)	Thermal
Shear	0.83 (ksi)	2.701	3.1 (ksi)	Thermal
Compressive off Axis	-5.14 (ksi)	1.050	-10.5 (ksi)	Thermal
Tensile off Axis	6.08 (ksi)	0.688	10.3 (ksi)	No Thermal

3.5.6.1 Compressive Strength

The rib's most critical region in compressive stress on the σ_1 axis is on the rib near the lower skin at the inboard attachment point. Figure 187 shows the overall stress distribution in the ribs and Figure 188 shows the region in the ribs found to be the most critical with the critical element highlighted.

Patran 2008r1 04-Mar-12 21:22:47
 Fringe: Combined, A1 Static Subcase, Stress Tensor, .X Component, 17 of 19 layers (Minimum)

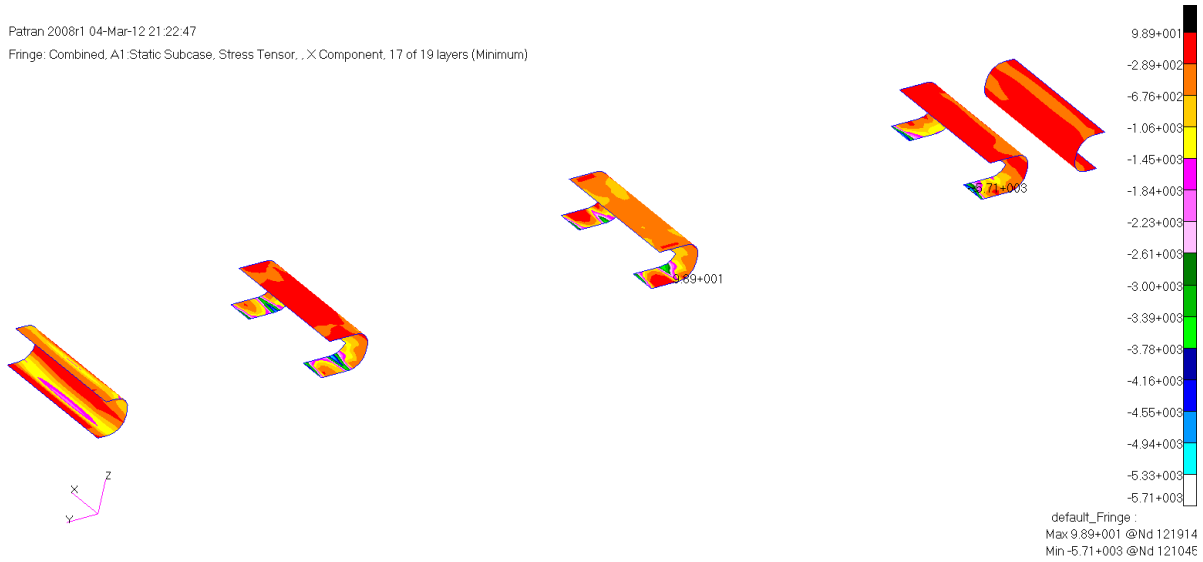


Figure 187: Ribs σ_1 Component Compressive Stress Distribution

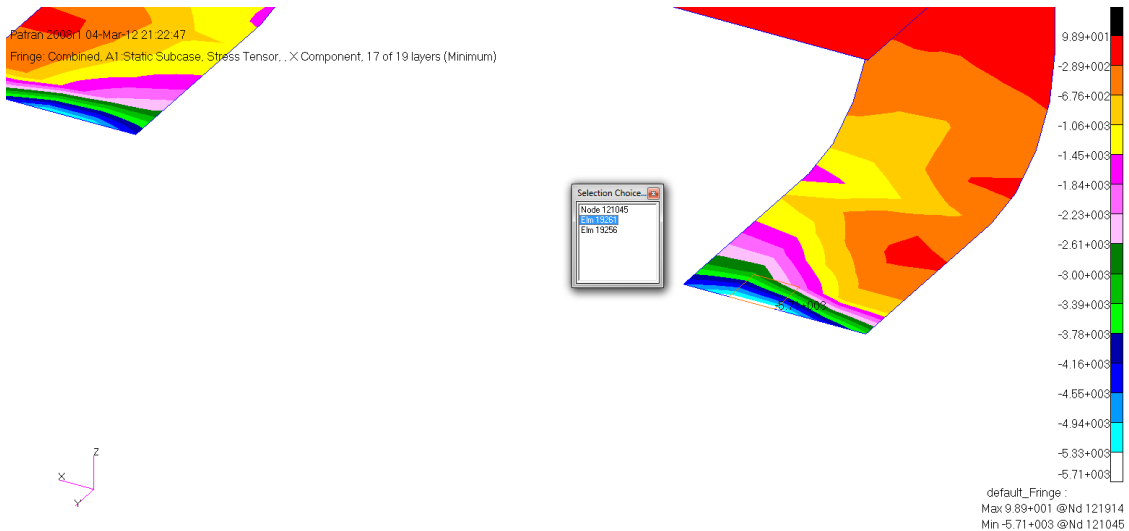


Figure 188: Ribs σ_1 Component Compressive Stress Critical Region

ELEMENT ID	PLY ID	STRESSES IN FIBER AND MATRIX DIRECTIONS			COMPOSITE ELEMENTS (QUAD4)			INTER-LAMINAR STRESSES			PRINCIPAL STRESSES (ZERO SHEAR)			MAX SHEAR
		NORMAL-1	NORMAL-2	SHEAR-12	SHEAR XZ-MAT	SHEAR YZ-MAT	ANGLE	MAJOR	MINOR		MAJOR	MINOR		
0	19261	1	5.82414E+03	1.30448E+03	2.57085E+02	2.67715E+01	1.80113E+01	3.25	5.83872E+03	1.28991E+03	2.27441E+03	2.27441E+03		
0	19261	2	3.84529E+03	2.15797E+03	-5.04344E+02	6.38735E+01	4.17897E+01	-15.44	3.98455E+03	2.01871E+03	9.82319E+02	9.82319E+02		
0	19261	3	3.10755E+03	1.82917E+03	-4.28090E+02	9.47918E+01	6.16050E+01	-16.91	3.23767E+03	1.69905E+03	7.69306E+02	7.69306E+02		
0	19261	4	6.22635E+02	3.16474E+03	-1.03589E+02	1.10090E+02	7.18972E+01	-87.67	3.16895E+03	6.18421E+02	1.27526E+03	1.27526E+03		
0	19261	5	1.63207E+03	1.17156E+03	-2.75584E+02	1.28641E+02	8.37864E+01	-25.06	1.76093E+03	1.04270E+03	3.59118E+02	3.59118E+02		
0	19261	6	8.94335E+02	8.42755E+02	-1.99331E+02	1.41008E+02	9.17125E+01	-41.31	1.06954E+03	6.67553E+02	2.00992E+02	2.00992E+02		
0	19261	7	8.20228E+02	-1.18230E+02	-4.99074E+01	1.44833E+02	9.42856E+01	-3.04	8.22875E+02	-1.20877E+02	4.71876E+02	4.71876E+02		
0	19261	8	-5.81145E+02	1.85148E+02	-4.68243E+01	1.44833E+02	9.42856E+01	-86.52	1.87999E+02	-5.83995E+02	3.85997E+02	3.85997E+02		
0	19261	9	-8.47743E+02	-5.92468E+02	-1.52238E+02	1.41008E+02	9.17125E+01	-64.99	-5.21440E+02	-9.18771E+02	1.98665E+02	1.98665E+02		
0	19261	10	-2.05662E+03	-4.72459E+02	1.05682E+02	1.28641E+02	8.37864E+01	86.20	-4.65440E+02	-2.06364E+03	7.99102E+02	7.99102E+02		
0	19261	11	-2.79436E+03	-8.01262E+02	1.81935E+02	1.10090E+02	7.18972E+01	84.83	-7.84791E+02	-2.81084E+03	1.01302E+03	1.01302E+03		
0	19261	12	-1.36869E+03	-3.19095E+03	3.05734E+02	9.47918E+01	6.16050E+01	9.27	-1.31876E+03	-3.24087E+03	9.61056E+02	9.61056E+02		
0	19261	13	-4.26984E+03	-1.45887E+03	3.34442E+02	6.38735E+01	4.17897E+01	83.31	-1.41963E+03	-4.30909E+03	1.44473E+03	1.44473E+03		
0	19261	14	-5.00758E+03	-1.78767E+03	4.10695E+02	2.67715E+01	1.80113E+01	82.84	-1.73611E+03	-5.05914E+03	1.66151E+03	1.66151E+03		
0	19261	15	-5.85166E+03	-2.01518E+03	-4.59230E+02	1.84862E-12	1.19097E-12	-83.27	-1.96098E+03	-5.90586E+03	1.97244E+03	1.97244E+03		

Figure 189: Ribs σ_1 Component Compressive Critical Stress

Figure 189 shows the maximum compressive stress of 5.85 ksi in the ribs captured from the results file at the critical region. The margin of safety for this method of failure is shown below:

$$MS = \frac{\sigma_{allowable}}{FS \bullet \sigma_{actual}} - 1 = \frac{-36990 psi}{3 \bullet -5852 psi} - 1 = 1.107$$

The spar's most critical region in compressive stress on the σ_2 axis is on the rib near the lower skin at the inboard attachment point. Figure 190 shows the overall stress distribution in the ribs and Figure 191 shows the region in the ribs found to be the most critical with the critical element highlighted.

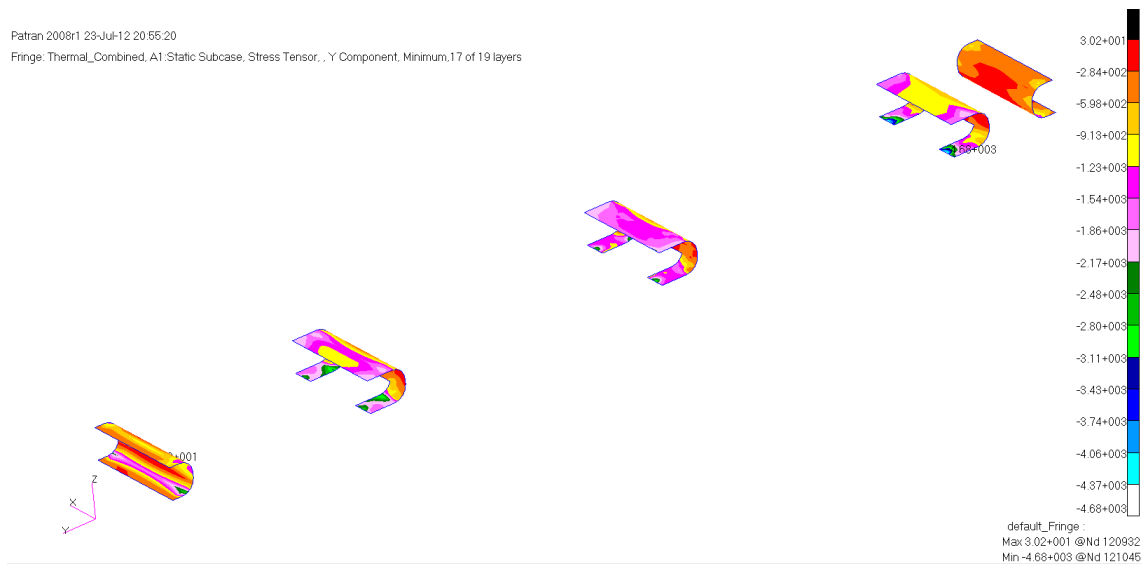


Figure 190: Ribs σ_2 Component Compressive Stress Distribution

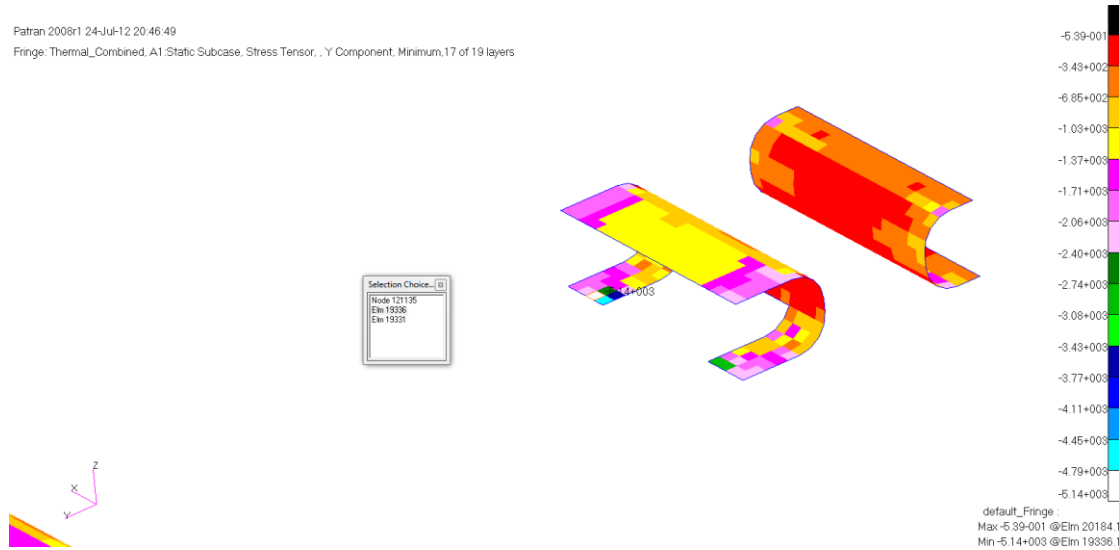


Figure 191: Ribs σ_2 Component Compressive Stress Critical Region

		STRESSES IN FIBER AND MATRIX DIRECTIONS				COMPOSITE ELEMENTS (QUAD4)				INTER-LAMINAR STRESSES				PRINCIPAL STRESSES (ZERO SHEAR)				MAX	
		NORMAL-1		NORMAL-2		SHEAR-12		SHEAR XZ-MAT		SHEAR YZ-MAT		ANGLE		MAJOR		MINOR		SHEAR	
0	19336	1	7.84263E+02	5.69878E+03	4.17952E+02	-2.62368E+01	1.74839E+01	85.17	5.73407E+03	7.48972E+02	2.49255E+03								
0	19336	2	4.26335E+03	1.37743E+03	6.03469E+02	-6.25978E+01	4.05660E+01	11.35	4.38446E+03	1.25632E+03	1.56407E+03								
0	19336	3	3.54001E+03	1.05935E+03	5.29467E+02	-9.28987E+01	5.98011E+01	11.56	3.64829E+03	9.51066E+02	1.34861E+03								
0	19336	4	3.54474E+03	4.76979E+01	-2.65684E+02	-1.07891E+02	6.97919E+01	-4.32	3.56481E+03	2.76280E+01	1.76859E+03								
0	19336	5	2.09332E+03	4.23180E+02	3.81465E+02	-1.26072E+02	8.13330E+01	12.28	2.17632E+03	3.40178E+02	9.18073E+02								
0	19336	6	1.36998E+03	1.05096E+02	3.07463E+02	-1.38192E+02	8.90270E+01	12.96	1.44075E+03	3.43194E+01	7.03217E+02								
0	19336	7	-6.84121E+02	1.05470E+03	1.13417E+02	-1.41940E+02	9.15247E+01	86.28	1.06206E+03	-6.91488E+02	8.76775E+02								
0	19336	8	-7.67135E+01	-5.31071E+02	1.59461E+02	-1.41940E+02	9.15247E+01	17.53	-2.63352E+01	-5.81449E+02	2.77557E+02								
0	19336	9	-1.17358E+03	-4.93332E+02	1.19049E+01	-1.38192E+02	8.90270E+01	89.00	-4.93124E+02	-1.17379E+03	3.40333E+02								
0	19336	10	-1.52340E+03	-1.16724E+03	1.14581E+01	-1.26072E+02	8.13330E+01	88.16	-1.16687E+03	-1.52377E+03	1.78450E+02								
0	19336	11	-2.24675E+03	-1.48532E+03	-6.25432E+01	-1.07891E+02	6.97919E+01	-85.34	-1.48022E+03	-2.25185E+03	3.85816E+02								
0	19336	12	-2.95544E+03	-1.81736E+03	1.40363E+02	-9.28987E+01	5.98011E+01	83.07	-1.80030E+03	-2.97250E+03	5.86098E+02								
0	19336	13	-3.69344E+03	-2.12149E+03	-2.10546E+02	-6.25978E+01	4.05660E+01	-82.50	-2.09378E+03	-3.72115E+03	8.13686E+02								
0	19336	14	-4.41678E+03	-2.43957E+03	-2.84547E+02	-2.62368E+01	1.74839E+01	-81.97	-2.39944E+03	-4.45692E+03	1.02874E+03								
0	19336	15	-2.64197E+03	-5.19374E+03	-2.92630E+02	-1.81170E-12	1.15610E-12	-6.60	-2.60811E+03	-5.17127E+03	1.28158E+03								

Figure 192: Ribs σ_2 Component Compressive Critical Stress

Figure 192 shows the maximum compressive stress of 5.14 ksi in the ribs captured from the results file at the critical region. The margin of safety for this method of failure is shown below:

$$MS = \frac{\sigma_{allowable}}{FS \cdot \sigma_{actual}} - 1 = \frac{-31590 \text{ psi}}{3 \cdot -5137.4 \text{ psi}} - 1 = 1.05$$

3.5.6.2 Tensile Strength

The rib's most critical region in compressive stress on the σ_1 axis is on the lower skin at the inboard attachment point. Figure 193 shows the overall stress distribution in the ribs and Figure 194 shows the region in the ribs found to be the most critical with the critical element highlighted.

Patran 2008r1 24-Jul-12 20:57:52
 Fringe: Thermal_Combined, A1:Static Subcase, Stress Tensor, ,X Component, Maximum,17 of 19 layers

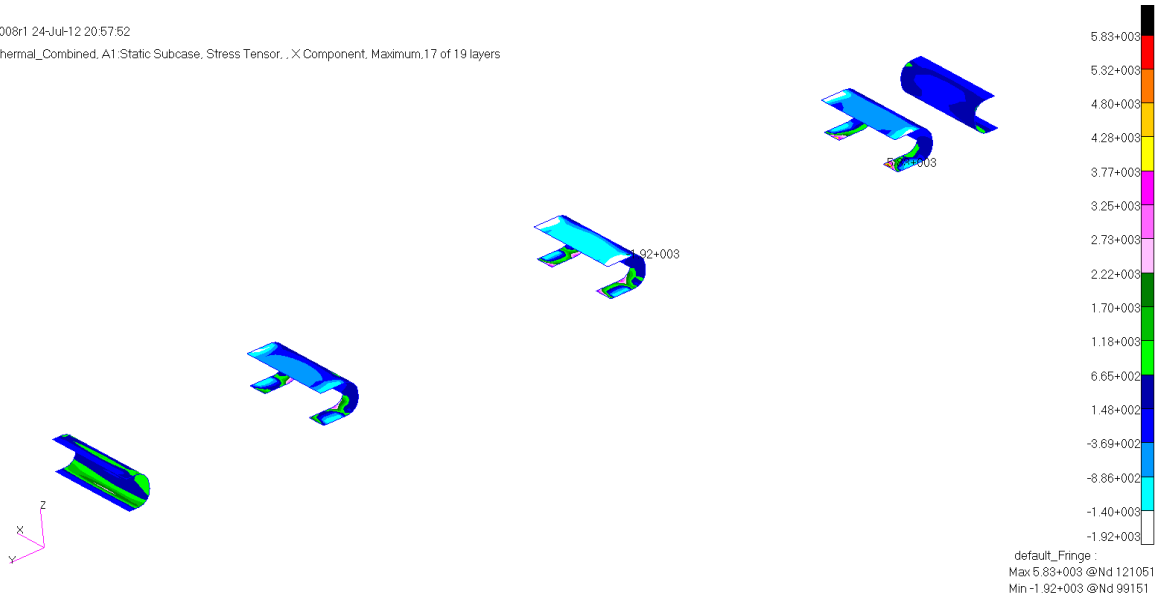


Figure 193: Ribs σ_1 Component Tensile Stress Distribution

Patran 2008r1 24-Jul-12 21:00:14
 Fringe: Thermal_Combined, A1:Static Subcase, Stress Tensor, ,X Component, Maximum,17 of 19 layers

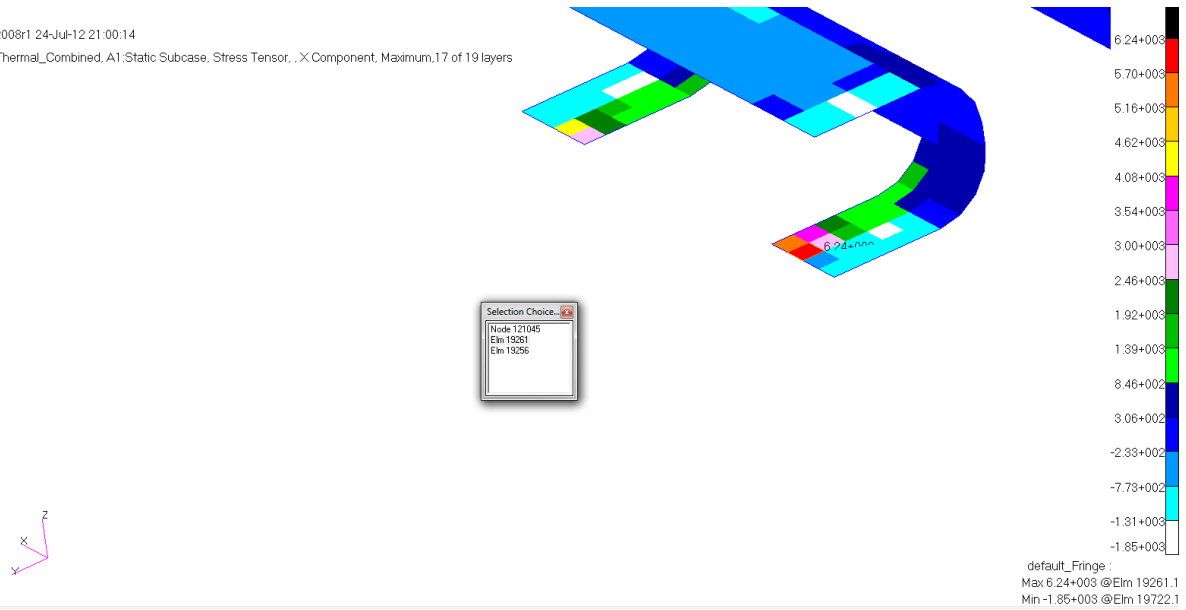


Figure 194: Ribs σ_1 Component Tensile Stress Critical Region

ELEMENT ID	PLY ID	STRESSES IN FIBER AND MATRIX DIRECTIONS			COMPOSITE ELEMENTS (QUAD4)			INTER-LAMINAR STRESSES			PRINCIPAL STRESSES (ZERO SHEAR)			MAX SHEAR
		NORMAL-1	NORMAL-2	SHEAR-12	SHEAR XZ-MAT	SHEAR YZ-MAT	ANGLE	MAJOR	MINOR		MAJOR	MINOR		
0	19261	1	5.24083E+03	7.79048E+02	4.14641E+02	2.72344E+01	1.86850E+01	4.32	6.27213E+03	7.47750E+02	2.76219E+03	1.56824E+03		
0	19261	2	4.37699E+03	1.50591E+03	-6.31354E+02	6.49781E+01	4.33528E+01	-11.87	4.50969E+03	1.37320E+03	1.56824E+03	1.56824E+03		
0	19261	3	3.63394E+03	1.16508E+03	-5.55915E+02	9.64311E+01	6.39093E+01	-12.12	3.75334E+03	1.04568E+03	1.35383E+03	1.35383E+03		
0	19261	4	3.48014E+03	3.54499E+03	-2.64004E+02	1.11994E+02	7.45864E+01	-85.72	3.56473E+03	1.50565E+01	1.77484E+03	1.77484E+03		
0	19261	5	2.14785E+03	4.83432E+02	-4.05036E+02	1.30865E+02	8.69203E+01	-12.98	2.24118E+03	3.90100E+02	9.25540E+02	9.25540E+02		
0	19261	6	1.40480E+03	1.42607E+02	-3.29597E+02	1.43447E+02	9.51430E+01	-13.79	1.48569E+03	6.17228E+01	7.11982E+02	7.11982E+02		
0	19261	7	1.20188E+03	-7.12744E+02	1.13367E+02	1.47337E+02	9.78122E+01	3.38	1.20857E+03	-7.19434E+02	9.64001E+02	9.64001E+02		
0	19261	8	-8.12927E+01	-5.39042E+02	-1.78719E+02	1.47337E+02	9.78122E+01	-18.99	-1.97813E+01	-6.00553E+02	2.90386E+02	2.90386E+02		
0	19261	9	-4.77772E+02	-1.21001E+03	1.29421E+01	1.43447E+02	9.51430E+01	1.01	-4.77543E+02	-1.21024E+03	3.66347E+02	3.66347E+02		
0	19261	10	-1.56739E+03	-1.22069E+03	-2.78405E+01	1.30865E+02	8.69203E+01	-85.44	-1.21847E+03	-1.56961E+03	1.75569E+02	1.75569E+02		
0	19261	11	-2.31043E+03	-1.56152E+03	4.75987E+01	1.11994E+02	7.45864E+01	86.38	-1.55850E+03	-2.31345E+03	3.77472E+02	3.77472E+02		
0	19261	12	-2.05321E+03	-2.85520E+03	1.37695E+02	9.64311E+01	6.39093E+01	9.48	-2.03023E+03	-2.87818E+03	4.23976E+02	4.23976E+02		
0	19261	13	-3.79653E+03	-2.24316E+03	1.98477E+02	6.49781E+01	4.33528E+01	82.83	-2.21821E+03	-3.82149E+03	8.01640E+02	8.01640E+02		
0	19261	14	-4.53957E+03	-2.58399E+03	2.73916E+02	2.72344E+01	1.86850E+01	82.18	-2.54635E+03	-4.57722E+03	1.01544E+03	1.01544E+03		
0	19261	15	-5.51673E+03	-2.70180E+03	-2.88332E+02	1.88059E-12	1.23552E-12	-84.21	-2.67257E+03	-5.54596E+03	1.43669E+03	1.43669E+03		

Figure 195: Ribs σ_1 Component Tensile Critical Stress

Figure 195 shows the maximum tensile stress of 6.24 ksi in the ribs captured from the results file at the critical region. The margin of safety for this method of failure is shown below:

$$MS = \frac{\sigma_{allowable}}{FS \bullet \sigma_{actual}} - 1 = \frac{32100 psi}{3 \bullet 6240.8 psi} - 1 = .715$$

The rib's most critical region in tensile stress on the σ_2 axis is on the lower skin at the inboard attachment point. Figure 196 shows the overall stress distribution in the ribs and Figure 197 shows the region in the ribs found to be the most critical with the critical element highlighted.

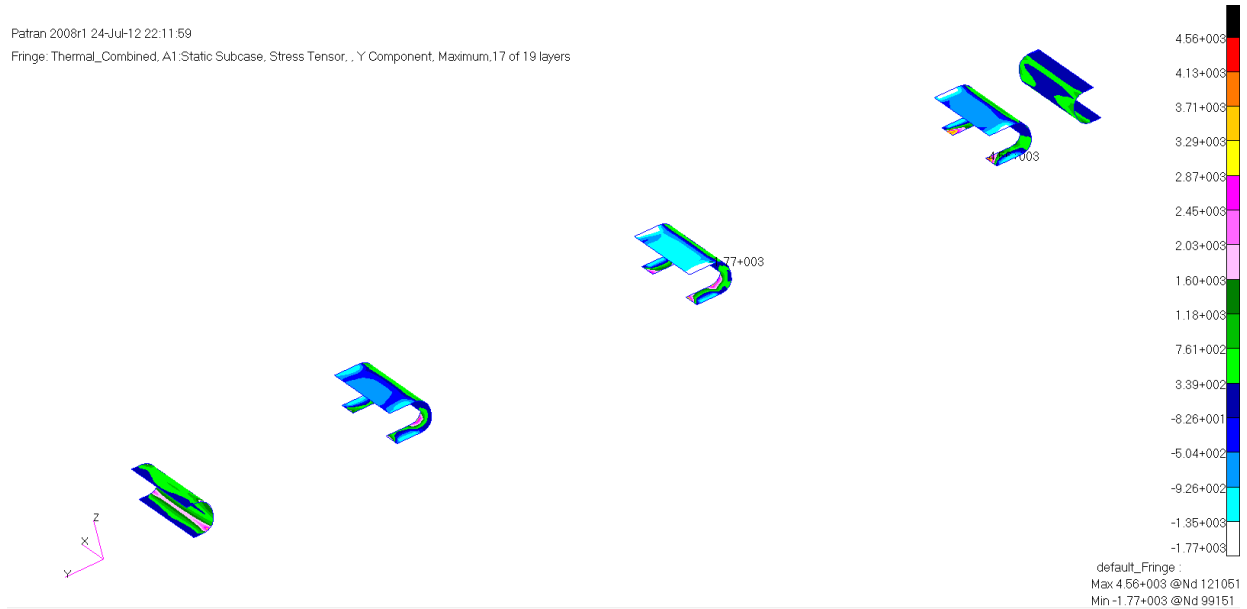


Figure 196: Ribs σ_2 Component Tensile Stress Distribution

Patran 2008r1 24-Jul-12 22:12:35

Fringe: Thermal_Combined, A1:Static Subcase, Stress Tensor, Y Component, Maximum, 17 of 19 layers

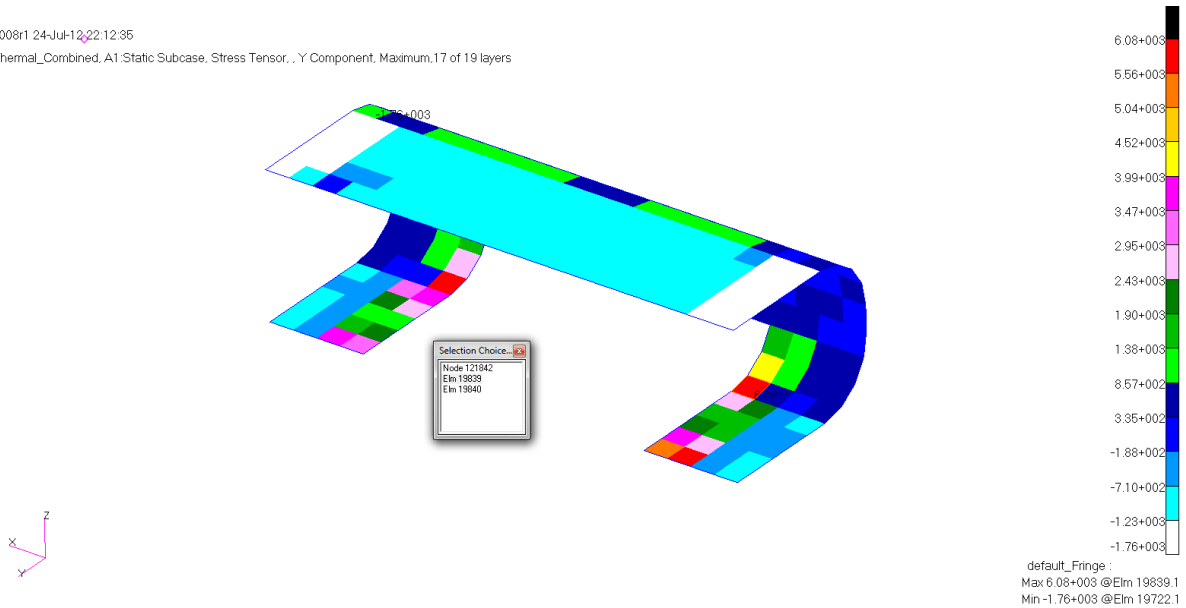


Figure 197: Ribs σ_2 Component Tensile Stress Critical Region

ELEMENT ID	PLY ID	STRESSES IN FIBER AND MATRIX DIRECTIONS			COMPOSITE ELEMENTS (QUAD4)			INTER-LAMINAR STRESSES			PRINCIPAL STRESSES (ZERO SHEAR)			MAX SHEAR
		NORMAL-1	NORMAL-2	SHEAR-12	SHEAR XZ-MAT	SHEAR YZ-MAT	ANGLE	MAJOR	MINOR		MAJOR	MINOR		
0	19839	1	3.67702E+03	2.15338E+03	-1.11675E+03	7.53830E-01	-4.62470E+01	-27.85	4.26705E+03	1.56335E+03	1.35185E+03	1.35185E+03	1.35185E+03	1.35185E+03
0	19839	2	-1.11559E+03	6.08358E+03	-1.26294E+02	1.79855E+00	-1.07302E+02	-89.00	6.08580E+03	-1.11780E+03	3.60180E+03	3.60180E+03	3.60180E+03	3.60180E+03
0	19839	3	-9.15679E+02	5.25788E+03	-6.79727E+01	2.66915E+00	-1.58181E+02	-89.37	5.25863E+03	-9.16427E+02	3.08753E+03	3.08753E+03	3.08753E+03	3.08753E+03
0	19839	4	1.93143E+03	1.91044E+03	6.99680E+02	3.09991E+00	-1.84608E+02	44.57	2.62069E+03	1.22117E+03	6.99758E+02	6.99758E+02	6.99758E+02	6.99758E+02
0	19839	5	-5.15860E+02	3.60647E+03	4.86696E+01	3.62226E+00	-2.15136E+02	89.32	3.60705E+03	-5.16435E+02	2.06174E+03	2.06174E+03	2.06174E+03	2.06174E+03
0	19839	6	-3.15951E+02	2.78077E+03	1.06991E+02	3.97050E+00	-2.35488E+02	88.02	2.78446E+03	-3.19643E+02	1.55205E+03	1.55205E+03	1.55205E+03	1.55205E+03
0	19839	7	3.33949E+02	1.52640E+03	-2.82608E+02	4.07819E+00	-2.42094E+02	-77.32	1.58999E+03	2.70362E+02	6.59813E+02	6.59813E+02	6.59813E+02	6.59813E+02
0	19839	8	8.38677E+01	1.12936E+03	2.23633E+02	4.07819E+00	-2.42094E+02	78.42	1.17519E+03	3.80409E+01	5.68574E+02	5.68574E+02	5.68574E+02	5.68574E+02
0	19839	9	-7.80408E+02	1.31741E+03	-4.56011E+00	3.97050E+00	-2.35488E+02	-89.88	1.31742E+03	-7.80417E+02	1.04892E+03	1.04892E+03	1.04892E+03	1.04892E+03
0	19839	10	4.83686E+02	-5.22046E+02	3.40275E+02	3.62226E+00	-2.15136E+02	17.04	5.87995E+02	-6.26355E+02	6.07175E+02	6.07175E+02	6.07175E+02	6.07175E+02
0	19839	11	6.83596E+02	-1.34775E+03	3.98597E+02	3.09991E+00	-1.84608E+02	10.71	7.59010E+02	-1.42316E+03	1.09109E+03	1.09109E+03	1.09109E+03	1.09109E+03
0	19839	12	1.05386E+03	-2.33574E+03	-4.12512E+02	2.66915E+00	-1.58181E+02	-6.84	1.10334E+03	-2.38522E+03	1.74428E+03	1.74428E+03	1.74428E+03	1.74428E+03
0	19839	13	1.08341E+03	-2.99916E+03	5.15239E+02	1.79855E+00	-1.07302E+02	7.08	1.14744E+03	-3.06318E+03	2.10531E+03	2.10531E+03	2.10531E+03	2.10531E+03
0	19839	14	1.28332E+03	-3.82486E+03	5.73560E+02	7.53830E-01	-4.62470E+01	6.33	1.34693E+03	-3.88847E+03	2.61770E+03	2.61770E+03	2.61770E+03	2.61770E+03
0	19839	15	-4.12348E+03	6.90425E+02	8.29583E+02	5.20534E-14	-3.05803E-12	80.49	8.29377E+02	-4.26243E+03	2.54590E+03	2.54590E+03	2.54590E+03	2.54590E+03

Figure 198: Ribs σ_2 Component Tensile Critical Stress

Figure 198 shows the maximum σ_2 tensile stress of 6.08 ksi in the ribs captured from the results file at the critical region. The margin of safety for this method of failure is shown below:

$$MS = \frac{\sigma_{allowable}}{FS \bullet \sigma_{actual}} - 1 = \frac{30810 \text{ psi}}{3 \bullet 6083.6 \text{ psi}} - 1 = .688$$

3.5.6.3 Shear

The rib's most critical region in compressive stress on the τ_{12} axis is on the rib near the lower skin at the inboard attachment point. Figure 199 shows the overall stress distribution in the ribs and Figure 200 shows the region in the ribs found to be the most critical with the critical element highlighted.

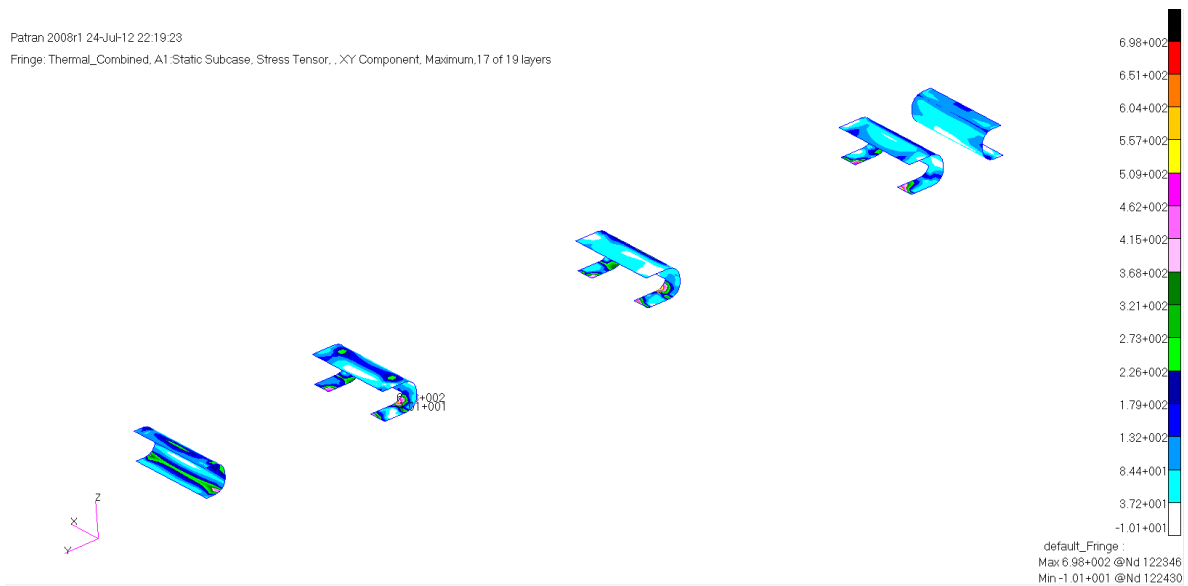


Figure 199: Ribs τ_{12} Shear Stress Distribution

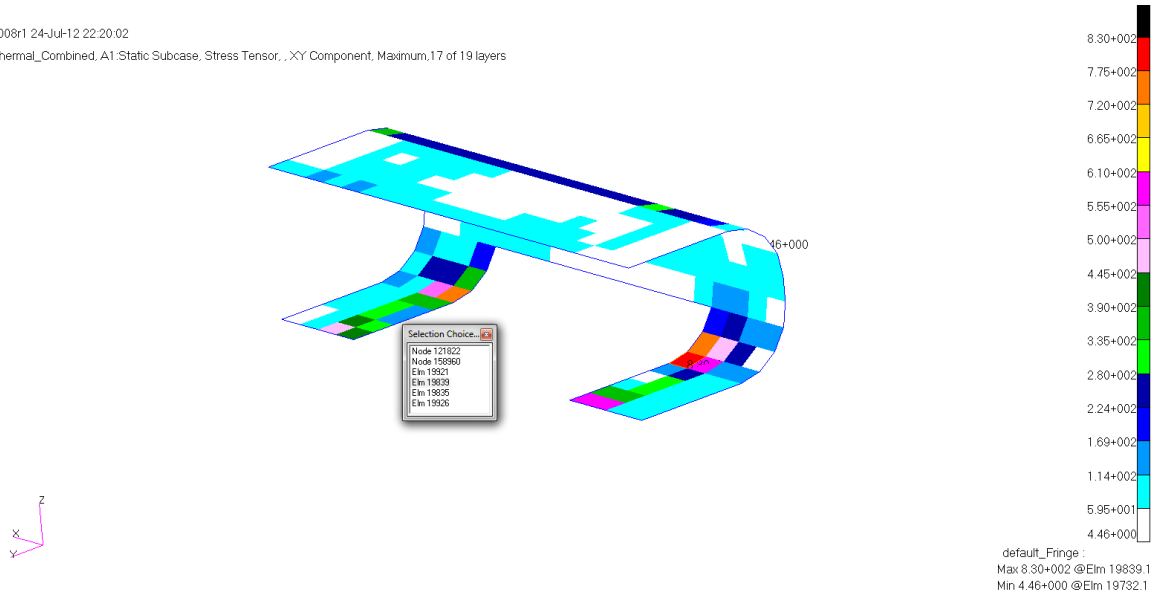


Figure 200: Ribs τ_{12} Shear Stress Critical Region

STRESSES IN LAYERED					COMPOSITE ELEMENTS (QUAD4)					INTER-LAMINAR STRESSES					PRINCIPAL STRESSES (ZERO SHEAR)					MAX SHEAR
STRESSES IN FIBER AND MATRIX DIRECTIONS					INTER-LAMINAR STRESSES					PRINCIPAL STRESSES (ZERO SHEAR)					PRINCIPAL STRESSES (ZERO SHEAR)					
ELEMENT ID	PLY ID	NORMAL-1	NORMAL-2	SHEAR-12	SHEAR XZ-MAT	SHEAR YZ-MAT	ANGLE	MAJOR	MINOR		MAJOR	MINOR		MAJOR	MINOR					
0 19839	1	3.67702E+03	2.15338E+03	-1.11675E+03	7.53830E-01	-4.62470E+01	-27.85	4.26705E+03	1.56335E+03	1.35185E+03	1.35185E+03	1.35185E+03	1.35185E+03	1.35185E+03	1.35185E+03	1.35185E+03				
0 19839	2	-1.11559E+03	6.08358E+03	-1.26294E+02	1.79855E+00	-1.07302E+02	-89.00	6.08580E+03	-1.11780E+03	3.60180E+03	3.60180E+03	3.60180E+03	3.60180E+03	3.60180E+03	3.60180E+03	3.60180E+03				
0 19839	3	-9.15679E+02	5.25788E+03	-6.79727E+01	2.66915E+00	-1.58181E+02	-89.37	5.25863E+03	-9.16427E+02	3.08753E+03	3.08753E+03	3.08753E+03	3.08753E+03	3.08753E+03	3.08753E+03	3.08753E+03				
0 19839	4	1.93143E+03	1.91044E+03	6.99680E+02	3.09991E+00	-1.84608E+02	44.57	2.62069E+03	1.22117E+03	6.99758E+02	6.99758E+02	6.99758E+02	6.99758E+02	6.99758E+02	6.99758E+02	6.99758E+02				
0 19839	5	-5.15860E+02	3.60647E+03	4.86696E+01	3.62226E+00	-2.15136E+02	89.32	3.60705E+03	-5.16435E+02	2.06174E+03	2.06174E+03	2.06174E+03	2.06174E+03	2.06174E+03	2.06174E+03	2.06174E+03				
0 19839	6	-3.15951E+02	2.78077E+03	1.06991E+02	3.97050E+00	-2.35488E+02	88.02	2.78446E+03	-3.19643E+02	1.55205E+03	1.55205E+03	1.55205E+03	1.55205E+03	1.55205E+03	1.55205E+03	1.55205E+03				
0 19839	7	3.33949E+02	1.52640E+03	-2.82608E+02	4.07819E+00	-2.42094E+02	-77.32	1.58999E+03	2.70362E+02	6.59813E+02	6.59813E+02	6.59813E+02	6.59813E+02	6.59813E+02	6.59813E+02	6.59813E+02				
0 19839	8	8.38677E+01	1.12936E+03	2.23633E+02	4.07819E+00	-2.42094E+02	78.42	1.17519E+03	3.80409E+01	5.68574E+02	5.68574E+02	5.68574E+02	5.68574E+02	5.68574E+02	5.68574E+02	5.68574E+02				
0 19839	9	-7.80408E+02	1.31741E+03	-4.56011E+00	3.97050E+00	-2.35488E+02	-89.88	1.31742E+03	-7.80417E+02	1.04892E+03	1.04892E+03	1.04892E+03	1.04892E+03	1.04892E+03	1.04892E+03	1.04892E+03				
0 19839	10	4.83686E+02	-5.22046E+02	3.40275E+02	3.62226E+00	-2.15136E+02	17.04	5.87995E+02	-6.26355E+02	6.07175E+02	6.07175E+02	6.07175E+02	6.07175E+02	6.07175E+02	6.07175E+02	6.07175E+02				
0 19839	11	6.83596E+02	-1.34775E+03	3.98597E+02	3.09991E+00	-1.84608E+02	10.71	7.59010E+02	-1.42316E+03	1.09109E+03	1.09109E+03	1.09109E+03	1.09109E+03	1.09109E+03	1.09109E+03	1.09109E+03				
0 19839	12	1.05386E+03	-2.33574E+03	-4.12512E+02	2.66915E+00	-1.58181E+02	-6.84	1.10334E+03	-2.38522E+03	1.74428E+03	1.74428E+03	1.74428E+03	1.74428E+03	1.74428E+03	1.74428E+03	1.74428E+03				
0 19839	13	1.08341E+03	-2.99916E+03	5.15239E+02	1.79855E+00	-1.07302E+02	7.08	1.14744E+03	-3.06318E+03	2.10531E+03	2.10531E+03	2.10531E+03	2.10531E+03	2.10531E+03	2.10531E+03	2.10531E+03				
0 19839	14	1.28332E+03	-3.82486E+03	5.73560E+02	7.53830E-01	-4.62470E+01	6.33	1.34693E+03	-3.88847E+03	2.61770E+03	2.61770E+03	2.61770E+03	2.61770E+03	2.61770E+03	2.61770E+03	2.61770E+03				
0 19839	15	-4.12348E+03	6.90425E+02	8.29537E+02	5.20534E-14	-3.05803E-12	80.49	8.29377E+02	-4.26243E+03	2.54590E+03	2.54590E+03	2.54590E+03	2.54590E+03	2.54590E+03	2.54590E+03	2.54590E+03				

Figure 201: Ribs τ_{12} Shear Critical Stress

Figure 201 shows the maximum shear stress of .83 ksi in the ribs captured from the results file at the critical region. The margin of safety for this method of failure is shown below:

$$MS = \frac{\tau_{allowable}}{FS \bullet \tau_{actual}} - 1 = \frac{9210 psi}{3 \bullet 829.6 psi} - 1 = 2.701$$

3.5.7 Rib Inserts

The most critical margin of safety for the ribs is in tensile failure as seen in Table 38. The results are presented below in the same order as the previous section.

Table 38: Rib Insert Failure Methods

Stress Type	Stress	Margin	Allowable	Load Case
Compressive	-12.05 (ksi)	0.365	-16.4 (ksi)	Thermal
Tensile	13.21 (ksi)	0.245	16.4 (ksi)	Thermal
Shear	4.58 (ksi)	1.596	11.9 (ksi)	Thermal

3.5.7.1 Tensile Stress

The rib insert's most critical region in tensile stress is in the forward insert at the inboard attachment point. Figure 202 shows the overall stress distribution in the insert and Figure 203 shows the region in the insert found to be the most critical with the critical element highlighted.

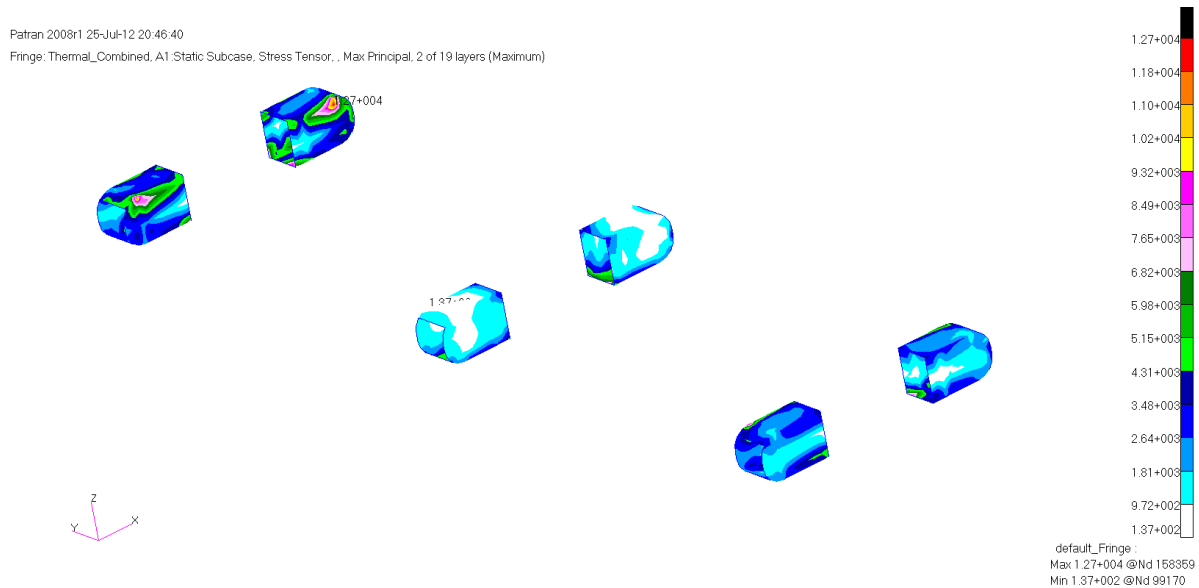


Figure 202: Ribs Inserts Tensile Stress Distribution

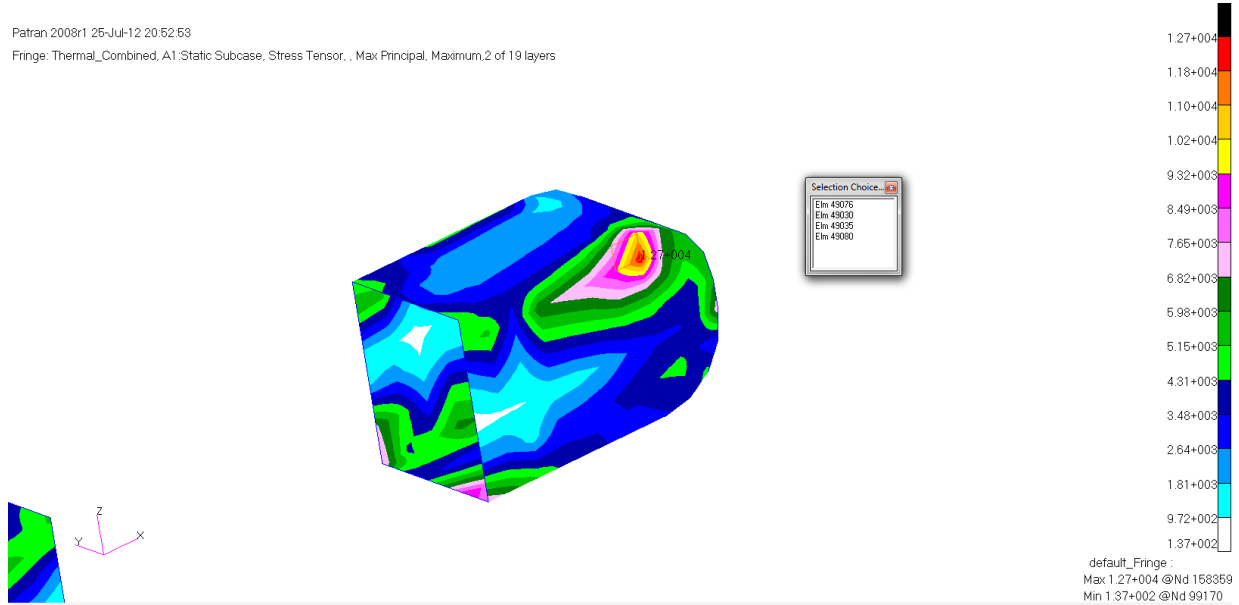


Figure 203: Ribs Inserts Tensile Stress Critical Region

STRESSES IN QUADRILATERAL ELEMENTS (QUAD4)										
OPTION = BILIN										
ELEMENT ID	GRID-ID	FIBER DISTANCE	STRESSES IN NORMAL-X	STRESSES IN NORMAL-Y	SYSTEM SHEAR-XY	PRINCIPAL STRESSES (ZERO ANGLE)	MAJOR	SHEAR MINOR	VON MISES	
0	49030	CEN/4	-1.250000E-01	1.307528E+03	-9.762311E+02	1.048947E+03	21.2855	1.716190E+03	-1.384893E+03	2.690720E+03
			1.250000E-01	5.869377E+03	1.315774E+04	6.090917E+02	85.2556	1.320829E+04	5.818826E+03	1.146564E+04
	99361	-1.250000E-01	3.702793E+03	2.136338E+03	1.048947E+03	26.6260	4.228663E+03	1.610468E+03	3.696630E+03	
		1.250000E-01	7.430139E+03	1.651722E+04	6.090917E+02	86.1823	1.655787E+04	7.389495E+03	1.436709E+04	
	99360	-1.250000E-01	3.702793E+03	-4.088800E+03	1.048947E+03	7.5348	3.841538E+03	-4.227545E+03	6.990695E+03	
		1.250000E-01	7.430139E+03	9.798263E+03	6.090917E+02	76.3892	9.945739E+03	7.282663E+03	8.917592E+03	
	158360	-1.250000E-01	-1.087738E+03	-4.088800E+03	1.048947E+03	17.4777	-7.574539E+02	-4.419084E+03	4.093261E+03	
		1.250000E-01	4.308616E+03	9.798263E+03	6.090917E+02	83.7442	9.865030E+03	4.241847E+03	8.571239E+03	
	158359	-1.250000E-01	-1.087738E+03	2.136338E+03	1.048947E+03	73.4740	2.447567E+03	-1.398967E+03	3.372204E+03	
		1.250000E-01	4.308616E+03	1.651722E+04	6.090917E+02	87.1509	1.654754E+04	4.278303E+03	1.487714E+04	

Figure 204: Ribs Inserts Tensile Critical Stress

Figure 204 shows the maximum tensile stress of 13.21 captured from the results file. For this failure method local effects induced by the pylon substructure and skins have greatly increased the stresses in one of the nodes of the element. Since the actual stress from the pylon in this region will be more dispersed than the nodal stress from the finite element model the average element stress is used here instead of the nodal stress. This is a more aggressive approach but is necessary to keep the rib inserts from being unnecessarily large. The margin of safety for this method of failure is shown below:

$$MS = \frac{\sigma_{allowable}}{FS \bullet \sigma_{actual}} - 1 = \frac{37000 \text{ psi}}{2.25 \bullet 13208.3 \text{ psi}} - 1 = .245$$

3.5.7.2 Compressive Stress

The rib insert's most critical region in compressive stress is in the aft insert at the outboard attachment point. Figure 205 shows the overall stress distribution in the insert and Figure 206 shows the region in the insert found to be the most critical with the critical element highlighted.

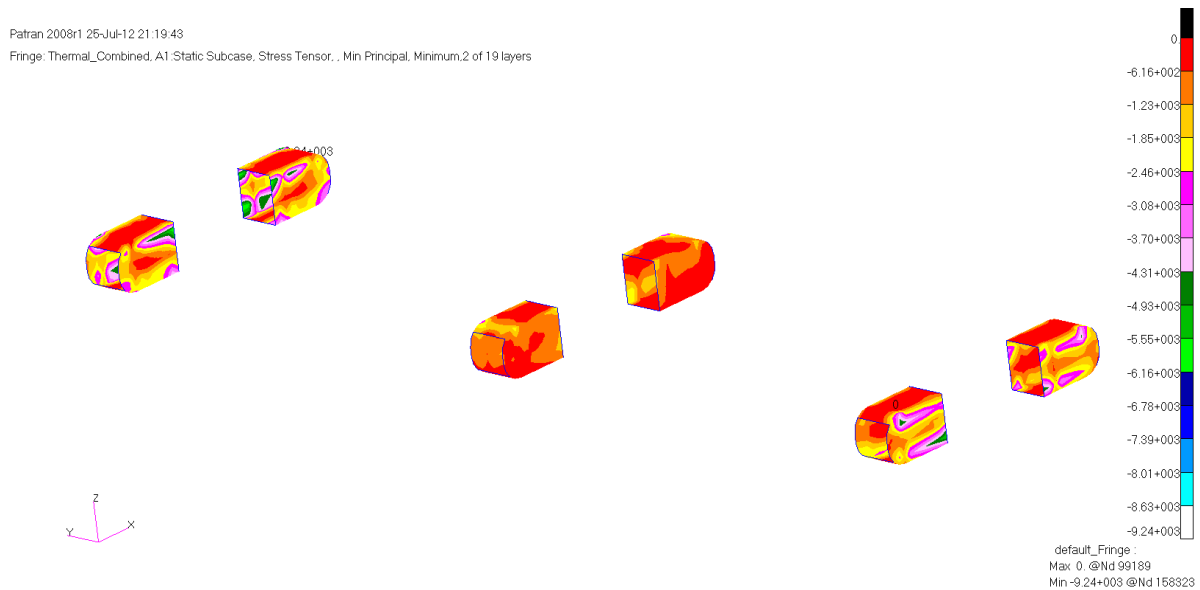


Figure 205: Ribs Inserts Compressive Stress Distribution

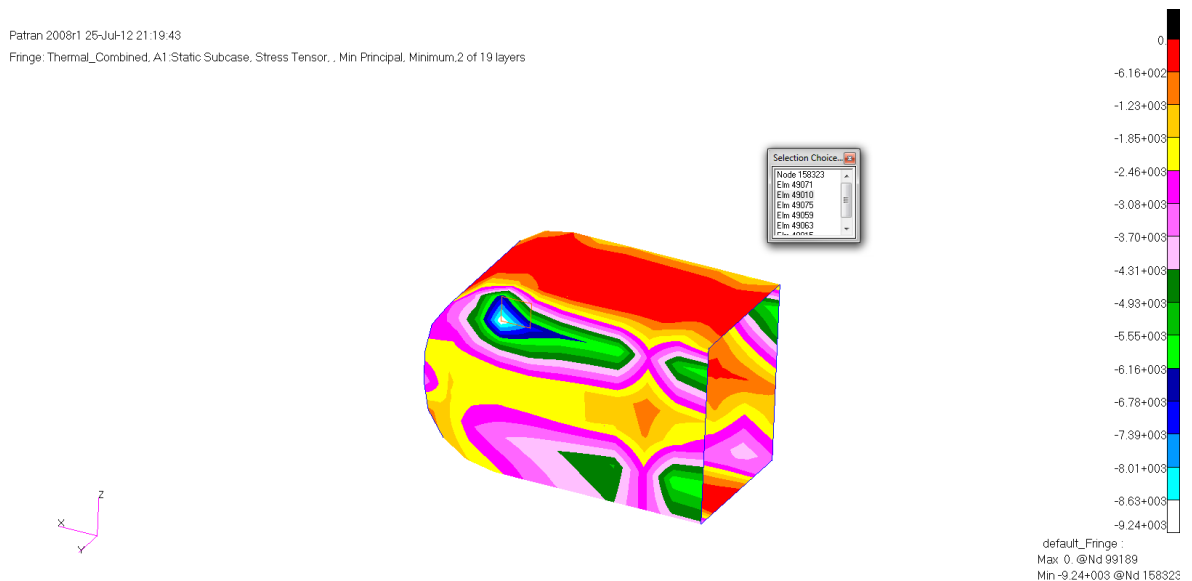


Figure 206: Ribs Inserts Compressive Stress Critical Region

STRESSES IN QUADRILATERAL ELEMENTS (QUAD4)											OPTION = BILIN
ELEMENT ID	GRID-ID	FIBER DISTANCE	STRESSES IN ELEMENT COORD SYSTEM			PRINCIPAL STRESSES (ZERO SHEAR)			VON MISES		
			NORMAL-X	NORMAL-Y	SHEAR-XY	ANGLE	MAJOR	MINOR			
0	49010	CEN/4	-1.250000E-01	-3.565030E+03	-1.003267E+04	-6.270365E+01	-0.5554	-3.564422E+03	-1.003328E+04	8.809592E+03	
			1.250000E-01	8.373432E+02	2.949299E+03	-7.589049E+01	-87.9447	2.952023E+03	8.346197E+02	2.635757E+03	
		99391	-1.250000E-01	-4.261349E+03	-1.204624E+04	-5.387888E+01	-0.3965	-4.260976E+03	-1.204661E+04	1.058047E+04	
			1.250000E-01	-6.586719E+02	1.177648E+03	-6.594098E+01	-87.9461	1.180013E+03	-6.610367E+02	1.615374E+03	
		99390	-1.250000E-01	-4.261299E+03	-8.019108E+03	-6.808379E+01	-1.0376	-4.260066E+03	-8.020341E+03	6.950313E+03	
			1.250000E-01	-6.586278E+02	4.720932E+03	-7.843922E+01	-89.1648	4.722075E+03	-6.597712E+02	5.084170E+03	
		158324	-1.250000E-01	-2.866374E+03	-7.998761E+03	-7.160593E+01	-0.7992	-2.865375E+03	-7.999760E+03	7.020271E+03	
			1.250000E-01	2.338379E+03	4.738846E+03	-8.591553E+01	-87.9528	4.741917E+03	2.335308E+03	4.106775E+03	
		158323	-1.250000E-01	-2.866425E+03	-1.206657E+04	-5.725754E+01	-0.3566	-2.866069E+03	-1.206692E+04	1.091972E+04	
			1.250000E-01	2.338334E+03	1.159771E+03	-7.329105E+01	-3.5448	2.342874E+03	1.155231E+03	2.029053E+03	

Figure 207: Ribs Inserts Compressive Critical Stress

Figure 207 shows the maximum compressive stress of 12.05 ksi in the insert captured from the results file at the critical region. The margin of safety for this method of failure is shown below:

$$MS = \frac{\sigma_{allowable}}{FS \bullet \sigma_{actual}} - 1 = \frac{-37000 psi}{2.25 \bullet -12046.61 psi} - 1 = .365$$

3.5.7.3 Shear Stress

The rib insert's most critical region in shear stress is in the aft insert at the outboard attachment point. Figure 208 shows the overall stress distribution in the insert and Figure 209 shows the region in the insert found to be the most critical with the critical element highlighted.

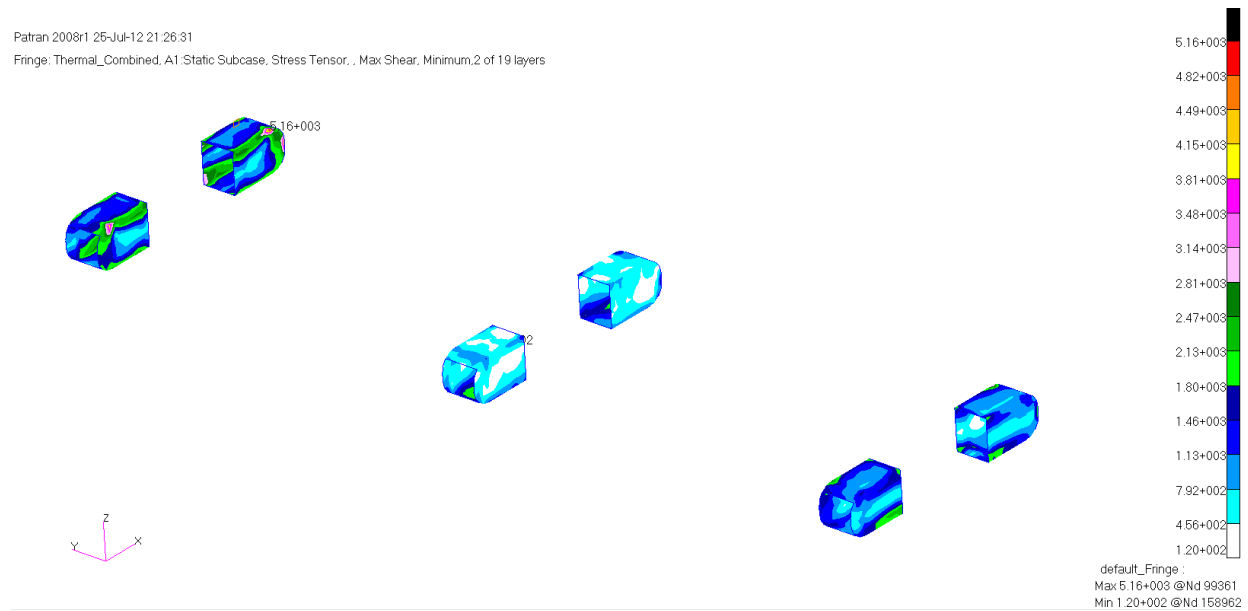


Figure 208: Ribs Inserts Shear Stress Distribution

Patran 2008r1 25-Jul-12 21:26:31

Fringe: Thermal_Combined, A1:Static Subcase, Stress Tensor, , Max Shear, Minimum,2 of 19 layers

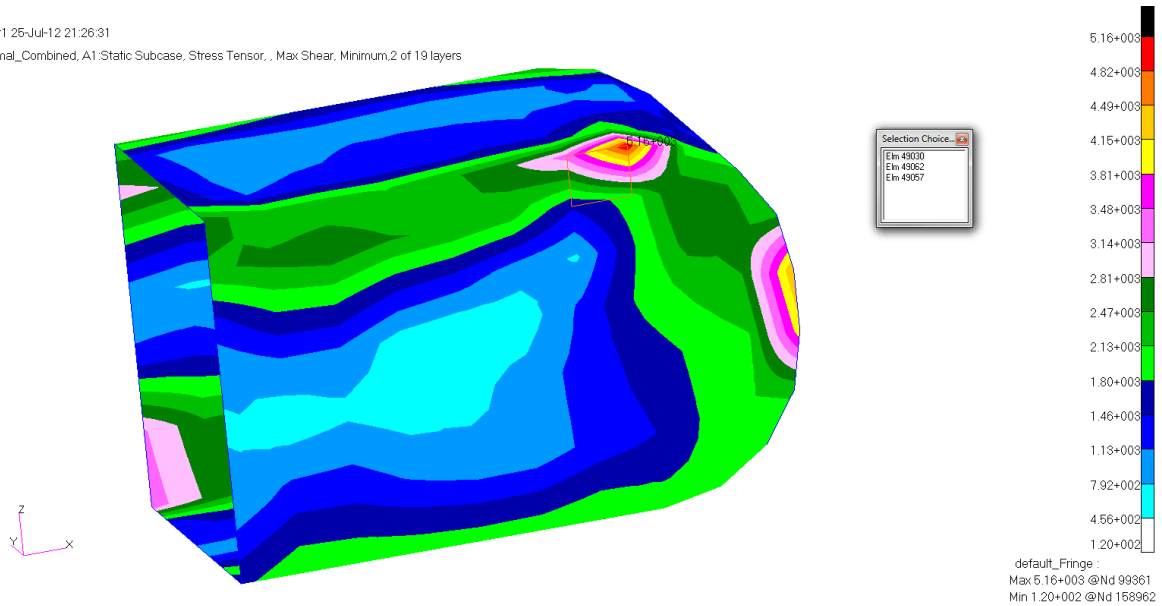


Figure 209: Ribs Inserts Shear Stress Critical Region

49030	CEN/4	-1.250000E-01	7.692191E+02	-2.092070E+01	9.074662E+02	33.2369	1.363884E+03	-6.155856E+02	1.754626E+03
		1.250000E-01	3.895683E+03	9.966622E+03	5.984127E+02	84.4239	1.002505E+04	3.837260E+03	8.761130E+03
99361		-1.250000E-01	2.688207E+03	2.531526E+03	9.074662E+02	42.5330	3.520708E+03	1.699025E+03	3.049639E+03
		1.250000E-01	5.136204E+03	1.277025E+04	5.984127E+02	85.5450	1.281687E+04	5.089581E+03	1.117781E+04
99360		-1.250000E-01	2.688207E+03	-2.573368E+03	9.074662E+02	9.5157	2.840320E+03	-2.725481E+03	4.820468E+03
		1.250000E-01	5.136204E+03	7.162996E+03	5.984127E+02	74.7190	7.326490E+03	4.972710E+03	6.478641E+03
158360		-1.250000E-01	-1.149769E+03	-2.573368E+03	9.074662E+02	25.9450	-7.082455E+02	-3.014891E+03	2.730549E+03
		1.250000E-01	2.655163E+03	7.162996E+03	5.984127E+02	82.5655	7.241083E+03	2.577076E+03	6.357183E+03
158359		-1.250000E-01	-1.149769E+03	2.531526E+03	9.074662E+02	76.8780	2.743068E+03	-1.361310E+03	3.621015E+03
		1.250000E-01	2.655163E+03	1.277025E+04	5.984127E+02	86.6260	1.280553E+04	2.619883E+03	1.171735E+04

Figure 210: Ribs Inserts Shear Critical Stress

Figure 210 shows the maximum shear stress of 4.58 ksi in the insert captured from the results

file at the critical region. The margin of safety for this method of failure is shown below:

$$MS = \frac{\tau_{allowable}}{FS \bullet \tau_{actual}} - 1 = \frac{26775 \text{ psi}}{2.25 \bullet 4584.2 \text{ psi}} - 1 = 1.596$$

3.5.8 Pylon Spar / Ribs

The most critical margin of safety for the ribs is in tensile failure as seen in Table 39. The results are presented below in the same order as the previous section.

Table 39: Pylon Substructure Failure Methods

Stress Type	Stress	Margin	Allowable	Load Case
Compressive	-24.30 (ksi)	0.116	-27.1 (ksi)	Thermal
Tensile	25.32 (ksi)	0.071	27.1 (ksi)	Thermal
Shear	7.57 (ksi)	0.821	13.8 (ksi)	Thermal

3.5.8.1 Shear Stress

The pylon substructure's most critical region in shear stress is at the outboard aft attachment point. Figure 211 shows the overall stress distribution in the insert and Figure 212 shows the region in the insert found to be the most critical with the critical element highlighted.

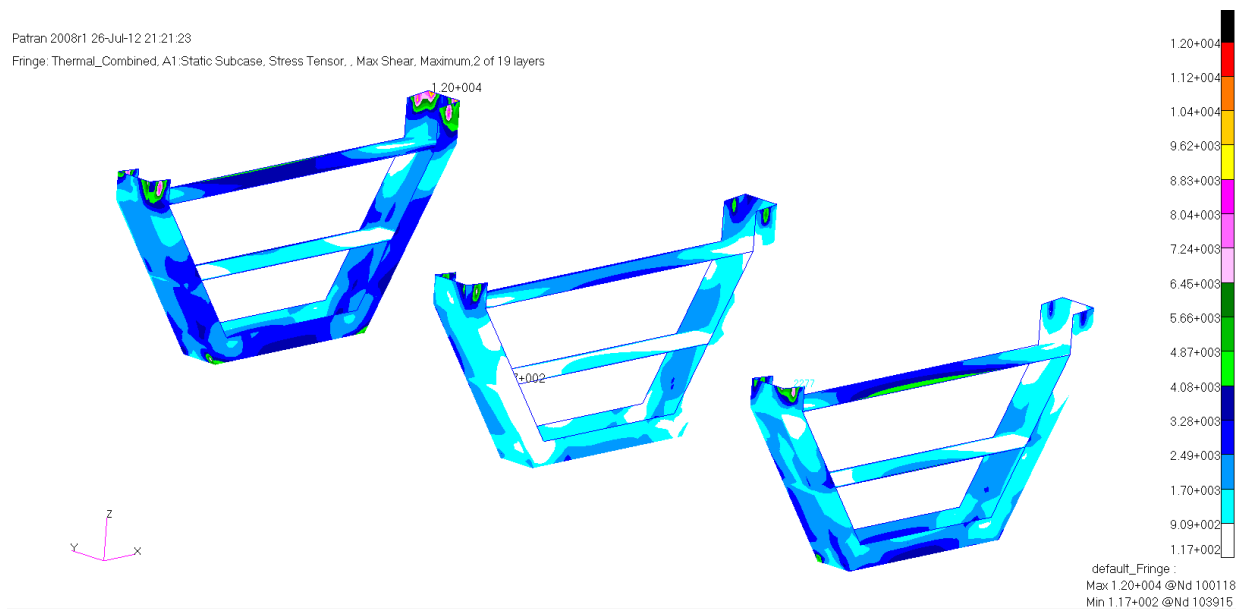


Figure 211: Pylon Substructure Shear Stress Distribution

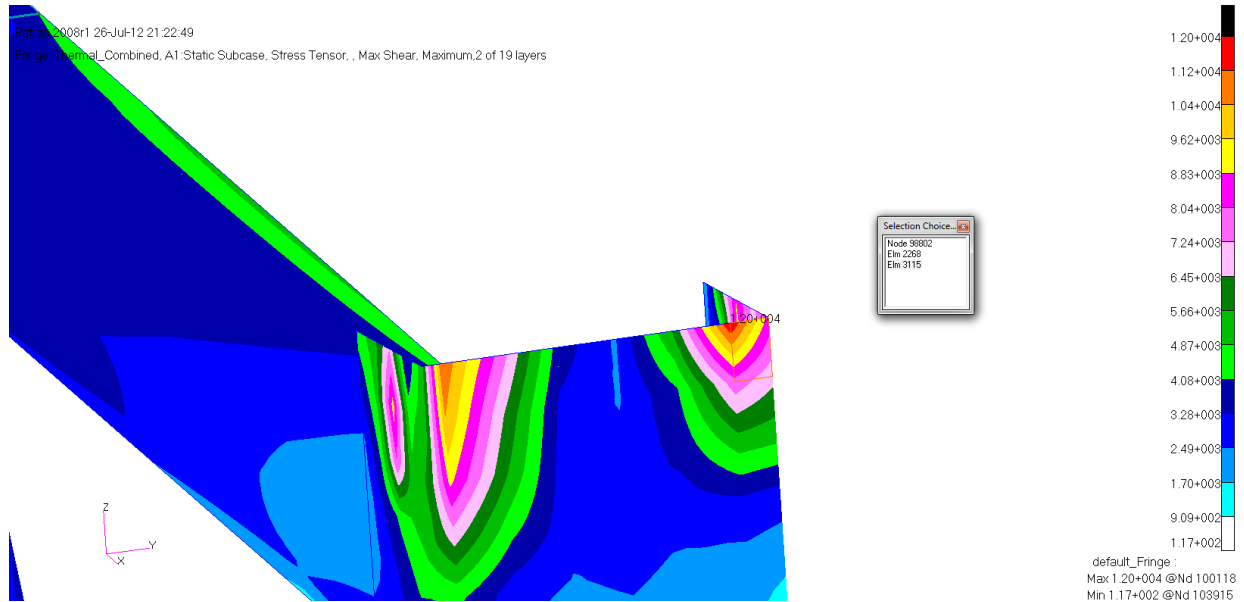


Figure 212: Pylon Substructure Shear Stress Critical Region

STRESSES IN QUADRILATERAL ELEMENTS (QUAD 4)										OPTION = BILIN	
ELEMENT ID	GRID-ID	FIBER DISTANCE	STRESSES IN ELEMENT COORD SYSTEM			PRINCIPAL STRESSES (ZERO SHEAR)			VON MISES		
			NORMAL-X	NORMAL-Y	SHEAR-XY	ANGLE	MAJOR	MINOR			
0	3115	CEN/4	-3.100000E-02	4.693152E+03	2.428344E+04	-4.630992E+03	-77.3480	2.532301E+04	3.653586E+03	2.370830E+04	
			3.100000E-02	-3.841260E+03	-1.844165E+04	1.991322E+03	7.6289	-3.574539E+03	-1.870837E+04	1.720193E+04	

Figure 213: Pylon Substructure Shear Critical Stress

Figure 213 shows the maximum shear stress of 7.57 ksi in the substructure captured from the results file at the critical region. The stress in this region artificially rises due to the sharp corner of the structure along with the interactions to the attachment structure. Due to these reasons the centroid was used rather than the nodal stress value. The margin of safety for this method of failure is shown below:

$$MS = \frac{\tau_{allowable}}{FS \bullet \tau_{actual}} - 1 = \frac{31100 psi}{2.25 \bullet 7566.9 psi} - 1 = .821$$

3.5.8.2 Tensile Stress

The pylon substructure's most critical region in tensile stress is at the outboard aft attachment point. Figure 214 shows the overall stress distribution in the substructure and Figure 215 shows the region in the structure found to be the most critical with the critical element highlighted.

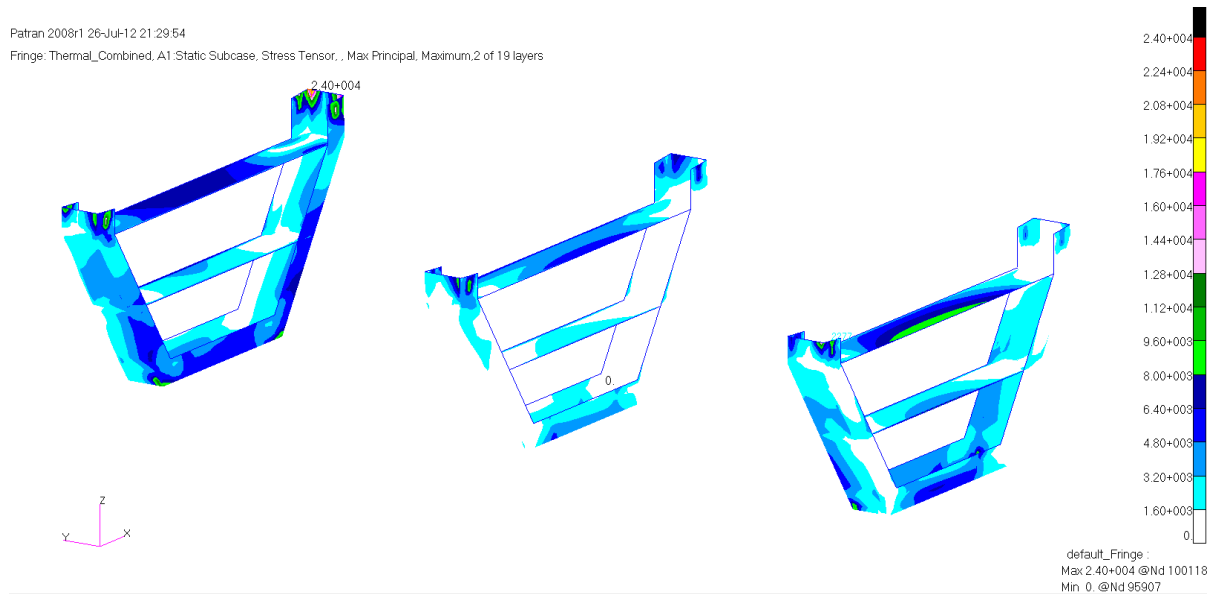


Figure 214: Pylon Substructure Tensile Stress Distribution

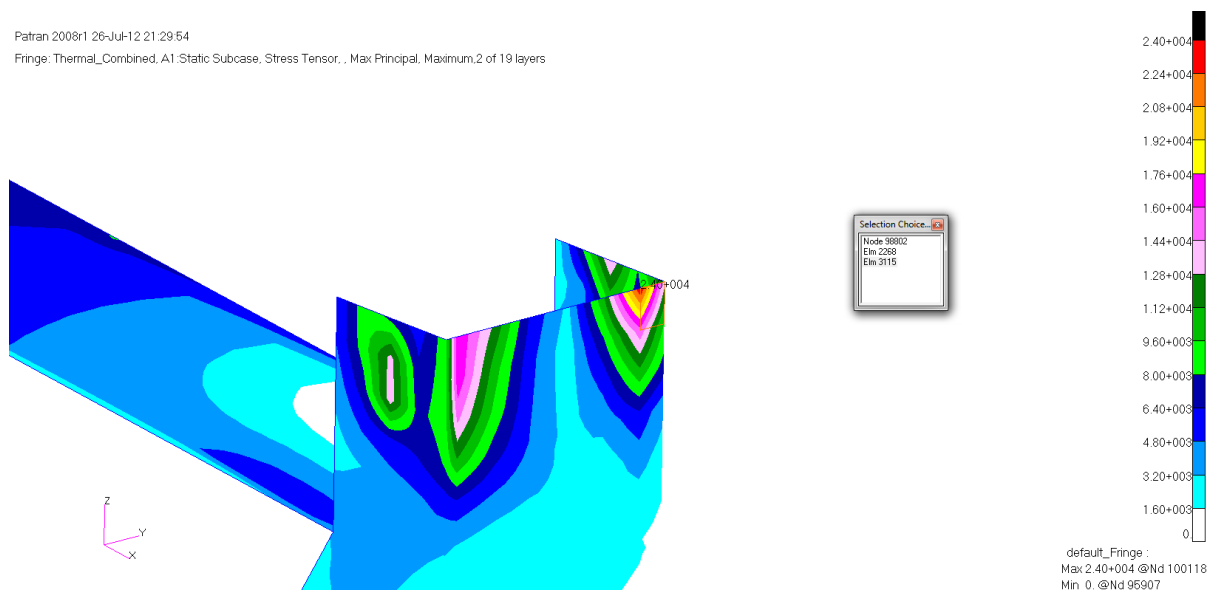


Figure 215: Pylon Substructure Tensile Stress Critical Region

STRESSES IN QUADRILATERAL ELEMENTS (QUAD4)										OPTION = BILIN
ELEMENT ID	GRID-ID	FIBER DISTANCE	STRESSES IN ELEMENT COORD SYSTEM			PRINCIPAL STRESSES (ZERO SHEAR)			VON MISES	
			NORMAL-X	NORMAL-Y	SHEAR-XY	ANGLE	MAJOR	MINOR		
0	3115	CEN/4	-3.100000E-02	4.693152E+03	2.428344E+04	-4.630992E+03	-77.3480	2.532301E+04	3.653586E+03	2.370830E+04
			3.100000E-02	-3.841260E+03	-1.844165E+04	1.991322E+03	7.6289	-3.574539E+03	-1.870837E+04	1.720193E+04

Figure 216: Pylon Substructure Tensile Critical Stress

Figure 216 shows the maximum tensile stress of 25.3 ksi in the substructure captured from the results file at the critical region. The margin of safety for this method of failure is shown below:

$$MS = \frac{\sigma_{allowable}}{FS \bullet \sigma_{actual}} - 1 = \frac{61000 psi}{2.25 \bullet 25323 psi} - 1 = .071$$

3.5.8.3 Compressive Stress

The pylon substructure's most critical region in compressive stress is at the outboard aft attachment point. Figure 217 shows the overall stress distribution in the substructure and Figure 218 shows the region in the structure found to be the most critical with the critical element highlighted.

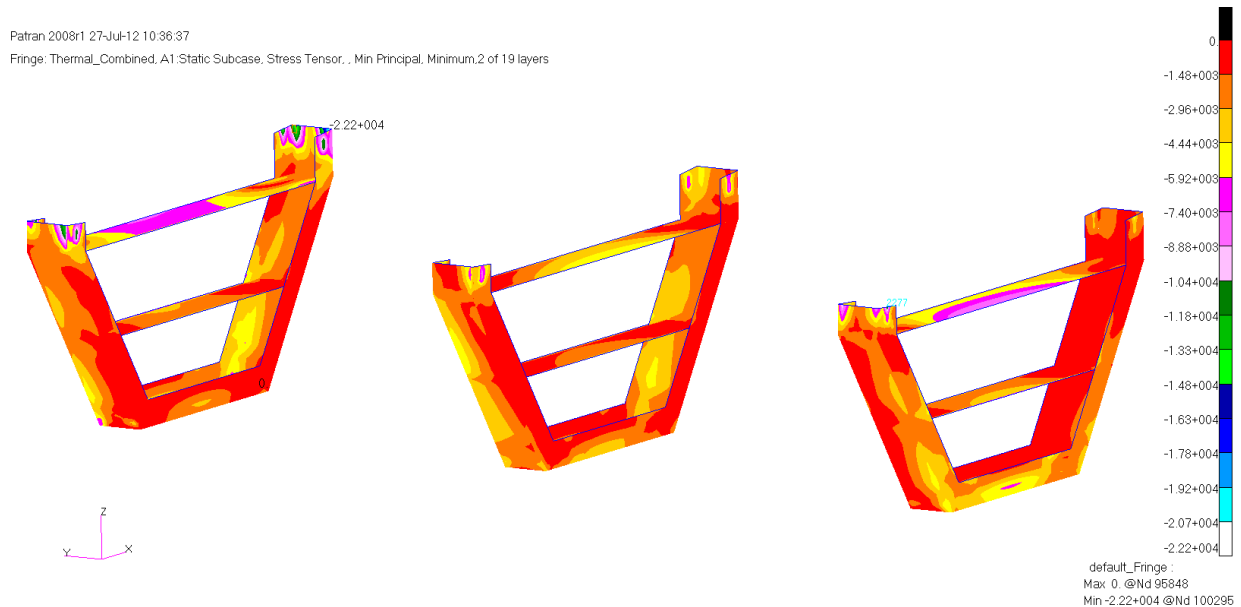


Figure 217: Pylon Substructure Compressive Stress Distribution

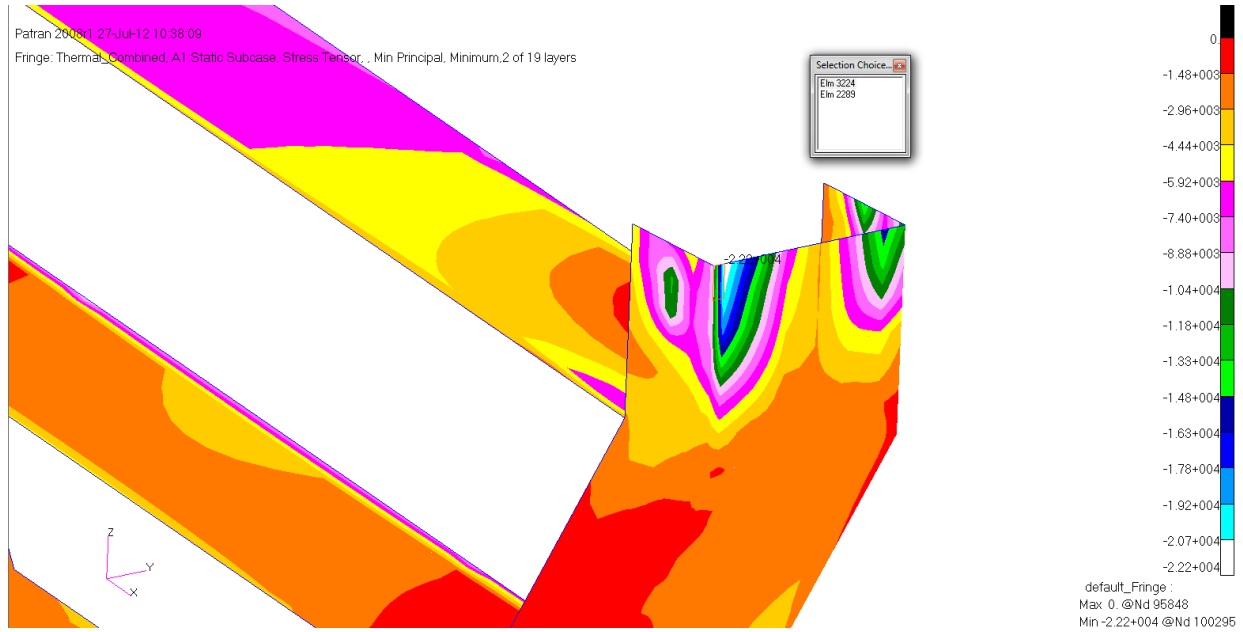


Figure 218: Pylon Substructure Compressive Stress Critical Region

STRESSES IN QUADRILATERAL ELEMENTS (QUAD4) OPTION = BILIN										
ELEMENT ID	GRID-ID	FIBER DISTANCE	STRESSES IN ELEMENT COORD SYSTEM			PRINCIPAL STRESSES (ZERO SHEAR)			VON MISES	
			NORMAL-X	NORMAL-Y	SHEAR-XY	ANGLE	MAJOR	MINOR		
0 3224	CEN/4	-3.100000E-02	-2.388146E+04	-5.288457E+03	2.660500E+03	82.0149	-4.915252E+03	-2.425466E+04	2.220879E+04	1.796858E+04
		3.100000E-02	1.949537E+04	4.179135E+03	-1.506547E+03	-5.5647	1.964215E+04	4.032353E+03	1.796858E+04	
98828		-3.100000E-02	-2.384763E+04	-5.704807E+03	2.660464E+03	81.8273	-5.322723E+03	-2.422971E+04	2.205544E+04	1.900322E+04
		3.100000E-02	2.048926E+04	3.961342E+03	-1.503927E+03	-5.1571	2.062499E+04	3.825610E+03	1.900322E+04	
100293		-3.100000E-02	-2.384764E+04	-4.872137E+03	2.660719E+03	82.1673	-4.506115E+03	-2.421366E+04	2.230464E+04	1.886342E+04
		3.100000E-02	2.048903E+04	4.396925E+03	-1.503794E+03	-5.2932	2.062835E+04	4.257603E+03	1.886342E+04	
100295		-3.100000E-02	-2.391545E+04	-4.865729E+03	2.660538E+03	82.1968	-4.501129E+03	-2.428004E+04	2.237171E+04	1.693904E+04
		3.100000E-02	1.849664E+04	4.400262E+03	-1.509179E+03	-6.0429	1.865641E+04	4.240498E+03	1.693904E+04	
98833		-3.100000E-02	-2.391545E+04	-5.711216E+03	2.660279E+03	81.8540	-5.330421E+03	-2.429625E+04	2.211813E+04	1.707070E+04
		3.100000E-02	1.849642E+04	3.957976E+03	-1.509315E+03	-5.8649	1.865146E+04	3.802939E+03	1.707070E+04	

Figure 219: Pylon Substructure Compressive Critical Stress

Figure 219 shows the maximum compressive stress of 24.30 ksi in the substructure captured from the results file. The margin of safety for this method of failure is shown below:

$$MS = \frac{\sigma_{allowable}}{FS \bullet \sigma_{actual}} - 1 = \frac{-65000 psi}{2.25 \bullet -24296.3 psi} - 1 = .116$$

3.5.9 Pylon Plate

The most critical margin of safety for the ribs is in tensile failure as seen in Table 40. The results are presented below in the same order as the previous section.

Table 40: Pylon Plate Failure Modes

Stress Type	Stress	Margin	Allowable	Load Case
Compressive	-22.16 (ksi)	0.404	-31.1 (ksi)	Thermal
Tensile	23.29 (ksi)	0.507	35.1 (ksi)	Thermal
Shear	16.38 (ksi)	0.221	20.0 (ksi)	Thermal

3.5.9.1 Compressive Stress

The pylon attachment plate's most critical region in compressive stress is at the outboard aft attachment point. Figure 220 shows the overall stress distribution in the plate and Figure 221 shows the region in the insert found to be the most critical with the critical element highlighted.



Figure 220: Attachment Plates Compressive Stress Distribution

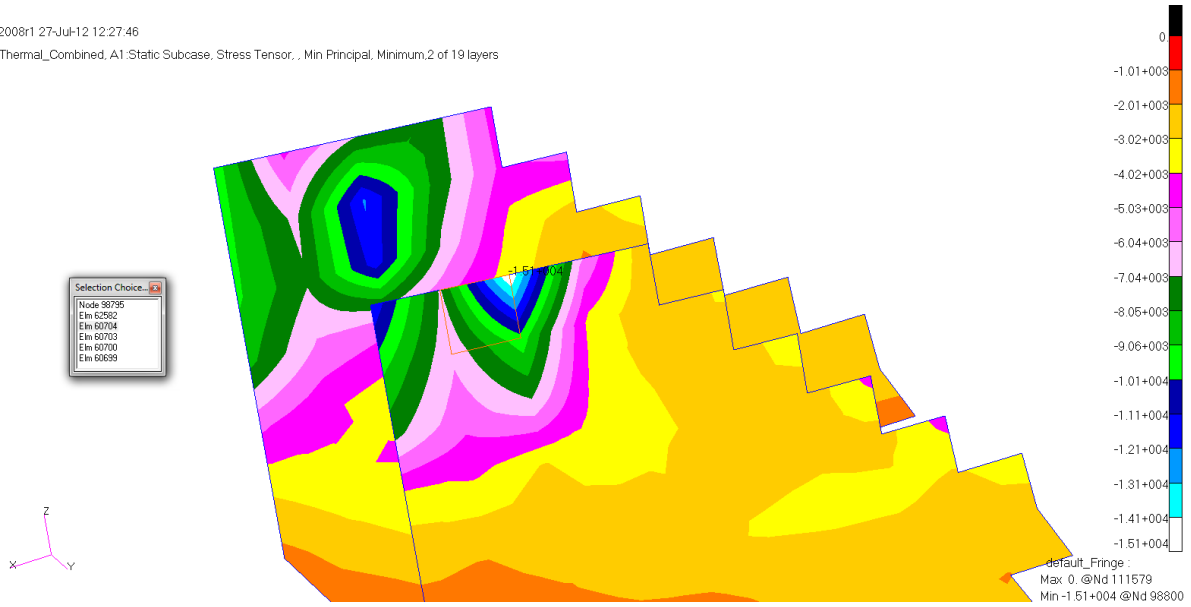


Figure 221: Attachment Plates Compressive Stress Critical Region

STRESSES IN QUADRILATERAL ELEMENTS (QUAD4)										OPTION = BILIN	
ELEMENT ID	GRID-ID	FIBER DISTANCE	STRESSES IN ELEMENT COORD SYSTEM			PRINCIPAL STRESSES (ZERO SHEAR)			VON MISES		
			NORMAL-X	NORMAL-Y	SHEAR-XY	ANGLE	MAJOR	MINOR			
0	60704	CEN/4	-6.250000E-02	1.552730E+04	1.063883E+04	8.272204E+03	36.7694	2.170882E+04	4.457312E+03	1.985894E+04	
			6.250000E-02	-1.419231E+04	-1.108950E+04	-9.448726E+03	-49.6622	-3.065660E+03	-2.221615E+04	2.085302E+04	

Figure 222: Attachment Plates Compressive Critical Stress

Figure 222 shows the maximum compressive stress of 22.2 ksi in the plate captured from the results file at the critical region. The margin of safety for this method of failure is shown below:

$$MS = \frac{\sigma_{allowable}}{FS \cdot \sigma_{actual}} - 1 = \frac{-79000 psi}{2.25 \cdot -22161.5 psi} - 1 = .404$$

3.5.9.2 Tensile Stress

The pylon attachment plate's most critical region in tensile stress is at the outboard aft attachment point. Figure 223 shows the overall stress distribution in the plate and Figure 224 shows the region in the plate found to be the most critical with the critical element highlighted.

Patran 2008r1 27-Jul-12 12:34:30

Fringe: Thermal_Combined, A1:Static Subcase, Stress Tensor, , Max Principal, Maximum,2 of 19 layers

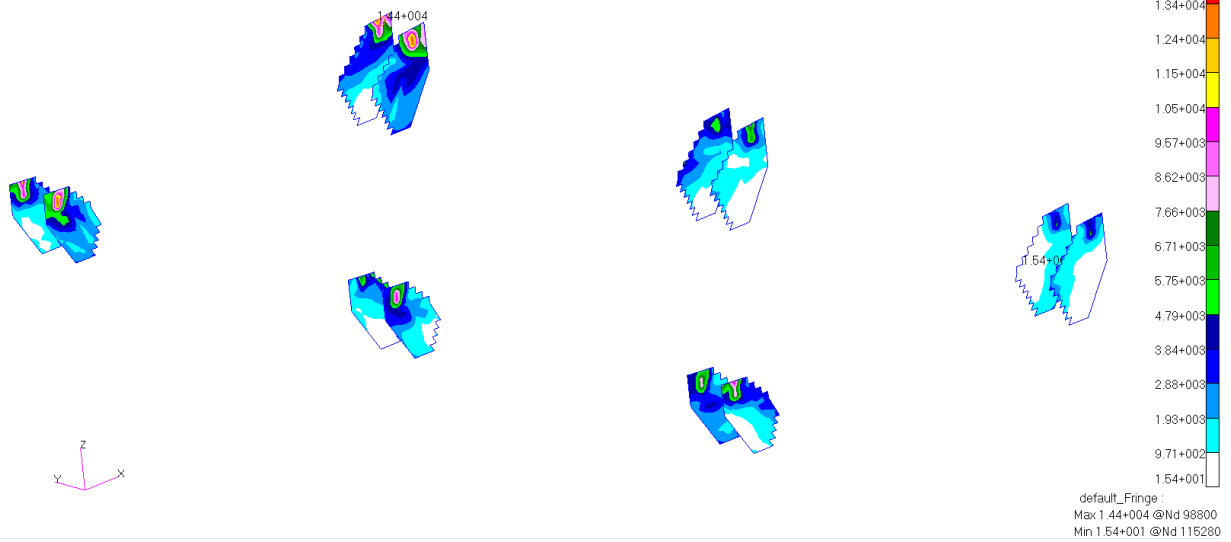


Figure 223: Attachment Plates Tensile Stress Distribution

Patran 2008r1 27-Jul-12 12:36:38

Fringe: Thermal_Combined, A1:Static Subcase, Stress Tensor, , Max Principal, Maximum,2 of 19 layers

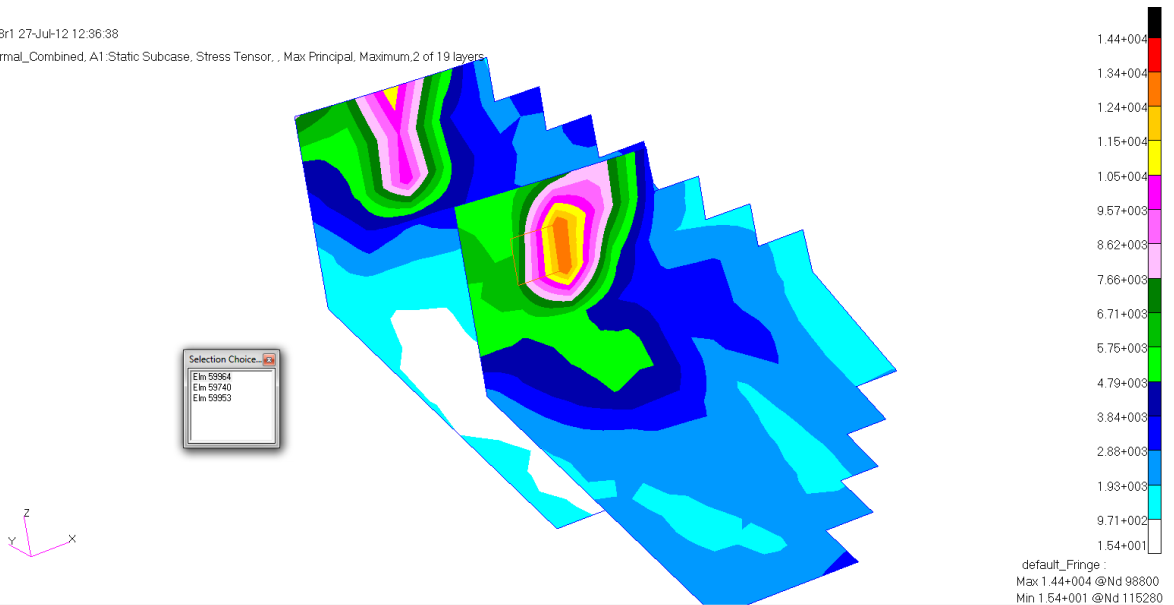


Figure 224: Attachment Plates Tensile Stress Critical Region

STRESSES IN QUADRILATERAL ELEMENTS (QUAD4)										OPTION = BILIN
ELEMENT ID	GRID-ID	FIBER DISTANCE	STRESSES IN ELEMENT COORD SYSTEM			PRINCIPAL STRESSES (ZERO SHEAR)			VON MISES	
			NORMAL-X	NORMAL-Y	SHEAR-XY	ANGLE	MAJOR	MINOR		
0	59964	CEN/4	-6.250000E-02	-1.640572E+04	-1.844218E+04	-3.913418E+03	-37.7078	-1.338023E+04	-2.146766E+04	1.877895E+04
			6.250000E-02	1.585531E+04	2.141251E+04	3.738028E+03	63.3123	2.329154E+04	1.397629E+04	2.030525E+04

Figure 225: Attachment Plates Tensile Critical Stress

Figure 225 shows the maximum tensile stress of 23.3 ksi in the plate captured from the results file at the critical region. The margin of safety for this method of failure is shown below:

$$MS = \frac{\sigma_{allowable}}{FS \bullet \sigma_{actual}} - 1 = \frac{79000 \text{ psi}}{2.25 \bullet 23291.5 \text{ psi}} - 1 = .507$$

3.5.9.3 Shear Stress

The pylon attachment plate's most critical region in shear stress is at the outboard aft attachment point. Figure 226 shows the overall stress distribution in the plate and Figure 227 shows the region in the plate found to be the most critical with the critical element highlighted.

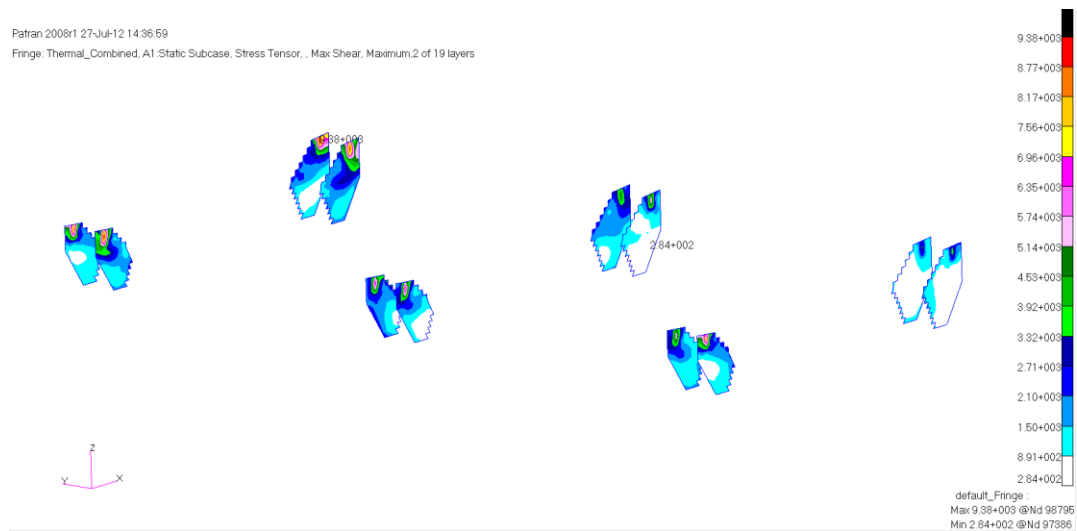


Figure 226: Attachment Plates Shear Stress Distribution

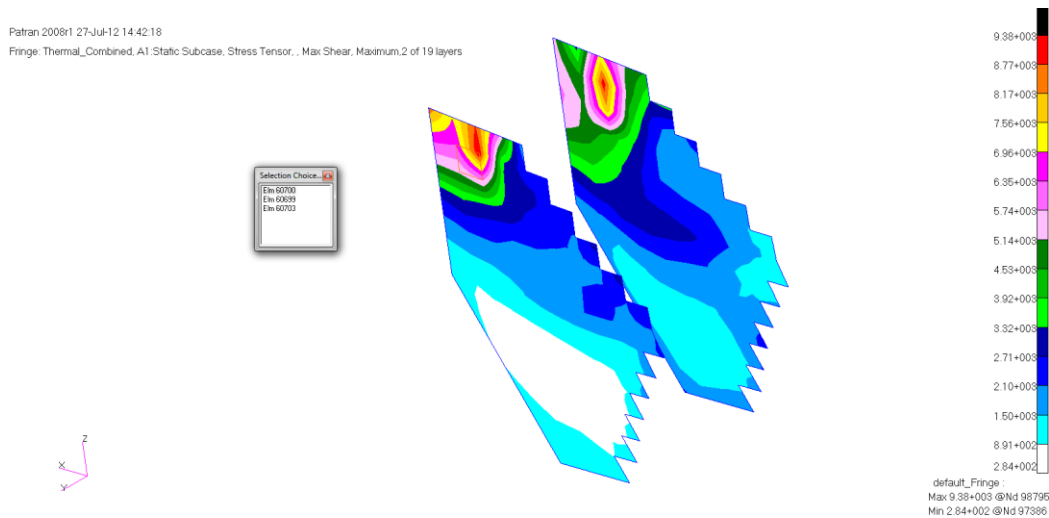


Figure 227: Attachment Plates Shear Stress Critical Region

STRESSES IN QUADRILATERAL ELEMENTS (QUAD4)										
OPTION = BILIN										
ELEMENT ID	GRID-ID	FIBER DISTANCE	STRESSES IN ELEMENT COORD SYSTEM			PRINCIPAL STRESSES (ZERO SHEAR)			VON MISES	
			NORMAL-X	NORMAL-Y	SHEAR-XY	ANGLE	MAJOR	MINOR		
0	60700	CEN/4	-6.250000E-02	1.777151E+03	-1.089175E+04	8.626824E+03	26.8556	6.145380E+03	-1.525998E+04	1.908955E+04
			6.250000E-02	-1.144252E+03	1.409440E+04	-1.050365E+04	-62.9785	1.945123E+04	-6.501086E+03	2.338950E+04
		98790	-6.250000E-02	-2.710207E+03	-2.248883E+04	8.036833E+03	19.5500	1.436832E+02	-2.534272E+04	2.541486E+04
			6.250000E-02	2.426596E+03	2.863123E+04	-9.833861E+03	-71.5551	8.191109E+04	-8.532579E+02	3.234616E+04
		98791	-6.250000E-02	-2.602962E+03	6.305472E+02	8.912812E+03	50.1407	8.072056E+03	-1.004447E+04	1.572034E+04
			6.250000E-02	2.326270E+03	-3.534036E+02	-1.093091E+04	-41.5060	1.199915E+04	-1.002629E+04	1.910008E+04
		98796	-6.250000E-02	6.190170E+03	6.407171E+02	9.211853E+03	36.6185	1.303612E+04	-6.205229E+03	1.700992E+04
			6.250000E-02	-4.656029E+03	-3.614791E+02	-1.116837E+04	-50.4416	8.864164E+03	-1.388167E+04	1.985758E+04
		98795	-6.250000E-02	6.231417E+03	-2.247849E+04	8.340923E+03	15.0793	8.478742E+03	-2.472581E+04	2.988141E+04
			6.250000E-02	-4.673613E+03	2.862302E+04	-1.007533E+04	-74.4091	3.143438E+04	-7.484964E+03	3.576912E+04

Figure 228: Attachment Plates Shear Critical Stress

Figure 228 shows the maximum shear stress of 16.38 ksi in the plates captured from the results file at the critical region. The margin of safety for this method of failure is shown below:

$$MS = \frac{\tau_{allowable}}{FS \bullet \tau_{actual}} - 1 = \frac{45000 \text{ psi}}{2.25 \bullet 16382 \text{ psi}} - 1 = .221$$

3.5.10 Pylon Skins

The most critical margin of safety for pylon skins is in buckling as seen in Table 41. The results are presented below in the same order as the previous section.

Table 41: Pylon Substructure Failure Methods

Stress Type	Stress	Margin	Allowable	Load Case
Compressive	-24.53 (ksi)	0.178	-28.9 (ksi)	No Thermal
Tensile	25.24 (ksi)	0.145	28.9 (ksi)	Thermal
Shear	8.44 (ksi)	1.105	17.8 (ksi)	No Thermal

3.5.10.1 Shear

The pylon skin's most critical region in shear stress is on the inboard skin near the middle pylon rib. Figure 229 shows the overall stress distribution in the skin and Figure 230 shows the region in the skin found to be the most critical with the critical element highlighted.

Patran 2008r1 05-Mar-12 19:53:47
 Fringe: Combined, A1 Static Subcase, Stress Tensor, Max Shear, 2 of 19 layers (Maximum)

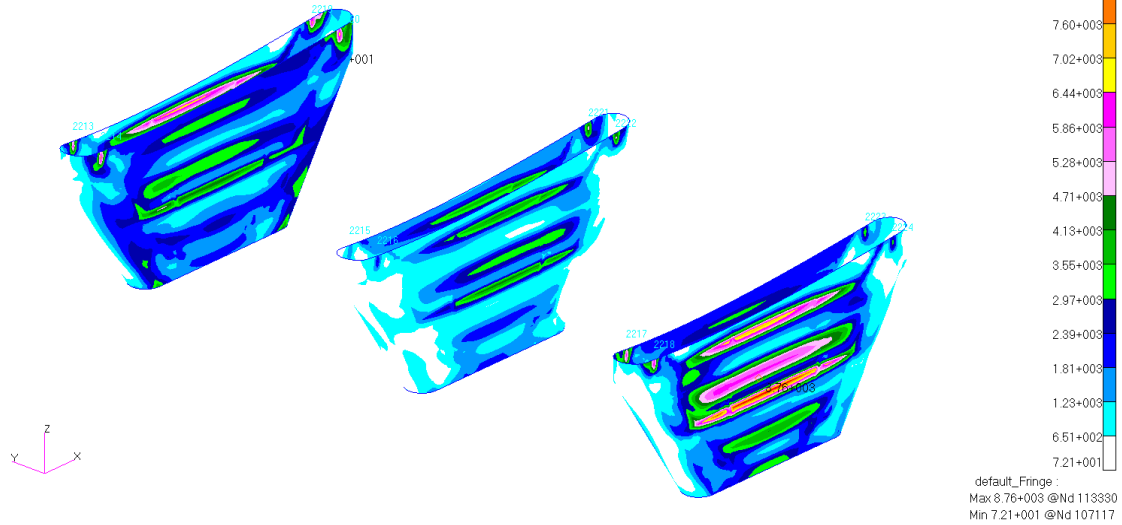


Figure 229: Pylon Skins Shear Stress Distribution

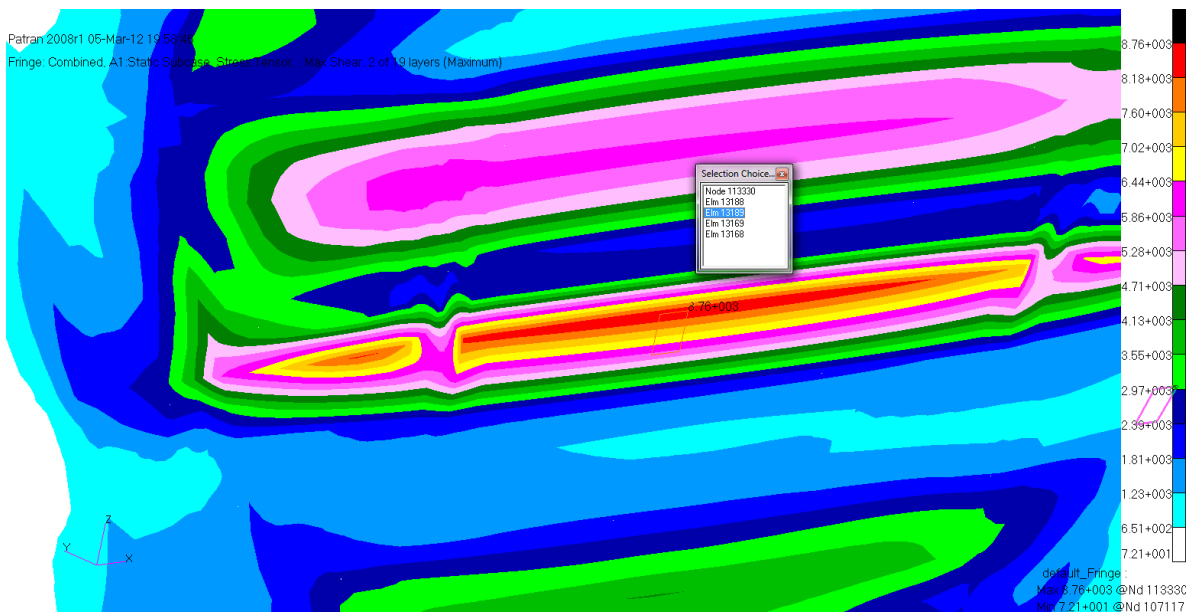


Figure 230: Pylon Skins Shear Stress Critical Region

0	13189	CEN/4	-1.600000E-02	7.602747E+03	2.430352E+04	3.995722E+02	88.6302	2.431308E+04	7.593193E+03	2.154457E+04
			1.600000E-02	-7.668160E+03	-2.451305E+04	4.943095E+02	1.6794	-7.653667E+03	-2.452754E+04	2.173599E+04
	113330		-1.600000E-02	7.630138E+03	2.431809E+04	3.995722E+02	88.6292	2.432765E+04	7.620577E+03	2.155265E+04
			1.600000E-02	-7.661832E+03	-2.452061E+04	4.943095E+02	1.6780	-7.647351E+03	-2.453509E+04	2.174452E+04
	113331		-1.600000E-02	7.630138E+03	2.428896E+04	3.995722E+02	88.6268	2.429854E+04	7.620560E+03	2.152495E+04
			1.600000E-02	-7.661832E+03	-2.450548E+04	4.943095E+02	1.6795	-7.647338E+03	-2.451997E+04	2.173013E+04
	101914		-1.600000E-02	7.575356E+03	2.428896E+04	3.995722E+02	88.6313	2.429851E+04	7.565809E+03	2.153651E+04
			1.600000E-02	-7.674487E+03	-2.450548E+04	4.943095E+02	1.6808	-7.659982E+03	-2.451999E+04	2.172746E+04
	101915		-1.600000E-02	7.575356E+03	2.431809E+04	3.995722E+02	88.6337	2.432762E+04	7.565826E+03	2.156423E+04
			1.600000E-02	-7.674487E+03	-2.452061E+04	4.943095E+02	1.6793	-7.659995E+03	-2.453510E+04	2.174185E+04

Figure 231: Pylon Skins Shear Critical Stress

Figure 231 shows the maximum shear stress of 8.44 ksi in the skin captured from the results file at the critical region. The margin of safety for this method of failure is shown below:

$$MS = \frac{\tau_{allowable}}{FS \bullet \tau_{actual}} - 1 = \frac{40000 \text{ psi}}{2.25 \bullet 8444 \text{ psi}} - 1 = 1.105$$

3.5.10.2 Tensile Stress

The pylon skin's most critical region in tensile stress is on the inboard skin near the middle pylon rib. Figure 232 shows the overall stress distribution in the skin and Figure 233 shows the region in the skin found to be the most critical with the critical element highlighted.

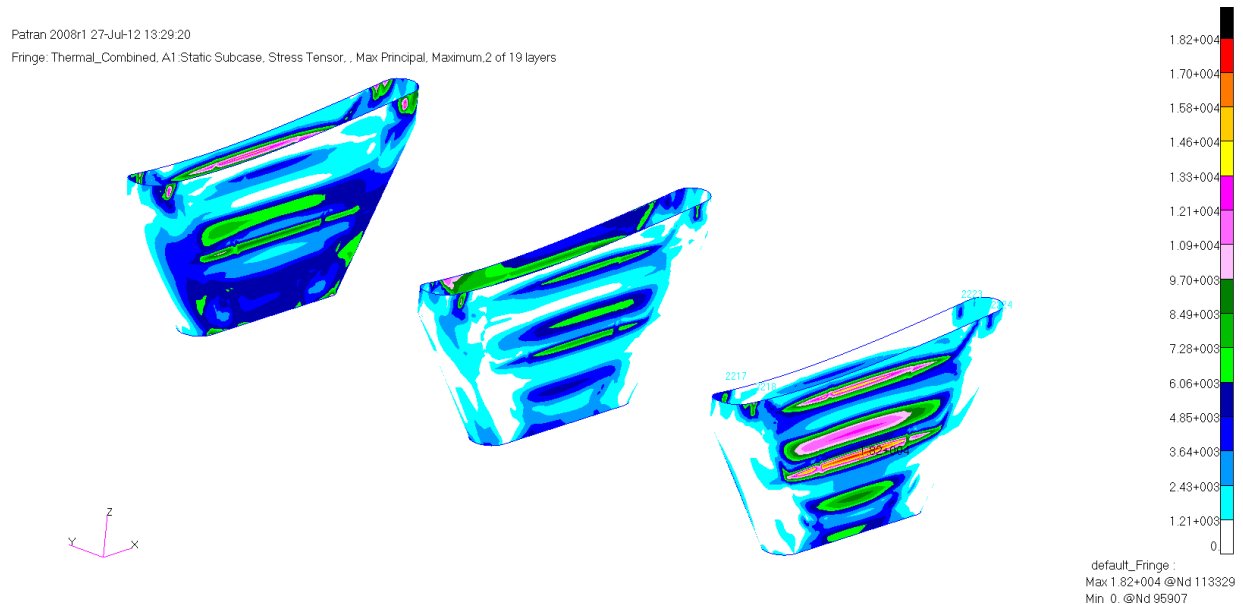


Figure 232: Pylon Skins Tensile Stress Distribution

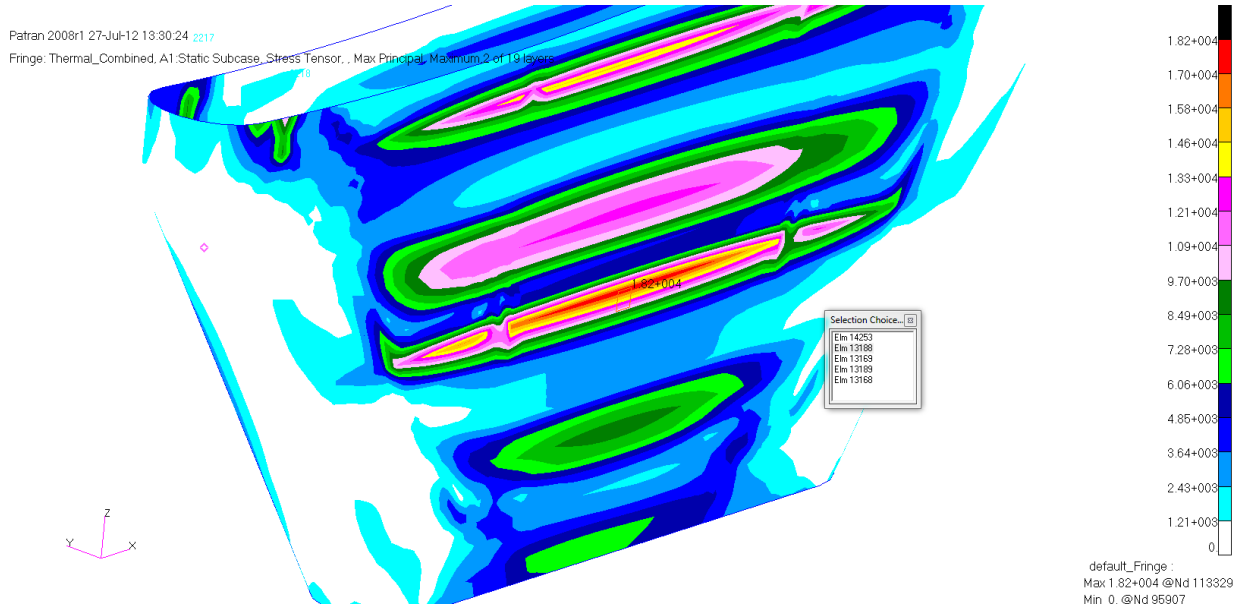


Figure 233: Pylon Skins Tensile Stress Critical Region

STRESSES IN QUADRILATERAL ELEMENTS (QUAD4)										OPTION = BILIN	
ELEMENT ID	GRID-ID	FIBER DISTANCE	STRESSES IN ELEMENT COORD SYSTEM			PRINCIPAL STRESSES (ZERO SHEAR)			VON MISES		
			NORMAL-X	NORMAL-Y	SHEAR-XY	ANGLE	MAJOR	MINOR			
0	13188	CEN/4	-1.600000E-02	7.995119E+03	2.523176E+04	3.154557E+02	88.9519	2.523754E+04	7.989348E+03	2.234125E+04	
			1.600000E-02	-7.379523E+03	-2.389400E+04	3.707177E+02	1.2853	-7.371206E+03	-2.390232E+04	2.120063E+04	
	113329	-1.600000E-02	8.021192E+03	2.523563E+04	3.154557E+02	88.9505	2.524141E+04	8.015414E+03	2.233955E+04		
		1.600000E-02	-7.382236E+03	-2.388541E+04	3.707177E+02	1.2862	-7.373913E+03	-2.389373E+04	2.119185E+04		
	113330	-1.600000E-02	8.021192E+03	2.522789E+04	3.154557E+02	88.9501	2.523368E+04	8.015411E+03	2.233220E+04		
		1.600000E-02	-7.382236E+03	-2.390260E+04	3.707177E+02	1.2849	-7.373921E+03	-2.391091E+04	2.120823E+04		
	101915	-1.600000E-02	7.969046E+03	2.522789E+04	3.154557E+02	88.9532	2.523366E+04	7.963282E+03	2.234298E+04		
		1.600000E-02	-7.376810E+03	-2.390260E+04	3.707177E+02	1.2844	-7.368498E+03	-2.391091E+04	2.120940E+04		
	101916	-1.600000E-02	7.969046E+03	2.523563E+04	3.154557E+02	88.9537	2.524140E+04	7.963284E+03	2.235034E+04		
		1.600000E-02	-7.376810E+03	-2.388541E+04	3.707177E+02	1.2858	-7.368490E+03	-2.389373E+04	2.119302E+04		

Figure 234: Pylon Skins Tensile Critical Stress

Figure 234 shows the maximum tensile stress of 25.41 ksi in the skin captured from the results file at the critical region. The margin of safety for this method of failure is shown below:

$$MS = \frac{\sigma_{allowable}}{FS \bullet \sigma_{actual}} - 1 = \frac{65000 \text{ psi}}{2.25 \bullet 25414 \text{ psi}} - 1 = .145$$

3.5.10.3 Compressive Stress

The pylon skin's most critical region in compressive stress is on the inboard skin near the middle pylon rib. Figure 235 shows the overall stress distribution in the skin and Figure 236 shows the region in the skin found to be the most critical with the critical element highlighted.

Patran 2008r1 05-Mar-12 20:12:24

Fringe: Combined, A1 Static Subcase, Stress Tensor, Min Principal, 2 of 19 layers (Minimum)

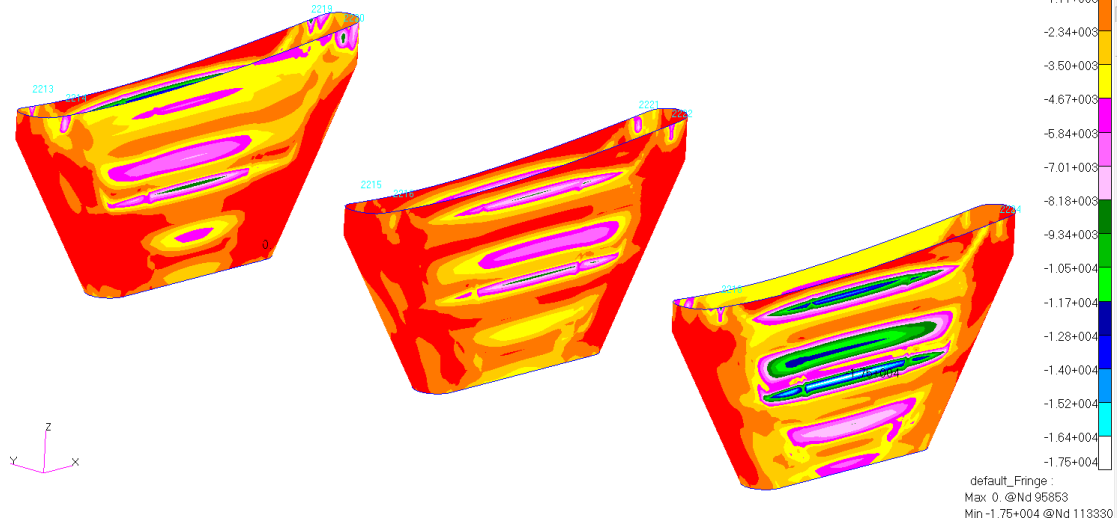


Figure 235: Pylon Skins Compressive Stress Distribution

Patran 2008r1 11-Mar-12 15:10:26

Fringe: Combined, A1 Static Subcase, Stress Tensor, Min Principal, 2 of 19 layers (Minimum)

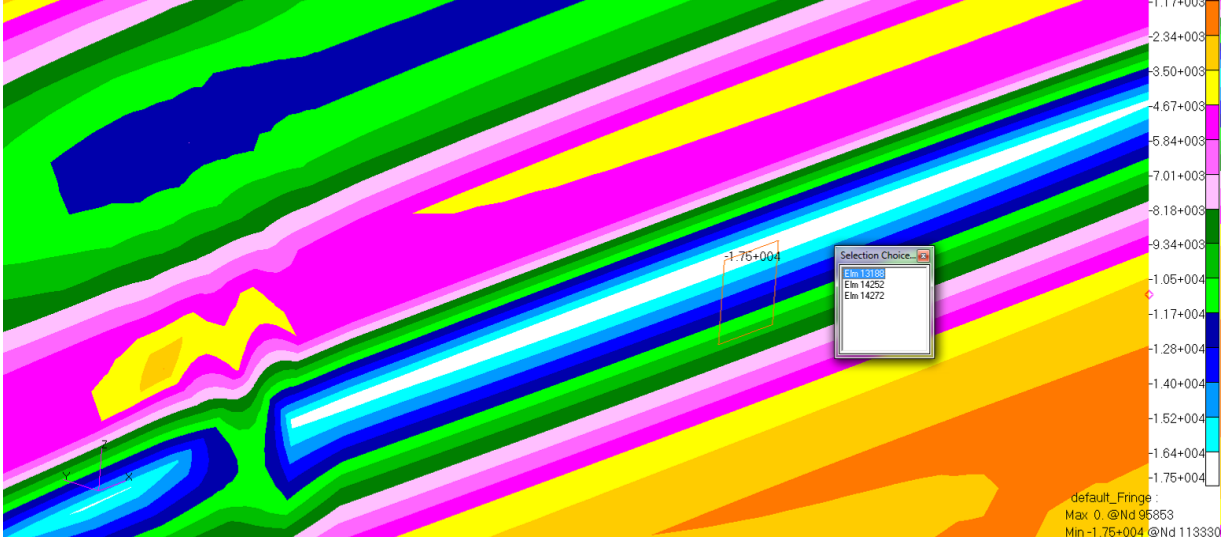


Figure 236: Pylon Skins Compressive Stress Distribution

STRESSES IN QUADRILATERAL ELEMENTS (QUAD4)											OPTION = BILIN
ELEMENT ID	GRID-ID	FIBER DISTANCE	STRESSES IN ELEMENT COORD SYSTEM		PRINCIPAL STRESSES (ZERO SHEAR)			VON MISES			
			NORMAL-X	NORMAL-Y	SHEAR-XY	ANGLE	MAJOR	MINOR			
0	13188	CEN/4	-1.600000E-02	7.620901E+03	2.431980E+04	4.031748E+02	88.6177	2.432953E+04	7.611172E+03	2.155643E+04	
			1.600000E-02	-7.662353E+03	-2.451695E+04	4.582301E+02	1.5562	-7.649903E+03	-2.452940E+04	2.173856E+04	
	113329		-1.600000E-02	7.651787E+03	2.431584E+04	4.031748E+02	88.6149	2.432559E+04	7.642038E+03	2.154618E+04	
			1.600000E-02	-7.660778E+03	-2.451510E+04	4.582301E+02	1.5562	-7.648329E+03	-2.452755E+04	2.173713E+04	
	113330		-1.600000E-02	7.651787E+03	2.432376E+04	4.031748E+02	88.6155	2.43350E+04	7.642043E+03	2.155371E+04	
			1.600000E-02	-7.660778E+03	-2.451880E+04	4.582301E+02	1.5559	-7.648332E+03	-2.453124E+04	2.174065E+04	
	101915		-1.600000E-02	7.590014E+03	2.432376E+04	4.031748E+02	88.6206	2.433347E+04	7.580306E+03	2.156672E+04	
			1.600000E-02	-7.663926E+03	-2.451880E+04	4.582301E+02	1.5562	-7.651478E+03	-2.453125E+04	2.173998E+04	
	101916		-1.600000E-02	7.590014E+03	2.431584E+04	4.031748E+02	88.6200	2.432555E+04	7.580301E+03	2.155919E+04	
			1.600000E-02	-7.663926E+03	-2.451510E+04	4.582301E+02	1.5565	-7.651475E+03	-2.452755E+04	2.173647E+04	

Figure 237: Pylon Skins Compressive Critical Stress

Figure 237 shows the maximum compressive stress of 24.53 ksi in the skin captured from the results file at the critical region. The margin of safety for this method of failure is shown below:

$$MS = \frac{\sigma_{allowable}}{FS \bullet \sigma_{actual}} - 1 = \frac{65000 \text{ psi}}{2.25 \bullet 24529 \text{ psi}} - 1 = .178$$

3.5.11 Trailing Edge Ribs

The most critical margin of safety for pylon skins is in tensile failure as seen in Table 42. The results are presented below in the same order as the previous section.

Table 42: Trailing Edge Ribs Failure Modes

Stress Type	Stress	Margin	Allowable
Compressive	-5.60	3.837	-27.1
Tensile	9.25	1.931	27.1
Shear	3.05	3.521	13.8

3.5.11.1 Compressive Stress

The trailing edge rib's most critical region in compressive stress is at the outboard rib along the spar near the lower skin. Figure 238 shows the overall stress distribution in the rib and Figure 239 shows the region in the rib found to be the most critical with the critical element highlighted.

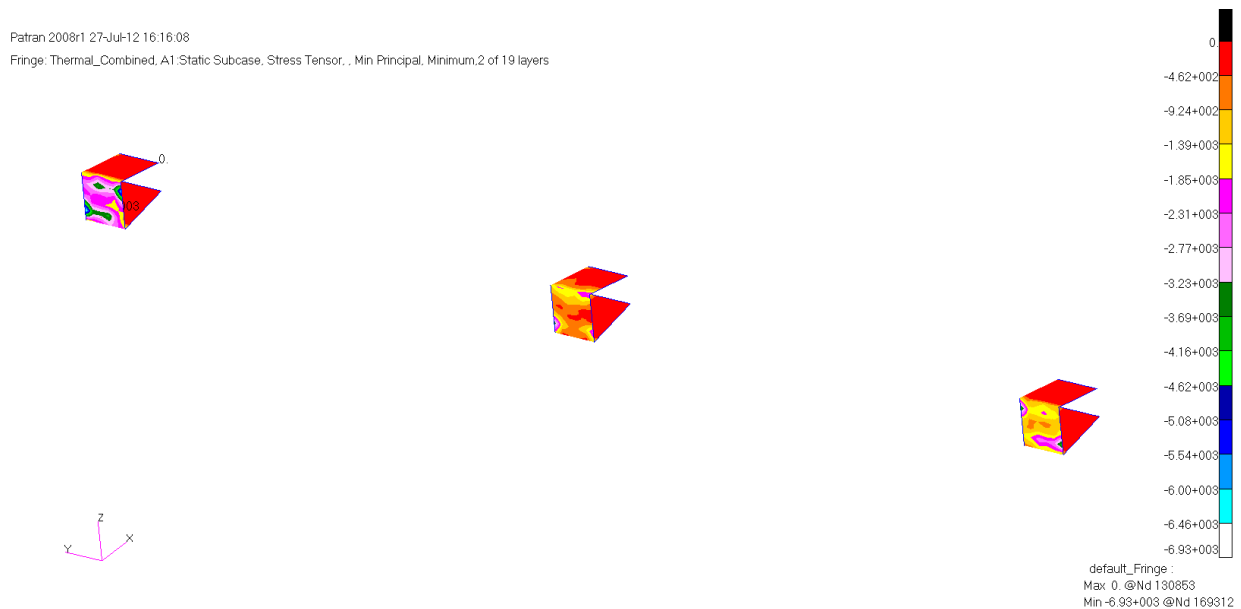


Figure 238: Trailing Edge Ribs Compressive Stress Distribution

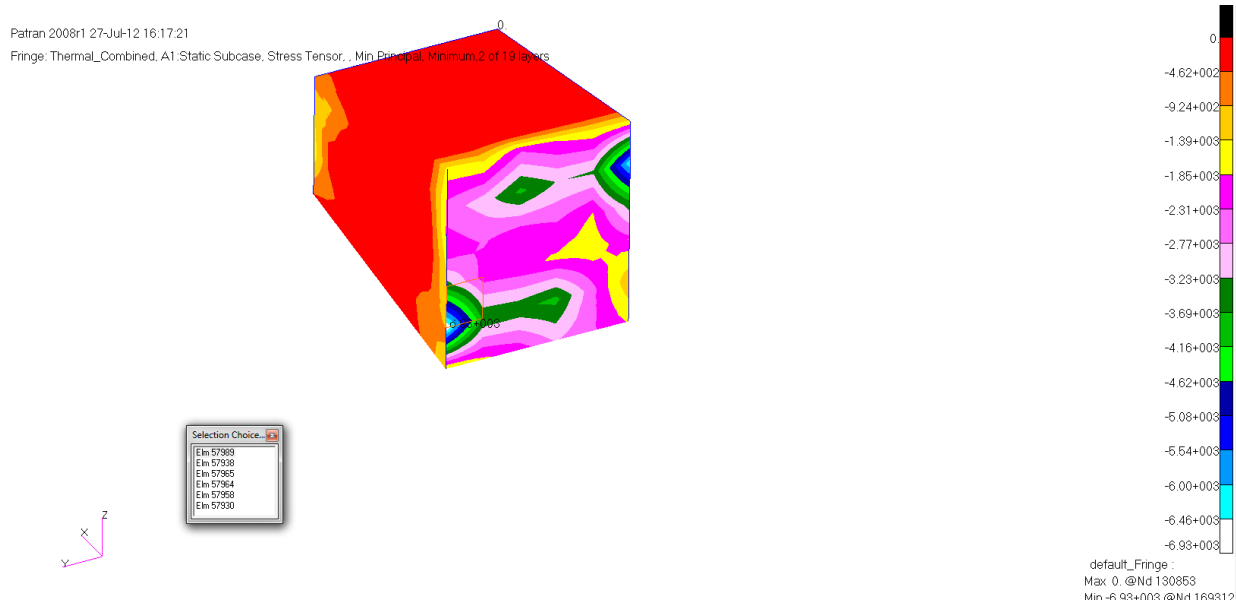


Figure 239: Trailing Edge Ribs Compressive Stress Critical Region

STRESSES IN QUADRILATERAL ELEMENTS (QUAD4)										
OPTION = BILIN										
ELEMENT ID	GRID-ID	FIBER DISTANCE	STRESSES IN ELEMENT COORD SYSTEM			PRINCIPAL STRESSES (ZERO SHEAR)			VON MISES	
			NORMAL-X	NORMAL-Y	SHEAR-XY	ANGLE	MAJOR	MINOR		
0	57989	CEN/4	-3.600000E-02	-5.127567E+03	1.357268E+03	76.7979	1.734914E+03	-5.505213E+03	6.547394E+03	6.547394E+03
			3.600000E-02	-5.736127E+03	7.049882E+02	79.0880	9.536252E+02	-5.984765E+03	6.514141E+03	6.514141E+03
	169312		-3.600000E-02	-8.902856E+03	-1.480036E+03	78.2722	-1.145733E+03	-9.237159E+03	8.720923E+03	8.720923E+03
			3.600000E-02	-9.602762E+03	-1.178783E+03	81.4851	-9.856295E+02	-9.795914E+03	9.342177E+03	9.342177E+03
	157370		-3.600000E-02	-8.902853E+03	4.194570E+03	83.0946	4.389537E+03	-9.097819E+03	1.191527E+04	1.191527E+04
			3.600000E-02	-9.602757E+03	2.588758E+03	84.0266	2.723715E+03	-9.737714E+03	1.134744E+04	1.134744E+04
	157368		-3.600000E-02	-1.352067E+03	4.195057E+03	74.9380	4.628144E+03	-1.785153E+03	5.733100E+03	5.733100E+03
			3.600000E-02	-1.869277E+03	2.589081E+03	74.9783	2.935063E+03	-2.215259E+03	4.474806E+03	4.474806E+03
	169315		-3.600000E-02	-1.352063E+03	-1.480522E+03	43.8576	1.948354E+02	-3.027420E+03	3.129390E+03	3.129390E+03
			3.600000E-02	-1.869273E+03	-1.179105E+03	52.4903	-1.892064E+02	-2.859172E+03	2.769420E+03	2.769420E+03

Figure 240: Trailing Edge Ribs Compressive Critical Stress

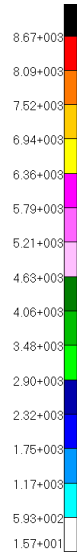
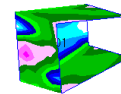
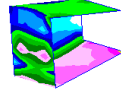
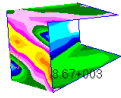
Figure 240 shows the maximum compressive stress of 9.80 ksi in the rib captured from the results file at the critical region. The margin of safety for this method of failure is shown below:

$$MS = \frac{\sigma_{allowable}}{FS \bullet \sigma_{actual}} - 1 = \frac{-61000 psi}{2.25 \bullet -9795.9 psi} - 1 = 1.768$$

3.5.11.2 Tensile Stress

The trailing edge rib's most critical region in tensile stress is at the outboard rib along the aft spar. Figure 241 shows the overall stress distribution in the rib and Figure 242 shows the region in the rib found to be the most critical with the critical element highlighted.

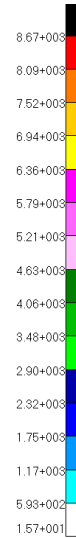
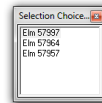
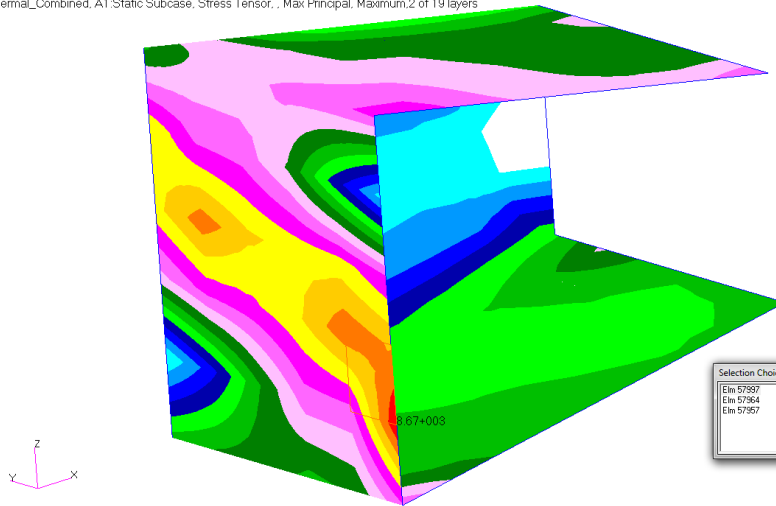
Patran 2008r1 27-Jul-12 17:26:30
 Fringe: Thermal_Combined, A1:Static Subcase, Stress Tensor, , Max Principal, Maximum,2 of 19 layers



default_Fringe :
 Max 8.67+003 @Nd 169327
 Min 1.57+001 @Nd 169387

Figure 241: Trailing Edge Ribs Tensile Stress Distribution

Patran 2008r1 28-Jul-12 10:58:26
 Fringe: Thermal_Combined, A1:Static Subcase, Stress Tensor, , Max Principal, Maximum,2 of 19 layers



default_Fringe :
 Max 8.67+003 @Nd 169327
 Min 1.57+001 @Nd 169387

Figure 242: Trailing Edge Ribs Tensile Stress Critical Region

STRESSES IN QUADRILATERAL ELEMENTS (QUAD4)										OPTION = BILIN	
ELEMENT ID	GRID-ID	FIBER DISTANCE	STRESSES IN ELEMENT COORD SYSTEM			PRINCIPAL STRESSES (ZERO SHEAR)			VON MISES		
			NORMAL-X	NORMAL-Y	SHEAR-XY	ANGLE	MAJOR	MINOR			
0	57997	CEN/4	-3.600000E-02	7.617251E+03	4.057221E+03	31.6771	9.806277E+03	1.868194E+03	9.018492E+03		
			3.600000E-02	5.281981E+03	2.277540E+03	34.4253	7.943321E+03	-3.838004E+02	8.142009E+03		
	169324		-3.600000E-02	1.714153E+03	1.038911E+03	42.2823	4.940798E+03	-2.187733E+03	6.325094E+03		
			3.600000E-02	1.132884E+03	1.100992E+03	44.8824	5.000502E+03	-2.766626E+03	6.818634E+03		
	157362		-3.600000E-02	1.712973E+03	7.075731E+03	63.5414	8.841324E+03	-5.261990E+01	8.867751E+03		
			3.600000E-02	1.132054E+03	3.454165E+03	53.3230	6.346264E+03	-1.760044E+03	7.385292E+03		
	157360		-3.600000E-02	1.352153E+04	7.075734E+03	23.8696	1.509100E+04	5.506270E+03	1.322732E+04		
			3.600000E-02	9.431909E+03	3.454167E+03	26.2056	1.134290E+04	1.543173E+03	1.065546E+04		
	169327		-3.600000E-02	1.352035E+04	1.038908E+03	14.8075	1.445811E+04	1.011541E+02	1.440779E+04		
			3.600000E-02	9.431080E+03	1.100991E+03	21.4962	1.096031E+04	-4.282362E+02	1.118058E+04		

Figure 243: Trailing Edge Ribs Tensile Critical Stress

Figure 243 shows the maximum tensile stress of 15.09 ksi in the rib captured from the results file at the critical region. The margin of safety for this method of failure is shown below:

$$MS = \frac{\sigma_{allowable}}{FS \bullet \sigma_{actual}} - 1 = \frac{61000\,psi}{2.25 \bullet 15091\,psi} - 1 = .797$$

3.5.11.3 Shear Stress

The trailing edge rib's most critical region in shear stress is at the outboard rib along the aft spar. Figure 244 shows the overall stress distribution in the rib and Figure 245 shows the region in the rib found to be the most critical with the critical element highlighted.

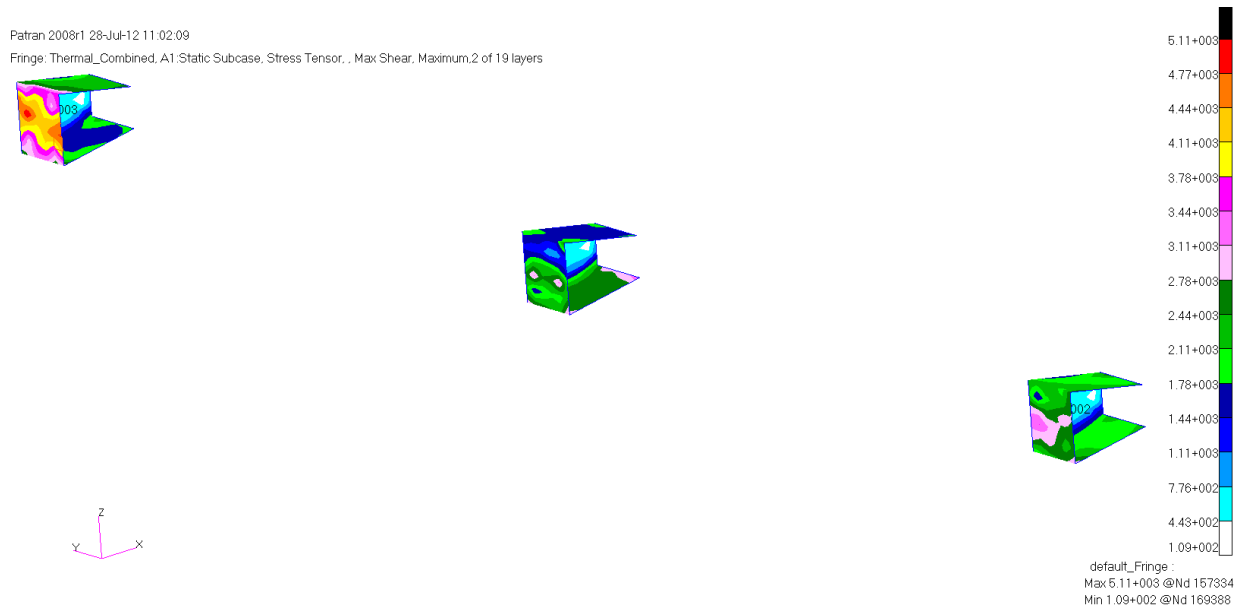


Figure 244: Trailing Edge Ribs Shear Stress Distribution

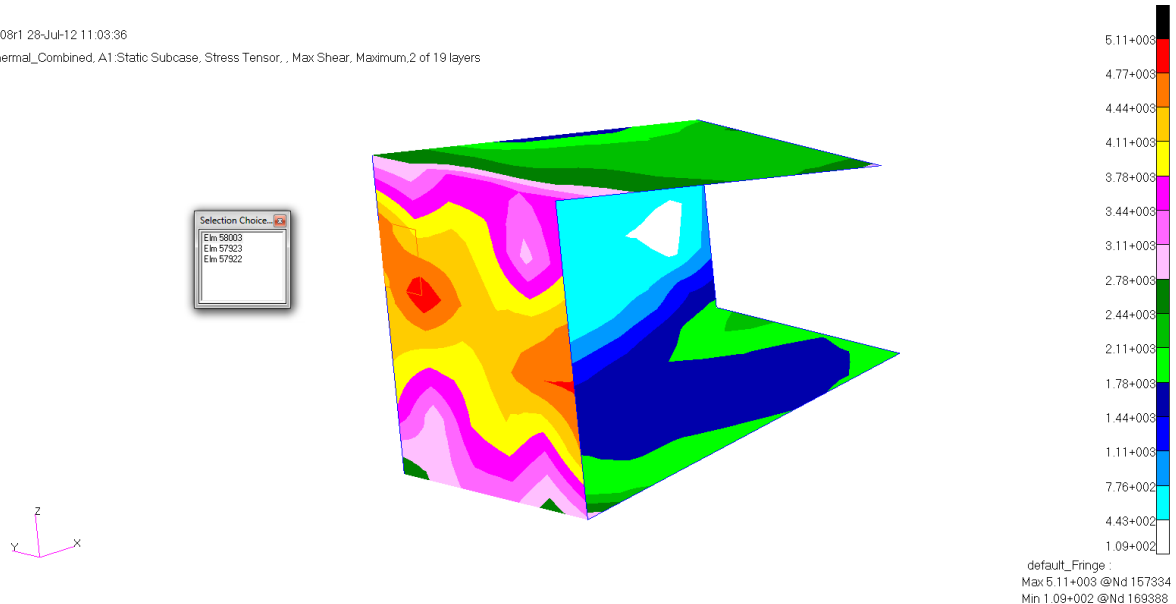


Figure 245: Trailing Edge Ribs Shear Stress Critical Region

STRESSES IN QUADRILATERAL ELEMENTS (QUAD4)											OPTION = BILIN
ELEMENT ID	GRID-ID	FIBER DISTANCE	STRESSES IN ELEMENT COORD SYSTEM			PRINCIPAL STRESSES (ZERO SHEAR)			VON MISES		
			NORMAL-X	NORMAL-Y	SHEAR-XY	ANGLE	MAJOR	MINOR			
0	58003	CEN/4	-3.600000E-02	6.659933E+03	3.947921E+03	4.178624E+03	36.0106	9.697063E+03	9.107899E+02	9.275268E+03	
			3.600000E-02	4.015536E+03	2.473404E+03	4.503752E+03	40.1424	7.813750E+03	-1.324810E+03	8.553453E+03	
	157329	-3.600000E-02	1.239913E+04	7.030421E+03	4.177962E+03	28.6396	1.468077E+04	4.748779E+03	1.297537E+04		
		3.600000E-02	8.242430E+03	3.865820E+03	4.503344E+03	32.0418	1.106100E+04	1.047251E+03	1.057633E+04		
	169342	-3.600000E-02	1.239913E+04	8.654215E+02	4.178521E+03	17.9631	1.375383E+04	-4.892867E+02	1.400489E+04		
		3.600000E-02	8.242426E+03	1.080989E+03	4.503597E+03	25.7563	1.041531E+04	-1.091894E+03	1.100197E+04		
	169345	-3.600000E-02	9.204105E+02	8.648930E+02	4.179286E+03	44.8097	5.072030E+03	-3.286726E+03	7.293726E+03		
		3.600000E-02	-2.115944E+02	1.080750E+03	4.504160E+03	49.0820	4.984852E+03	-4.115696E+03	7.893278E+03		
	157334	-3.600000E-02	9.204047E+02	7.030950E+03	4.178727E+03	63.0862	9.152206E+03	-1.200851E+03	9.807923E+03		
		3.600000E-02	-2.115987E+02	3.866058E+03	4.503907E+03	57.1777	6.771115E+03	-3.116655E+03	8.755842E+03		

Figure 246: Trailing Edge Ribs Shear Critical Stress

Figure 246 shows the maximum tensile stress of 7.12 ksi in the rib captured from the results file at the critical region. The margin of safety for this method of failure is shown below:

$$MS = \frac{\tau_{allowable}}{FS \bullet \tau_{actual}} - 1 = \frac{31000 psi}{2.25 \bullet 7121.6 psi} - 1 = 0.935$$

3.6 Fastener Sizing

Fasteners were used to tie the components in the fairing. This was done to allow access to the antennas within the fairing. Ideally the fairing skin to spar and rib connections would be bonded to prevent the stress concentrations that fasteners induce but maintenance on the antennas do not allow this. To develop the fastener loads the nodal forces in the model were examined. All of these loads were assumed to travel through the fastener. Since the fastener spacing is larger than the nodal spacing multiple nodes were summed to develop a critical fastener load.

3.6.1 Upper Skin Fasteners

Figure 247 shows the nodal forces in the upper skin and Figure 248 shows the region found to be critical between the spar and trailing edge fasteners. 3/16th inch AN3 fasteners were used spaced at 3" along this region. Since the nodal spacing is .5" the fastener is forced to take the load of 6 nodes.

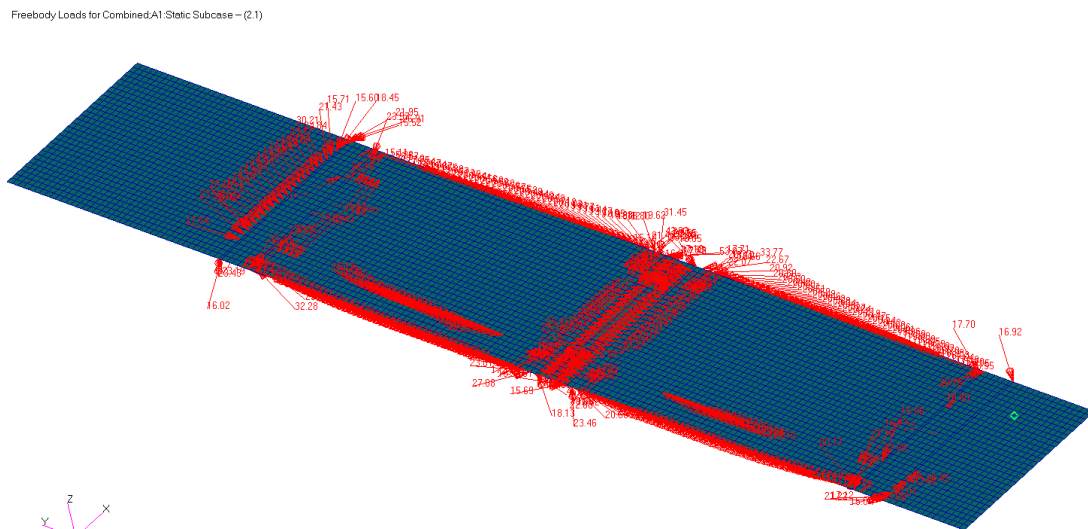


Figure 247: Upper Skin Nodal Forces

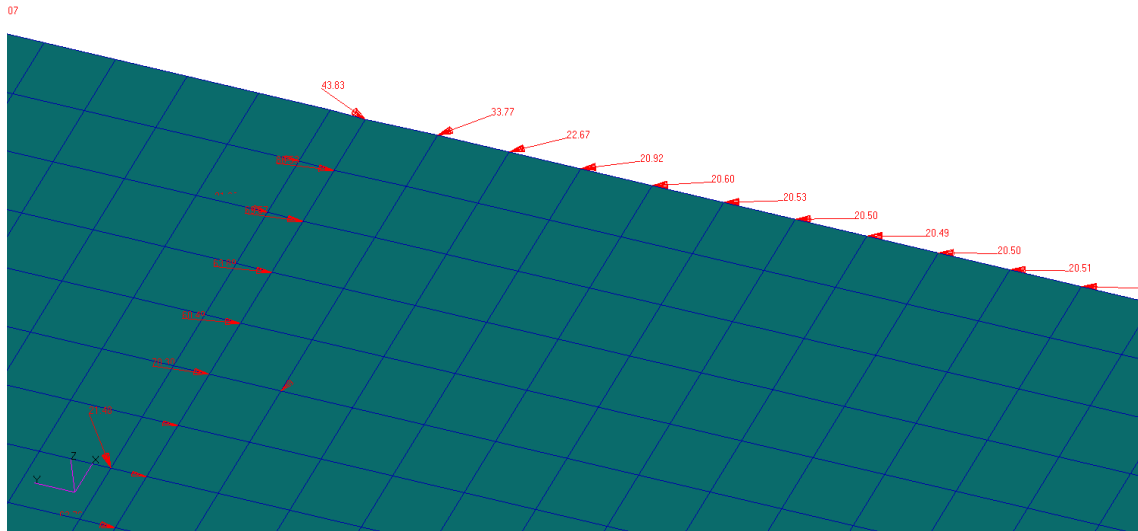


Figure 248: Spar to Trailing Edge Fastener Critical Region

The shear allowable for the bolts and bearing allowable for the skin are shown below. The bearing allowable for the skin is the critical margin of safety for the fasteners.

$$MS = \frac{FF * \tau_{shear\ allowable}}{FS * \tau_{shear\ actual}} - 1 = \frac{2125\ psi \cdot 0.9}{2.5 \cdot (33.8 + 22.67) \cdot 3\ psi} - 1 = 4.52$$

$$MS = \frac{\sigma_{BRU} \cdot t \cdot D}{FS \cdot P_{actual}} - 1 = \frac{31600\ psi \cdot 0.0101\ in \cdot 8 \cdot .1875\ in}{2.25 \cdot (33.8 + 22.67) \cdot 3\ psi} - 1 = .130$$

Figure 249 shows the region found to be critical between the spar and upper skin. 3/16th inch AN3 fasteners were used spaced at 3" along this region. Since the nodal spacing is .5" the fastener is forced to take the load of 6 nodes.

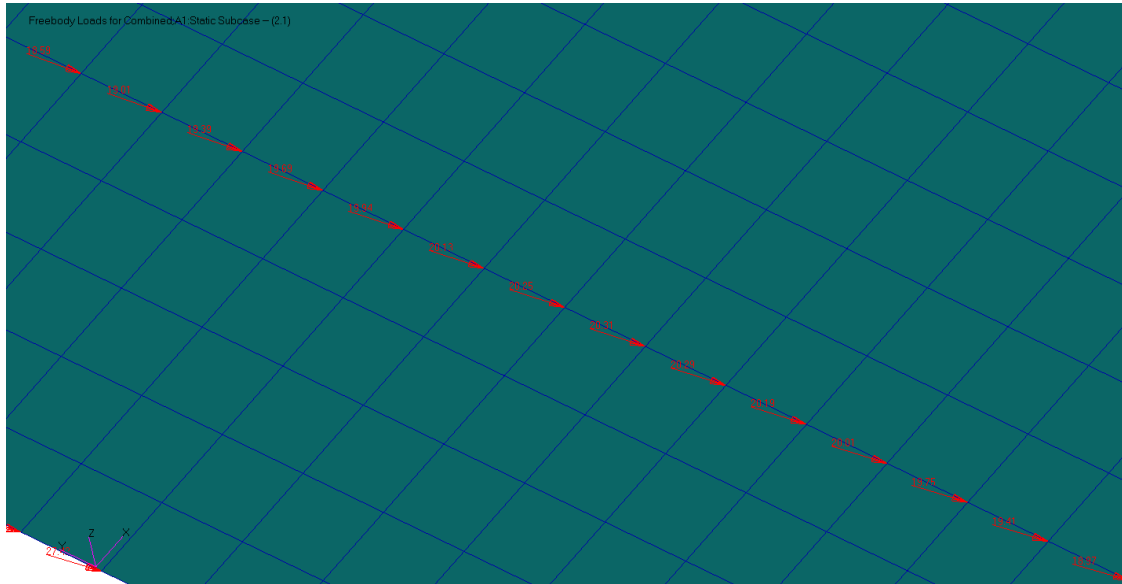


Figure 249: Spar to Upper Skin Critical Region

The shear allowable for the bolts and bearing allowable for the skin are shown below. The bearing allowable for the skin is the critical margin of safety for the fasteners.

$$MS = \frac{FF * \tau_{shear\ allowable}}{FS * \tau_{shear\ actual}} - 1 = \frac{2125\ psi * 0.9}{2.5 * (20.31 + 20.29\ psi) * 3} - 1 = 5.28$$

$$MS = \frac{\sigma_{BRU} * t * D}{FS * P_{actual}} - 1 = \frac{31600\ psi * 0.0101\ in * 8 * .1875\ in}{2.5 * (20.31 + 20.29\ psi) * 3} - 1 = .572$$

Figure 250 shows the region found to be critical between the spar and upper skin. 3/16th inch AN3 fasteners were used spaced at 1.25" along this region. Since the nodal spacing is .5" the fastener is forced to take the load of 3 nodes.

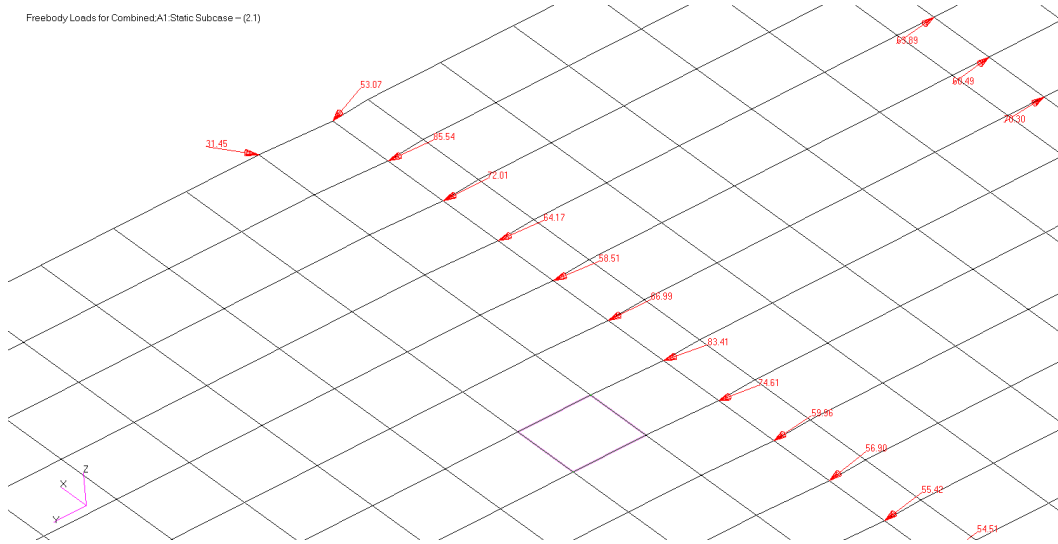


Figure 250: Ribs to Upper Skin Critical Region

The shear allowable for the bolts and bearing allowable for the skin are shown below. The bearing allowable for the skin is the critical margin of safety for the fasteners.

$$MS = \frac{FF * \tau_{shear\ allowable}}{FS * \tau_{shear\ actual}} - 1 = \frac{2125\ psi \bullet 0.9}{2.5 \bullet (86.99 + 83.41\ psi) \bullet 1.25} - 1 = 2.592$$

$$MS = \frac{\sigma_{BRU} \cdot t \cdot D}{FS \cdot P_{actual}} - 1 = \frac{31600\ psi \cdot 0.0101\ in \cdot 8 \cdot .1875\ in}{2.5 \cdot (86.99 + 83.41\ psi) \cdot 1.25} - 1 = .011$$

Figure 251 shows the nodal forces in the lower skin and Figure 252 shows the region found to be critical between the spar and leading edge fasteners. 3/16th inch AN3 fasteners were used spaced at 2.5" along this region. Since the nodal spacing is .5" the fastener is forced to take the load of 5 nodes.



The shear allowable for the bolts and bearing allowable for the skin are shown below. The bearing allowable for the skin is the critical margin of safety for the fasteners.

$$MS = \frac{FF * \tau_{shear\ allowable}}{FS * \tau_{shear\ actual}} - 1 = \frac{2125\ psi \cdot 0.9}{2.5 \bullet (36.94 + 36.92\ psi) \cdot 2.5} - 1 = 3.143$$

$$MS = \frac{\sigma_{BRU} \cdot t \cdot D}{FS \cdot P_{actual}} - 1 = \frac{31600\ psi \cdot 0.0101\ in \cdot 8 \cdot .1875\ in}{2.5 \cdot (36.94 + 36.92\ psi) \cdot 2.5} - 1 = .037$$

Figure 253 shows the region found to be critical between the spar and lower skin fasteners. 3/16th inch AN3 fasteners were used spaced at 3" along this region. Since the nodal spacing is .5" the fastener is forced to take the load of 6 nodes.

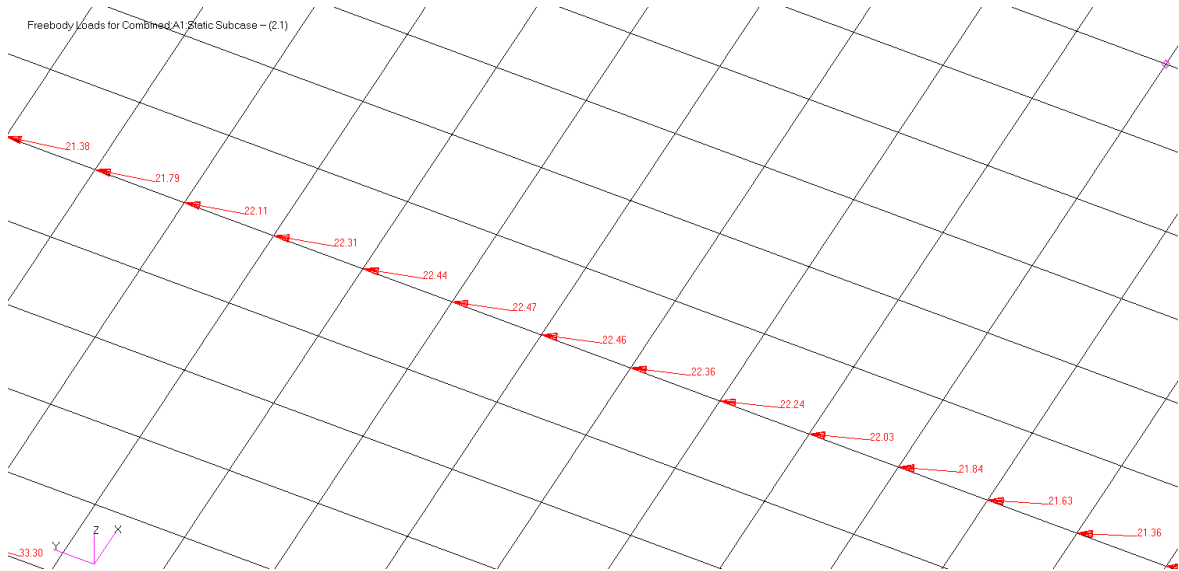


Figure 253: Lower Skin to Spar Critical Region

The shear allowable for the bolts and bearing allowable for the skin are shown below. The bearing allowable for the skin is the critical margin of safety for the fasteners.

$$MS = \frac{FF * \tau_{shear\ allowable}}{FS * \tau_{shear\ actual}} - 1 = \frac{2125\ psi \bullet 0.9}{2.25 \bullet (22.47 + 22.46\ psi) \bullet 3} - 1 = 4.672$$

$$MS = \frac{\sigma_{BRU} \cdot t \cdot D}{FS \cdot P_{actual}} - 1 = \frac{31600 \text{ psi} \cdot 0.0101 \text{ in} \cdot 8 \cdot .1875 \text{ in}}{2.25 \cdot (22.47 + 22.46 \text{ psi}) \cdot 3} - 1 = .420$$

Figure 253 shows the region found to be critical between the spar and lower skin fasteners.

3/16th inch AN3 fasteners were used spaced at 3" along this region. Since the nodal spacing is .5" the fastener is forced to take the load of 6 nodes.

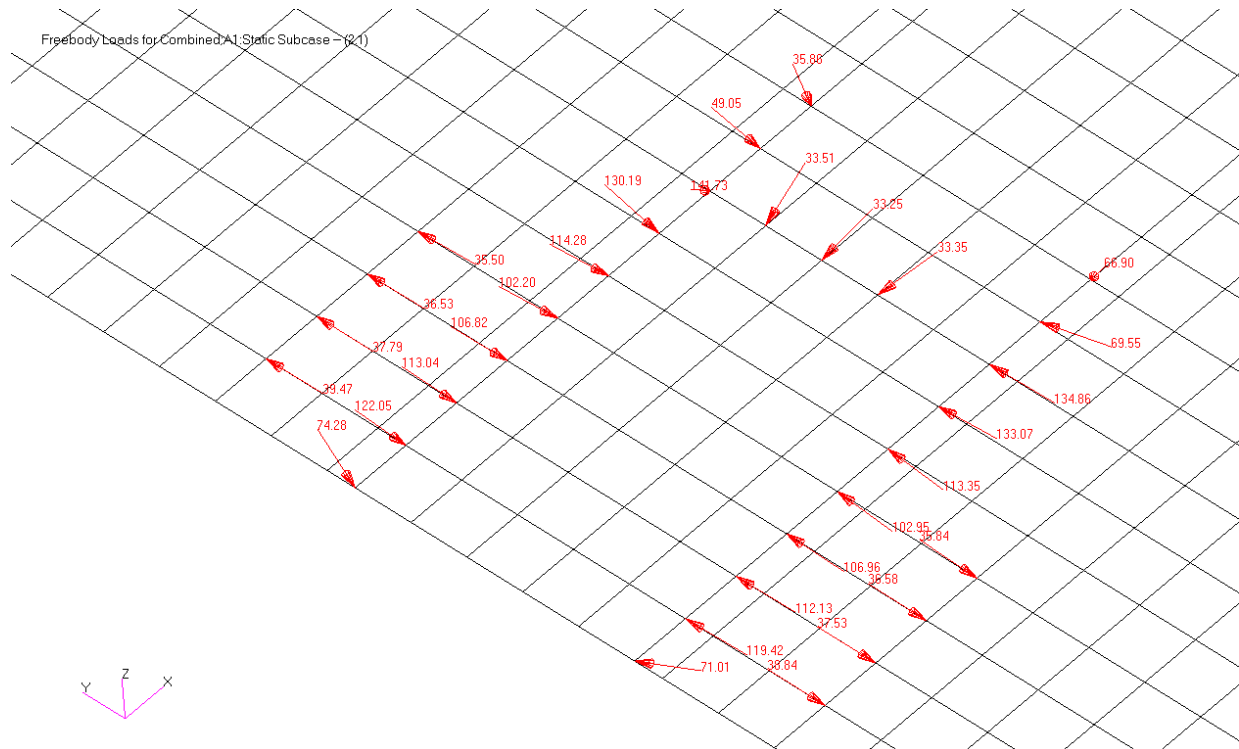


Figure 254: Lower Skin to Ribs Fasteners

The shear allowable for the bolts and bearing allowable for the skin are shown below. The bearing allowable for the skin is the critical margin of safety for the fasteners.

$$MS = \frac{FF \cdot \tau_{shear \text{ allowable}}}{FS \cdot \tau_{shear \text{ actual}}} - 1 = \frac{2125 \text{ psi} \cdot 0.9}{2.5 \cdot (122.05 + 113.04 \text{ psi}) \cdot 1.5} - 1 = 1.169$$

$$MS = \frac{\sigma_{BRU} \cdot t \cdot D}{FS \cdot P_{actual}} - 1 = \frac{31600 \text{ psi} \cdot 0.0101 \text{ in} \cdot 17 \cdot .1875 \text{ in}}{2.5 \cdot (122.05 + 113.04 \text{ psi}) \cdot 1.5} - 1 = .154$$

3.6.3 Rib Fasteners

Figure 255 shows the nodal forces in the ribs and Figure 256 shows the region found to be critical between the ribs and pylon substructure. 3/16th inch AN3 fasteners were used spaced at 1.25" along this region. Since the nodal spacing is .5" the fastener is forced to take the load of 3 nodes.

Freebody Loads for Combined.A1:Static Subcase - (2.1)

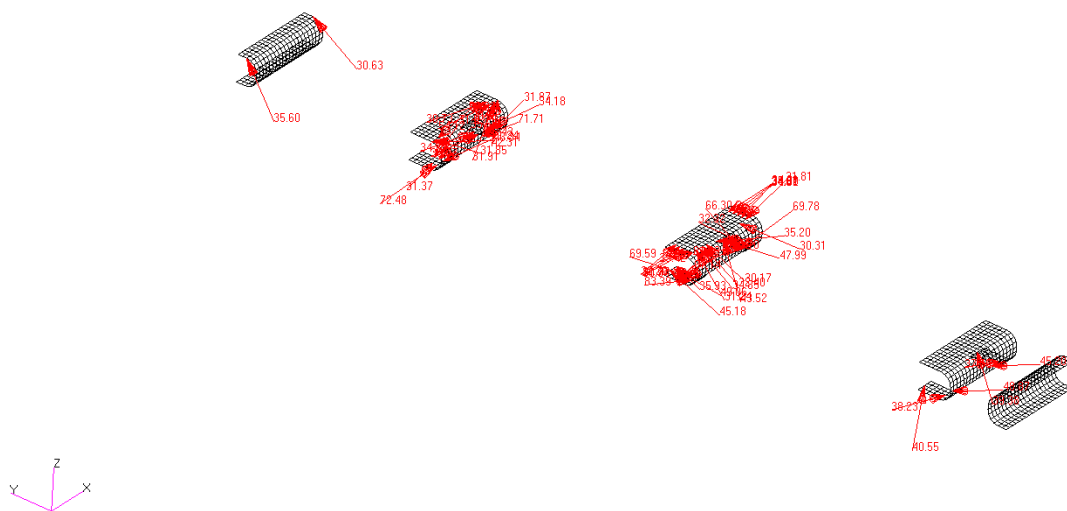


Figure 255: Rib Nodal Stress Distribution

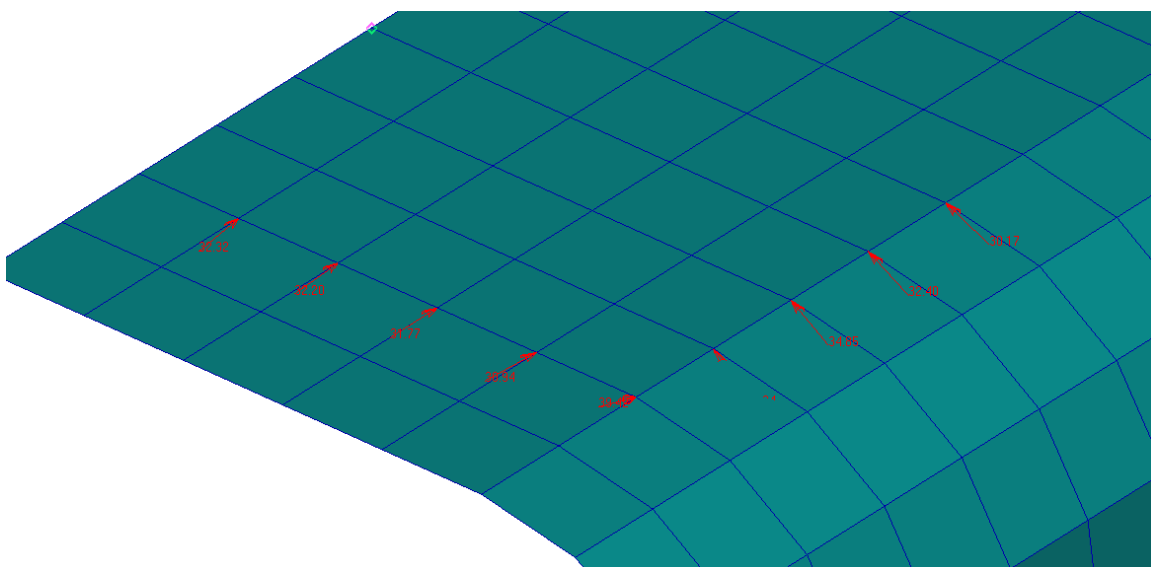


Figure 256: Rib to Pylon Fasteners

The shear allowable for the bolts and bearing allowable for the rib are shown below. The bearing allowable for the rib is the critical margin of safety for the fasteners.

$$MS = \frac{FF * \tau_{shear\ allowable}}{FS \bullet \tau_{shear\ actual}} - 1 = \frac{2125\ psi \cdot 0.9}{2.5 \cdot (32.32 + 32.2) \cdot 1.25\ psi} - 1 = 3.802$$

$$MS = \frac{\sigma_{BRU} \cdot t \cdot D}{FS \cdot P_{actual}} - 1 = \frac{31600\ psi \cdot 0.0101\ in \cdot 15 \cdot .1875\ in}{2.5 \cdot (22.47 + 22.46\ psi) \cdot 1.25} - 1 = 1.982$$

3.6.4 Pylon Fasteners

Figure 257 shows the nodal forces in the ribs and Figure 258 shows the region found to be critical between the pylon substructure and pylon skins. 3/16th inch AN3 fasteners were used spaced at 1.25" along this region. Since the nodal spacing is .5" the fastener is forced to take the load of 3 nodes.

Freebody Loads for Combined A1 Static Subcase - (2.1)

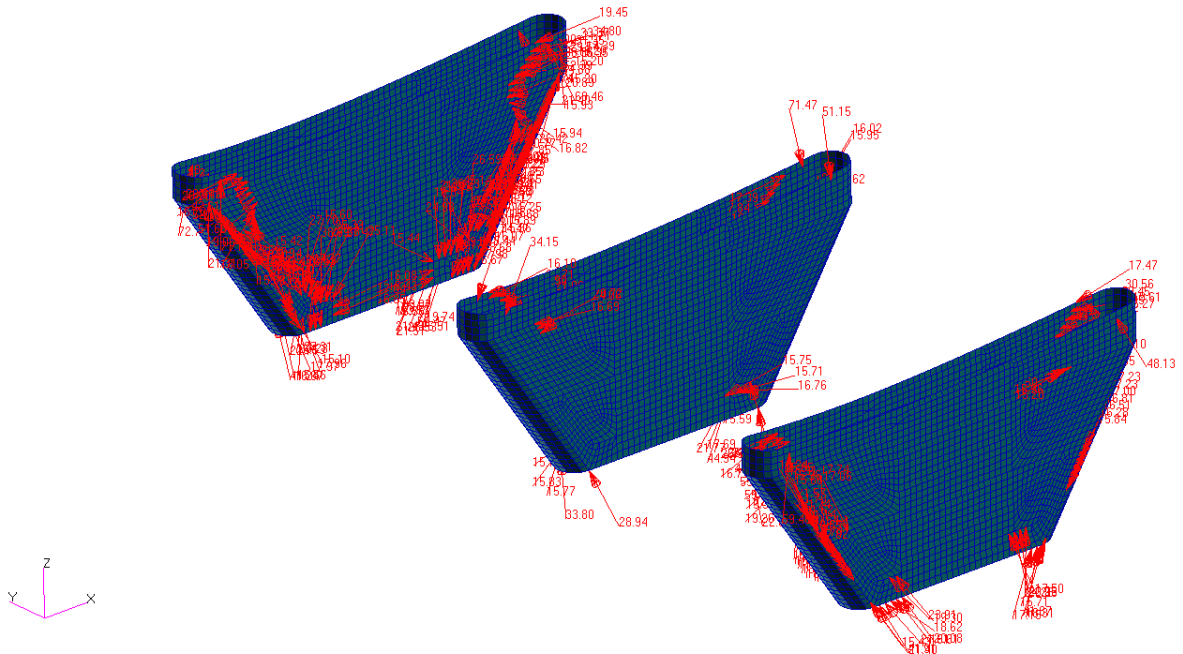


Figure 257:Pylon Skin Nodal Forces

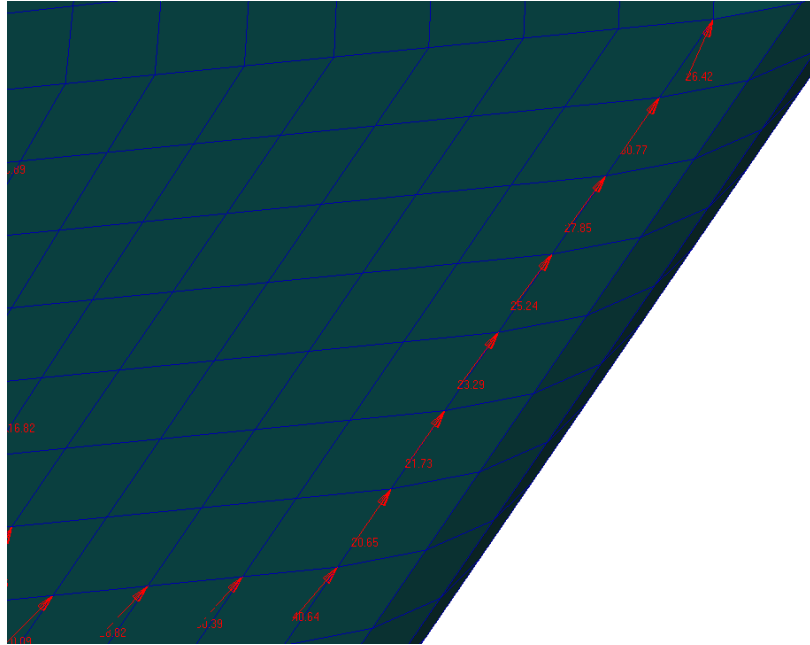


Figure 258: Pylon Fasteners Critical Region

The shear allowable for the bolts and bearing allowable for the rib are shown below. The bearing allowable for the rib is the critical margin of safety for the fasteners.

$$MS = \frac{FF * \tau_{shear\ allowable}}{FS * \tau_{shear\ actual}} - 1 = \frac{2125\ psi \cdot 0.9}{2.5 \cdot (27.85 + 25.24) \cdot 3\ psi} - 1 = 3.802$$

$$MS = \frac{\sigma_{BRU} \cdot t \cdot D}{FS \cdot P_{actual}} - 1 = \frac{20333\ psi \cdot 0.032\ in \cdot .1875\ in}{2.5 \cdot (22.47 + 22.46\ psi) \cdot 3} - 1 = .306$$

3.7 Modal Analysis

The fairing structure was also checked against possible sources of vibration. The only known source of vibration for the representative UAV is the engine. This produces two possible vibration frequencies which are the engine rpm and blade pass frequency. The engine selected for the representative UAV is a Honeywell TPE-331 turboprop engine with a three bladed propeller attached. Reference 24 indicated that the prop shaft rpm for that engine is 2000 rpm. This is equivalent to a frequency of 33.3 hz. The calculation for the blade pass frequency is shown below. To be safe both frequencies of interest were avoided by at least 5 hertz.

$$\text{Blade Pass Frequency} = \frac{(\text{engine rpm})(\text{number of blades})}{60} = \frac{(2000 \text{ rpm})(3 \text{ blades})}{60} = 100 \text{ hz}$$

Figure 259 through Figure 262 show the first four modes closest to the blade pass frequency to demonstrate the frequency is avoided.

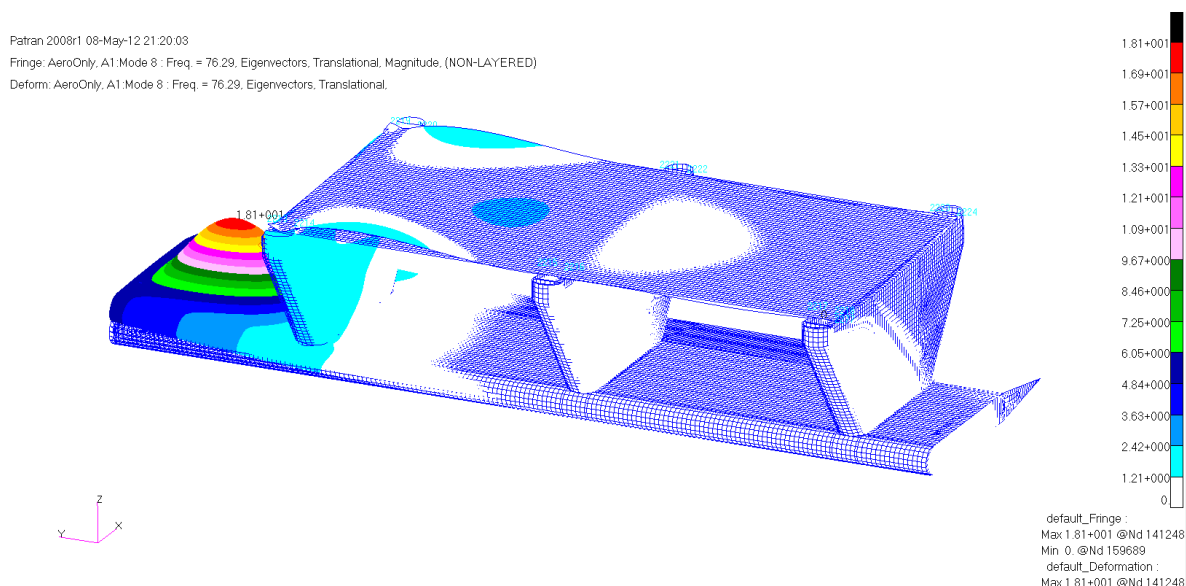


Figure 259: First Fairing Mode (76.29 Hz)

Patran 2008r1 08-May-12 21:20:42
 Fringe: AeroOnly, A1 Mode 9 : Freq. = 79.556, Eigenvectors, Translational, Magnitude, (NON-LAYERED)
 Deform: AeroOnly, A1 Mode 9 : Freq. = 79.556, Eigenvectors, Translational.

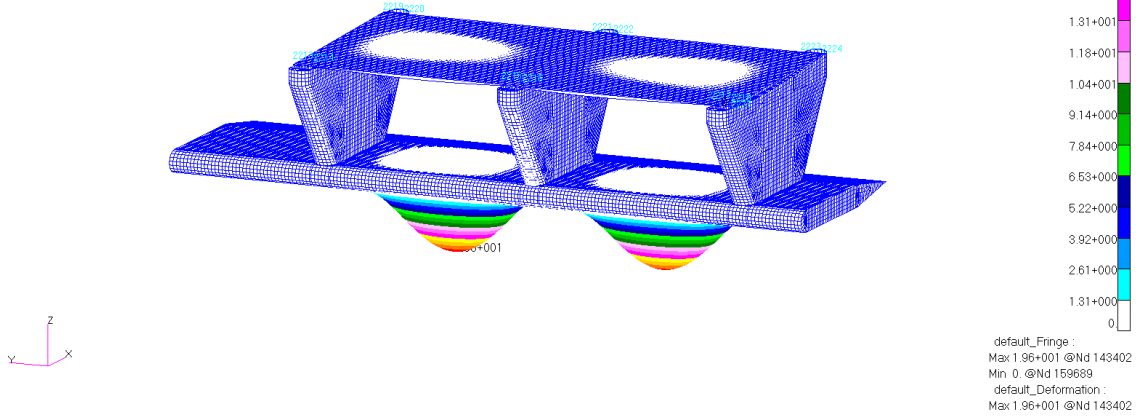


Figure 260: Second Fairing Mode (79.556 Hz)

Patran 2008r1 08-May-12 21:21:33
 Fringe: AeroOnly, A1 Mode 10 : Freq. = 79.944, Eigenvectors, Translational, Magnitude, (NON-LAYERED)
 Deform: AeroOnly, A1 Mode 10 : Freq. = 79.944, Eigenvectors, Translational.

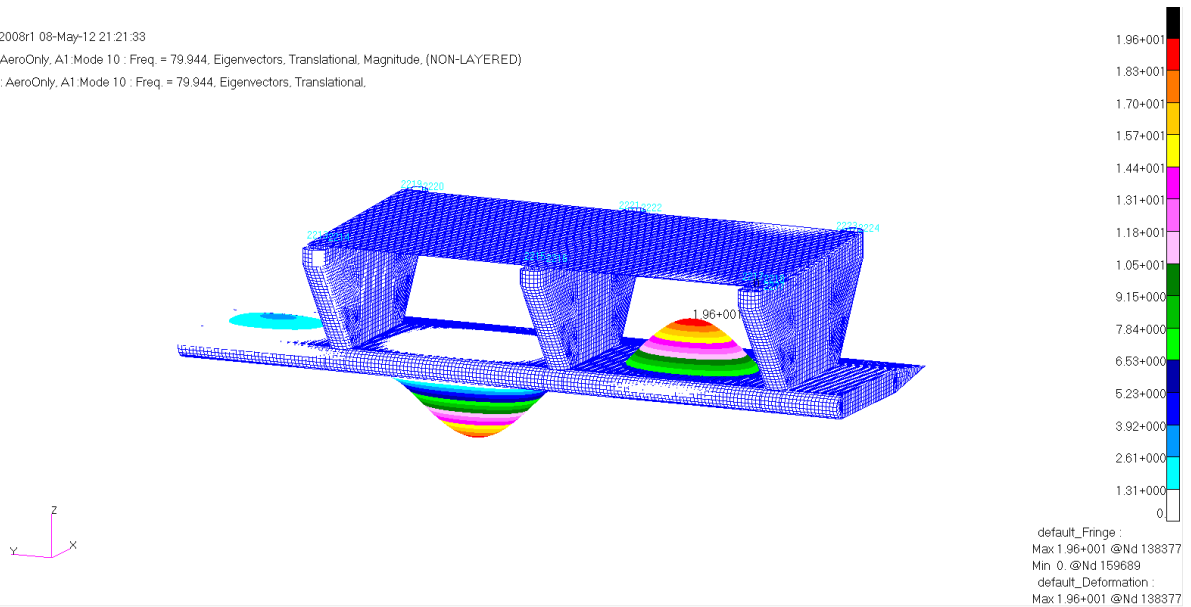


Figure 261: Third Fairing Mode (79.944 Hz)

Patran 2008r1 08-May-12 21:22:19

Fringe: AeroOnly, A1 Mode 11 : Freq. = 111.24, Eigenvectors, Translational, Magnitude, (NON-LAYERED)

Deform: AeroOnly, A1 Mode 11 : Freq. = 111.24, Eigenvectors, Translational,

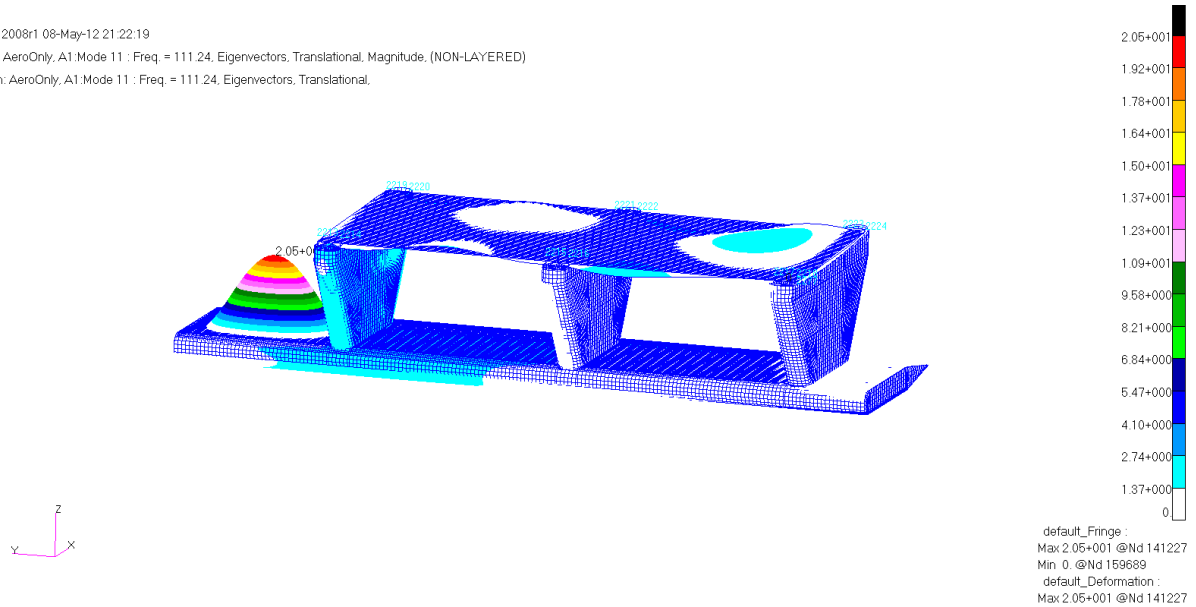


Figure 262: Fourth Fairing Mode (111.24 Hz)

The modeled structure meets the 5 hertz requirement since the closest mode to 100 hertz is at 111.24 hertz and the closest mode to 33.3 hertz is at 76.29 hertz. However this model does not account for the energy that the fasteners will absorb so it likely over predicts the frequencies at which vibration occurs. This means that the fourth mode on a manufactured array could lie very close to 100 hertz. If in production this is found to be a problem adding core to the outboard region would be a low weight effective solution.

4 Performance Comparison

The most important factor to the end user of the representative UAV is the performance capabilities of the platform. This section addresses the performance impacts of the radar array on the representative UAV.

To develop a baseline range for the representative UAV the Advanced Aircraft Analysis (AAA) software package was used. To develop a performance model the aircraft specifications in Table 4 for the representative UAV were added to the AAA model. One of the most important characteristics that the model was developed for was the aircraft drag equations. Table 43 shows the results of this analysis.

$$C_D = C_{D_0\text{Clean}} + B_{DP\text{Clean}} C_L^2$$

Table 43: Aircraft Clean Drag

$C_{D_0\text{Clean}}$	0.0316
$B_{DP\text{Clean}}$	0.0233

With drag information and engine information it is possible to generate range performance for the representative UAV using the equation below.

$$R_{C_{N=const}} = 326 \cdot \left(\frac{\eta_p}{c_p} \right) \cdot \left(\frac{C_L}{C_D} \right) \cdot \ln \left(\frac{W_{Cr}}{W_{Cr} - W_{F_{Cr}}} \right)$$

Using this method AAA predicted a range of 4616 nm for the representative UAV. This number matches the currently existing MALE UAV's ranges nearly exactly. Next an accurate drag model of the arrays was needed.

Ideally a CFD or wind tunnel study or both would be performed to determine the drag characteristics of the array. Fortunately a CFD study was conducted on a nearly identical array in Reference 22. This study was based upon an array which was mounted aboard a P-3 aircraft and was conducted at a dynamic pressure 60% higher than the pressure for the representative UAV. Fortunately the study contains all of the lift and drag components as well as the geometry of the structure so it is easy to solve for the drag coefficient of the structure using the equation below.

$$Drag = F_D = \frac{1}{2} \rho V^2 C_D A$$

The fairing is symmetric and flown at close to zero angle of attack. Thus very little induced drag is created and parasite drag dominates. The drag, F_D , is given section by section in the report and ρv^2 is defined by the flight condition of the aircraft. The A is given by the geometry. Simply rearranging the terms gives the equation below. The results are shown in Table 44.

$$C_D = \frac{2F_D}{\rho v^2 A}$$

Table 44: Drag Coefficients of Fairing Components

Structure	C_D
Pylon with Sharp Trailing Edge	0.108332
Pylon with Circular Trailing Edge	0.433327
Fairing with Sharp Trailing Edge	0.047693
Fairing with Circular Trailing Edge	0.190772

The components in Table 44 all have different reference areas so they are not directly comparable. To study the effects these components have they had to be normalized to the

aircraft reference area and then summed. New drag coefficients were summed for a variety of configuration using the method below. The results are shown in Table 45.

$$C_{D_{Total}} = C_{D_{Clean\ Aircraft}} + \frac{A_{Pylon}}{A_{Aircraft}} C_{D_{Pylon}} + \frac{A_{Fairing}}{A_{Aircraft}} C_{D_{fairing}}$$

Table 45: Drag Coefficient by Configuration

Configuration	C_{D_0}
Clean Aircraft	0.0316
All Sharp Trailing Edges	0.0357
Circular Pylon Sharp Fairing	0.0390
Circular Fairing Sharp Pylon	0.0444
All Circular Trailing Edges	0.0478

The aircraft range was then recalculated with the additional range and the added weight of the fairing. The results of those range calculations are shown in Table 46.

Table 46: Range Comparison

Configuration	Range (nm)	Range Preserved
Clean Aircraft	4616.4	~
All Sharp Trailing Edges	4136.521	89.6%
Dirty Pylon Sharp Fairing	3838.989	83.2%
Dirty Fairing Clean Pylon	3443.208	74.6%
Dirty Aircraft	3234.269	70.1%

Table 46 shows the importance of the trailing edges. Using more streamlined trailing edges results in an array that only decreases the aircraft's range by 480 nautical miles and around 90% of the aircraft range. The circular trailing edges result in almost triple the loss in range at 1380 nautical miles and only 70% of the aircraft range is preserved. A visual representation of the range is shown in Figure 263 as an out and back mission.

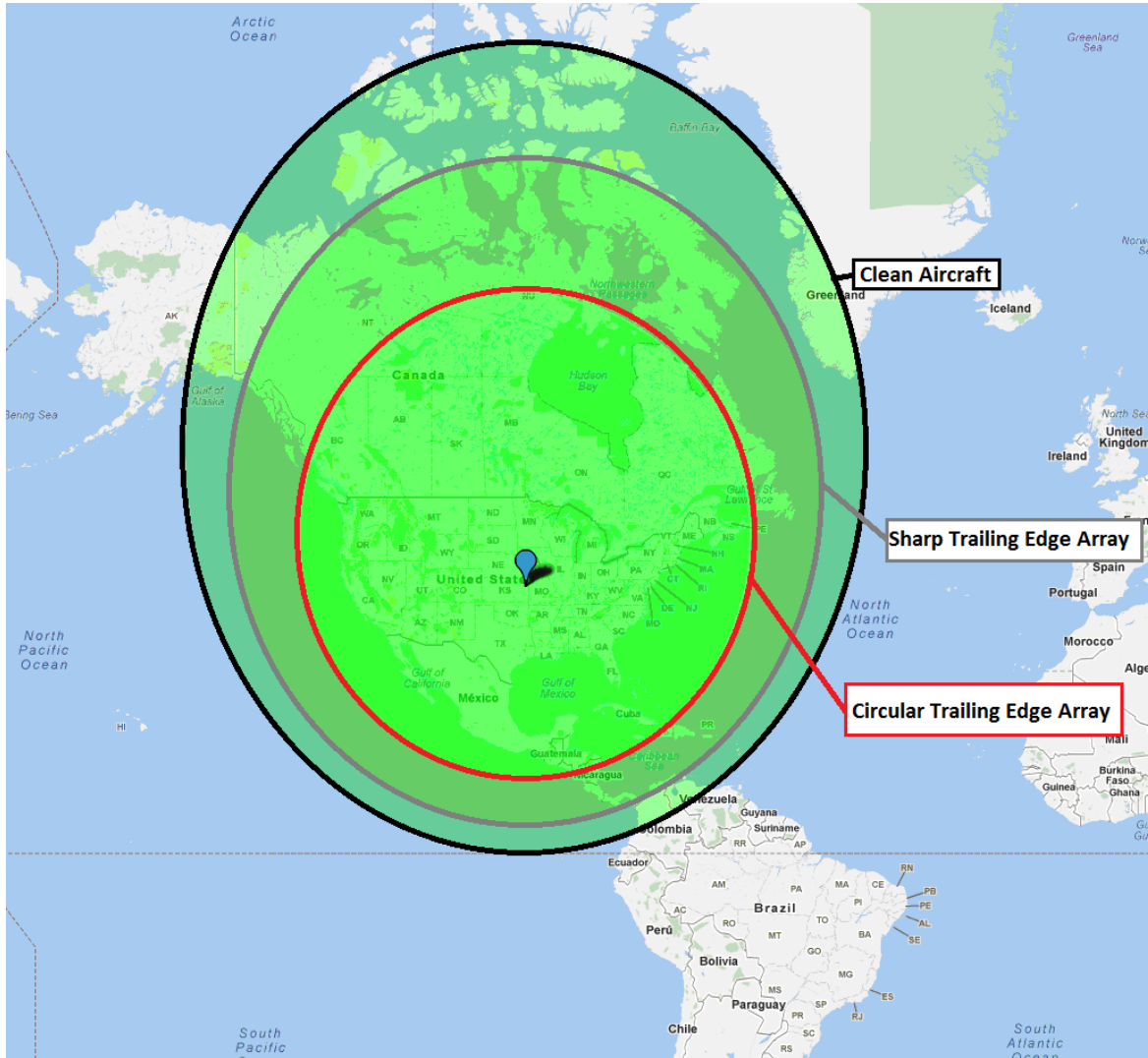


Figure 263: Aircraft Range (Out and back)

Next the takeoff performance of the aircraft was examined. Both the takeoff distance and required field length were examined. These were calculated using the equations from reference 25 in AAA. The first equations shown below were used to calculate the takeoff flight path angle and the average thrust.

$$\bar{T} = 5.75 P_{TO} \left(\frac{\sigma D_p^2}{P_{TO}} \right)^{\frac{1}{3}} \quad \gamma_{LOF} = 0.9 \left(\frac{\bar{T}}{W} \right)_{TO} - \frac{0.3}{\sqrt{AR}}$$

Next the takeoff distance and takeoff ground run were calculated. This was done using equation 5.6 and 5.14 from Reference 25. The equations are shown below. All of the variables used in the calculations are shown in Table 47.

$$S_{TO} = f_{TO} h_{obs} \left\{ \frac{1}{\gamma_{LOF}} + \frac{\left(\frac{V_3}{V_{S_{TO}}} \right)^2 \left(\frac{W}{S} \right)_{TO} \left\{ \left[\left(\frac{\bar{T}}{W} \right)_{TO} - \mu_g + \frac{.72 C_{D_{TO}}}{C_{L_{max TO}}} \right]^{-1} + 1.414 \right\}}{h_{obs} \rho g C_{L_{max TO}} (1 + 1.414 \gamma_{LOF})} \right\}$$

$$S_{TOG} = \frac{\frac{V_{LOF}}{2g}}{\left(\frac{\bar{T}}{W} \right)_{TO} - \mu_g + \frac{.72 C_{D_{TO}}}{C_{L_{max TO}}}}$$

Table 47: Takeoff Distance Variables

Variable	Value	Source	Variable	Value	Source
f_{TO}	1 (~)	MIL-C-005011B	μ_g	.02 (~)	AAA Estimate
h_{obs}	50 ft	MIL-C-005011B	P_{TO}	900 hp	Aircraft Specification
D_P	9.5 ft	Aircraft Specification	$C_{L_{max TO}}$.2 (~)	AAA Estimate
$\frac{V_3}{V_{S_{TO}}}$	1.15 (~)	MIL-C-005011B	ρ	0.00238 slugs/ft ³	Standard Atmosphere
$\frac{W}{S}$	38.7 lb/ft ²	Aircraft Specification	g	32.2 ft/s ²	Standard Gravity
AR	16.04 (~)	Aircraft Specification	σ	1 (~)	Standard Atmosphere

To find the differences between the configurations the $C_{D_{to}}$ variable was adjusted for the different fairing configurations. AAA was used to do these calculations. The AAA inputs and results are shown in Figure 288 through Figure 292 in Appendix B. The numerical results of this comparison are shown in Table 48.

Table 48: Takeoff Distance Results

Configuration	Takeoff Ground Run (ft)	Takeoff Field Length (ft)	Takeoff Field Length Performance Preserved
Clean Aircraft	1911	2219	-
All Sharp Trailing Edges	1926	2230	99.50%
Circular Pylon Sharp Fairing	1938	2239	99.10%
Circular Fairing Sharp Pylon	1957	2254	98.40%
All Circular Trailing Edges	1970	2264	98.00%

The results of this seem to indicate that the addition of the array does not greatly affect the takeoff performance of the aircraft. These calculations were performed under the assumption that the array does not interfere with the flaps of the aircraft. Since the pylon attachment points are located where it is possible to mount munitions to the aircraft this seems reasonable but this should be verified on an actual aircraft. A CFD analysis is also recommended on a real installation to ensure that the array does not aerodynamically interfere with the operation of the flaps.

Next the climb performance of the aircraft was examined. Equation 5.21 from Reference 25 was used to determine the climb performance of the aircraft and is shown below.

$$RC = 33,000 \left[\frac{\eta_p}{\left(\frac{W}{P}\right)} - \frac{\left(\frac{W}{S}\right)^{\frac{1}{2}}}{19 \left(\frac{C_L^{\frac{3}{2}}}{C_D}\right) \sigma^{\frac{1}{2}}} \right]$$

The difference in performance based on the configuration was analyzed similar to the takeoff performance. The C_D value for the different configurations was adjusted due to the different C_{D_0} values of the configurations. Representative $C_L^{\frac{3}{2}}/C_D$ information could not be found so a value was assumed. With this assumption in mind the data is only comparable with itself. The results of these calculations are shown in Table 49.

Table 49: Climb Performance Comparison

Configuration	Clean Performance Preserved
Sharp Trailing Edges	99.3%
Sharp Fairing Circular Pylons	93.8%
Sharp Pylons Circular Fairing	92.9%
All Circular	92.3%

The results seem to show a discrepancy with the takeoff distance and climb performance being affected very little by the changes in configuration of the design but the effect on the range of the aircraft is much more prominent. This is largely due to the design characteristics of the MALE UAV platform. The aircraft in this category have high thrust to weight ratios and have an abundance of available power. This means that the engine can likely overcome the addition of drag on takeoff or climb without too much difficulty. However if this drag is carried over the entire mission, and remembering we have selected high endurance aircraft, the range of the platform can be greatly reduced.

In addition to the range, takeoff, and climb performance other aircraft performance factors will have to be addressed if a wing mounted array concept is to be considered for an actual mission. For example the roll performance of the aircraft with the array will need to be examined. Since the array weighs less than the munitions for which the hardpoints were designed it is unlikely that the inertias of the array will be a problem. Also since the array is carried inboard away from the ailerons it is unlikely that they will interfere with their

performance. Nevertheless these performance issues should be investigated before a real life application is pursued.

5 Conclusions and Recommendations

5.1 Conclusions

An MCoRDS array for a representative MALE UAV has been presented. To develop loads for the structure a range of wing structures were investigated to develop a range of representative wing curvatures. The wing curvatures were found to be consistent enough across the possible substructure arrangements that a structural sizing was pursued. The structural arrangement with the most substructure was found to have the greatest curvature so it was used as the model wing for later fairing structural analysis. Aerodynamic loading was found from utilizing previous CFD studies of a similar cross section at a different flight speed. These flight conditions were adjusted using the dynamic pressures in the free stream of the flight conditions. The design of the array was based on this previous design due to the success of the previous array and also the availability of these aerodynamic studies.

Using this information an array that housed three MCoRDs antennas was designed. It is attached to the wing at three pylon attachment points. The design utilizes glass composites in the two spars, ribs, and the skins of the fairing due to the requirement of avoiding electrically conductive structure in proximity to the radar antennas. The sizing analysis showed that an under wing radar array for this class of aircraft is feasible based upon likely weight limitations or wing harpoints intended for munitions.

Next the aircraft performance of the MALE UAV was examined to determine if the mission was feasible. To do this a performance model for the aircraft was created and the aerodynamic impact of the fairing components was examined from a predominately drag-based assessment. From this analysis it was determined that an array can be fielded to the

representative UAV with around 90% of the aircraft range preserved, and with acceptable take-off and climb performance. A platform with these capabilities would offer significant potential for Operation Ice Bridge and other future missions.

5.2 Recommendations

Several things must be investigated further before an array is pursued for integration into an actual UAV. First, a new CFD analysis for the array must be conducted, and must use actual aircraft and fairing geometry. The current analysis is only sufficient for a preliminary sizing. Since the actual flight regime of the aircraft is likely considerably different than the one on which the original CFD analysis was conducted, then the resulting pressure distributions could differ from those assumed herein. Also while the shapes of the structures are similar there are some key differences. The length of the fairing is considerably shorter since the proposed array only houses three antennas. The original arrays housed four antennas. This was shortened since the hard point spacing on representative unmanned aircraft appeared tighter than the hard points of the much larger aircraft in Reference 22. New CFD analysis should also be pursued to investigate how the pylons shed vortices and how those vortices interact with the aircraft. The representative aircraft shown has a pusher prop configuration. If the fairing sheds significant vortices these could interact with the propeller and do significant damage if not accounted for. Analyses should be performed to determine the strength and possible effects of these vortices.

Additionally, the communication method for the chosen aircraft must be examined. The mission that the aircraft is designed around requires operation in extreme latitudes near the poles. Some unmanned aircraft use satellite communication networks which do not have proper

coverage near the poles. This difficulty could eliminate several aircraft from consideration if a solution is not planned for.

Another consideration is the icing conditions for the scientific mission. Several UAV's are originally conceived for desert missions and generally avoid cold weather conditions. Cold weather conditions present additional challenges especially in the form of icing. The ice will not only accumulate on the wings but the fairing itself provides an ideal location for ice to accumulate. If the aircraft chosen is one with a pusher prop this ice could damage the prop as it falls off the aircraft and possibly into the propeller. Runway icing and field landing conditions should also be examined in greater detail.

It is also recommended to investigate additional load cases. The dive load case which was used for the majority of the sizing in this paper was based upon the predominate load case for the similar array from Reference 22 but in that analysis several other load cases were investigated to ensure that the structure was safe. Since the design is only based upon a representative aircraft it is impossible to know the exact flight conditions a future aircraft would encounter but if a specific unmanned aircraft is selected it will be important to examine the entire range of flight conditions for that aircraft. Those flight conditions will also give information on the cyclic loading of the platform which will also allow a fatigue study to be performed.

6 **References**

1. "Ocean" NOAA. April 21st 2012 <www.noaa.gov/ocean.html>
2. Beckley et al, 2007 B.D. Beckley, F.G. Lemoine, S.B. Luthcke, R.D. Ray and N.P. Zelensky, A reassessment of global and regional sea level trends from TOPEX and Jason-1 altimetry based on revised reference frame and orbits, *Geophysical Research Letters* 34 (2007), p. L14608.
3. Miller, L. and B. C. Douglas, Mass and Volume Contributions to 20th Century Global Sea Level Rise, *Nature*, 248, 407-409, 2004.
4. Rignot E., J.E. Box, E. Burgess, et al, (2008), Mass balance of the Greenland ice sheet from 1958 to 2007. *Geophysical Research Letters*, v.35, issue 20, No. L20502
5. Thomas, R., E. Frederick, W. Krabill, S. Manizade and C. Martin. (2006). Progressive increase in ice loss from Greenland. *Geophys. Res. Lett.*, 33(10), L10503. (10.1029/2006GL026075).
6. Zwally, H.J., W. Abdalati, T. Herring, K. Larson, J. Saba and Konrad Steffen (2002), Surface Melt- Induced Acceleration of Greenland Ice-Sheet Flow. *Science*, 297 (5579), 218-222.
7. Joughin I., Das S.B., King M.A., Smith B.E., Howat I.M. Moon T. (2008). "Seasonal speedup along the western flank of the Greenland Ice Sheet". *Science* 320: 781–783. doi:10.1126/science.1153288
8. Nicholls, R.J., P. P. Wong, V. R. Burkett, J. O. Codignotto, J. E. Hay, R. F. McLean, S. Ragoonaden and D. Woodroffe, 2007: Coastal systems and low-lying areas. *Climate Change 2007: Impacts, Adaptation and Vulnerability. Contribution of Working Group II to the Fourth Assessment Report of the Intergovernmental Panel on Climate Change*, M. L. Parry, O. F. Canziani, J. P. Palutikof, P. J. van der Linden and C. E. Hanson, Eds., Cambridge University Press, Cambridge, UK, 315-356.
9. Lemke, P., Ren, J., Alley, R., Allison, I., Carrasco, J., Flato, G., Fujii, Y., Kaser, G., Mote, P., Thomas, R. and Zhang, T. 2007: Chapter 4: Observations: changes in snow, ice and frozen ground. In Solomon, S., Qin, D., Manning, M., Chen, Z., Marquis, M.C., Averyt, K., Tignor,
10. Englehardt, Hermann and Barclay Kamb, "Basal hydraulic system of a West Antarctica ice stream: constraints from borehole observations," *Journal of Glaciology*, vol 43, no 144, pp 207-229, 1998.
11. Paden, J., "Synthetic Aperture Radar for Imaging the Basal Conditions of the Polar Ice Sheets," June 2003.

12. Crocker, R., Maslanik, J., Adler, J., Palo, S., Herzfeld, U., and Emery, W., "A Sensor Package for Ice Surface Observations Using Small Unmanned Aircraft Systems", IEEE Transactions on Geoscience and Remote Sensing, vol 50, no 4, pp 1033-1047, April 2012
13. "Sensors Development // RADAR" May 28th 2012 <www.cresis.ku.edu/research/sensors-development/radar>
14. J. Li, J. Paden, C. Leuschen, F. Rodriguez-Morales, R. Hale, E. Arnold, R. Crowe, D. Gomez-Garcia and P. Gogineni. "High-Altitude Radar Measurements of Ice Thickness over the Antarctic and Greenland Ice Sheets as a part of Operation Ice Bridge." IEEE Transactions on Geoscience and Remote Sensing. Accepted with minor revision.2012
15. Byers, K., A.R. Harish, S.A. Seguin, C.J. Leuschen, F. Rodriguez-Morales, J. Paden, E.J. Arnold and R.D. Hale. "A Modified Wideband Dipole Antenna for an Airborne VHF Ice-Penetrating Radar." IEEE Transactions on Instrumentation and Measurement. Accepted with revision. In press. (2012).
16. Allen, C, L. Shi, R. Hale, C. Leuschen, J. Paden, B. Panzer, E. Arnold, W. Blake, F. Rodriguez-Morales, J. Ledford, and S. Seguin. "Antarctic Ice Depth sounding Radar Instrumentation for the NASA DC-8." AES Magazine. Accepted. In Press. (2012)
17. F. Rodriguez-Morales, P. Gogineni, C. Leuschen, J. Paden, J. Li, C. Lewis, B. Panzer, D. Gomez-Garcia, A. Patel, K. Byers, R. Crowe, K. Player, R. Hale, E. Arnold, L. Smith, C. Gifford, D. Braaten, and C. Panton. "Advanced Multi-Frequency Radar Instrumentation for Polar Research." Submitted to IEEE Transactions on Geoscience and Remote Sensing. 2012.
18. "Unmanned Aircraft Systems Roadmap", Office of the Secretary of Defense. August 4th 2005.
19. "GA-ASI MQ-1B and RQ-1A Predator" 15 March 2011 Jane's Unmanned Aerial Vehicles and Targets. IHS Jane's Defense & Security & Analysis. KU Libraries, Lawrence, KS. April 19th 2012 <www.janes.com>
20. "GA-ASI MQ-9 Reaper, Predator B and Mariner" 28 October 2010 Jane's Unmanned Aerial Vehicles and Targets. IHS Jane's Defense & Security & Analysis. KU Libraries, Lawrence, KS. April 21st 2012 <www.janes.com>
21. "IAI Heron TP Eitan" 21 Jun 2011 Jane's Unmanned Aerial Vehicles and Targets. IHS Jane's Defense & Security & Analysis. KU Libraries, Lawrence, KS. April 12th 2012 <www.janes.com>

22. Hale, R., Arnold, E., Wanbo, L., Po, K., Roberts, N., and Thakur, A., "Aerodynamic and Structural Analysis of the P-3 Antenna Assembly", April 29th 2010.
23. Curtis, Howard, "Fundamentals of Aircraft Structural Analysis," McGraw-Hill, 1997.
24. "Garrett TPE331 Turboprop Pilots Brief & Operational Tips." Allied Signal Aerospace Nov. 1993
25. Roskam, J., "Airplane Design: Part VII Determination of Stability, Control and Performance Characteristics: FAR and Military Requirements," DAR Corporation, 2006.

Appendix A: Aerodynamic Regions

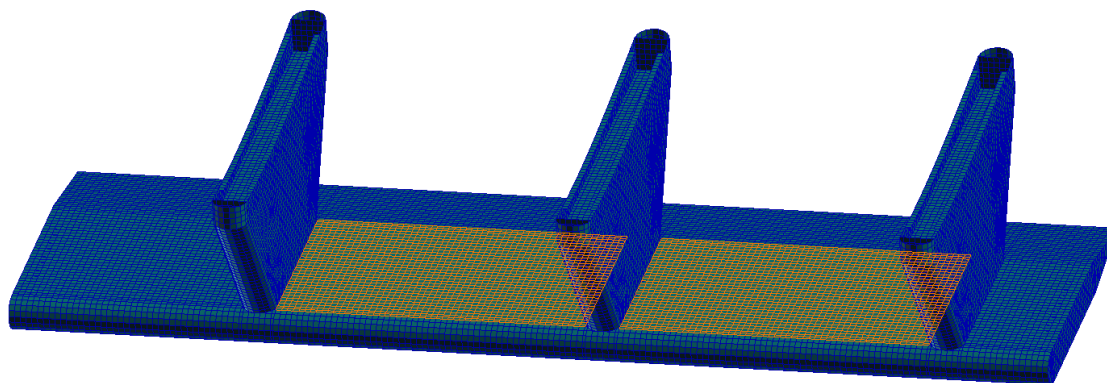


Figure 264: Center Fairing Region (-0.63817 lb/in²)

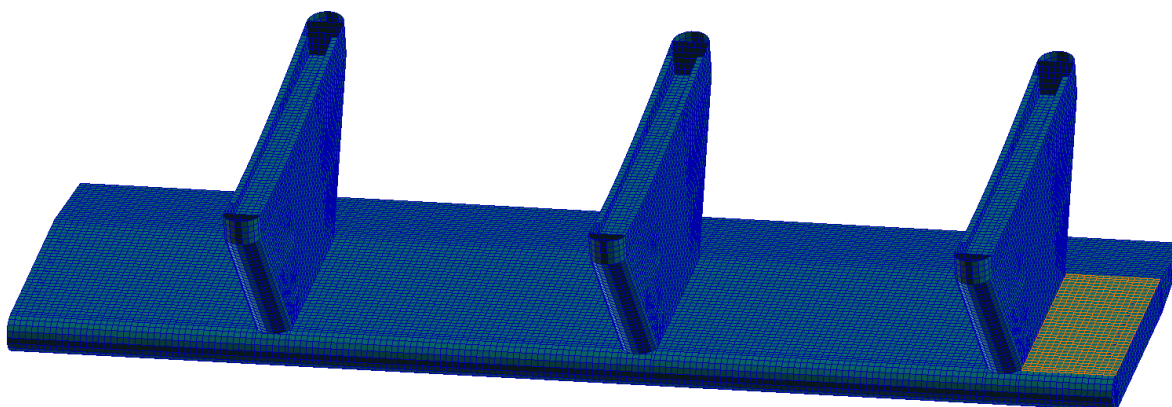


Figure 265: Inboard Fairing Region (-1.36335 lb/in²)

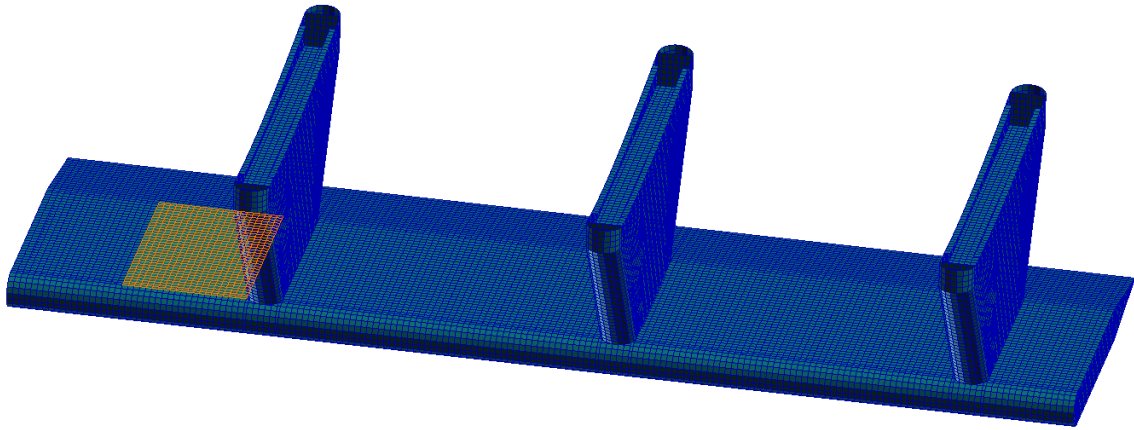


Figure 266: Outboard Inboard Fairing Region (-1.2473246 lb/in²)

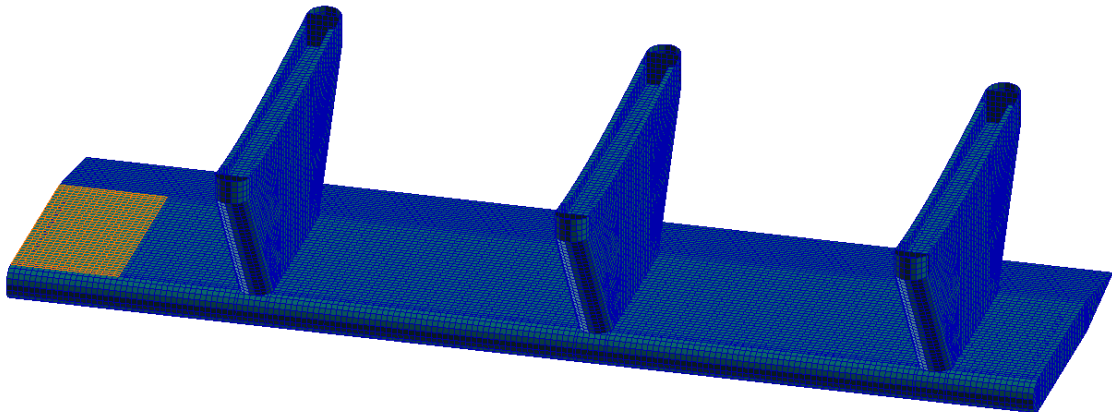


Figure 267: Outboard Outboard Fairing Region (-0.89923 lb/in²)

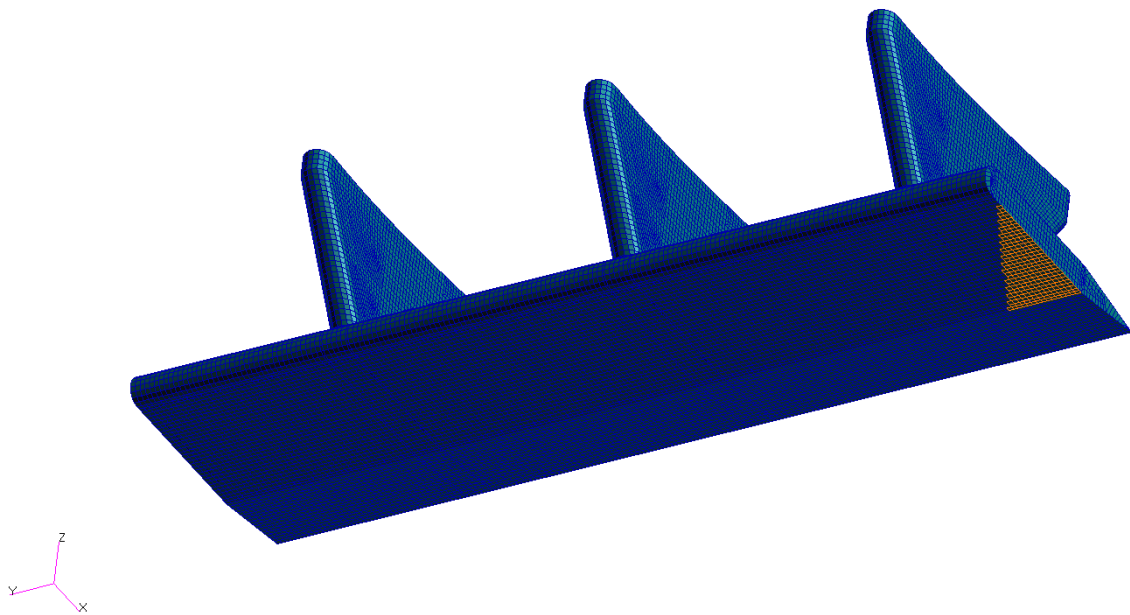


Figure 268: Inboard Lower Triangle Fairing Region (-1.59542 lb/in²)

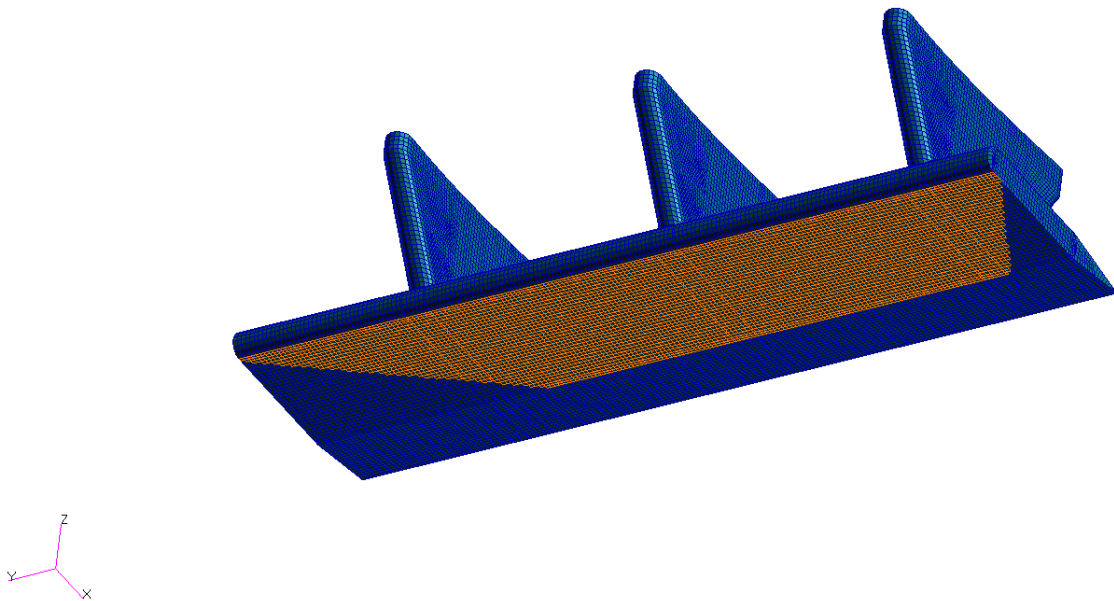


Figure 269: Lower Trapezoid Fairing Region (-2.0885434 lb/in²)

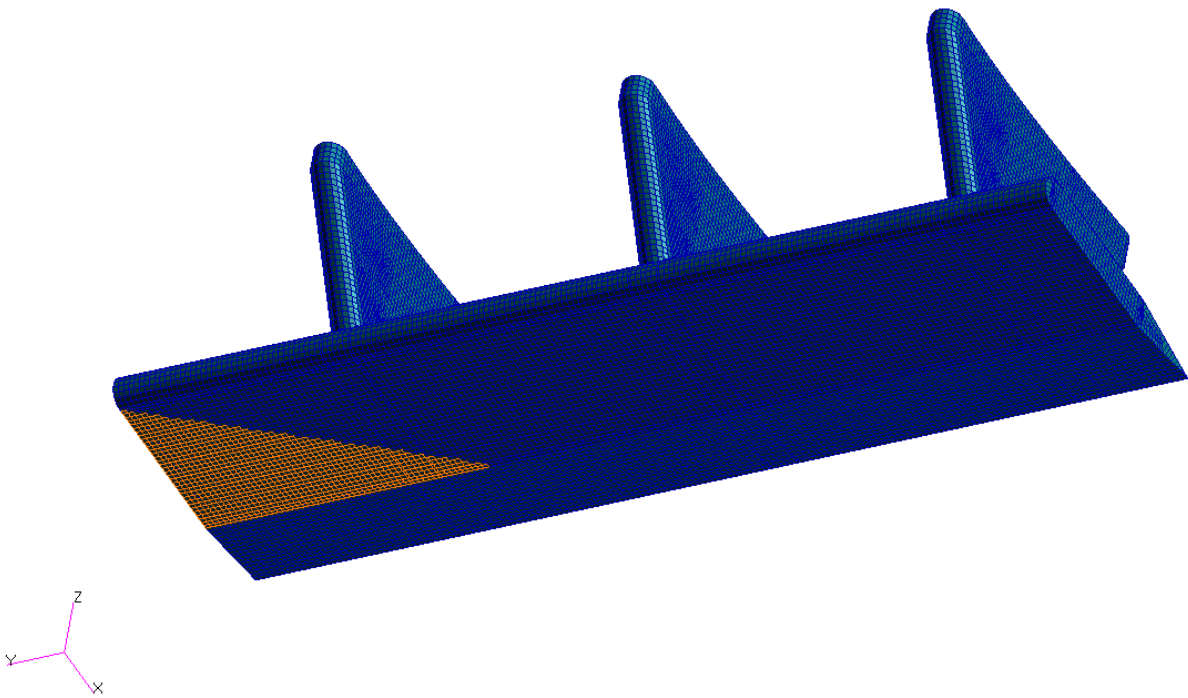


Figure 270: Outboard Lower Triangle Fairing Region (-1.3053401 lb/in²)

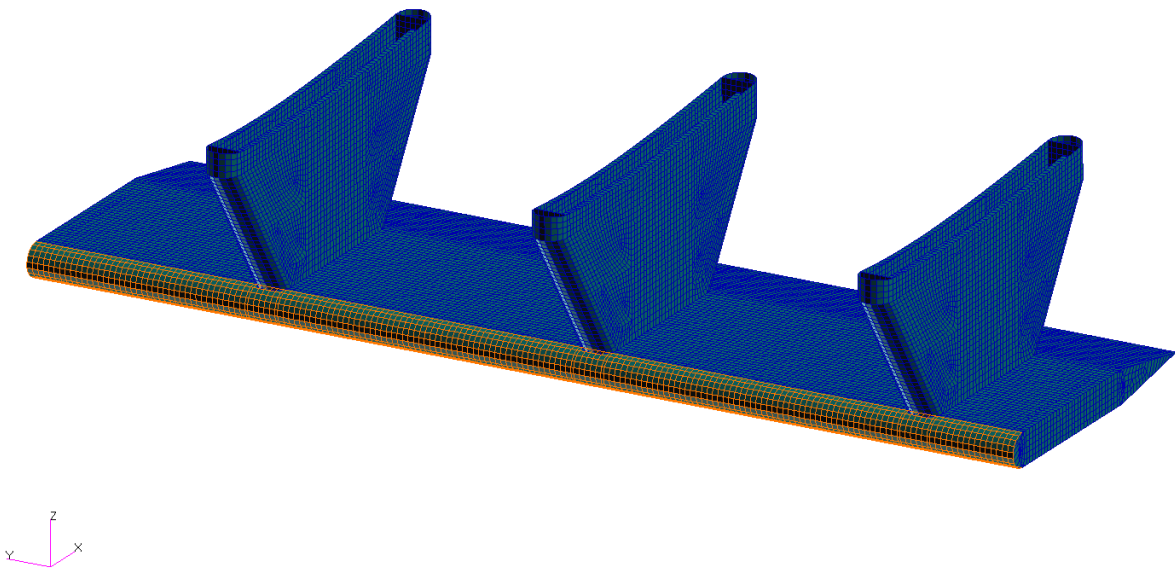


Figure 271: Leading Edge Fairing Region (1.914498 lb/in²)

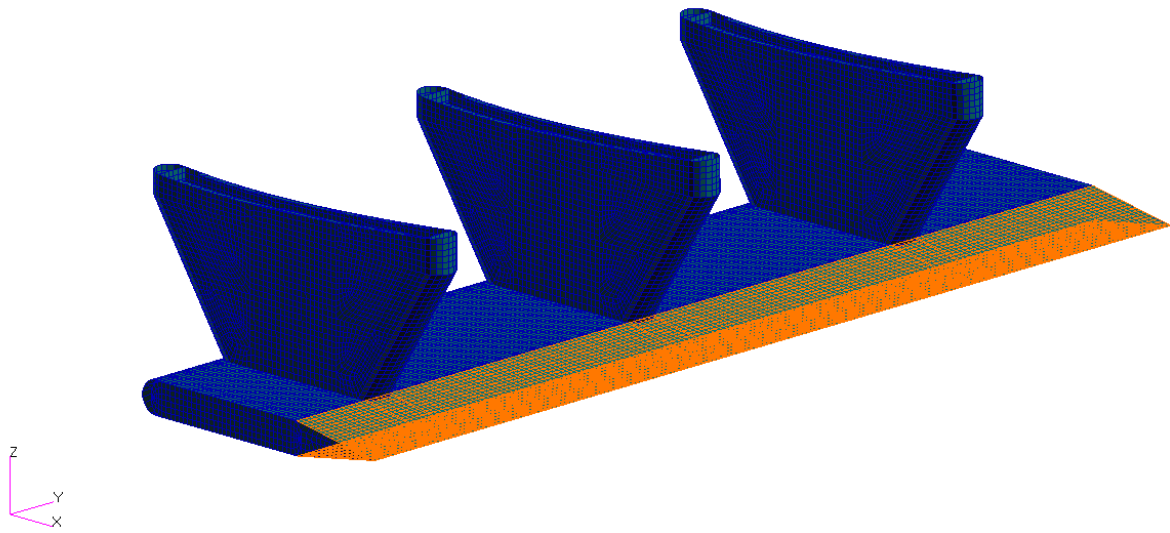


Figure 272: Trailing Edge Fairing Region (-0.69618112 lb/in²)

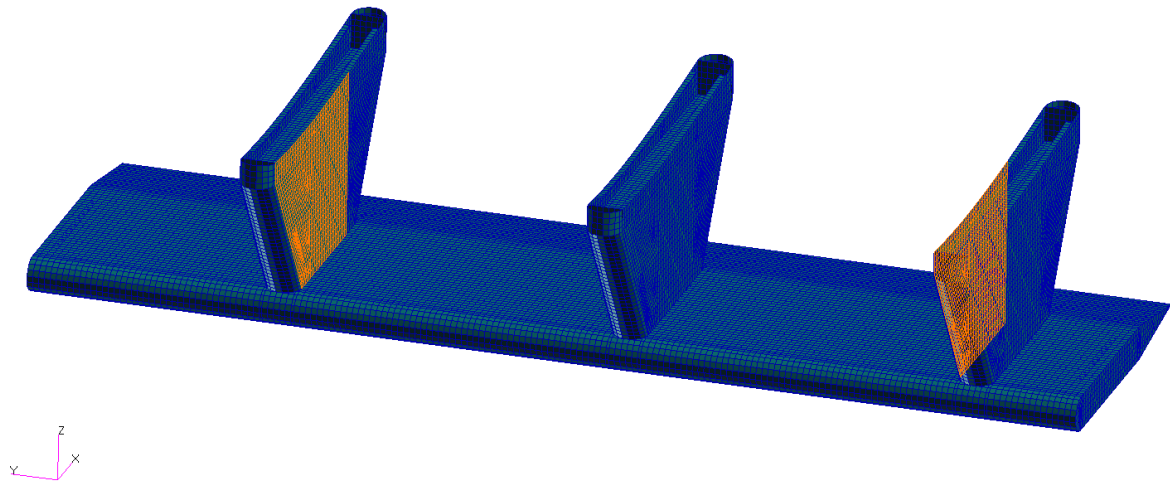


Figure 273: Forward Inboard Pylon Region (-0.43511 lb/in²)

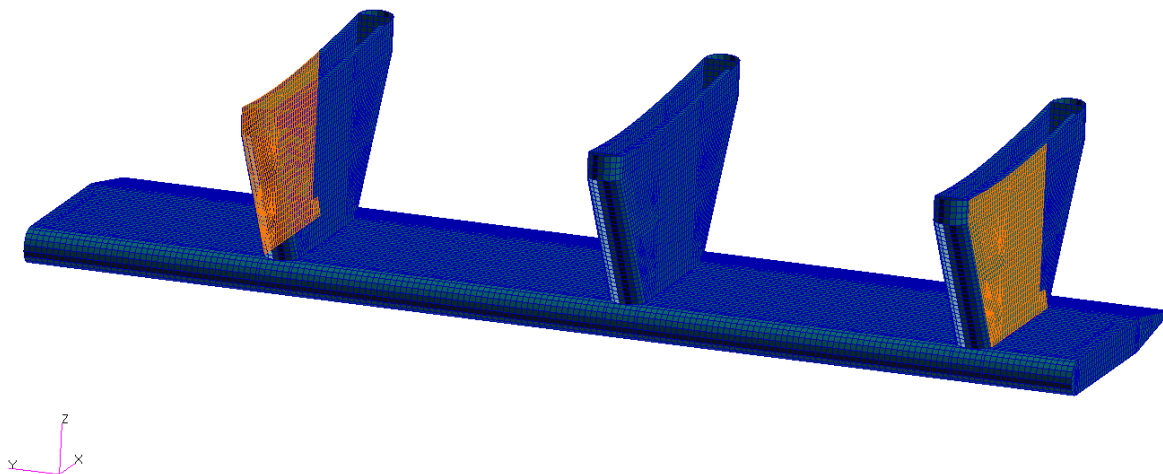


Figure 274: Forward Outboard Pylon Region (-1.45038 lb/in²)

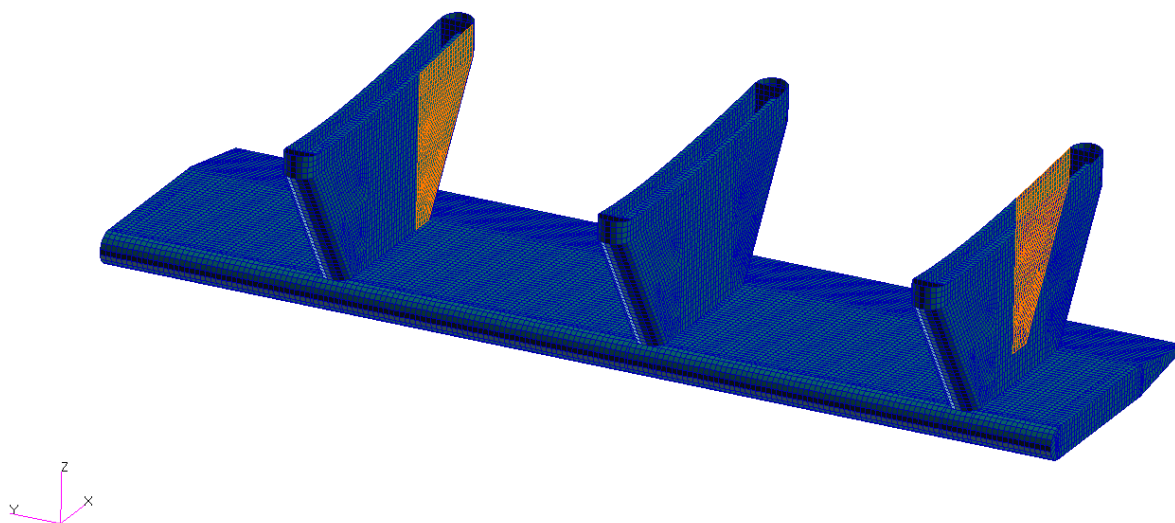


Figure 275: Aft Inboard Pylon Region (-1.01526 lb/in²)

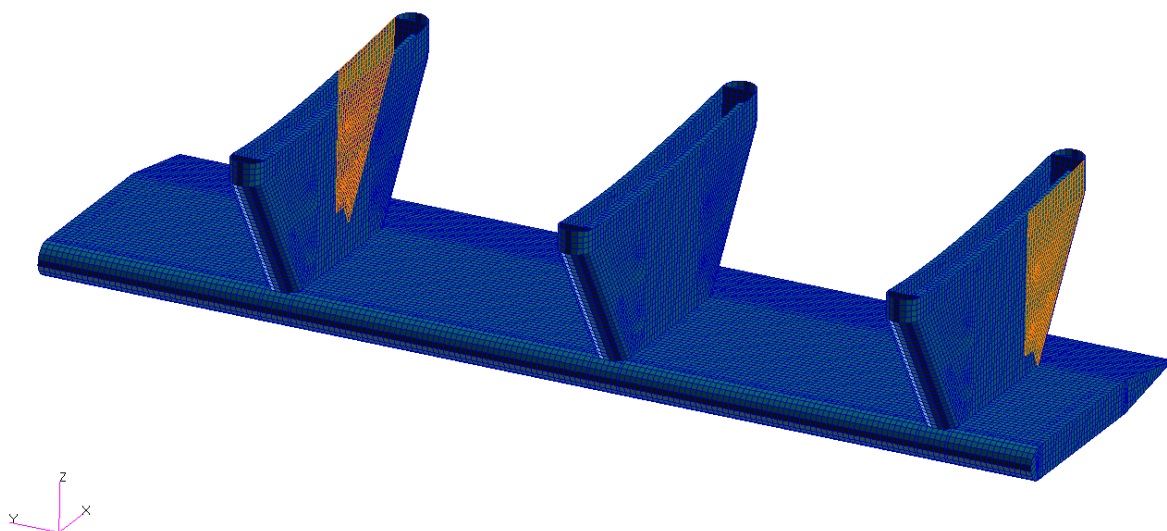


Figure 276: Aft Outboard Pylon Region (-2.03053 lb/in^2)

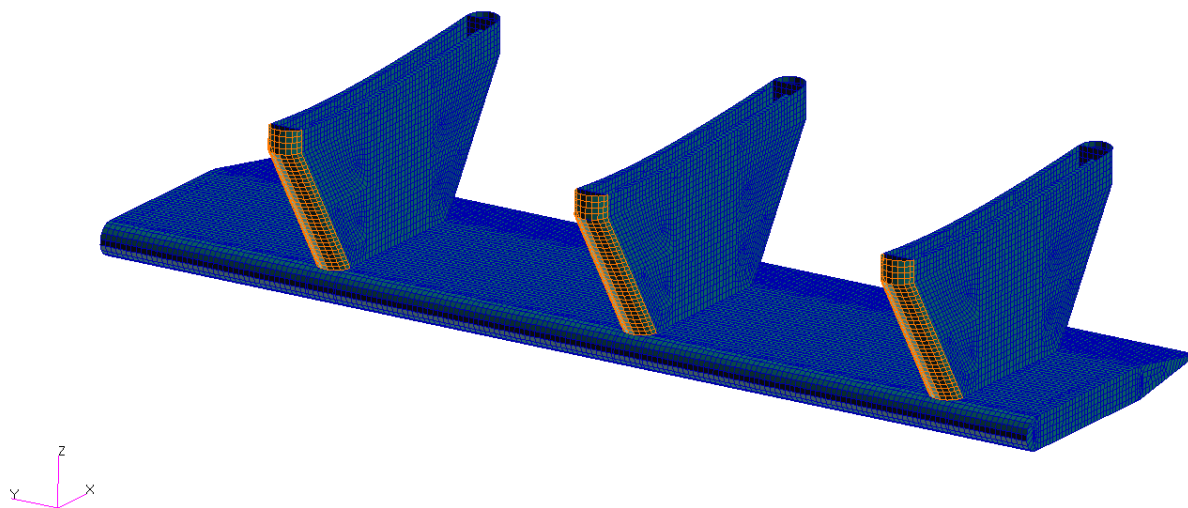


Figure 277: Leading Edge Pylon Region ($0.69618112 \text{ lb/in}^2$)

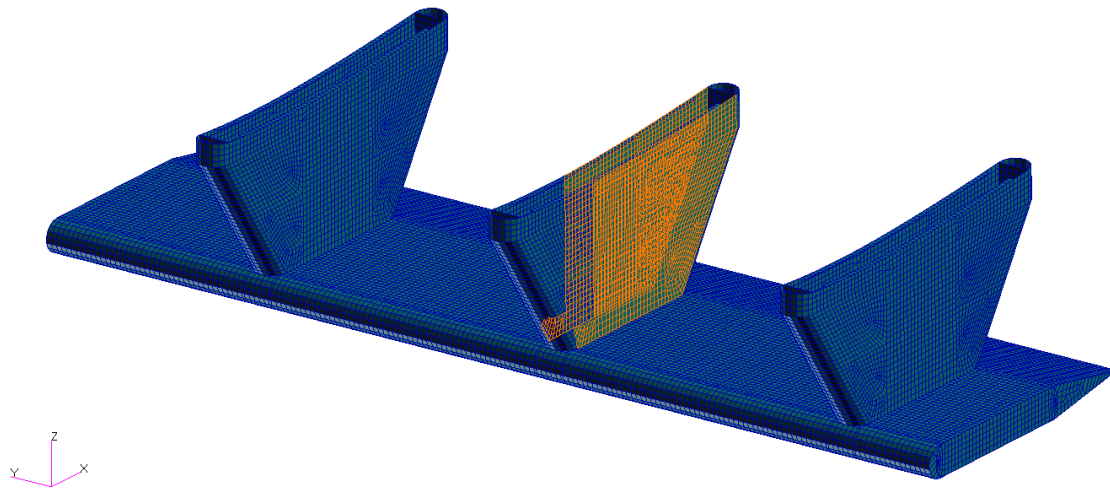


Figure 278: Aft Middle Pylon Region (-1.01526 lb/in²)

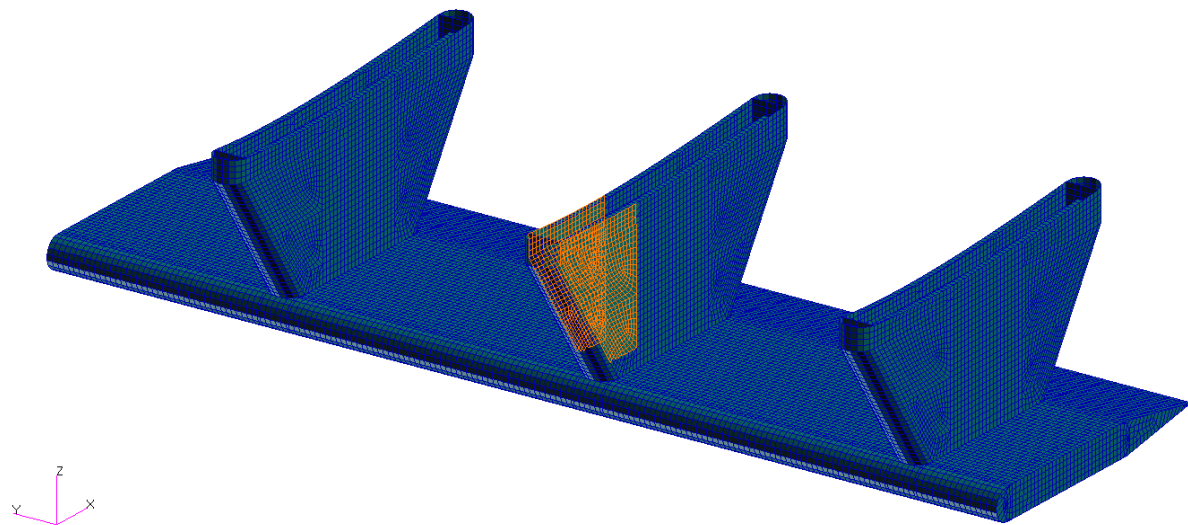


Figure 279: Forward Middle Pylon Region (-0.43511 lb/in²)

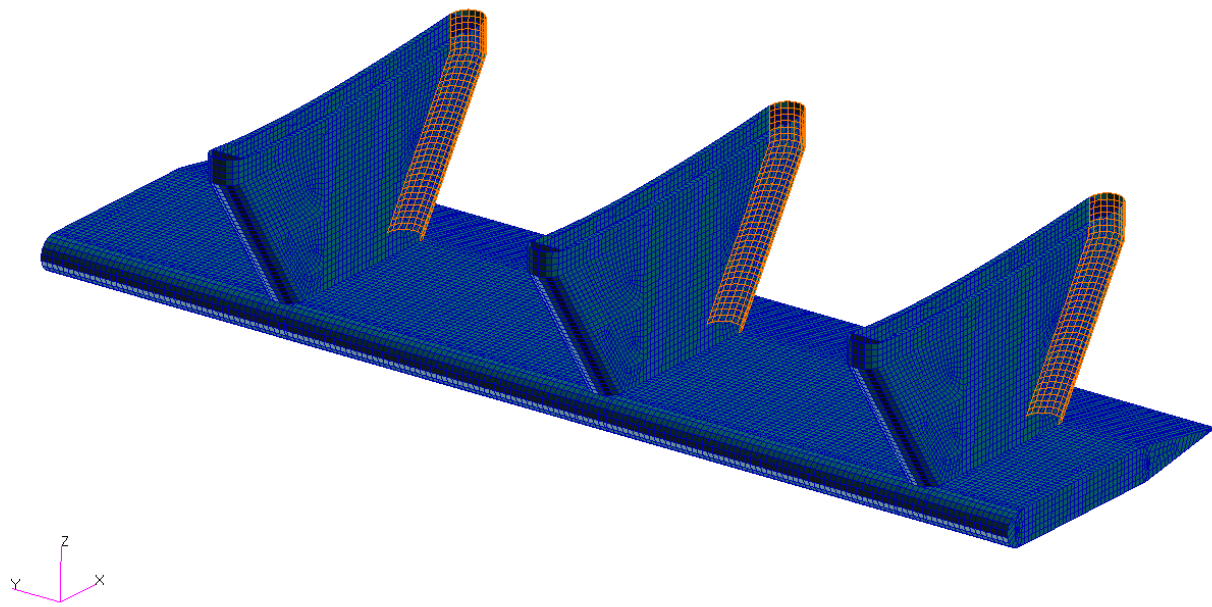


Figure 280: Trailing Edge Pylon Region (-1.1666255 lb/in²)

Appendix B: AAA Model Information

Straight Tapered Wing Geometry: Flight Condition 1							
Input Parameters							
b_w	<input type="text" value="66.00"/> ft	c_w	<input type="text" value="2.83"/> ft	y_{offset_w}	<input type="text" value="0.00"/> ft		
c_w	<input type="text" value="5.40"/> ft	Λ_{cid_w}	<input type="text" value="2.0"/> deg				
Output Parameters							
S_w	<input type="text" value="271.59"/> ft ²	λ_w	<input type="text" value="0.52"/>	y_{mpc_w}	<input type="text" value="14.78"/> ft	Λ_{LE_w}	<input type="text" value="3.1"/> deg
AR_w	<input type="text" value="16.04"/>	\bar{c}_w	<input type="text" value="4.25"/> ft	x_{mpc_w}	<input type="text" value="0.80"/> ft	Λ_{TE_w}	<input type="text" value="-1.3"/> deg
Advanced Aircraft Analysis 3.2 Project 03/24/12 11:14 AM							

Figure 281: AAA Wing Geometry

Straight Tapered V-Tail Geometry: Flight Condition 1							
Input Parameters							
AR_{vee}	<input type="text" value="14.20"/>	λ_{vee}	<input type="text" value="0.39"/>	$y_{offset_{vee}}$	<input type="text" value="0.00"/> ft		
S_{vee}	<input type="text" value="41.40"/> ft ²	$\Lambda_{cid_{vee}}$	<input type="text" value="12.3"/> deg				
Output Parameters							
c_{vee}	<input type="text" value="2.46"/> ft	b_{vee}	<input type="text" value="24.25"/> ft	$y_{mpc_{vee}}$	<input type="text" value="5.17"/> ft	$\Lambda_{LE_{vee}}$	<input type="text" value="13.9"/> deg
c_{vee}	<input type="text" value="0.95"/> ft	\bar{c}_{vee}	<input type="text" value="1.82"/> ft	$x_{mpc_{vee}}$	<input type="text" value="1.28"/> ft	$\Lambda_{TE_{vee}}$	<input type="text"/> deg
Advanced Aircraft Analysis 3.2 Project 03/24/12 11:16 AM							

Figure 282: AAA Tail Geometry

Airplane Range: Flight Condition 1			
Input Parameters			
S_w <input type="text" value="271.59"/> ft ²	W_{Cr} <input type="text" value="8400.0"/> lb	η_{prop} <input type="text" value="0.800"/>	C_{l_o} <input type="text" value="0.3086"/>
Altitude <input type="text" value="25000"/> ft	$W_{F_{Cr}}$ <input type="text" value="4000.00"/> lb	C_p <input type="text" value="0.53"/> <small>lb/hr hp</small>	α_{low} <input type="text" value="0.0"/> deg
ΔT <input type="text" value="0.0"/> deg F	$C_{D_{o_{clean,M}}}$ <input type="text" value="0.0316"/>	Φ_T <input type="text" value="0.0"/> deg	α_{high} <input type="text" value="8.0"/> deg
U_1 <input type="text" value="165.00"/> kts	$B_{DP_{clean}}$ <input type="text" value="0.0233"/>	$C_{l_{\alpha}}$ <input type="text" value="5.9116"/> rad ⁻¹	
Output Parameters			
P_{req} <input type="text" value="223"/> hp	α <input type="text" value="2.52"/> deg	$R_{C_{l_{\alpha}}_{V_{const}}}$ <input type="text" value="4616.4"/> nm	
P_{avail} <input type="text" value="587"/> hp	C_{l_1} <input type="text" value="0.5682"/>		

Advanced Aircraft Analysis 3.2 Project 04/15/12 5:06 PM

Figure 283: AAA Clean Aircraft Range Calculation

Airplane Range: Flight Condition 1			
Input Parameters			
S_w <input type="text" value="271.59"/> ft ²	W_{Cr} <input type="text" value="8571.4"/> lb	η_{prop} <input type="text" value="0.800"/>	C_{l_o} <input type="text" value="0.3086"/>
Altitude <input type="text" value="25000"/> ft	$W_{F_{Cr}}$ <input type="text" value="4000.00"/> lb	C_p <input type="text" value="0.53"/> <small>lb/hr hp</small>	α_{low} <input type="text" value="0.0"/> deg
ΔT <input type="text" value="0.0"/> deg F	$C_{D_{o_{clean,M}}}$ <input type="text" value="0.0357"/>	Φ_T <input type="text" value="0.0"/> deg	α_{high} <input type="text" value="8.0"/> deg
U_1 <input type="text" value="165.00"/> kts	$B_{DP_{clean}}$ <input type="text" value="0.0233"/>	$C_{l_{\alpha}}$ <input type="text" value="5.9116"/> rad ⁻¹	
Output Parameters			
P_{req} <input type="text" value="248"/> hp	α <input type="text" value="2.66"/> deg	$R_{C_{l_{\alpha}}_{V_{const}}}$ <input type="text" value="4136.5"/> nm	
P_{avail} <input type="text" value="587"/> hp	C_{l_1} <input type="text" value="0.5832"/>		

Advanced Aircraft Analysis 3.2 Project 04/15/12 5:03 PM

Figure 284: AAA Sharp Trailing Edges Ranges Calculation

Airplane Range: Flight Condition 1			
Input Parameters			
S_w	<input type="text" value="271.59"/> ft^2	W_{Cr}	<input type="text" value="8571.4"/> lb
η_{prop}	<input type="text" value="0.800"/>	C_{D_o}	<input type="text" value="0.3086"/>
Altitude	<input type="text" value="25000"/> ft	$W_{F_{Cr}}$	<input type="text" value="4000.00"/> lb
c_p	<input type="text" value="0.53"/> $\frac{\text{lb/hr}}{\text{hp}}$	α_{low}	<input type="text" value="0.0"/> deg
ΔT	<input type="text" value="0.0"/> deg F	$C_{D_{o_{clean,M}}}$	<input type="text" value="0.0390"/>
Φ_T	<input type="text" value="0.0"/> deg	α_{high}	<input type="text" value="8.0"/> deg
U_1	<input type="text" value="165.00"/> kts	$B_{DP_{clean}}$	<input type="text" value="0.0233"/>
$C_{L_{\alpha}}$	<input type="text" value="5.9116"/> rad^{-1}		
Output Parameters			
P_{req}	<input type="text" value="267"/> hp	α	<input type="text" value="2.66"/> deg
$R_{C_{r_{V_{uconst}}}}$	<input type="text" value="3839.0"/> nm		
P_{avail}	<input type="text" value="587"/> hp	C_{L_1}	<input type="text" value="0.5830"/>

Advanced Aircraft Analysis 3.2 Project 04/15/12 5:04 PM

Figure 285: AAA Sharp Fairing, Circular Pylons Trailing Edges Range Calculation

Airplane Range: Flight Condition 1			
Input Parameters			
S_w	<input type="text" value="271.59"/> ft^2	W_{Cr}	<input type="text" value="8571.4"/> lb
η_{prop}	<input type="text" value="0.800"/>	C_{D_o}	<input type="text" value="0.3086"/>
Altitude	<input type="text" value="25000"/> ft	$W_{F_{Cr}}$	<input type="text" value="4000.00"/> lb
c_p	<input type="text" value="0.53"/> $\frac{\text{lb/hr}}{\text{hp}}$	α_{low}	<input type="text" value="0.0"/> deg
ΔT	<input type="text" value="0.0"/> deg F	$C_{D_{o_{clean,M}}}$	<input type="text" value="0.0444"/>
Φ_T	<input type="text" value="0.0"/> deg	α_{high}	<input type="text" value="8.0"/> deg
U_1	<input type="text" value="165.00"/> kts	$B_{DP_{clean}}$	<input type="text" value="0.0233"/>
$C_{L_{\alpha}}$	<input type="text" value="5.9116"/> rad^{-1}		
Output Parameters			
P_{req}	<input type="text" value="298"/> hp	α	<input type="text" value="2.66"/> deg
$R_{C_{r_{V_{uconst}}}}$	<input type="text" value="3443.2"/> nm		
P_{avail}	<input type="text" value="587"/> hp	C_{L_1}	<input type="text" value="0.5828"/>

Advanced Aircraft Analysis 3.2 Project 04/15/12 5:02 PM

Figure 286: AAA Sharp Pylons, Circular Fairing Trailing Edges Range Calculation

Airplane Range: Flight Condition 1			
Input Parameters			
S_w <input type="text" value="271.59"/> ft ²	W_{Cr} <input type="text" value="8571.4"/> lb	η_{prop} <input type="text" value="0.800"/>	C_{L_o} <input type="text" value="0.3086"/>
Altitude <input type="text" value="25000"/> ft	$W_{F_{Cr}}$ <input type="text" value="4000.00"/> lb	C_p <input type="text" value="0.53"/> <small>lb/hr hp</small>	α_{low} <input type="text" value="0.0"/> deg
ΔT <input type="text" value="0.0"/> deg F	$C_{D_{clean,M}}$ <input type="text" value="0.0478"/>	Φ_T <input type="text" value="0.0"/> deg	α_{high} <input type="text" value="8.0"/> deg
U_1 <input type="text" value="165.00"/> kts	$B_{DIP_{clean}}$ <input type="text" value="0.0233"/>	$C_{L_{ix}}$ <input type="text" value="5.9116"/> rad ⁻¹	
Output Parameters			
P_{req} <input type="text" value="317"/> hp	α <input type="text" value="2.66"/> deg	$R_{C_{r_{V_{const}}}}$ <input type="text" value="3234.3"/> nm	
P_{avail} <input type="text" value="587"/> hp	C_{L_1} <input type="text" value="0.5826"/>		

Advanced Aircraft Analysis 3.2 Project 04/15/12 5:05 PM

Figure 287: AAA Circular Trailing Edges Range Calculation

Take-off Distance: Flight Condition 1			
Input Parameters			
S_w <input type="text" value="271.59"/> ft ²	W_{TO} <input type="text" value="10500.0"/> lb	$V_o/V_{S_{TO}}$ <input type="text" value="1.15"/>	D_{prop} <input type="text" value="9.50"/> ft
AR_w <input type="text" value="16.04"/>	$C_{L_{max_{TO}}}$ <input type="text" value="2.000"/>	μ_G <input type="text" value="0.0200"/>	Φ_T <input type="text" value="0.0"/> deg
h_{TO} <input type="text" value="0"/> ft	$C_{D_{a_{TO_down}}}$ <input type="text" value="0.0363"/>	\bar{a}/g <input type="text" value="0.40"/>	$C_{L_{ix_{TO}}}$ <input type="text" value="0.5730"/> rad ⁻¹
ΔT_{TO} <input type="text" value="0.0"/> deg F	$(L/D)_{OEI}$ <input type="text" value="14.75"/>	SHP_{set} <input type="text" value="900"/> hp	$C_{L_{o_{TO}}}$ <input type="text" value="-1.0000"/>
Output Parameters			
P_{TO}/ND_p^2 <input type="text" value="9.97"/> <small>hp ft²</small>	V_{LOF} <input type="text" value="91.97"/> kts	S_{TOG} <input type="text" value="1911"/> ft	
$V_{S_{TO}}$ <input type="text" value="83.60"/> kts	S_{TO} <input type="text" value="2219"/> ft	BFL <input type="text" value=""/> ft	

Advanced Aircraft Analysis 3.2 Project 05/26/12 4:43 PM

Figure 288: Clean Takeoff Distance

Take-off Distance: Flight Condition 1			
Input Parameters			
S_w <input style="width: 80%;" type="text" value="271.59"/> ft ²	W_{TO} <input style="width: 80%;" type="text" value="10500.0"/> lb	$V_{g}/V_{S_{TO}}$ <input style="width: 80%;" type="text" value="1.15"/>	D_{prop} <input style="width: 80%;" type="text" value="9.50"/> ft
AR_w <input style="width: 80%;" type="text" value="16.04"/>	$C_{L_{max_{TO}}}$ <input style="width: 80%;" type="text" value="2.000"/>	μ_G <input style="width: 80%;" type="text" value="0.0200"/>	Φ_T <input style="width: 80%;" type="text" value="0.0"/> deg
h_{TO} <input style="width: 80%;" type="text" value="0"/> ft	$C_{D_{0_{TO_down}}}$ <input style="width: 80%;" type="text" value="0.0404"/>	\bar{a}/g <input style="width: 80%;" type="text" value="0.40"/>	$C_{L_{\alpha_{TO}}}$ <input style="width: 80%;" type="text" value="0.5730"/> rad ⁻¹
ΔT_{TO} <input style="width: 80%;" type="text" value="0.0"/> deg F	$(L/D)_{OEI}$ <input style="width: 80%;" type="text" value="14.75"/>	SHP_{set} <input style="width: 80%;" type="text" value="900"/> hp	$C_{L_{\alpha_{TO}}}$ <input style="width: 80%;" type="text" value="-1.0000"/>
Output Parameters			
P_{TO}/ND_p^2 <input style="width: 80%;" type="text" value="9.97"/> $\frac{hp}{ft^2}$	V_{LOF} <input style="width: 80%;" type="text" value="91.97"/> kts	S_{TOG} <input style="width: 80%;" type="text" value="1926"/> ft	
$V_{S_{TO}}$ <input style="width: 80%;" type="text" value="83.60"/> kts	S_{TO} <input style="width: 80%;" type="text" value="2230"/> ft	BFL <input style="width: 80%;" type="text" value=""/>	

Advanced Aircraft Analysis 3.2 Project 05/26/12 4:56 PM

Figure 289: Sharp Trailing Edges Takeoff Distance

Take-off Distance: Flight Condition 1			
Input Parameters			
S_w <input style="width: 80%;" type="text" value="271.59"/> ft ²	W_{TO} <input style="width: 80%;" type="text" value="10500.0"/> lb	$V_{g}/V_{S_{TO}}$ <input style="width: 80%;" type="text" value="1.15"/>	D_{prop} <input style="width: 80%;" type="text" value="9.50"/> ft
AR_w <input style="width: 80%;" type="text" value="16.04"/>	$C_{L_{max_{TO}}}$ <input style="width: 80%;" type="text" value="2.000"/>	μ_G <input style="width: 80%;" type="text" value="0.0200"/>	Φ_T <input style="width: 80%;" type="text" value="0.0"/> deg
h_{TO} <input style="width: 80%;" type="text" value="0"/> ft	$C_{D_{0_{TO_down}}}$ <input style="width: 80%;" type="text" value="0.0437"/>	\bar{a}/g <input style="width: 80%;" type="text" value="0.40"/>	$C_{L_{\alpha_{TO}}}$ <input style="width: 80%;" type="text" value="0.5730"/> rad ⁻¹
ΔT_{TO} <input style="width: 80%;" type="text" value="0.0"/> deg F	$(L/D)_{OEI}$ <input style="width: 80%;" type="text" value="14.75"/>	SHP_{set} <input style="width: 80%;" type="text" value="900"/> hp	$C_{L_{\alpha_{TO}}}$ <input style="width: 80%;" type="text" value="-1.0000"/>
Output Parameters			
P_{TO}/ND_p^2 <input style="width: 80%;" type="text" value="9.97"/> $\frac{hp}{ft^2}$	V_{LOF} <input style="width: 80%;" type="text" value="91.97"/> kts	S_{TOG} <input style="width: 80%;" type="text" value="1938"/> ft	
$V_{S_{TO}}$ <input style="width: 80%;" type="text" value="83.60"/> kts	S_{TO} <input style="width: 80%;" type="text" value="2239"/> ft	BFL <input style="width: 80%;" type="text" value=""/>	

Advanced Aircraft Analysis 3.2 Project 05/26/12 5:00 PM

Figure 290: Sharp Fairing Circular Pylon Trailing Edges Takeoff Distance

Take-off Distance: Flight Condition 1			
Input Parameters			
S_w <input type="text" value="271.59"/> ft ²	W_{TO} <input type="text" value="10500.0"/> lb	$V_{g}/V_{S_{TO}}$ <input type="text" value="1.15"/>	D_{prop} <input type="text" value="9.50"/> ft
AR_w <input type="text" value="16.04"/>	$C_{L_{max_{TO}}}$ <input type="text" value="2.000"/>	μ_G <input type="text" value="0.0200"/>	Φ_T <input type="text" value="0.0"/> deg
h_{TO} <input type="text" value="0"/> ft	$C_{D_{0_{TO_down}}}$ <input type="text" value="0.0491"/>	\bar{a}/g <input type="text" value="0.40"/>	$C_{L_{\alpha_{TO}}}$ <input type="text" value="0.5730"/> rad ⁻¹
ΔT_{TO} <input type="text" value="0.0"/> deg F	$(L/D)_{OEI}$ <input type="text" value="14.75"/>	SHP_{set} <input type="text" value="900"/> hp	$C_{L_{\alpha_{TO}}}$ <input type="text" value="-1.0000"/>
Output Parameters			
P_{TO}/ND_p^2 <input type="text" value="9.97"/> $\frac{hp}{ft^2}$	V_{LOF} <input type="text" value="91.97"/> kts	S_{TOG} <input type="text" value="1957"/> ft	
$V_{S_{TO}}$ <input type="text" value="83.60"/> kts	S_{TO} <input type="text" value="2254"/> ft	BFL <input type="text" value=""/>	

Advanced Aircraft Analysis 3.2 Project 05/26/12 5:01 PM

Figure 291: Circular Fairing Sharp Pylon Trailing Edges Takeoff Distance

Take-off Distance: Flight Condition 1			
Input Parameters			
S_w <input type="text" value="271.59"/> ft ²	W_{TO} <input type="text" value="10500.0"/> lb	$V_{g}/V_{S_{TO}}$ <input type="text" value="1.15"/>	D_{prop} <input type="text" value="9.50"/> ft
AR_w <input type="text" value="16.04"/>	$C_{L_{max_{TO}}}$ <input type="text" value="2.000"/>	μ_G <input type="text" value="0.0200"/>	Φ_T <input type="text" value="0.0"/> deg
h_{TO} <input type="text" value="0"/> ft	$C_{D_{0_{TO_down}}}$ <input type="text" value="0.0525"/>	\bar{a}/g <input type="text" value="0.40"/>	$C_{L_{\alpha_{TO}}}$ <input type="text" value="0.5730"/> rad ⁻¹
ΔT_{TO} <input type="text" value="0.0"/> deg F	$(L/D)_{OEI}$ <input type="text" value="14.75"/>	SHP_{set} <input type="text" value="900"/> hp	$C_{L_{\alpha_{TO}}}$ <input type="text" value="-1.0000"/>
Output Parameters			
P_{TO}/ND_p^2 <input type="text" value="9.97"/> $\frac{hp}{ft^2}$	V_{LOF} <input type="text" value="91.97"/> kts	S_{TOG} <input type="text" value="1970"/> ft	
$V_{S_{TO}}$ <input type="text" value="83.60"/> kts	S_{TO} <input type="text" value="2264"/> ft	BFL <input type="text" value=""/>	

Advanced Aircraft Analysis 3.2 Project 05/26/12 5:01 PM

Figure 292: Circular Trailing Edges Takeoff Distance